

**STRUCTURAL TRANSFORMATIONS RELATED  
TO ORGANIC SOLID-STATE REACTIONS:  
CORRELATION STUDIES OF NMR AND X-RAY  
ANALYSIS**

Dissertation  
zur Erlangung des Grades

Doktor der Naturwissenschaften

im Promotionsfach Chemie

am Fachbereich Chemie,  
Pharmazie und Geowissenschaften  
der Johannes Gutenberg-Universität Mainz

vorgelegt von

**MUJEEB KHAN**

geboren in Hyderabad (Indien)

Mainz, 2008

D77(Dissertation Universität Mainz)

# TABLE OF CONTENTS

<b>1. INTRODUCTION .....</b>	<b>5</b>
1.1. MOTIVATION .....	5
<b>2. ORGANIC SOLID-STATE REACTIONS .....</b>	<b>9</b>
2.1. TOPOCHEMICAL CONTROL OF SOLID-STATE ORGANIC REACTIONS.....	9
2.2. TOPOCHEMISTRY .....	11
2.2.1. Topochemical vs. nontopochemical processes .....	11
2.2.2. Schmidt's topochemical principle.....	11
2.3. SOLID SOLUTIONS.....	14
2.3.1. Examples of homogeneous and heterogeneous mechanisms .....	15
2.4. SINGLE-CRYSTAL-TO-SINGLE-CRYSTAL TRANSFORMATION .....	19
2.4.1. Significance of SCSC transformations .....	20
2.4.2. Characterization techniques for SCSC transformations .....	20
2.4.3. SCSC transformations using tail-irradiation.....	21
2.5. CRYSTAL ENGINEERING.....	25
2.5.1. Intermolecular forces in crystals .....	26
2.5.2. Hydrogen Bonding .....	28
2.5.3. Cocrystals.....	29
2.5.4. Supramolecular synthons .....	30
<b>3. FUNDAMENTALS OF EXPERIMENTAL TECHNIQUES .....</b>	<b>33</b>
3.1. INTRODUCTION OF NMR ANALYSIS .....	33
3.2. BASICS OF NMR AND INTERACTIONS .....	33
3.3. ZEEMAN- INTERACTION .....	36
3.4. EFFECTS OF RADIO FREQUENCY FIELD ( $B_1$ ) .....	38
3.5. CHEMICAL SHIELDING .....	39

## Table of contents

---

<b>3.6. DIPOLE-DIPOLE INTERACTION.....</b>	<b>41</b>
<b>3.7. MAGIC ANGLE SPINNING .....</b>	<b>42</b>
<b>3.8. SINGLE-PULSE EXCITATION AND SINGLE PULSE DETECTION.....</b>	<b>43</b>
<b>3.9. CROSS POLARIZATION (CP).....</b>	<b>44</b>
<b>3.10. INTRODUCTION OF X-RAY ANALYSIS.....</b>	<b>46</b>
3.10.1. Bragg's law .....	46
3.10.2. Single crystal X-ray diffraction.....	47
3.10.3. Powder diffraction .....	49
<b>4. TRANSIENT STATES IN [2+2] PHOTODIMERIZATION OF CINNAMIC ACID .....</b>	<b>50</b>
<b>4.1. INTRODUCTION.....</b>	<b>50</b>
<b>4.2. CONFORMATION OF CARBOXYL GROUP .....</b>	<b>52</b>
<b>4.3. SOLID-STATE <sup>13</sup>C-CPMAS NMR APPLICATION.....</b>	<b>52</b>
<b>4.4. REPLACING CARBOXYL ACID MIOETY.....</b>	<b>55</b>
<b>4.5. DYNAMICS OF HYDROGEN BONDS.....</b>	<b>57</b>
<b>4.6. STRUCTURAL CORRELATIONS.....</b>	<b>58</b>
<b>4.7. DEUTERIUM NMR MEASUREMENTS.....</b>	<b>59</b>
<b>4.8. HIGH TEMPERATURE X-RAY ANALYSIS .....</b>	<b>61</b>
<b>4.9. SYNPLANAR Vs. ANTIPLANAR CONFORMATION .....</b>	<b>61</b>
<b>4.10. AB INITIO COMPUTATIONS.....</b>	<b>65</b>
<b>4.11. CONCLUSIONS .....</b>	<b>65</b>
<b>4.12. EXPERIMENTAL.....</b>	<b>66</b>
4.12.1. Synthesis of truxillic acid.....	66
4.12.2. Synthesis of methyl ester of truxillic acid.....	67
4.12.3. Solid-State NMR measurment .....	68
4.12.4. Solution NMR and mass .....	68
4.12.5. DFT-based chemical shift calculations.....	68
4.12.6. Single Crystal X-ray Analysis .....	69
<b>5. O-H...N HETEROSYNTHON: A ROBUST SUPRAMOLECULAR UNIT FOR CRYSTAL ENGINEERING .....</b>	<b>70</b>

## Table of contents

---

<b>5.1. INTRODUCTION.....</b>	<b>70</b>
<b>5.2. HYDROGEN BOND MEDIATED SELF ASSEMBLY .....</b>	<b>72</b>
<b>5.3. CO-CRYSTALLIZATION OF RESORCINOLS AND MONOPYRIDINES LEADING TO THE DESIRED STRUCTURES .....</b>	<b>74</b>
<b>5.4. CO-CRYSTALLIZATION OF RESORCINOLS AND DIPYRIDINES LEADING TO THE DESIRED STRUCTURES .....</b>	<b>75</b>
<b>5.5. CO-CRYSTALLIZATION OF RESORCINOLS WITH MONO- OR DIPYRIDINES LEADING TO THE UNDESIRED STRUCTURES.....</b>	<b>77</b>
<b>5.6. MOLECULAR RECOGNITION OF PHOTOREACTIVE CONJUGATED DIPYRIDINES .....</b>	<b>80</b>
<b>5.7. MONITORING THE STRUCTURAL CHANGES BY X-RAY ANALYSIS</b>	<b>83</b>
<b>5.8. TILTING AND DEFORMATION OF PYRIDYL AND PHENYL RINGS ..</b>	<b>86</b>
<b>5.9. CONCLUSIONS .....</b>	<b>89</b>
<b>5.10. Experimental Section.....</b>	<b>90</b>
5.10.1. General Details .....	90
5.10.2. Preparations of photoreactive conjugated dipyridines .....	90
5.10.3. 2,6-Bis[(E)-2-(4-pyridyl)ethenyl]naphthalene (bpen).....	91
5.10.4. Crystal Preparation .....	91
<b>6. PROBING STRUCTURAL TRANSFORMATIONS IN 2(BPE):2(RES) HETEROSYNTHON BY NMR METHODS IN THE SOLID-STATE.....</b>	<b>93</b>
<b>6.1. INTRODUCTION.....</b>	<b>93</b>
<b>6.2. MOLECULAR CONFORMATION OF RESORCINOL .....</b>	<b>95</b>
<b>6.3. MOLECULAR CONFORMATION OF BPE.....</b>	<b>99</b>
<b>6.4. MOLECULAR SPECIFICITY OF THE O-H...N HERETOSYNTHON ...</b>	<b>101</b>
<b>6.5. NEW POLYMORPH OF 2(BPE):2(RES) MONOMER.....</b>	<b>102</b>
<b>6.6. MOLECULAR CONFORMATION OF 2(BPE):2(RES) MONOMER.....</b>	<b>104</b>
<b>6.7. OBSERVATION OF A NEW POLYMORPH OF 2(BPE):2(RES) DIMER</b>	<b>107</b>
<b>6.8. THERMAL ANALYSIS OF 2(BPE):2(RES) DIMER .....</b>	<b>109</b>
<b>6.9. REMOVAL OF TEMPLATE FROM 2(BPE):2(RES) DIMER .....</b>	<b>110</b>
<b>6.10. CONCLUSIONS .....</b>	<b>113</b>
<b>6.11. EXPERIMENTAL.....</b>	<b>114</b>
6.11.1. Preparation of 2(bpe):2(res) monomer complex .....	114

## Table of contents

---

6.11.2. Co-crystallization of resorcinol, bpe and bpet .....	115
6.11.3. Extraction of tetrakis(4-pyridyl)cyclobutane .....	115
6.11.4. Solid-State NMR analysis .....	116
6.11.5. Solution NMR and mass .....	116
6.11.6. DFT-based chemical shift calculations .....	116
6.11.7. Single Crystal X-Ray Analysis .....	116
<b>7. PROBING STRUCTURAL TRANSFORMATIONS IN 2(BPE):2(RES) HETEROSYNTHON VIA SINGLE CRYSTAL X-RAY ANALYSIS .....</b>	<b>117</b>
7.1. INTRODUCTION.....	117
7.2. TAILORED [2+2] PHOTODIMERIZATION.....	117
7.3. SOLID-STATE REACTIVITY .....	120
7.4. CHANGES IN LATTICE PARAMETERS .....	122
7.5. POLYMORPHISM.....	123
7.6. ANALYSIS OF SUBSTITUTIONAL MIXED CRYSTALS .....	123
7.7. CONCLUSIONS .....	125
<b>8. SUMMARY .....</b>	<b>127</b>
<b>REFERENCES .....</b>	<b>130</b>
<b>APPENDIX.....</b>	<b>138</b>

# CHAPTER 1

## INTRODUCTION

### 1.1. MOTIVATION

This dissertation deals with *organic photoreactions* in the crystalline state. The main objective of this work comprises the investigation of the intermediate states that are obtained during different organic solid-state reactions like  $[2+2]$  *photoaddition* by the application of various characterization techniques such as solid-state NMR and single crystal X-ray analysis. Organic photoreactions in the crystalline state have been extensively studied.<sup>[1,2]</sup> In particular, lattice control over reaction pathways now seems to be entering a period of flowering and growth. Indeed, deeper understanding of packing effects and insights into topochemistry facilitates a more rationalized approach to organic solid-state reactions. The combination of X-ray crystallography, solid-state NMR spectroscopy and high resolution electron microscopy, provided insights into structure property relations, thus allowing for products with tailored properties.

A  $[2+2]$  photodimerization is a photon-induced chemical reaction in which a pair of double bonds forms a cyclobutane ring (cf. Figure 1.1). The theoretical foundations of the reaction have been described by Woodward and Hoffmann,<sup>[3]</sup> and the geometry criteria for the reaction to proceed in the solid-state have been laid out by Schmidt and co-workers.<sup>[4-9]</sup> Schmidt has summarized criteria in a set of topochemical postulates notifying that a pair of double bonds must be parallel and separated by a distance of 4.2 Å or less to react. Indeed,  $[2+2]$  Photodimerizations are among the most extensively studied organic solid-state reactions.<sup>[1,10]</sup>

The range of reactions that have since then been reported to be topochemically controlled has increased significantly, but naturally cannot compete with synthetic chemistry in solution. What has given particular impetus to the study of organic solid-state reactions is the appreciation that the “frozen” state of the reactant can allow very detailed exploration of the mechanistic aspect of the solid-state reactions.<sup>[11,12]</sup> Other developments in the areas of morphology control, crystal growth inhibition, crystal-to-crystal conversions,<sup>[13]</sup> absolute asymmetric synthesis, and, more recently, supramolecular design<sup>[14]</sup> and molecular recognition have all impinged on the development of organic solid-state chemistry.

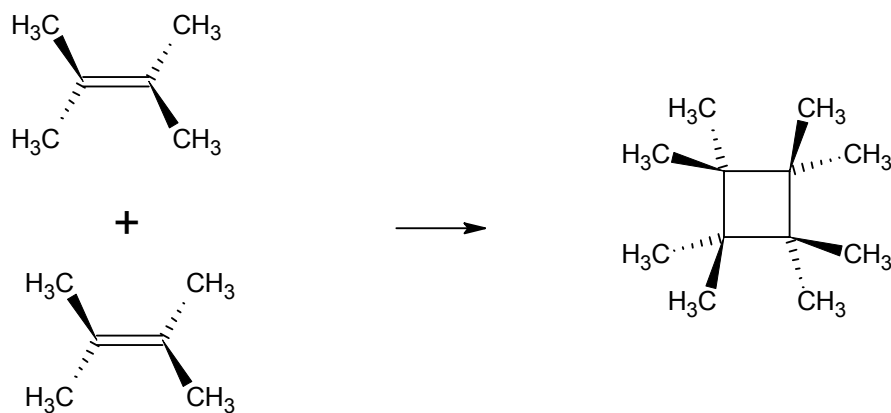


**Figure 1.1:** Addition across two double bonds to form a cyclobutane ring

The topotactic nature of the reaction intermediates and products obtained during organic solid-state reactions has been revealed by applying various techniques such as atomic force microscopy (AFM),<sup>[15,16]</sup> vibrational spectroscopy,<sup>[17-20]</sup> X-ray diffraction<sup>[21-23]</sup> and solid-state NMR.<sup>[24-28]</sup> Since AFM is primarily sensitive to *surfaces*, structural information cannot be obtained directly. In contrast, vibrational spectroscopy monitors the topotactic nature of organic solid-state reactions, but conformational details of possible intermediate states remain vague. X-ray crystallography is an excellent tool to investigate photodimerization reactions of single crystals. However, many crystals tend to shatter into microcrystalline particles as the dimerization proceeds, rendering an X-ray analysis of obtained products difficult.

Nonetheless, by utilizing a selective reaction procedure<sup>[29-34]</sup> (tail-irradiation technique) where the photoactive crystals are irradiated by the light for which they have low absorptivity, a single-crystal-to-single-crystal<sup>[13]</sup> (SCSC) transformation can be facilitated which is a chemical reaction of a single crystal wherein the product of the reaction forms within the solid phase of the reactant. With this technique even crystals (and their corresponding X-ray structures) at *intermediate* stages of the photodimerization can be obtained. These can be characterized as substitutional mixed crystals in which the dimer and monomer pair occupies the same lattice site with occupancy according to the conversion. However, a severe limitation of this technique stems from the fact that it is not suitable for the characterization of either amorphous or rather ill-defined solids that lack long-range translational order. In addition, the localization of lighter atoms (e.g. hydrogen-bonded protons)<sup>[35,36]</sup> may be difficult even with sophisticated X-ray diffraction methods.<sup>[37]</sup>

In more recent studies it has been demonstrated that solid-state NMR can also be successfully applied to monitor organic solid-state photoreactions.<sup>[24-28]</sup> Its unique selectivity allows for the differentiation of chemically distinct sites, including protons,<sup>[38]</sup> on the basis of the NMR chemical shift.<sup>[39]</sup> Thus, solid-state NMR reveals molecular species present in the sample, including products, reactants, possible side products as well as polymorphs.<sup>[40]</sup> However, as polymorphs may not always yield observably different NMR spectra<sup>[41]</sup> since small chemical shift differences could be obscured by moderately large spectral linewidths. Hence, the combination of solid-state NMR and (single crystal) X-ray analysis to study topochemical reactions provides in-depth information about the topotactic nature of the reactions as well as structural changes that occurred at the molecular level during the reaction. In addition, different polymorphic products which are commonly obtained during topochemical reaction (such as as-dimerized (as-irradiated prior to recrystallization) and recrystallized products) can also be characterized properly.

The complete thesis is comprised of eight chapters. In the first three chapters the motivation, a general introduction of the topics studied during the work (e.g. organic



---

solid-state reactions) and fundamentals of the experimental techniques that have been used through-out the work is given. In chapter four, the crystalline state [2+2] cycloaddition of *trans*-cinnamic acid is discussed. In the next chapter (chapter 5) the robust nature of template resorcinols used as reliable spacers in organic solid-state reactions is emphasized. Moreover, the organizational consequences of hydrogen bonds in the hydroxyl...pyridine heterosynthon in the presence of other competitive hydrogen bonding functional groups are also discussed. Complementary insights into the structural transformation of crystal engineered single-crystal solid-state reactions of *trans*-1,2-bis(4-pyridyl)ethylene yielding tetrakis(4-pyridyl) cyclobutane are presented in detail in chapter six and seven. Finally, chapter 8 briefly summarizes the conclusions of the work.

# CHAPTER 2

## ORGANIC SOLID-STATE REACTIONS

### 2.1. TOPOCHEMICAL CONTROL OF SOLID-STATE ORGANIC REACTIONS

In conventional organic chemistry, chemical reactivity and the products of chemical reactions are governed by the molecular structures of the compounds involved. In certain reactions that take place in the solid-state,<sup>[42]</sup> and which are subject to topochemical control,<sup>[43]</sup> an additional factor comes into play; the crystal structure of the starting materials. In most crystals, molecules are packed in a highly ordered and regular manner and are present in only a very limited number of orientations with limited local mobilities.<sup>[44]</sup> Adjacent molecules are able to react only if the “right” orientation and sufficient proximity is given.<sup>[45]</sup> For instance, polymerization reactions may occur among olefinic groups ( $\text{CH}_2=\text{CH}_2$ ) in adjacent molecules in the solid-state,<sup>[46]</sup> if double bonds of the olefinic groups are approximately parallel and no further than  $\sim 4 \text{ \AA}$  apart. Addition of two olefinic groups yields a cyclobutane linking unit. Reactions in the solid-state do not tend to occur spontaneously but rather need a catalyst such as UV light. Indeed, products of topochemically controlled solid-state reactions are often quite different from those obtained in solution, facilitating synthetic routes to new dimers,<sup>[1,5-8]</sup> oligomers<sup>[47]</sup> and polymers.<sup>[48]</sup>

In general, most organic molecules in either liquid or gaseous states are flexible and may change their shape. A simple example is cyclohexane which can exist in chair and boat form.<sup>[49]</sup> The molecules readily change their conformation flipping from one

form to other while no bonds are broken. In the solid-state such flexibility is usually not observed. Instead, one particular molecular shape or conformation is effectively frozen in, restricting subsequent reactions (cf. Figure 2.1). Such fixed molecules, however, give rise to stereochemically pure products.<sup>[50]</sup>

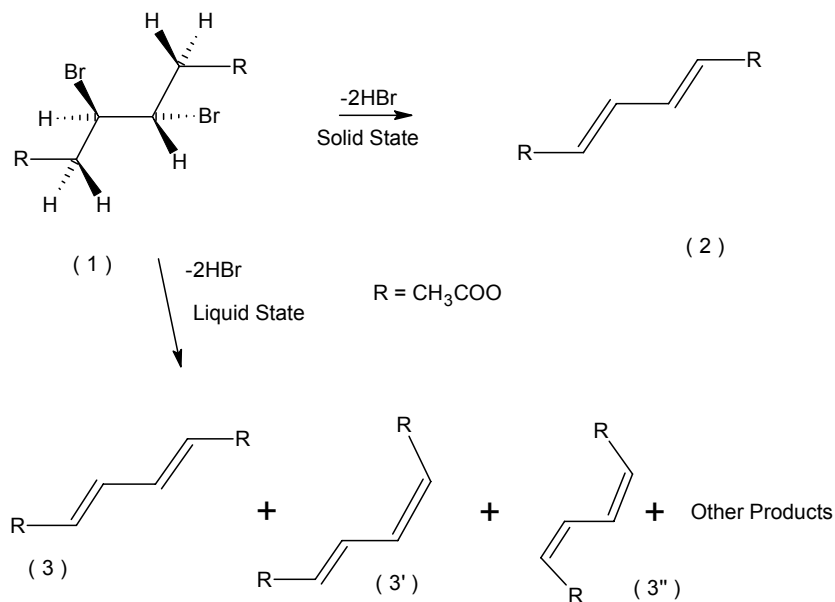


**Figure 2.1:** Elimination reactions of dimethyl meso- $\beta$ ,  $\beta'$ -dibromoadipate.<sup>[51,52]</sup> By reaction of gaseous ammonia with dimethyl meso- $\beta$ ,  $\beta'$ -dibromoadipate (1) two molecules of HBr are eliminated, and the product adopts the conformation as shown in 2, in the solid-state to give dimethyl trans, trans- $\mu$ -conate (2).<sup>[51]</sup> Both reactant (1) and product (2) are centrosymmetric. However, if the same reaction is carried out in the liquid state, molecule (1) adopts a variety of conformations, each of which gives a different isomers 3, 3', 3'' on elimination of HBr

Reactivity in the solid-state is always connected with specific motions allowing for necessary contacts among the reacting groups. In most cases *solid-state* reactions proceed by diffusion of reactants to centers of reactivity or by nucleation of the product phase at centers of disorder. This leads to the total destruction of the parent lattice. In contrast, *topochemical reactions* are facilitated by specific rotations of the monomers on their lattice sites. During topochemical reactions in solid-state the centers of reacting

molecules ideally remain fixed, as a consequence the reaction mode which requires the smallest atom displacements will prevail (least motion principle). Reactivity is only observed if the separation of the reaction atoms is less than a limiting distance of approximately 4 Å.<sup>[53,54]</sup> More details about topochemical vs. nontopochemical process will be described in the later paragraphs.

## 2.2. TOPOCHEMISTRY

### 2.2.1. Topochemical vs. nontopochemical processes

Most photodimerization reactions of conjugated molecules fall into the broad class of organic solid-state reactions known as *topochemical* reactions that are controlled by the three-dimensional regularity of the lattice of reacting phases. If a reaction starts or continues in a crystal region where the parent lattice is lost, e.g. by a phase transformation, the reaction is said to proceed nontopochemically. Some topochemical reactions do not reach quantitative conversion (photodimerization of ortho-ethoxy-trans-cinnamic acid and many more),<sup>[55-57]</sup> due to enhanced reactivity of solids at crystal defects.

### 2.2.2. Schmidt's topochemical principle

As described above, in topochemical reactions the chemical transformation is directed by the parent lattice throughout the transformation with direct transition from reactants to products *without the destruction of the crystal lattice and without the formation of non-crystalline intermediate states*.<sup>[46]</sup> Where as in nontopochemical reactions there is random diffusion of molecules to a center of reactivity, in an ideal topochemical reaction, the center of mass of each molecule is stationary; therefore the molecules do not lose their location in the lattice. For example, in the cases of topochemical polymerizations, the molecules are often pictured swivelling on their lattice positions to come within bonding distance. This notion was first described by Hirshfeld and Schmidt<sup>[56]</sup> and experimentally observed for the polymerization of diacetylenes.<sup>[45,58]</sup>

This lattice-point swivel motion shown in Figure 2.2a, is a schematic illustration of the polymerization of diacetylenes.<sup>[45]</sup> However, this type of motion also applies to the polymerization of distyrylpyrazine<sup>[59]</sup> as shown in Figure 2.2b. The two remaining olefins in the dimer pictured in the central stack of Figure 2.2b are now closer to their reacting partners than they were in the unreacted monomer stack. Also in dimerization reactions, the molecule is seen to pucker, that is, the center moves in one direction while the edges moves in opposite direction, and thus the center of mass is kept constant. Figure 2.2b demonstrate how this is the case for [2+2] photodimerizations as well. Reported three major principles for topochemical reactions are as follows,<sup>[6]</sup>

- (1) *Chemically closely-related compounds show significant differences in chemical behaviour in the solid state.*
- (2) *A given compound reacts differently in the solid and dispersed phases.*
- (3) *Polymorphic modifications of a given compound show significant differences in chemical behaviour.*

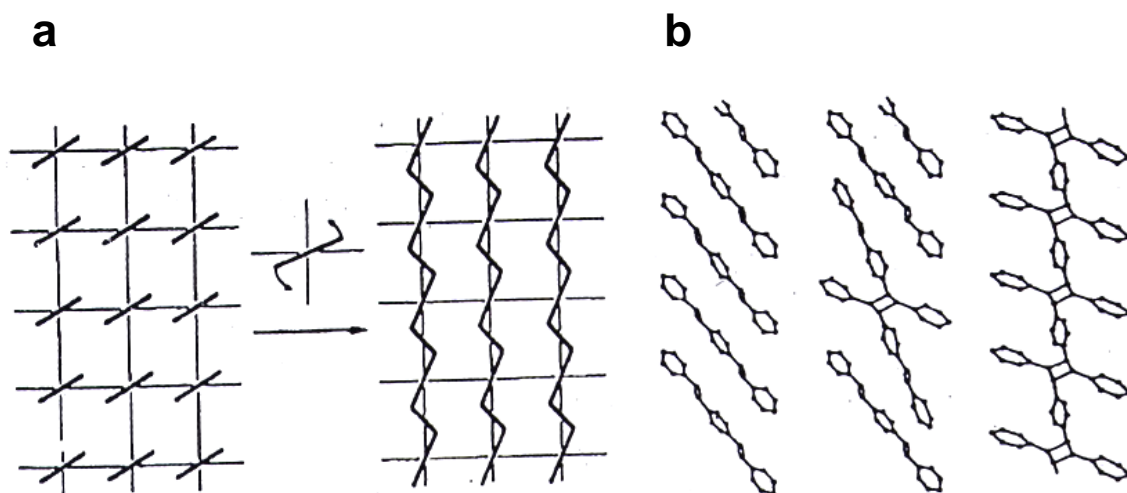


**Figure 2.2:** Topochemical polymerization: stacks of difunctional monomers may react in a regularly ordered crystal lattice, without the aid of defect, by rotating on their lattice positions. The rotation of one molecule brings its reactive ends into contact with two others and so on in a zipper like mechanism.

- (a) Schematic diagram of diacetylene chain polymerization.<sup>[45]</sup>
- (b) Illustration of [2+2] step polymerization of DSP.<sup>[59]</sup>

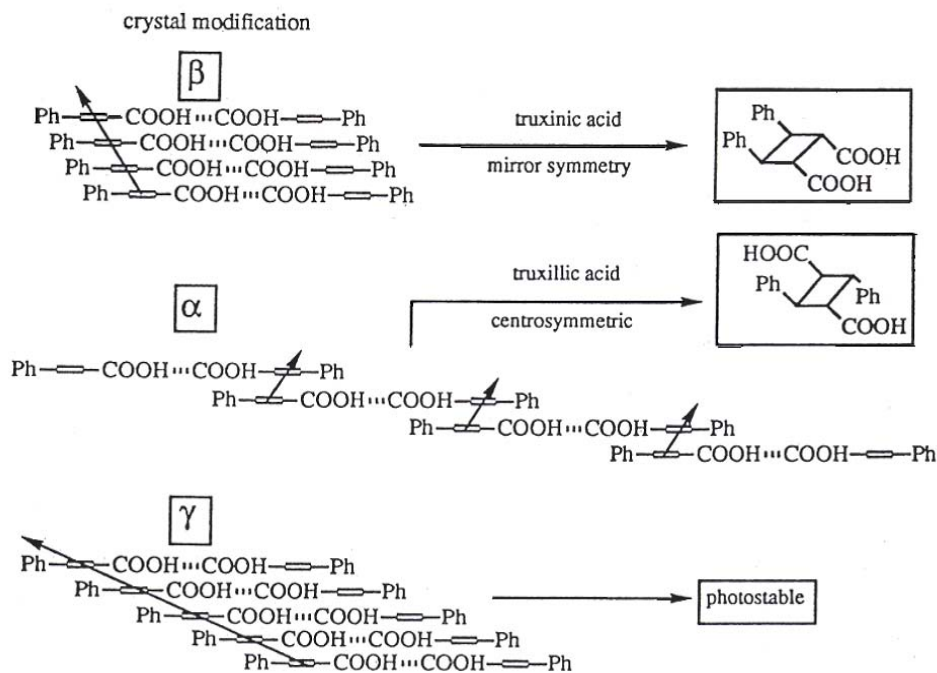


**Figure 2.3:** the crystal modifications of cinnamic acids have been identified with their lattice symmetries and in turn with the stereochemical identity of their photoproducts or with their photostability.

Based on extensive studies about cinnamic acid, it has been established that the molecular symmetry of the photoproducts is related with the crystallographic symmetry of the reacting monomer. Crystallographic packing of cinnamic acid derivatives have been classified in three different forms.<sup>[5-8]</sup> Figure 2.3 shows that each type is built from a unit of two monomers, hydrogen-bonded to one another and approximately in the same plane. These units form parallel stacks that bring monomers within certain distances and relative orientations to one another. In  $\beta$  form the monomers in a stack are highly overlapped compared to the other two modifications and the distance between reactive centers, which are related by mirror symmetry, is approximately 4 Å. In the  $\gamma$  form, the decreased overlap within the stack results in a distance between nearest double bond contacts of 5 Å. However, in the  $\alpha$  form, the overlap offset is so great, that the closest

monomer pairs in a reactive orientation are not in the same stack, but in the neighboring stacks. Thus, while neighbors within a stack are related by mirror symmetry and are over 5.5 Å apart, the reacting pairs are only 4 Å apart and are related to one another by a center of symmetry. Thus it is easily seen that in  $\beta$  lattice, the most easily formed dimer i.e the dimer formed with the least atomic or molecular motion is the head-to-head dimer. However, in  $\alpha$  lattice the head-to-tail dimer is the dimer formed with least lattice disturbance. In all twenty-eight cases investigated by Schmidt,<sup>[5-9]</sup> lattice symmetry matched the stereochemistry of the products or predicted the photostability of the lattice in the cases where the  $\gamma$  modification occurred.

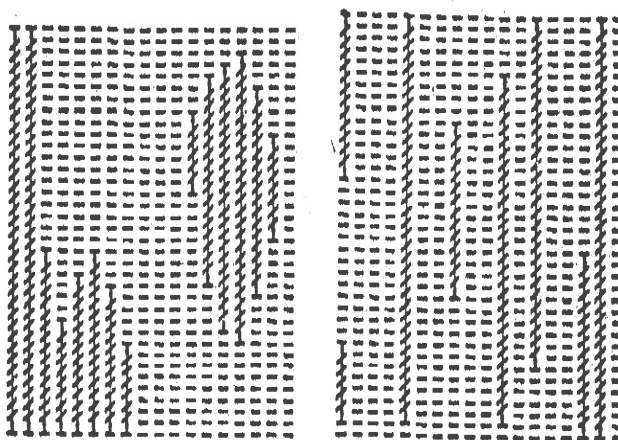


**Figure 2.4:** A heterogeneous mechanism of topochemical polymerization is pictured on the left, a homogeneous mechanism on the right. In the heterogeneous mechanism, nuclei of the product phase formed, whereas in the homogeneous case, the product is formed randomly and a solid solution of monomer and polymer is maintained.

### 2.3. SOLID SOLUTIONS

The terms *homogeneous* and *heterogeneous* were established to describe the two types of mechanisms by which topochemical reactions occurred and illustrates them as shown in Figure 2.4.<sup>[46,60-62]</sup> The figure on the right illustrates polymer-formation proceeding homogeneously inside the monomer crystal starting at randomly distributed

points where polymerization has been initiated. The resulting product is dispersed within the undisturbed monomer matrix so that a solid solution of product and reactant is obtained. Thus, coherence between all parts of the crystal, including the single-crystal texture, is retained, as indeed reported for the polymerization of several diacetylenes yielding macroscopic single crystals of extended chain polymers.<sup>[45,46]</sup>

Braun *et al.* demonstrated that the photopolymerization of distyrylpyrazine (DSP)<sup>[63,64]</sup> is either homogeneous or heterogeneous depending on the irradiation conditions. When the UV-VIS photoactive DSP crystals are irradiated with light of wavelengths for which the chromophore has a large extinction coefficient, most of the light is absorbed at the crystal surface, according to Beer's Law. Thus product formation is isolated at the crystal surface while the interior of the crystal, that receives rather little intensity of the UV irradiation remains unreacted. The product eventually reaches its limit of solubility at the crystal surface and precipitates out. The dimensional mismatch between the parent phase and newly formed phase leads to incoherent phase boundaries and subsequently to disintegration of the crystal into polycrystalline powder.<sup>[8,46,65]</sup> Most of the solid-state photoreactions proceed by such a heterogeneous mechanism, illustrated in Figure 2.4 on the left.

However, when DSP crystals are irradiated with wavelengths of light for which the chromophore has a small extinction coefficient, for example, in the absorption tail of the monomer, light is then absorbed relatively evenly throughout the bulk of the crystal facilitating randomly distributed product formation throughout the crystal (e.g. Just as in the diacetylene polymerization).<sup>[45]</sup> This random product formation results in a single-phase transformation from DSP monomer to oligomer and preserving the single-crystal texture of the monomer.

### 2.3.1. Examples of homogeneous and heterogeneous mechanisms

Figure 2.5 summarizes some of the courses documented for the emergence of the product phase in solid-state reactions. First as described originally by Schmidt, product



accumulates in the parent crystal in solid solution with reactant.<sup>[8,60,61]</sup> This is path Ia, in Figure 2.5. As Schmidt and Cohen suggest, this produces a substitutional mixed crystal of reactant and product, *R*, *P*. There are two possibilities for this solid solution as the reaction proceeds and the product concentration increases: either continuation of a single-phase transformation, paths I, which are extremely rare, or phase separation, paths II. Under the category of single-phase transformations, consider the case where the product remains in the solid solution with the reactant until quantitative conversion is reached following the ideal homogeneous mechanism<sup>[63-66]</sup> (eg. polymerization of diacetylene 1,6-bis(p-toluene sulfonate) of 2,4-hexadiyne diol (PTS) and the oligomerization of DSP). Ia. A characteristic of the PTS polymerization is the smooth and continuous change in cell parameters from monomer to polymer phase due to the solid solution of monomer and polymer. The lattice changes to accommodate the gradual increase in concentration of the polymer and decrease in monomer concentration. Other single-crystal-to-single-crystal transformation that have been documented to occur with a smooth, continuous change in lattice parameters are the BBCP photodimerization<sup>[67,68]</sup> and the racemization of a coboxalime complex.<sup>[69]</sup>

Before quantitative conversion is reached, however, at some critical concentration, a single-crystal-to-single-crystal structural phase transition may take place, Ib, after which the homogeneous topochemical reaction continues, Ia. This phenomenon has been documented for the polymerization of two diacetylene monomers, 1,6-Di-(N-Carbazolyl)-2,4-hexadiyne (DCH) and PTS-12.<sup>[45]</sup> The category of phase separation is more complex. Any type of product phase separation, whether this second phase emerges as crystalline or amorphous, has the potential to destroy the parent crystal and lead the reaction into a non-topochemical mode by introducing *defects* or *impurities* into the parent crystal.

However, assuming the parent crystal is not destroyed, the product phase may nucleate in a certain crystalline modification, and proceed with coherent contact between the parent crystal phase and product phase. Or the phase boundaries may be incoherent due to a mismatch in the dimension of parent and product phases. Build-up of product

such that phase separation occurs across incoherent phase boundaries is the dominant mechanism of product formation in topochemical reactions documented thus far. This is path IIa in Figure 2.5 and is the established mechanism for most topochemical reactions based on [2+2] photodimerizations which are induced by strongly absorbed irradiation and occur to yield the product as a polycrystalline powder. It must be emphasized that there is an intimate relationship between paths Ia and IIa in Figure 2.5 for topochemical reactions induced with light in the UV regions of the spectrum. For example, it is possible to switch from the mechanism of path Ia to the mechanism of path IIa with proper choice of irradiation conditions as described for the oligomerization of DSP<sup>[63-66]</sup> and in the studies conducted for the photodimerization of trans-cinnamic acid.<sup>[70]</sup>

If the product phase emerges as crystalline or amorphous, but in coherent contact with the parent crystal, then a topotactic reaction is possible, (path IIb). Figure 2.5 shows that although topochemical control may often lead naturally to topotaxy, the phenomena of topotaxy can even occur through an amorphous intermediate, and thus is not restricted to topochemistry. Examples of topotactic reactions in the literature are reported for trioxane<sup>[71]</sup> and Ni coordination complex polymerizations.<sup>[72]</sup> An example of a nontopochemical reaction, (path IIc), in which an amorphous polymer is produced from crystalline monomer is the [2+2] photodimerization of meta-substituted methyl ester of phenylenediacrylic acid, m-PDA Me.<sup>[73]</sup>

Figure 2.5 summarizes the two principle paths established for the mechanism of product phase formation in topochemical reactions. The homogeneous mechanism is a single-phase transformation, whereas, the heterogeneous mechanism involves phase separation. In some cases of topochemical photoreactions, these mechanisms can be controlled with irradiation conditions. A few other solid-state processes, bearing on the emergence of the product phase, have also been inserted into the scheme as they relate to these two main mechanisms.

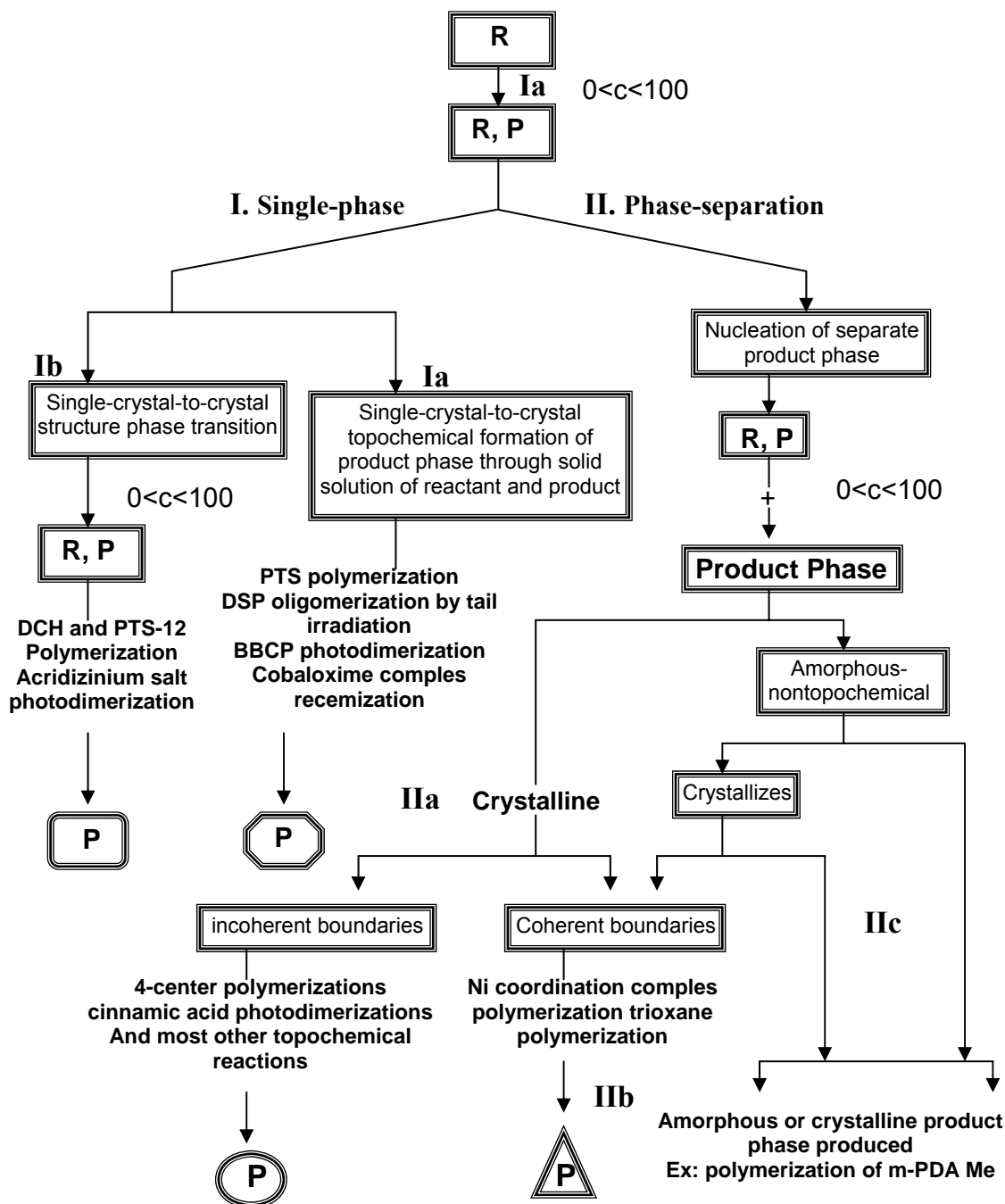


**Figure 2.5:** A summary of some of the ways in which a product phase may emerge in a solid-state reactions. The main mechanisms are homogeneous, Ia, and heterogeneous IIa.

---

## 2.4. SINGLE-CRYSTAL-TO-SINGLE-CRYSTAL TRANSFORMATION

A single-crystal-to-single-crystal (SCSC) reaction involves a chemical reaction of a single crystal wherein the product of the reaction forms within the solid phase of the reactant.<sup>[13]</sup> In such a reaction, the integrity of a single crystal (i.e. transparency, shape) remains virtually unchanged as reactant molecules are converted to product. It is largely for this reason that SCSC reactions have intrigued chemists. Not only is it possible to gain an atomic-level understanding of structural changes of reactants in the solid-state via single-crystal X-ray crystallography, but the fact that the composition, and therefore possible bulk physical properties (e.g. optical), of such crystalline materials change during a SCSC reaction make such solids attractive for applications in materials science (e.g. data storage).

There is an inherent relationship between the terms *SCSC* reaction and *topotactic* reaction. These two terms are often used interchangeably, and can be a source of confusion. However, a SCSC reaction transforms a single crystal of a reactant into a single crystal of a product. Such a transformation may proceed either homogeneously or heterogeneously.<sup>[74]</sup> In the homogeneous case as described above the reactant and product form a solid solution during the entire reaction. Consequently, the lattice sites of the corresponding products differ only slightly or not at all from the lattice sites of the reactants.<sup>[75]</sup> In the heterogeneous case, the product separates from the reactant as a different phase, which means that there is a phase boundary between the product and reactant and a correspondence between the reactant and product lattices do not require. The term topotactic reaction,<sup>[76]</sup> on the contrary, describes a solid-state reaction in which the product, which may or may not be a single crystal, forms in an oriented fashion, requiring at least some lattice points of the product to coincide with the lattice points of the reactant.<sup>[75-77]</sup> Thus, although sometimes used in a synonymous fashion,<sup>[78]</sup> the terms topotactic and SCSC reactions are not considered identical, since a topotactic reaction can involve the loss of integrity of the single crystal.

### 2.4.1. Significance of SCSC transformations

SCSC reactions possess all properties considered advantageous for solid-state reactions (e.g. absence of solvent, stereocontrol of reactivity etc.). Particularly, the ability to monitor *in situ* the course of reaction *via* single-crystal X-ray diffraction can offer valuable insights into reaction mechanism and intermediates (e.g. reaction pathways).<sup>[79]</sup> For instance, *in situ* monitoring of the course of SCSC reactions has revealed the ability of bonds to form and break and molecules to rotate in solids.<sup>[80]</sup> Additional technological applications such as high-density data storage (e.g. compact discs mainly densities of up to  $6.5 \times 10^{12}$  bits  $\text{cm}^{-3}$ )<sup>[81]</sup> and properties like high absorbance and low writing powers, resistance to oxidation and periodic structures<sup>[82]</sup> are considered promising. The significance of SCSC reactions for the construction of highly-ordered crystalline polymers has also been recognized.<sup>[83]</sup> A homogeneous SCSC polymerization offers an intriguing ability to generate polymers and composites<sup>[84]</sup> based on the size and shape of the reacting crystal. These advantages are, however, limited to the paucity of molecules that undergo such transformation.

### 2.4.2. Characterization techniques for SCSC transformations

A good indicator of a SCSC reaction is the observation *via* optical microscopy, that a crystal does not display significant macroscopic changes (or crystal does not crumble) on reaction, although such an observation does not present a reliable proof.<sup>[85]</sup> A more reliable indicator is the conservation of crystallinity, established *via* X-ray diffraction. Indeed, most homogeneous SCSC reactions have been realized through comparison of structures of single crystals before and after conversion to the product, using the same or a different crystal. The most reliable means to establish the existence of a homogeneous SCSC reaction is by the application of dynamic X-ray crystal structure determination,<sup>[21]</sup> along with optical microscopy.<sup>[86]</sup> The method is based on the smooth transition of the reactant diffraction pattern into that of the product.<sup>[21]</sup> Consequently, a series of crystal structures can be obtained from the same crystal, at different yields of the reaction. The refinement of the occupational parameters of the product allows the yield to be determined. Comparison of intensities of selected X-ray diffraction peaks may also

provide information concerning yields of SCSC reactions.<sup>[87]</sup> The application of dynamic X-ray diffraction is some times complicated by the possibility of crystal cracking or reaction upon exposure to X-ray. In such cases, an alternative to dynamic X-ray diffraction is either to employ different single crystals at different yields or tail-irradiate the same crystal.

In addition to X-ray diffraction, Raman phonon spectroscopy can be used to determine whether a solid-state reaction proceeds in a homogeneous or heterogeneous fashion.<sup>[18]</sup> In a homogeneous SCSC reaction, a shift in phonon vibration bands is observed, while the formation of new peaks is indicative of a heterogeneous reaction. Combined use of phonon spectroscopy and single crystal X-ray diffraction also allow for identification of rate-determining factors in a SCSC reaction. Infrared (IR) micro-spectroscopy has also been used to characterize SCSC reactions,<sup>[88]</sup> a principle advantage being the ability to employ relatively small crystals for the experiment. The analysis of phase diagrams involving reactant and product mixtures can also provide information on whether a reaction occurs homo-or heterogeneously.

### 2.4.3. SCSC transformations using tail-irradiation

Similarities in molecular and crystal structures of reactants and products are expected to promote SCSC reactivity.<sup>[89]</sup> In cases where the reaction involves significant changes to molecular shape and/or orientation, strain can build up in the single crystal. Accumulation of such strain may lead to the perturbation of the crystalline environment, allowing the reaction to proceed in a SCSC manner to a certain extent. Thus, relatively small changes in atomic positions are considered beneficial for SCSC reactions, which implies that SCSC reactions are expected to be promoted in crystalline environment flexible enough to support molecular movement.<sup>[90]</sup> The presence of defects in a single crystal can sometimes prevent the reaction to proceed in SCSC manner.<sup>[46]</sup> Conditions under which the solid-state reaction is conducted, such as radiation intensity, radiation wavelength as well as crystal size and temperature also play a significant role in promoting SCSC reactions.<sup>[21,87,88]</sup>

Compounds	a (Å)	b (Å)	c (Å)	$\beta$ (°)	Mosaicity (°)
<b><math>\alpha</math>-trans-cinnamic acid</b>	5.63	17.97	7.73	96.88	0.49
<b>10 min irradiated</b>	5.54	17.97	7.52	98.11	2.20
<b>20 min irradiated</b>	5.55	17.97	7.56	98.83	2.80
<b>30 min irradiated</b>	5.61	18.45	7.77	102.2	9.50

**Table 2.1:** Lattice parameters of  $\alpha$ -trans-cinnamic acid irradiated under broad band conditions

The irradiation wavelength has a marked influence on the mechanism of SCSC [2+2] photodimerizations. The heterogeneous mechanism described above is observed in the case when irradiation is in the vicinity of the absorption maximum of the reacting chromophores. Under these condition the absorptivity of the sample is high and thus a steep profile of product concentration will be formed. Since all solid-state reactions are connected with small but significant changes of the unit cell dimensions, lattice mismatch between monomer and product leads to a destruction of the parent crystal. However, if the irradiation is in the tail of the absorption a uniform light intensity throughout the crystal can be accomplished (see for example Figure 5.11).<sup>[29]</sup>

Figure 2.6 shows a series of diffraction patterns of  $\alpha$ -trans-cinnamic acid at various times under broad band UV irradiation. Under these conditions, the reaction proceeds heterogeneously (i.e the parent crystal disintegrates), which is clearly visible by the decaying quality of diffraction pattern. As the reaction proceeds, the reflections broaden and finally are reminiscent of debye rings. The lattice parameters derived from this data are given in Table 2.1. While going from monomer to dimer the mosaicity parameter (the mean angle between the mosaic blocks which build up the crystal) increases and reaches an apparent maximum  $\sim 10^\circ$  after 30 min, i.e. the deterioration of the single crystals rendering the sample textured with preferred orientation.

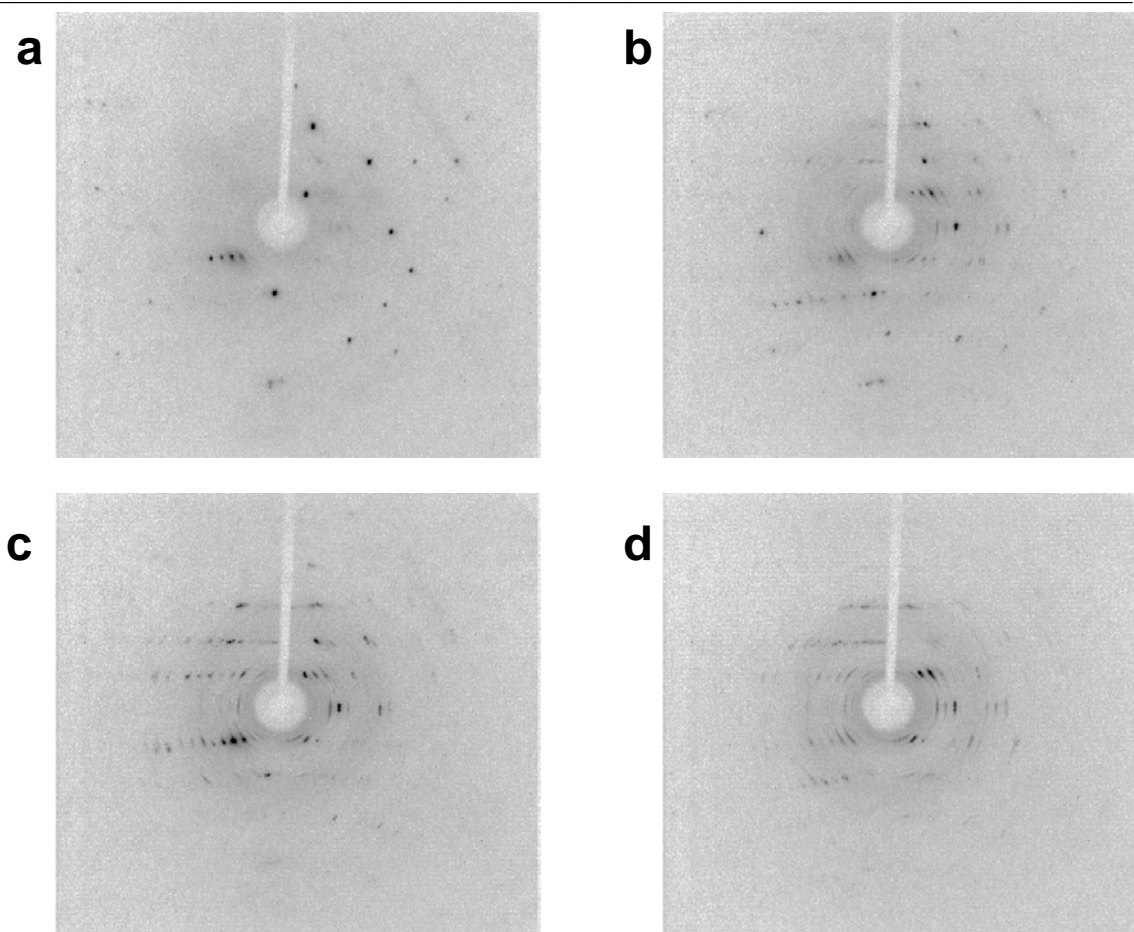


**Figure 2.6:** Diffraction patterns of  $\alpha$ -trans-cinnamic acid irradiated under broad band conditions a) monomer prior to irradiation b) after 10 minutes of irradiation c) 20 minutes of irradiation d) 30 minutes (Note the continuous broadening of the reflections with increasing time)

Many topochemical photoreactions have been demonstrated to proceed homogeneously as crystal-to-crystal transformations under the condition of the tail irradiation technique. Enkelmann and Wegner<sup>[70]</sup> were the first to demonstrate that  $\alpha$ -cinnamic acid undergoes a SCSC [2+2]photoreaction. To achieve SCSC reactivity, single crystals of the acid were irradiated with UV energy that corresponds to the tail-end UV absorption of the solid. The tail-end was used to avoid rapid build-up of photodimers, and resulting strain, at or near the crystal surface and thereby permit greater penetration depth of the energy into the solid. As a result, the photoreaction occurred uniformly through the solid. The technique enabled the progress of the photoreaction to be monitored via dynamic X-ray crystallography ( cf. Figure 2.7).



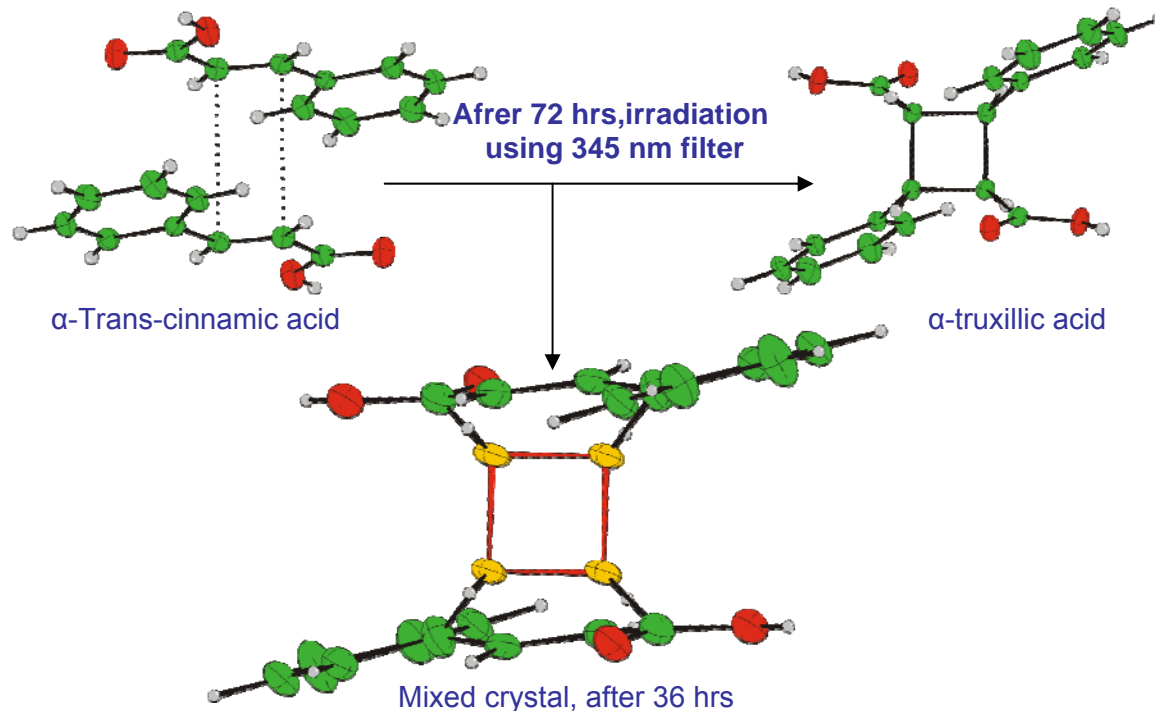


**Figure 2.7:** Crystal structures of  $\alpha$ -trans-Cinnamic acid at different stages of reaction.

The tail-end irradiation method has also been used by the same group to achieve SCSC reactivity in a series of salts of mono- and diolefin styrylpyrilium cations. Depending on the nature of the counter ion (e.g.  $\text{BF}_4^-$ ,  $\text{ClO}_4^-$ ), either dimers or oligomers are formed.<sup>[91,92]</sup> A related study involving a dimerization and thermal back reaction of 4,6-di-tert-butyl-4-[(4-methoxyphenyl)ethenyl]pyrilium trifluoromethane sulfonate has also been used to construct single crystals that can be used as a medium for a holographic grating.<sup>[93]</sup> The intermediate states of a crystal-to-crystal transformation are mixed crystals, i.e. crystals containing a second constituent which fits into and is distributed in the lattice of the host crystal. Here the monomer and product molecules occupy the same lattice sites with an occupancy according to the conversion. The crystals obtained by this method are non equilibrium structures. Upon crystallization stable polymorphs are formed.

## 2.5. CRYSTAL ENGINEERING

Crystal engineering includes the design of new solids with tailored physical and chemical properties, and exploitation of intermolecular interactions such as crystal packing effects etc.<sup>[94,95]</sup> Indeed a crystal is therefore a respectable synthetic target, and can be considered as a supermolecule par excellence (cf. Figure 2.8). Supermolecules are not merely collections of molecules but they have structural features and properties that are characteristic not of the molecules themselves but of larger, more extended assemblies.<sup>[96-100]</sup> In keeping with this, structural chemists and crystallographers have had little difficulty in recognising an organic crystal as the ultimate example of a supermolecule. Therefore, if a crystal is a supermolecule, then crystal engineering is the solid-state supermolecular equivalent of organic synthesis.

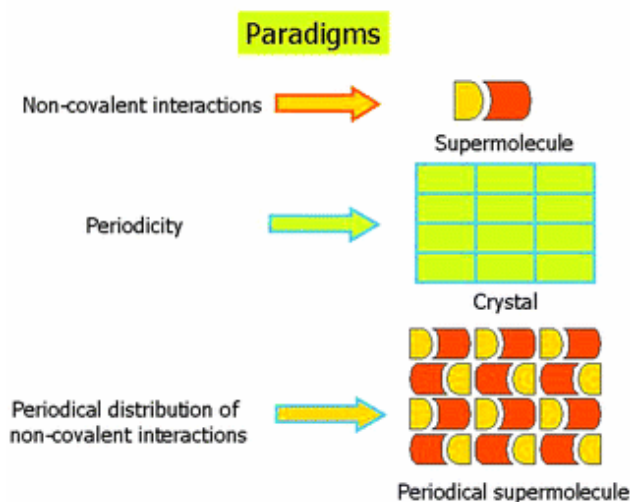


**Figure 2.8:** From molecule to periodical supermolecule: the collective properties of molecular crystal result from the convolution of the properties of the individual molecules/ionic building blocks with the periodical distribution of intermolecular non-covalent bonding of the crystal.<sup>[97]</sup>

Simply, crystal engineering is *making crystals by design*. This definition implies the ability to assemble molecular or ionic components into the desired architecture by engineering a target network of supramolecular interactions. These interactions can be covalent bonds between atoms, as well as coordination bonds between ligands and metal

centers, coulombic attractions and repulsions between ions, and non-covalent bonds between neutral molecules (van der Waals, hydrogen bonds, etc.) or any combination of these linkages. These bonding interactions span a very wide energy range, from the tiny energies involved in the van der Waals interactions between neutral atoms in neutral molecules to the high ones involved in breaking and forming of covalent bonds (cf. Figure 2.9). The difference in bonding types offers a practical way to differentiate target materials, and hence synthetic strategies, as a function of the energy involved in the bond breaking-bond forming processes that lead from building block to superstructure.

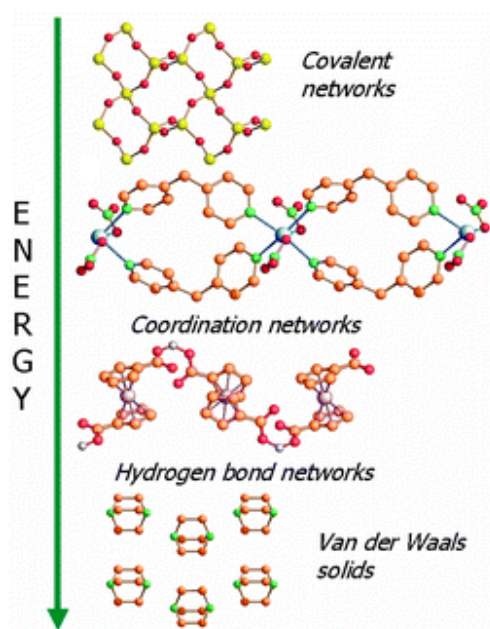


**Figure 2.9:** Bonding interactions between building blocks span a very wide energy range, the difference in bonding types offers a practical way to differentiate target materials, and hence synthetic strategies, as a function of the energy involved in the bond breaking-bond forming processes that lead from building block to superstructure.<sup>[97]</sup>

### 2.5.1. Intermolecular forces in crystals

It is well-known that attractive forces between molecules are responsible for many important phenomena in chemical and biological sciences. If these attractive forces did not exist, physical reality would be reduced to ideal gases. The very existence of liquids and solids depends on intermolecular attraction. Simultaneously, molecules in

crystals also repel one another as attested by the fact that the compressibilities of condensed media are negligibly small when compared to those of the gases. Intermolecular forces or interactions are the fundamental causes for the crystallization and dissolution of organic molecules, for the formation of intermolecular complexes and for the presence or absence of characteristic geometrical patterns and particular crystallographic symmetry elements. Similar interactions are also to be found within a molecule between atoms which are not directly bonded or linked by a conjugated framework. Such interactions define the shape and conformation of molecules.

Intermolecular interactions are divided into two classes: isotropic, medium-range forces and anisotropic, long-range forces.<sup>[101-103]</sup> Isotropic forces define the shape of the individual molecules, as well as size and close packing of molecules, whereas anisotropic forces determine intermolecular orientations and functions. For example, the three-dimensional shapes of biomolecules, such as proteins and enzymes, are the result of medium-range intermolecular interactions. At a simple level, all molecular recognition can be said to arise from isotropic interactions, in other words by fitting together of bumps and hollows among the components of supramolecular structure. But most directional effects (and function is related to these effects) depend on the anisotropic interactions. Generally, anisotropic interactions involve partially charged atoms, such as *nitrogen, oxygen, chlorine, phosphorus and sulphur*.

Isotropic interactions include van der Waals forces, which act between all atoms and molecules. These can be repulsive or attractive depending on the distance between the interacting non-bonded atoms, and are responsible for gross supramolecular arrangements. Although these forces are individually weak, (they have bond energies of 8 kJ mol<sup>-1</sup> compared with alone 400 kJ mol<sup>-1</sup> of a covalent C-H bond) they become significant when considered in numbers. This is the essence of supramolecular thinking. Although at a simple level of molecular recognition can be said to hinge on isotropic interactions, at a higher level it is an anisotropic interactions that is the master key: the hydrogen bond.<sup>[104]</sup> Indeed, after metal-coordination bonds and ionic interactions, the strongest interactions in crystal engineering are hydrogen bonds. They are also

directionally specific, and this is distinctly advantageous in crystal design, wherein they are widely used.<sup>[105]</sup>

### 2.5.2. Hydrogen Bonding

A hydrogen bond is based on attractive intermolecular forces that exist between two partial electric charges of opposite polarity. Although stronger than most other intermolecular forces, the hydrogen bond is much weaker than both the ionic bond and the covalent bond. In any hydrogen bond,  $D-H\cdots A$ , a hydrogen atom acts as a bridge between two atoms D (donor) and A (acceptor). These atoms always tend to be negatively charged (electronegative), which gives the hydrogen bond an electrostatic character, as the electropositive hydrogen atom holds the negative atoms in thrall. If D and A are both quite electronegative, for example in  $N-H\cdots O$  or  $O-H\cdots N$ , the hydrogen bond is *strong* or *conventional* ( $20-40 \text{ kJ mol}^{-1}$ ).<sup>[103]</sup> But if either or both D and A are of moderate to weak electronegativity, such as in  $C-H\cdots O$ , the hydrogen bond is weak or non-conventional ( $2-20 \text{ kJ mol}^{-1}$ ). Hydrogen bonds can also form between more than two atoms. In general, the hydrogen bond is a composite interaction, which can have pronounced covalent, electrostatic or van der Waals components and consequently span a wide energy range. The strength of interaction dictates the length and orientation of the hydrogen bond; short, linear bonds are always the strongest. But even weak bonds can have significant influence on molecular packing.

The distinctive geometrical attributes of a hydrogen bond  $D-H\cdots A-X$  (D=donor, A=acceptor) are the  $D\cdots A$  and  $H\cdots A$  lengths, the hydrogen bond angle  $D-H-A$  or  $\theta$ , the  $H-A-X$  angle or  $\phi$  and the planarity of the DHAX system.<sup>[14]</sup> Typical values for the  $H\cdots A$  distance are  $1.80$  to  $2.00 \text{ \AA}$  for  $N-H\cdots O$  bonds and  $1.60$  to  $1.80 \text{ \AA}$  for  $O-H\cdots O$  bonds. Ranges for  $\theta$  and  $\phi$  occur around  $150-160^\circ$  and around  $120-130^\circ$  respectively. The significance of hydrogen bonding in crystal engineering can hardly be underestimated. A vast amount of work has been carried out on the various aspects of hydrogen bonding. Especially, the work done by Margaret Cairns on the various types of hydrogen bonding that can exist in organic solids.<sup>[106-108]</sup> Etter together with MacDonald and Bernstein has

developed a graph theory-based approach for classifying and symbolically representing the different types of hydrogen bonds that can be formed and also developed rules that governs hydrogen bonding in solid-state. These rules require a classification of hydrogen bond donor and acceptor into *reliable* and *occasional* donor and acceptors (Table 2.2). Using these classification three basic rules were devised, which apply quite well to hydrogen bonding of small molecules.

- (1). All (or as many as possible) good proton donors and acceptors are used in hydrogen bonding.
- (2). If six-membered ring intramolecular hydrogen bonds can form, they will usually do so in preference to forming intermolecular hydrogen bonds.
- (3). The best proton donors and acceptors remaining after intramolecular hydrogen bond formation will form intermolecular hydrogen bonds.

Type	Functional Group Involved
Reliable Donors	-OH, -NH <sub>2</sub> , -NHR, -CONH <sub>2</sub> , -CONHR, -COOH
Occasional Donors	-COH, -XH, -SH, -CH
Reliable Acceptors	-COOH, -CONHCO-, -NHCONH-, -CON, -OH.
Occasional Acceptors	-O, -NO <sub>2</sub> , -CN, -CO, -COOR, N<, -Cl

**Table 2.2:** List of reliable and occasional hydrogen-bond donors and acceptors.

### 2.5.3. Cocrystals

An important aspect of research into hydrogen bonding involves the realization that cocrystals can be obtained from certain solutions containing more than one molecular species; they can also be formed by mixing (or) grinding two solids together.<sup>[109]</sup> Cocrystals are often formed between a hydrogen bond donor molecules and a hydrogen bond acceptor molecule. Cocrystals are generally those crystalline materials that

comprised by two or more unique solids at room temperature, in a stoichiometric ratio, where the dominant interactions in the formation of cocrystals are hydrogen bonds. However in more recent studies<sup>[109]</sup> it has been revealed that its not only the hydrogen bond that play crucial role in cocrystals formation but other intermolecular interactions such as  $\pi$ - $\pi$  interactions, van der Waals forces or halogen bonds are also important. Therefore, the cocrystal can now be defined as *a crystal constituted by heterosynthons, stabilized by hydrogen bonds, or other types of non-valency intermolecular interactions, and in which all the components synthons are solid under ambient conditions, when in their pure form.*

Cocrystals are not as widely studied as single-component crystals or solvates. For examples there are 1,487 hydrogen-bonded molecular cocrystals in the CSD (Cambridge Structure Database), i.e., only 0.42% of the structures archived in the CSD. On the other hand, there are 45,883 hydrates (ca. 13%) archived in the CSD.<sup>[110]</sup> Nevertheless, cocrystals are attracting attentions in the context of pharmaceuticals<sup>[111]</sup> as an alternative to the traditionally accepted crystalline forms (polymorphs, solvates/hydrates, and salts), and as media for solid-state (green) synthetic chemistry. In addition to these, cocrystals exhibit different properties than free drugs and salts. The solid form influences relevant physico-chemical parameters such as solubility, dissolution rate of the drug, chemical stability, melting point and hygroscopicity which can results in the solids with superior properties. Moreover, the use of cocrystals has also been recognized in supramolecular synthesis (crystal engineering)<sup>[110]</sup> which has many advantages over single molecule approach. Since the molecules required for cocrystal approach will likely be less complex and therefore, molecular synthesis will be less demanding. Figure 2.10 provides a simplified schematic overview of the different solid forms.

#### 2.5.4. Supramolecular synthons

Organic crystals are supramolecular entities in that they are built from molecules. In crystal engineering, the supramolecular chemist aims to design and control packing arrangements to design crystals with specific properties. But this is not routinely possible

from the knowledge of the molecular structure alone. The best a chemist can do is to find recurring packing patterns adopted by certain functional groups and rely on the robustness of such motifs to create new solid-state structures. These small repetitive units are called supramolecular synthons.<sup>[14,103]</sup> They economically but fully define the essence of a structure, and embody specific intermolecular interactions (cf. Figure 2.11). Repetition is what qualifies a structural motif to be considered as synthon and it is repetition that is the key to successful crystal engineering.

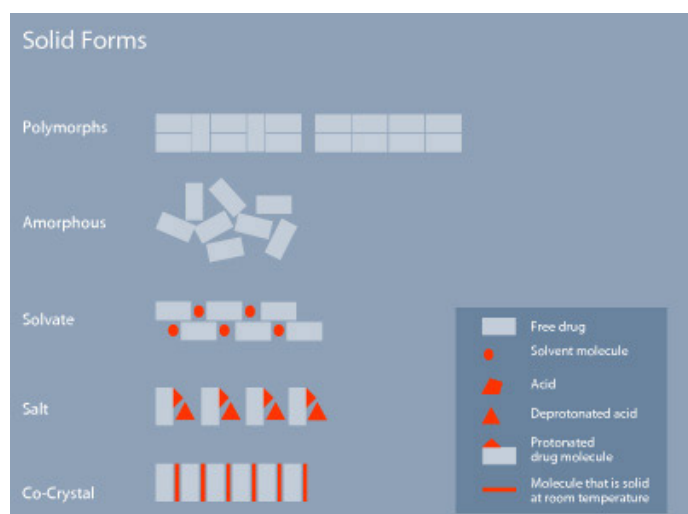


**Figure 2.10:** Schematic overview of possible solid species.<sup>97</sup>

Thus, supramolecular synthons are structural units within supermolecules which can be formed and/or assembled by known or conceivably synthetic operations involving intermolecular interactions, and crystal engineering is a novel approach to organic synthesis. Precisely, supramolecular synthons are spatial arrangements of intermolecular interactions and play the same focusing role in supramolecular synthesis that conventional synthons do in molecular synthesis. In effect, the goal of crystal engineering is to recognize and design synthons that are robust enough to be exchanged from one network structure to another, which ensures generality and predictability. Such structural predictability leads, in turn, to the anticipation of one-, two-, and three-dimensional patterns formed with intermolecular interactions.



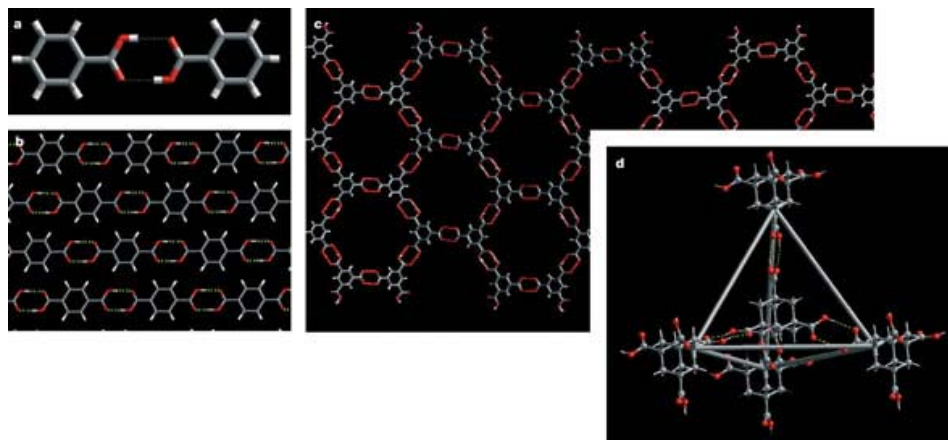


**Figure 2-11:** The building blocks of supramolecular chemistry. The structural features of supramolecular assemblies are best describe in terms of supramolecular synthons, spatial arrangements of molecules involving specific intermolecular interactions. A) the hydrogen-bonded symmetrical pair of carboxyl groups (COOH) is perhaps one of the easiest identified of supramolecular synthons. The two linear hydrogen bonds (dotted lines) provide a structural motif that is surprisingly durable and can be used to build structures based on b one-, c, two-and d, three-dimensional patterns.

The understanding of supramolecular synthons, their geometries, and their frequency of occurrence in the presence of other hydrogen bonding groups is a prerequisite for the rational design and supramolecular synthesis of novel cocrystals and for understanding the structure-function relationships in such compounds. In this context, it should be unsurprising that hydrogen-bonded supramolecular synthons are commonly used in crystal engineering of cocrystals due to their relatively high strength, predictability, ubiquity, and directionality.<sup>[105,110]</sup> There are two distinct categories of supramolecular synthons. One is *supramolecular homosynthons*, which are composed of self-complementary functional groups, as exemplified by the carboxylic acid dimer, and the other is *supramolecular heterosynthons*, which are composed of different but complementary functional groups. For instance, the latter include acid $\cdots$ pyridine, acid $\cdots$ amide, hydroxyl $\cdots$ pyridine, and hydroxyl $\cdots$ amine supramolecular synthons. It has been suggested in several studies<sup>[110]</sup> that some supramolecular heterosynthons are strongly favoured over related supramolecular homosynthons.

# CHAPTER 3

## FUNDAMENTALS OF EXPERIMENTAL TECHNIQUES

### 3.1. INTRODUCTION OF NMR ANALYSIS

Solid-state NMR spectroscopy<sup>[112,113]</sup> is a powerful (often indispensable) analytical tool for investigating the structure, organization and dynamics in different supramolecular systems.<sup>[115]</sup> To provide sufficient spectral resolution, the magic angle spinning (MAS)<sup>[114]</sup> technique was developed and is now a days routinely used. Basically, the application of fast mechanical sample rotation about an axis inclined at the magic angle ( $54.7^\circ$ ) with frequencies exceeding the strength of line broadening interactions like CSA and dipolar couplings (typically up to 30 kHz, in some cases 50 kHz, or even 70 kHz),<sup>[115]</sup> results in sharp spectral lines but comes at a price of a loss of valuable information inherent to these anisotropic interactions. Recoupling methods,<sup>[116]</sup> then selectively reintroduce interactions of interest.<sup>[35,117,118]</sup>

### 3.2. BASICS OF NMR AND INTERACTIONS

Nuclei with an odd mass or odd atomic number such as  $^1\text{H}$  and  $^{13}\text{C}$  have *nuclear spin* (in a similar fashion to the spin of electrons). The magnetic moments associated with the spin of nuclei are sufficiently different that NMR experiments can be sensitive for only one particular isotope of one particular element. Since a nucleus is a charged particle in motion, it will develop a magnetic field, and thus behave in a similar fashion to a simple, tiny bar magnet. In the absence of a magnetic field, these are randomly oriented but when a field is applied they line up parallel to the applied field (cf. Figure 3.1). The

more highly populated state is the lower energy state. In NMR, electro magnetic radiation such as RF (radio frequency) is used to flip the nuclear spins from the low energy state to the higher energy state. The energy required for this transition depends on the strength of the applied magnetic field (cf. Figure 3.2). As shown in the figure, the energy required for the spin-flip depends on the magnetic field strength at the nucleus. With no applied field, there is no energy difference between the spin states, but as the field increases so does the separation of energies of the spin states and therefore so does the frequency required to cause the spin-flip, this referred to as resonance.

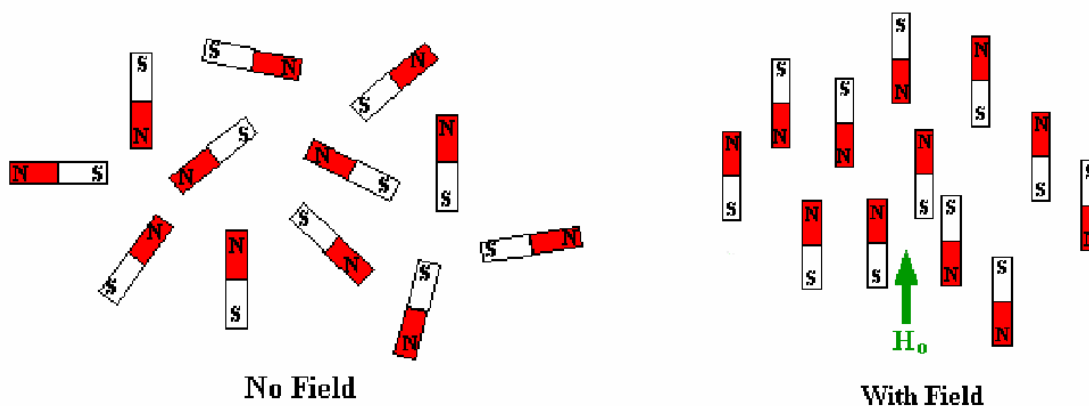


**Figure 3.1:** Schematic representation of nuclear spins under the influence of magnetic field

The nuclei of all atoms may be characterized by a nuclear spin quantum number ( $I$ ). The property of nuclear spin is fundamental to the NMR phenomenon. Each nucleus with a non-zero spin possesses a magnetic moment  $\mu$ , which is given by

$$\mu = \gamma \hbar I \quad (3.1)$$

where  $\hbar = h/2\pi$  is Planck's constant, and the  $\gamma$  is the *magnetogyric ratio* which is constant for any given nuclide and may be viewed as a measure of strength of the magnetic moment of the nuclei. The behavior of a spin system is well described quantum mechanically by the time-dependent Schrödinger equation.

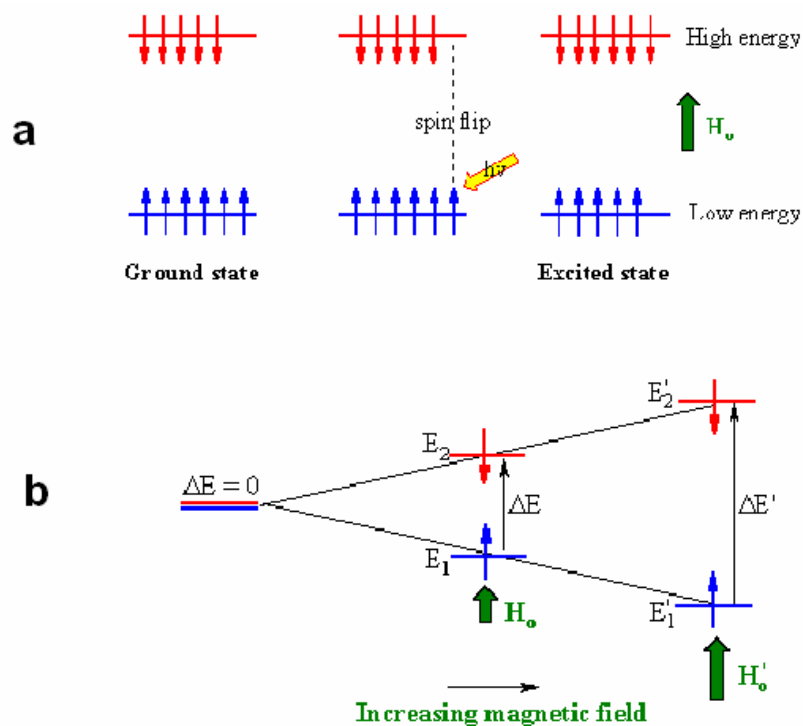


**Figure 3.2:** Schematic representation of the energy states of nuclear spin a) before the irradiation lower energy state is more populated than the higher energy state. b) With increasing magnetic field the difference between the energy level is also increases.

$$\frac{d}{dt}|\Psi(t)\rangle = \frac{-i}{\hbar}\hat{H}|\Psi(t)\rangle \quad (3.2)$$

The evolution of the state  $|\Psi(t)\rangle$  is determined by the Hamilton operator  $\hat{H}$  which describes the energy of the system. For a nucleus in a static magnetic field the majority of the spin interactions can be expressed in terms of a nuclear spin Hamiltonian

$$\hat{H} = \hat{H}_{external} + \hat{H}_{internal} \quad (3.3)$$

$$\hat{H} = \hat{H}_z + \hat{H}_{rf} + \hat{H}_Q + \hat{H}_{DD} + \hat{H}_{CS} + \hat{H}_J \quad (3.4)$$

Where  $\hat{H}_z$  describes the Zeeman interaction with the external magnetic field, and  $\hat{H}_{rf}$  the radio frequency interaction, which are both externally applied.  $\hat{H}_{DD}$  describes the direct

dipole-dipole coupling between spins,  $\hat{H}_{CS}$  the chemical shift interaction,  $\hat{H}_Q$  the quadrupolar coupling and  $\hat{H}_J$  the J-coupling, which is usually an isotropic indirect spin-spin coupling via electrons. All of these are internal spins interactions and therefore intrinsic to the material being studied. It is interesting to note that for NMR the external interactions can usually be much larger than the internal interactions, thus the nuclear spins are more strongly coupled to the external apparatus than to their own molecular environment. This is in contrast to most other forms of spectroscopy, where the behaviour of the system is set by the molecular structure itself and the information is gained by a relatively weak external perturbation.<sup>[119]</sup>

### 3.3. ZEEMAN- INTERACTION

The interaction inherently most important to NMR is the Zeeman interaction which is the interaction of nuclear spin  $I$  with an external static magnetic field  $B_0$  for nuclei with spin quantum number  $I \neq 0$ . The Zeeman interaction causes a splitting of the degenerated  $(2I + 1)$  energy levels, which are defined by the magnetic nuclear spin quantum number  $m_I = -I, -I + 1, \dots +I$ . For a spin  $-1/2$  nucleus such as the proton, there are two possible spin states denoted by  $+1/2$  and  $-1/2$ , whilst for  $I = 1$ , for example deuterium, the states are  $+1, 0, -1$ , (cf. Figure 3.3) and so on.

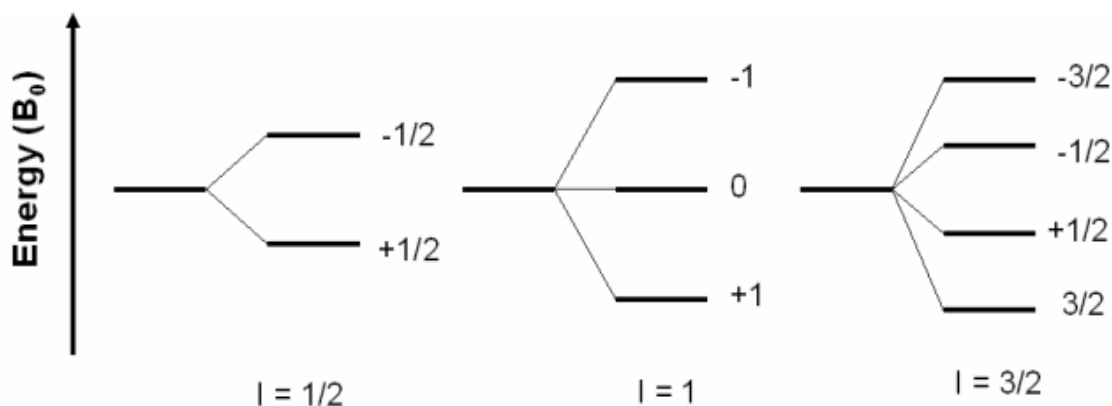


**Figure 3.3:** Energy level diagram showing the breakdown of nuclear spin degeneracy upon the application of magnetic field.

If the external magnetic field is oriented along the z-axis, only the z-component of the corresponding Hamiltonian deviates from zero. The break down of this degeneracy enables the absorption and emission of energy in the form of electromagnetic radiation.

$$\hat{H}_z = -\gamma\hbar\hat{I}_z B_0 \quad (3.5)$$

the *eigenvalues* of  $\hat{H}$  are the energies associated with the different possible states of the spin. The eigenvalues are obtained by operating  $\hat{H}$  on the spin wave functions:

$$\hat{H}_z |I, m\rangle = E_{I,m} |I, m\rangle \quad (3.6)$$

where  $E_{I,m}$  is the energy of the eigenstate  $|I, m\rangle$ . The quantum number  $m$  can take  $2I + 1$  values. From solving the Schrödinger equation with the Hamiltonian above, one obtains the energy levels

$$E_m = -m\hbar\gamma B_0 \quad (3.7)$$

For  $I = 1/2$  the energy splitting between the two levels is  $\Delta E = -\gamma\hbar B_0 = \hbar\omega_L$ , where  $\omega_L$  is the so called Larmor frequency (the precession frequency of angular momentum vector of nuclei about an external magnetic field). For example, a proton in a 7 T magnetic field has a Larmor frequency of 300 MHz, whereas in a 16.4 T magnetic field it has 700 MHz.

In the case of a strong external magnetic field  $B_0$ , the Zeeman interaction by far exceeds most other interactions listed in Eq. (3.4) This allows the weaker internal NMR interactions to be treated as perturbations of the strong Zeeman interactions. The secular approximation leads to some components of the internal spin interactions being masked by Zeeman interactions, thus simplifying the internal interactions Hamiltonian,  $\hat{H}_{internal}$ .

---

### 3.4. EFFECTS OF RADIO FREQUENCY FIELD ( $B_1$ )

One of the reasons for the great success of Fourier-transform (FT) NMR spectroscopy lies in the fact, that radio frequency (RF) pulses affect the spin system in a well-defined manner, which in turn allows for a defined manipulation of the system. The radio frequency corresponds to the transition frequency between Zeeman energy levels. For the description of pulsed NMR, a transition into a rotating frame of reference, which rotates with the Larmor frequency  $\omega_L$  around  $B_0$  is convenient. A  $B_1$  field oscillating with  $\omega_L$ , which is applied perpendicular to the  $B_0$  field, is static in the rotating frame.

To understand the effect of the radio frequency pulse, consider the precessing nuclei (cf. Figure 3.4a), as can be seen, there are more nuclei aligned with the field than against it. This means that there is a resultant magnetization vector aligned with the field. Now, imagine a frame spinning around the field at the Larmor frequency (the frequency of precession). To an observer in such a rotating frame, the nuclei would appear to be stationary, i.e. not precessing. Using the rotating frame of reference the magnetic behaviour of the system will be shown as in Figure 3.4b. A pulse of RF is applied along  $x'$  axis. In the rotating frame of reference,  $B_1$  and  $M_0$ , are stationary, and at right angles. The pulse causes the bulk magnetization vector,  $M_0$ , to rotate clockwise about the  $x'$  axis. The extent of the rotation is determined by the duration of the pulse.

In many FT-NMR experiments, the duration of the pulse is chosen so that the magnetization vector rotates by  $90^\circ$ . The detector is aligned along the  $y'$  axis. If we return to a static frame of reference (i.e. the laboratory frame) the net magnetic moment will be spinning around the  $y$  axis at the Larmor frequency (Figure 3.4c). This motion constitutes a radio-frequency signal which can be detected. When the pulse ends, the nuclei relax and return to their equilibrium positions, and the signal decays. Strictly speaking, the vector model only applies to uncoupled spins, and is only quantum mechanics which can give complete understanding of pulsed-NMR. However, even with its limitations, the vector model gives us a good start towards the understanding of RF pulses. For a more complete

description the reader is referred to a number of excellent text books explaining quantum mechanical description in great detail.<sup>[120]</sup>

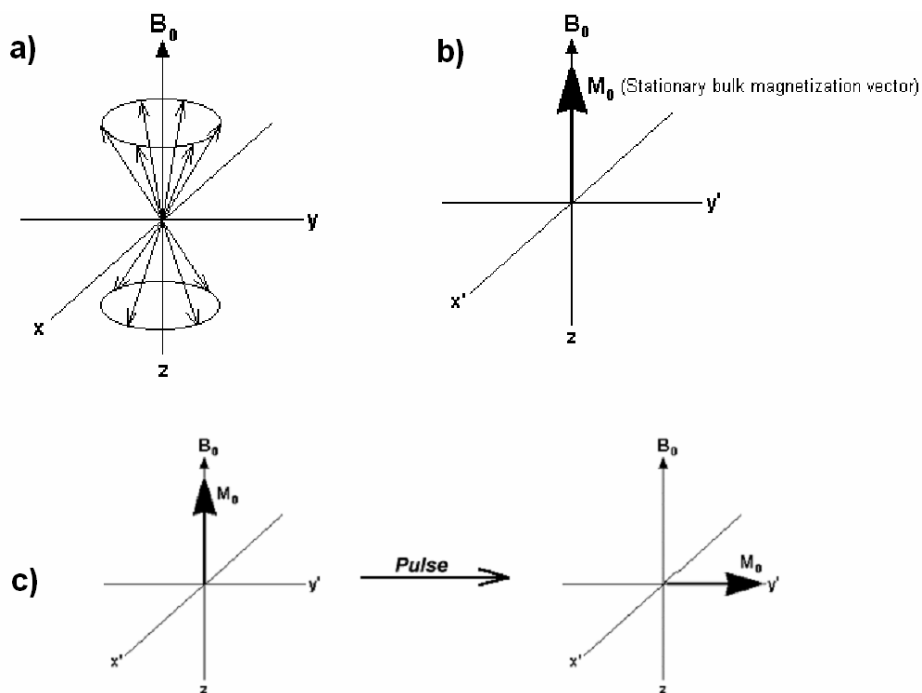


**Figure 3.4:** The vector model showing the effect of  $90^\circ$  pulse. (a) Shows the nuclei alignment along with the field, more number of nuclei aligned with the field than against it. (b) Stationary bulk magnetization vector before applying pulse (c) Magnetization vector after the pulse

### 3.5. CHEMICAL SHIELDING

Much of the chemical information in NMR spectra arises from chemical shifts due to the local magnetic fields generated at the nucleus by circulation of the surrounding electrons induced by the applied field. NMR therefore, became one of the most important and powerful structure elucidation techniques especially in organic synthesis field. If the



resulting magnetic fields oppose the applied field ( $B_0$ ) the effect is to shield the nucleus from it, and vice versa. The nucleus then experiences an effective field given by

$$B_{eff} = B_0(1 - \sigma) \quad (3.8)$$

where  $\sigma$ , the nuclear magnetic shielding tensor and the chemical shift Hamiltonian is given by

$$\hat{H}_{CS} = \gamma \hbar \hat{I} \cdot \sigma \cdot B_0 = \gamma \hbar (\hat{I}_x \sigma_{xx} + \hat{I}_y \sigma_{yy} + \hat{I}_z \sigma_{zz}) B_0 \quad (3.9)$$

Only the last (the symmetric part) of the shielding tensor  $\sigma$  turns out to affect the NMR spectrum within the *secular approximation*. Neglecting the antisymmetric part of the chemical shielding tensor and transforming to its principal axis system yields  $\sigma_{iso}$  (isotropic value), the anisotropy  $\Delta_{CS}$  and the asymmetry  $\eta_{CS}$ .<sup>[118]</sup> In rapidly tumbling liquid-state, the isotropic average is observed. However, in solids, where fast isotropic motions are absent, the orientation dependence of the chemical shift anisotropy (CSA) generally leads to a significant broadening of resonance lines. The CSA depends on the orientation of the PAS (principal axis system) with respect to the laboratory frame.

The isotropic part  $\sigma_{iso}$  is independent on the orientation of the sample with respect to the magnetic field. It leads to a site specific correction of the Larmor frequency for each nucleus in a molecule, which is called chemical shift  $\delta$  and commonly given in *ppm* of the Larmor frequency of the observed nucleus relative to the Larmor frequency of a suitable reference compound:

$$\delta [ppm] = \frac{\nu - \nu_{ref}}{\nu_{ref}} \cdot 10^6 \quad (3.10)$$

The great advantage of the *ppm*-scale is its independence of the strength of the external magnetic field  $B_0$ , which greatly simplifies the comparison between spectra measured at different spectrometers.

### 3.6. DIPOLE-DIPOLE INTERACTION

The presence of neighbouring magnetic nuclei alters the local field and therefore the energy of a nucleus. The dipole-dipole coupling is an anisotropic direct spin-spin interaction through space without involving the electron clouds. It is present between all types of spins with  $I > 0$ . Since each nuclear spin is magnetic, it generates a magnetic field, looping around in the surrounding space, according to the direction of the spin magnetic moment. Then a second nuclear spin interacts with this magnetic field. The interaction between the spins is mutual. The first nuclear spin also experiences the field generated by the second nuclear spin. The dipole-dipole coupling may be either intramolecular or intermolecular. In the *secular* approximation the Hamiltonian for a heteronuclear spin-pair  $I, J$  read as

$$\hat{H}_{D,\text{homo}}^{IJ} = -\frac{\mu_0 \hbar \gamma^2}{4\pi r^3} (3 \cos^2 \theta - 1) (3 \hat{I}_z \hat{J}_z - \hat{I} \cdot \hat{J}) \quad (3.11)$$

The dipole-dipole coupling depends on both, the distance between the two spins involved as well as the angle between the internuclear vector and the  $B_0$  field. Since the Larmor frequency of a heteronuclear spin pair differs significantly, the polarization exchange tends to zero and the dipolar Hamiltonian can be reduced to

$$\hat{H}_{D,\text{hetero}}^{IJ} = -\frac{\mu_0 \hbar \gamma_j \gamma_i}{2\pi r^3} (3 \cos^2 \theta - 1) (\hat{I}_z \hat{J}_z) \quad (3.12)$$

The magnetogyric ratio  $\gamma$  is a characteristic value of the isotope, which is about four times larger for  $^1\text{H}$  than for  $^{13}\text{C}$ . Thus, the homonuclear  $^1\text{H}$ - $^1\text{H}$  dipolar coupling constant is about four times larger than the heteronuclear  $^1\text{H}$ - $^{13}\text{C}$  dipolar coupling constant. In general, motion reduces dipolar couplings, this is well known from liquids, where all dipole-dipole couplings are averaged due to random motion of the molecules, which covers all possible angles  $\theta$ . This corresponds to an interaction of the space part of the dipolar Hamiltonian over a full sphere which is zero. But in anisotropic solids, the

strong dependency on the distance of the dipolar coupling constant gives valuable information on proximities between nuclei.

### 3.7. MAGIC ANGLE SPINNING

In solid-state NMR, most of the samples are in powder form. These powder samples consist of many crystallites with random orientations. The nuclear spin interactions which affect solid-state NMR spectra such as chemical shielding, dipole-dipole coupling and quadrupole coupling, all are dependent on the crystallite orientations. As a result of this, the spectrum of a powder sample contains broad lines, or powder patterns, as all the different molecular orientations present in the sample give rise to different spectral frequencies. Hence, it is necessary in solid-state NMR to apply techniques to achieve high resolution spectra. In the late 1950s, Andrew and Lowe introduced a technique where the sample is rapidly spun about an axis inclined at an angle  $54.7^\circ$  (cf. Figure 3.5) with respect to the magnetic field  $B_0$ , so that the orientation dependence is averaged out:  $(3 \cos^2 \theta - 1) = 0$ .<sup>[114,121]</sup> In the case of dipole-dipole coupling this process is called dipolar decoupling.

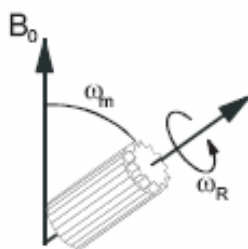


**Figure 3.5:** Magic angle spinning: MAS

However, complete averaging of an anisotropic interaction to zero is only achieved when the sample is spun with a frequency much greater than the characteristic interaction frequency. This is mechanically quite demanding. For this reason considerable effort has been taken to achieve the highest possible MAS frequency. Currently commercially available MAS hardware is capable of spinning at 70 kHz utilizing 1.3 mm

outer diameter rotor. Line broadening has been divided into homogeneous and inhomogeneous ones. Inhomogeneous line broadening is caused by the orientational dependence of anisotropic interactions, and is simply a superposition of resonance lines originating from different orientations of the molecules, where the broadening is refocused over a rotor period. This is the case for CSA, first order quadrupolar couplings and dipole-dipole coupling of isolated spin pairs. Homogeneous line broadening arises from dipole-dipole coupling between multiple spins. It occurs in particular for protons, as they have high natural abundance and high gyromagnetic ratio. Due to the spin-spin couplings the energy levels of single transitions are no longer degenerate, but split into a multitude of levels that prevents the complete refocusing of the signal after one rotor period. Since the homonuclear dipole-dipole coupling among protons can reach up to 100 kHz in solids, resolution in proton spectra usually suffer from homogeneous line broadening even under very fast MAS.

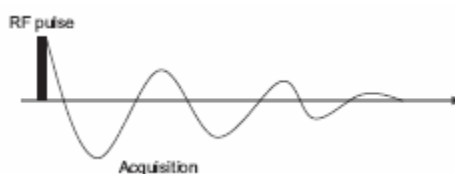


**Figure 3.6:** The single pulse experiment.

### 3.8. SINGLE-PULSE EXCITATION AND SINGLE PULSE DETECTION

The most basic experiment in FT-NMR consists of a single  $90^\circ$  pulse (cf. Figure 3.6). Starting from thermal equilibrium, after applying a  $90_x^\circ$  pulse the net magnetization is flipped from the z-axis to the (-y)axis and precesses in the xy-plane with its resonance frequency. This induces a weak oscillating voltage in the RF-coil, which is amplified and later converted into a digital signal (ADC) that can be handled by a computer. As ADCs are usually not fast enough and the signal is mixed with a reference frequency (Larmor

frequency) before digitization. To obtain the sign of the rotation it is necessary to also record the phase of the induced signal. In modern NMR spectrometers this is done by mixing the signal with two reference signals having the same frequency but a phase shift of 90° (so called quadrature detection). The data points are then collected in complex form.

### 3.9. CROSS POLARIZATION (CP)

Observing dilute spins such as  $^{13}\text{C}$  and  $^{15}\text{N}$  involves a number of problems, including the low abundance of the nuclei. This means that the signal-to-noise ratio is inevitably poor. Moreover, the relaxation times ( $T_1$ ) of low abundance nuclei tend to be very long, since the homonuclear dipolar interactions which can stimulate relaxation transitions are largely absent. The long relaxation time implies that long gaps must be left between scans and the spectra may take a very long time to be collected.<sup>[118]</sup>

However, using a technique known as cross polarization (CP) both the problems can be solved by deriving  $^{13}\text{C}$  polarization from more abundant nuclei with higher gyromagnetic ratio, such as  $^1\text{H}$  spins.<sup>[122,123]</sup> The polarization transfer is mediated by dipole-dipole interactions. Usually the so-called flip-flop term is suppressed for heteronuclear dipole-dipole interactions. In CP experiment it is reintroduced for a certain time (called contact time), by application of RF pulses on I and S spins at the same time. The amplitude of the two contact pulses in the cross polarization experiment has to be carefully set so as to achieve the Hartmann-Hahn matching conditions (Figure 3.7a)

$$\gamma_{\text{H}}B_1(^1\text{H}) = \gamma_{\text{S}}B_1(\text{S}) \quad (3.13)$$

In this simplistic approach, this sets the energy gap between the respective rotating frame spin states of  $^1\text{H}$  and S spins to be equal. This condition implies that in their respective rotating frames of reference the protons and carbons precess at equal

rates and that the effective energies are comparable, thus allowing a rapid transfer of magnetization. Under the MAS condition, this matching conditions changes to

$$\gamma_{\text{H}}B_1(^1\text{H}) = \gamma_{\text{X}}B_1(\text{S}) \pm n\omega_{\text{R}} \quad (3.14)$$

( $\omega_{\text{R}}$  being the spinning frequency) with maximum signal for  $n = \pm 1$

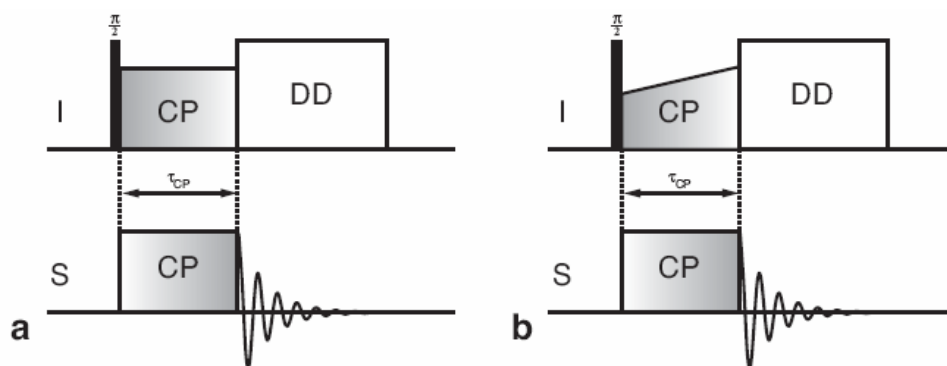


**Figure 3.7:** The cross-polarization experiment: (a) Hartmann-Hahn CP (b) Ramp-CP

MAS, which averages the dipolar coupling to zero, can severely disrupt cross polarization transfer if the spinning rate approaches the dipolar coupling constants governing the cross polarization transfer. This problem can be overcome by using a ramped-amplitude cross polarization sequence (ramped-CP).<sup>[124]</sup> In ramped-CP (cf. Figure 3.7b) the amplitude of the lock pulse on either channel is linearly increased over the contact time. This produces flat matching profiles over a wide range of matching conditions.

For  $^1\text{H}$ - $^{13}\text{C}$  CP experiments the carbon signal ideally can be enhanced up to a factor of four. Moreover, the repetition time of the experiment is then determined by proton  $T_1$  and no longer governed by the long carbon  $T_1$ . It should be noted that the efficiency of the polarization transfer depends on the local environment of the S spins, and the spectra cannot give exact quantitative information.

### 3.10. INTRODUCTION OF X-RAY ANALYSIS

X-rays are electromagnetic radiation of wavelength  $\sim 1 \text{ \AA}$  ( $10^{-10} \text{ m}$ ). In the electromagnetic spectrum X-rays are between  $\gamma$ -rays and the ultraviolet radiations and are produced when high energy charged particles, e.g. electrons accelerated through 30000 V, collide with matter. Atoms scatter X-rays, primarily through their electrons (X-ray striking an electron produces secondary spherical waves emanating from electron) known as scattering. X-ray crystallography is a method of determining the arrangement of atoms within a crystal from the manner in which a beam of X-ray is scattered from the electrons within the crystal.<sup>[174,175]</sup> The method produces a three dimensional picture of the density of electrons within the crystal, from which the mean atomic positions, chemical bonds, their disorder and other information can be derived. X-ray methods are generally useful in identifying known materials, characterizing new materials and discerning materials that appear similar by other experiments.

#### 3.10.1. Bragg's law

A crystal is a solid in which a particular arrangement of atoms (its unit cell) is repeated indefinitely along three principal directions known as the *basis* (or lattice) *vectors*. The Bragg approach to diffraction is to regard crystals where some of the X-rays are reflected off a plane with the angle of reflection equal to the angle of incidence, but the rest are transmitted to be subsequently reflected by succeeding planes. The Bragg's law is illustrated in Figure 3.8. The perpendicular distance between pairs of adjacent planes, the so-called *d*-spacing, *d*, and the angle of incidence or Bragg angle  $\theta$ , are related to the wavelength  $\lambda$  as shown in Eq. 3.15. If the Bragg's Law is satisfied, then the reflected beams are *in-phase* and interfere constructively. At angles of incidence other than the Bragg angle, reflected beams are *out-of-phase* and thus either destructive interference or complete cancellation occurs.

$$2d\sin \theta = n\lambda \quad (3.15)$$

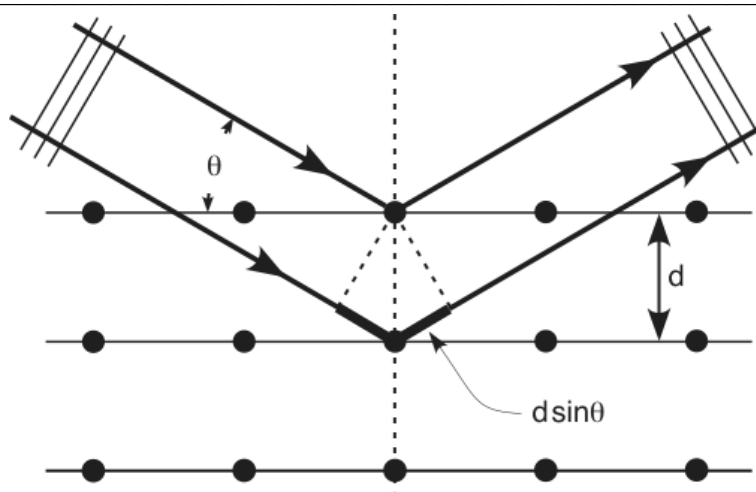


**Figure 3.8:** Schematic representation of X-ray diffraction. The incoming beam (coming from upper left) causes each scatterer (electrons) to re-radiate a small portion of its energy as a spherical wave. If scatterers are arranged symmetrically with a separation  $d$ , these spherical waves add constructively in directions where their path-length difference  $2 d \sin \theta$  equals an integer multiple of the wavelength  $\lambda$ . In that case, part of the incoming beam is deflected by an angle  $2\theta$ , producing a reflection spot in the diffraction pattern.<sup>[177]</sup>

### 3.10.2. Single crystal X-ray diffraction

The oldest and most precise method of X-ray crystallography is single crystal X-ray diffraction. Each reflection corresponds to one set of evenly spaced planes within the crystal. It can be shown that the electron density distribution  $\rho^{(x)}$  can be derived from the intensity of the reflections ( $\rho^{(x)}$  is the Fourier transformation of the structure factors  $F_{hkl}$  given in Equation 3.16).<sup>[177]</sup> It should be noted that the phase information is lost during the determination of the intensities. Therefore, the phases of the reflections have to be reconstructed in the course of the *structure determination*. Several techniques are available for this task e.g. heavy atom method, direct method.<sup>[177]</sup> The intensities are determined as the crystal is gradually rotated in the X-ray beam; this density together with supplementary data, allows the atomic positions to be inferred. The technique has three basic steps (cf. Figure 3.9). The first and often most difficult step is to obtain an adequate crystal of the material under study that should be sufficiently large (typically larger than 100  $\mu\text{m}$  in all dimensions), pure in composition and regular in structure with



no significant internal imperfections such as cracks or twinning. In the second step, the crystal is placed in an intense beam of X-rays producing the regular pattern of reflections. As the crystal is gradually rotated, the intensity of every spot is recorded at every orientation of the crystal. Finally, in the third step, this data is combined computationally with complementary chemical information to produce a model arrangement of atoms within the crystal (i.e. calculating the phases). This model is subsequently refined (usually by a least square refinement) to give the *crystal structure* which contains fractional coordinates and the vibrational parameters (temperature factors) of all atoms. Although it is most informative to diffract X-rays from a single, large crystal with few defects, such crystals some time may be difficult to obtain. However, it is also possible to reconstruct the atomic structure from the X-ray diffraction of polycrystalline samples using a technique known as powder diffraction.

$$\rho^{(x)} = \frac{1}{V} \sum_h \sum_k \sum_l F_{hkl} e^{-2\pi i(hx+ky+lz)} \quad (3.16)$$

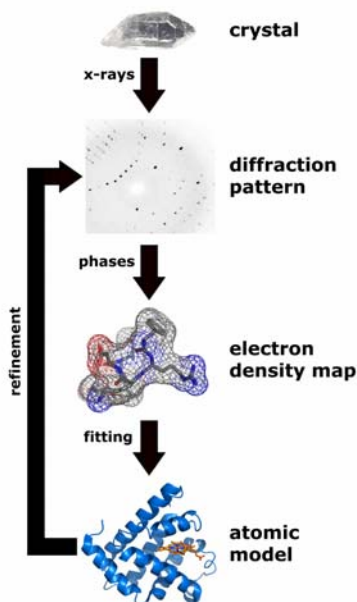


**Figure 3.9:** Schematic representation of the workflow for solving the structure of a molecule by X-ray crystallography.

---

### 3.10.3. Powder diffraction

An X-ray powder diffraction pattern is a set of lines or peaks, each of different intensity and position ( $d$ -spacing or Bragg angle  $\theta$ ), on either a strip of photographic film or on a length of chart paper. In this method all reflections which are three dimensionally distributed are projected along one line. Therefore, even at small angles it can be expected that reflections with equal or near-equal Bragg angles superimpose so that it will be difficult to determine their individual intensities. Nevertheless, for a given substance the line positions are essentially fixed and are characteristic of that substance. The intensity may vary from sample to sample, depending on the method of sample preparation and the instrumental conditions. For identification purposes, however, principal note is taken of line positions together with a semi quantitative consideration of intensities.<sup>[177]</sup>

Relative to other methods of structure analysis, powder diffraction allows for rapid, non-destructive analysis of multi-component mixtures without the need for extensive sample preparations. The most wide-spread use of powder diffraction is in the identification and characterization of crystalline solids that give very sharp signals in their powder pattern. In contrast, amorphous materials (liquid, gases etc.) produce a broad background signal. In addition, “the position of a diffraction peak is *independent* of the atomic positions within the cell and entirely determined by the size and shape of the *unit cell* of the crystalline phase”. Each peak represents a certain set of lattice planes and can therefore be characterized by a corresponding Miller index. This is particularly important in solid-state chemistry, e.g. to identify new materials.

# CHAPTER 4

## TRANSIENT STATES IN [2+2] PHOTODIMERIZATION OF CINNAMIC ACID

### 4.1. INTRODUCTION

The [2+2] photodimerization of *trans*-cinnamic acid (and many of its derivatives)<sup>[8]</sup> constitutes the classic example of a solid-state reaction that conforms to the topochemical principle. Numerous studies have been pursued on this class of compounds for basic design, planning and understanding of the solid-state reactions.<sup>[1,125,126]</sup> Schmidt *et al*<sup>[5]</sup> have classified the packing of *trans*-cinnamic acid and its derivatives in three different forms: an  $\alpha$ -form (where monomers are arranged in a head-to-tail manner),  $\beta$ -form (with the monomers arranged head-to-head) and a  $\gamma$ -form (where the monomers are unfavourably aligned). While in both, the  $\alpha$ - and  $\beta$ -forms the reactive double bonds approach each other by less than approximately 4 Å and which are photoactive yield head-to-tail and head-to-head dimers, respectively, (cf. Figure 4.1) the  $\gamma$ -form is photostable. The topotactic nature of the obtained reaction products has been revealed by applying various techniques such as atomic force microscopy (AFM),<sup>[15,16]</sup> vibrational spectroscopy,<sup>[17-20]</sup> X-ray diffraction<sup>[21-23,29]</sup> and solid-state NMR.<sup>[25-28]</sup>

In this chapter certain missing links in the evolving story of crystalline state [2+2] cycloaddition of *trans*-cinnamic acid are discussed. Single crystal X-ray analysis as well as solid-state NMR has been applied to monitor the [2+2] photodimerization of  $\alpha$ -*trans*-cinnamic acid to  $\alpha$ -truxillic acid. Crystal structures<sup>[29,127]</sup> suggest that  $\alpha$ -truxillic acid is a centrosymmetric photodimer. During the course of study, <sup>13</sup>C-CPMAS spectra were

measured for different conversion ratios ranging from  $\alpha$ -*trans*-cinnamic acid (0%) to  $\alpha$ -truxillic acid (100%).<sup>[28]</sup> In contrast to an anticipated centrosymmetric molecular geometry of  $\alpha$ -truxillic acid, the  $^{13}\text{C}$ -CPMAS spectra exhibited additional signals for the cyclobutane ring and carbonyl region, which Hayes *et al*<sup>[28]</sup> attributed to solid-state packing effects, e.g. distortions in the cyclobutane ring and/or dihedral angle twists of both the phenyl rings and carboxylic acid group. Alternatively, the observed signal splittings may originate from (possibly asymmetric) hydrogen-bondings, which are not only known to distinctly impact on  $^{13}\text{C}$  or  $^{15}\text{N}$  spectra<sup>[128,129]</sup> but more importantly are revealed by characteristic chemical shifts of up to 21 ppm in the respective solid-state proton NMR spectra.<sup>[129,130]</sup> Indeed, the comparison of both X-ray and NMR data turned out to be very fruitful in many different cases,<sup>[129,131]</sup> but proper care of the temperature settings must be taken.

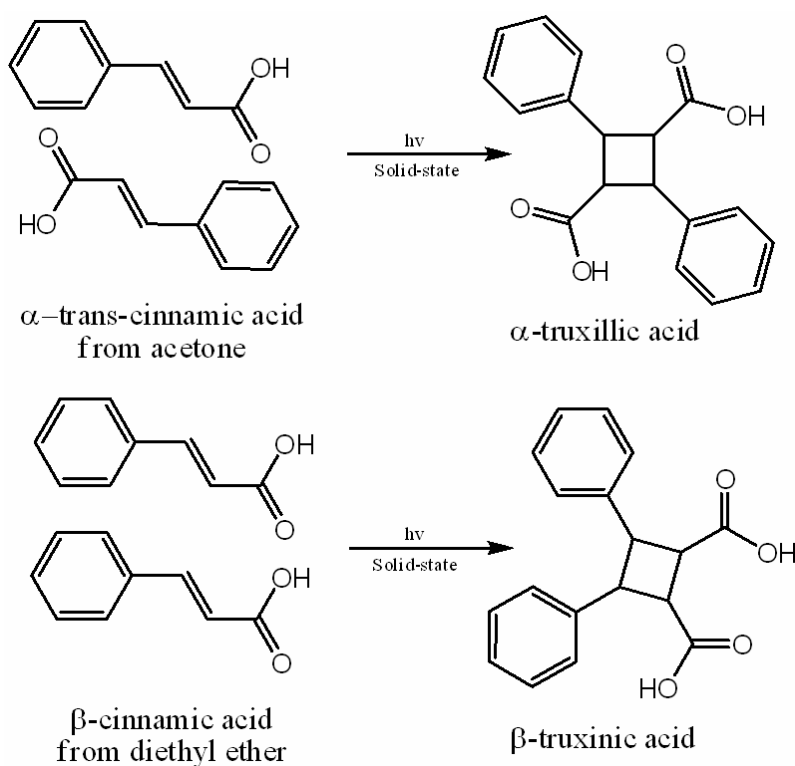


**FIGURE 4.1:** Diagram illustrating the conversion of the  $\alpha$ - and  $\beta$ -forms of *trans*-cinnamic acid to dimers via topochemical reactions.

## 4.2. CONFORMATION OF CARBOXYL GROUP

The carboxyl group in the majority of mono- and dicarboxylic acids in its crystalline phase either adopt a synplanar (cf. Figure 4.2a) or antiplanar (cf. Figure 4.2b) O=C-O-H conformation as shown in Figure 4.2.<sup>[132,133]</sup> The synplanar structure is the more stable conformer while the anti-planar form usually occurs when the O-H bond participates in an *intramolecular* O-H...O bond.  $\alpha$ -*trans*-Cinnamic acid, a non-substituted acid, which does not involve in any kind of intramolecular hydrogen bonding, adopts a synplanar conformation with respect to its carboxyl group. However, units of two monomers which are approximately in the same plane and connected via *intermolecular* hydrogen bonds, form highly overlapped parallel stacks in which monomers within certain distances and relative orientations come into close contact. In the  $\alpha$ -form, the overlap offset is so large, that the closest monomer pairing in a reactive orientation are not in the same stack, but in neighboring stacks (cf. Figure 4.2c). Thus, while neighbours within the same stack are related by mirror symmetry and are over 5.5 Å apart, the reacting pairs are only 4 Å apart. Therefore, in an  $\alpha$ -lattice head-to-tail centrosymmetric dimers are formed with least lattice disturbance.<sup>[7,29,127]</sup>

## 4.3. SOLID-STATE <sup>13</sup>C-CPMAS NMR APPLICATION

A series of <sup>13</sup>C-CPMAS NMR spectra for  $\alpha$ -*trans*-cinnamic acid and the corresponding [2+2] photodimerization products after various irradiation times were reported by Hayes *et al.*<sup>[28]</sup> They showed that solid-state NMR can be successfully applied to study this class of photodimerization reactions because of the good resolution of individual resonances and the large separation of the signals of reactant and product functional groups. In contrast to an anticipated centrosymmetric molecular geometry of  $\alpha$ -truxillic acid, the <sup>13</sup>C-CPMAS spectra exhibited additional <sup>13</sup>C signals for the cyclobutane ring and carbonyl region, which Hayes *et al.*<sup>[28]</sup> referred to as solid-state packing effects, e.g. distortions in the cyclobutane ring and/or dihedral angle twists of both the phenyl rings and carboxylic acid group. However, careful observation of the crystal structures of

mixtures as well as fully converted truxillic acid did not reveal *any* distortions or packing defects in the crystal lattice.

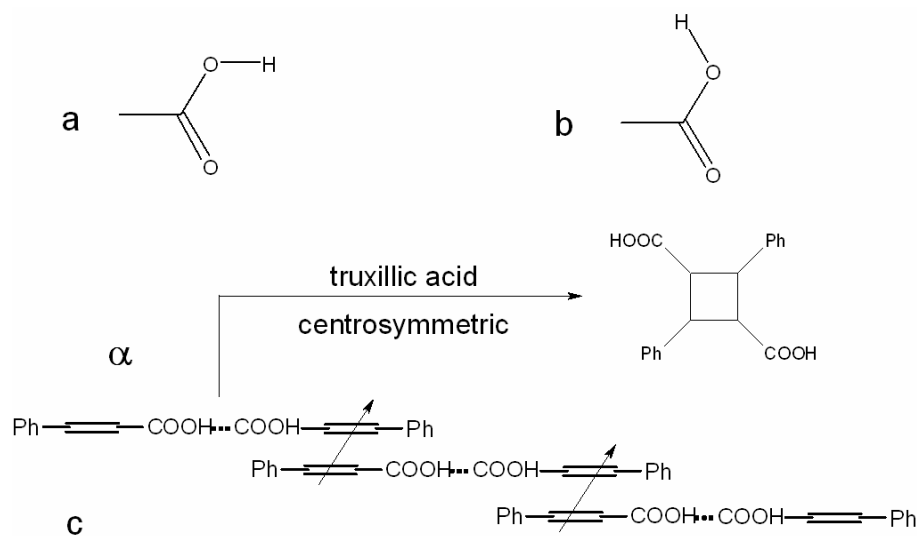


**Figure 4.2:** Shows O-H group conformation in carboxylic acids and packing mode of  $\alpha$ -*trans*-cinnamic acid in crystal lattice. (a) Synplanar conformation of carboxyl group (b) Anti planar conformation. (c) Schematic view of the  $\alpha$ -modification of cinnamic acid.

Even computed  $^{13}\text{C}$  chemical shifts of the  $\alpha$ -truxillic acid dimer based on an optimized X-ray geometry *neither* revealed any splitting in the carbonyl region *nor* any extra signals in the cyclobutane ring region. This prompted to consider the consequences of (possibly dynamic) hydrogen bonding present in the crystals. Indeed, each  $\alpha$ -truxillic acid photodimer is hydrogen bonded to *two* of its neighboring molecules forming a chain like structure.<sup>[127]</sup> Since X-ray methods suffer from the fact that heavy atoms tend to dominate the observed diffraction pattern, it is difficult to locate lighter atoms (e.g. hydrogen) accurately. In this case, solid-state NMR can provide complementary information. Figure 4.3 shows a series of  $^{13}\text{C}$ -CPMAS NMR spectra ranging from  $\alpha$ -*trans*-cinnamic (0% conversion) to asdimerized  $\alpha$ -truxillic acid ( $\text{P}2_1/\text{n}$  phase,<sup>[127]</sup> 100% conversion), where 4.3b and 4.3c are spectra for partial mixtures containing both monomer and dimer at  $\sim 25\%$  and  $\sim 50\%$  conversion, respectively.

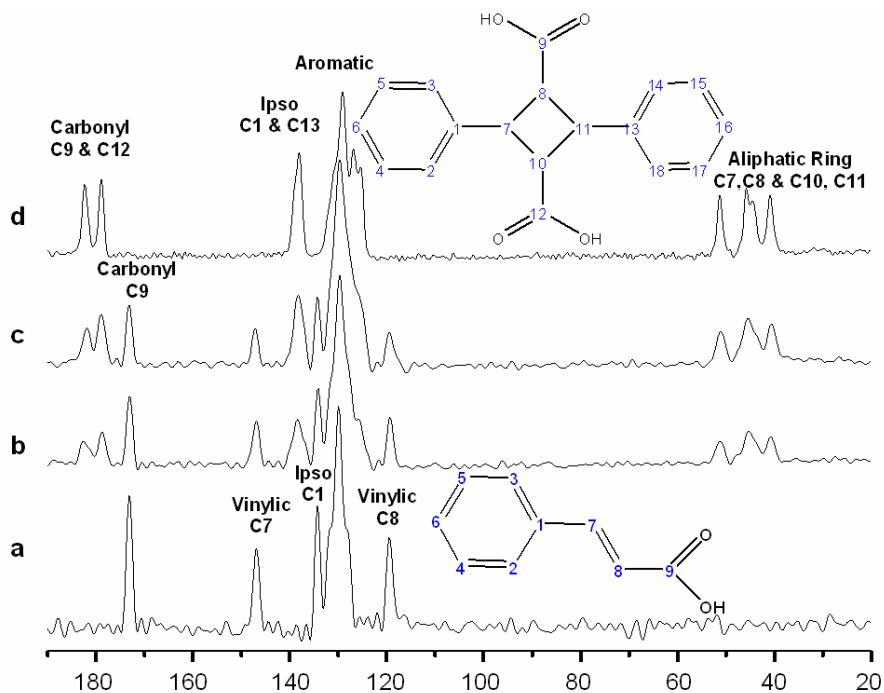


**Figure 4.3:** Solid-state  $^{13}\text{C}$ -CPMAS spectra ranging from  $\alpha$ -*trans*-cinnamic acid to  $\alpha$ -truxillic acid: (a) monomer prior to irradiation (b)  $\sim 25\%$  converted mixture (c)  $\sim 50\%$  converted mixture (d) dimer after complete conversion (as dimerized,  $P2_1/n$  phase, see also Figure 4.4).

As the dimerization proceeds, corresponding intensities of both the olefinic carbon and carbonyl carbon signals assigned to the monomer decreased with a gradual rise of new carbon signals attributed to the cyclobutane ring indicating successful formation of a photodimer. Additionally, the chemical shifts of the neighboring carbons, i.e. the *ipso* (non protonated) carbon and carbonyl carbon, display a small downfield shift upon conversion of the monomer into a dimer, possibly due to differences in inductive effects of neighboring groups (vinyl vs. cyclobutane). Full assignments of carbon sites in all samples are given in Table 4.1. Two signals in the carbonyl region and four different signals in the cyclobutane ring region are observed in both partially and fully converted dimer spectra (cf. Figures 4.3b-d). In contrast, the solution  $^{13}\text{C}$  NMR spectrum exhibits only two peaks in cyclobutane ring region and a single peak in the carbonyl region (as expected from a centrosymmetric molecular geometry). The latter resonance is downfield shifted from 173 ppm in solution to about 179 ppm in solid state, probably due to hydrogen bondings that are absent in solution.

#### 4.4. REPLACING CARBOXYL ACID MOIETY

To further explore possible influences of hydrogen-bonding within the crystalline compounds, the methyl ester of  $\alpha$ -truxillic acid was prepared. The corresponding  $^{13}\text{C}$ -CPMAS spectrum (cf. Figure 4.5) unambiguously reflects a centrosymmetric photodimer, that is, there are three signals in the aliphatic region, one is assigned to methyl carbon and the other two signals belong to the cyclobutane ring. Symmetry renders the two carbons attached to the carbonyl groups or phenyl rings equivalent. Moreover, the  $^{13}\text{C}$  chemical shifts of the ester compound are close to those  $^{13}\text{C}$  shift values obtained for  $\alpha$ -truxillic acid in solution (i.e.  $\sim 173$  ppm for carbonyl carbon). Taken together, this strongly suggests that any observed excess signals are not due to solid state packing effects but rather due to asymmetry of the (dynamic) hydrogen bonds which temporarily destroys the center of symmetry of the  $\alpha$ -truxillic acid photodimer.

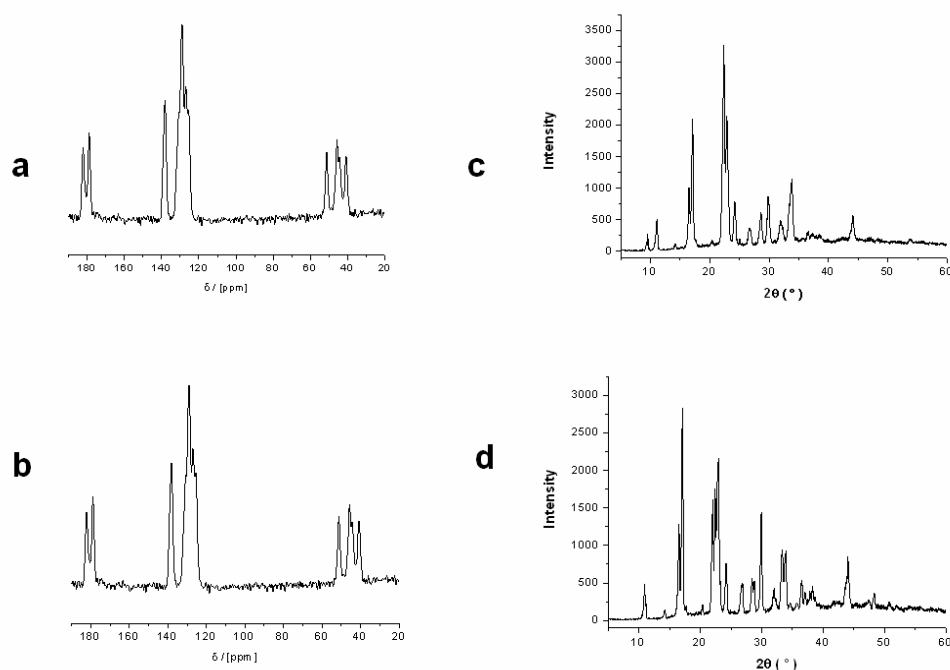


**Figure 4.4:**  $^{13}\text{C}$ -CPMAS spectra and powder diffractograms of  $\text{P2}_1/\text{n}$  and  $\text{C2}/\text{c}$  phase of truxillic acid. a) and b) are the  $^{13}\text{C}$ -CPMAS spectra of  $\text{P2}_1/\text{n}$  and  $\text{C2}/\text{c}$  phase; c) and d) are the powder diffractograms, respectively.



Sample	$\delta$ (ppm)	Assignment
<i><math>\alpha</math>-trans-cinnamic acid</i>	173.1 146.9 134.3 131.2-127.8 119.4	Carbonyl carbon (C9) Vinyl carbon (C7) Ipsos carbon (C1) Aromatic carbons (C2-C6) Vinyl carbon (C8)
<i><math>\alpha</math>-truxillic acid</i>	182.3 178.9 138.0 129.6 126.6 125.5 52.1 46.2 45.1 41.3	Carbonyl carbon (COO <sup>-</sup> ) Carbonyl carbon (COOH) Ipsos carbons (C1, C13) Aromatic (C2, C3, C14 & C18) Aromatic (C4, C5, C15 & C17) Aromatic (C6, C16) Cyclobutane ring carbon (C8) Cyclobutane ring carbon (C10) Cyclobutane ring carbon (C7) Cyclobutane ring carbon (C11)
<i><math>\alpha</math>-truxillic acid methyl ester</i>	172.7 139.4 126.1-128.9 52.8 47.1 40.0	Carbonyl carbon (C11, C19) Ipsos carbon (C5, C13) Aromatic carbons Methyl carbons (C22, C24) Aliphatic carbons (C2, C4) Aliphatic carbons (C1, C3)

**Table 4.1:** Resonance assignments for  *$\alpha$ -trans-cinnamic acid*,  *$\alpha$ -truxillic acid* and  *$\alpha$ -truxillic acid methyl ester* based on *ab initio* chemical shift calculations.

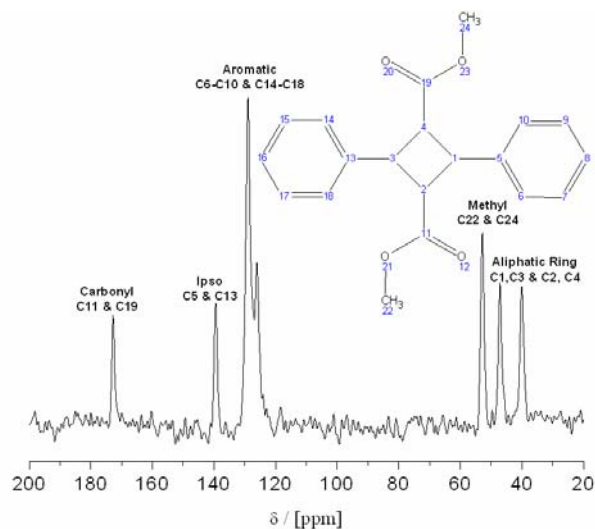


**Figure 4.5:**  $^{13}\text{C}$ -CPMAS of truxillic acid methyl ester (dimethyl-2, 4-diphenylcyclobutane-1, 3-dicarboxylate).

#### 4.5. DYNAMICS OF HYDROGEN BONDS

After concluding that the distortion of the symmetry is mainly caused by hydrogen bonds, possible dynamics in the hydrogen bonded pair was concerned. In the past, numerous studies have been published about dynamics of hydrogen atoms in carboxylic acid dimers suggesting various models to describe the motion of the hydrogen atom along the hydrogen bond.<sup>[134–138]</sup> According to Horsewill and Aibout,<sup>[138]</sup> (di-)carboxylic acids not only commonly yield centrosymmetric dimers in the solid-state where a ring-like structure is formed by *two* hydrogen bonds (cf. Figure 4.6) but also arrange as continuous polymeric chains of molecules stabilized by hydrogen bonds. This also exists in truxillic acid crystals.<sup>[127]</sup> Within a single dimer unit two conformations, labeled 1 and 2 are possible. The interconversion between the two configurations 1 and 2 should involve a simultaneous proton exchange across a symmetric transition structure X.

Due to this effect, the potential energy of the system with respect to the hydrogen atom position can conveniently be described with a double minimum, while in the solid-state the influence of neighbouring molecules breaks the symmetry of the potential so that the two potential wells may in general be of unequal depth. It is possible for the

hydrogen atoms to move in a coordinated fashion within the ring established by the two hydrogen bonds resulting in a change of the electronic structure and atomic arrangement within the dimer, e.g. a C=O bond turns into a C-O bond and *vice versa*. In the case of  $\alpha$ -truxillic acid, proton dynamics studies<sup>[134-138]</sup> suggest that either a thermally activated proton transfer takes place or tunneling occurs. This could be addressed in detail by either  $T_1$  relaxation measurements or (quasi)inelastic neutron scattering.

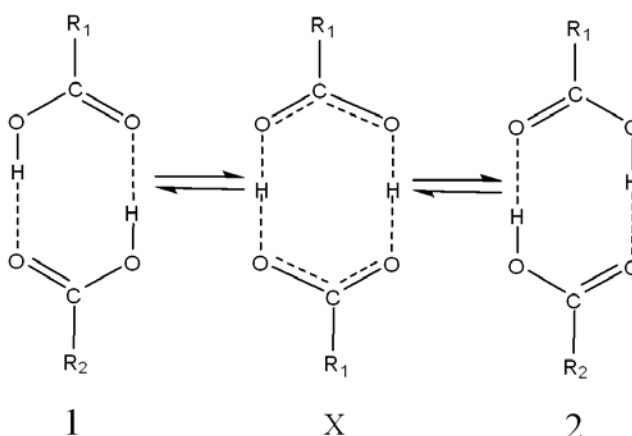


**Figure 4.6:** Interconversion of the molecular structure of a carboxylic acid dimer.<sup>[134]</sup>

#### 4.6. STRUCTURAL CORRELATIONS

Considering the double minimum potential approach, one might expect *two* different acidic proton peaks in the  $^1\text{H}$  MAS NMR spectrum of the truxillic acid, but the corresponding spectrum (cf. Figure 4.7) displays only two signals, a broad signal with a small shoulder represents both the aliphatic and aromatic protons, while the single peak at  $\sim 14$  ppm (FWHH = 1000 Hz) is assigned to the strongly hydrogen bonded carboxylic acid protons. In addition, variable-temperature NMR ( $T=225\text{K}$  to  $T=335\text{K}$ ) did not reveal any differences in the spectra indicating “constant” dynamics. Either, to freeze-in possible motions very low temperatures (e.g. 30 K) would be necessary to clearly distinguish two different proton positions or the underlying motion of the proton is much faster than the NMR time scale yielding an averaged peak position. To unambiguously

identify local mobilities, focused were put on static, variable-temperature deuterium NMR measurements.

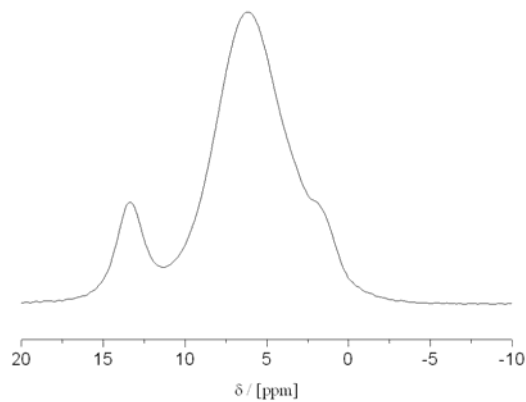


**Figure 4.7:**  $^1\text{H}$  MAS NMR spectrum of  $\alpha$ -truxillic acid measured at room temperature.

#### 4.7. DEUTERIUM NMR MEASUREMENTS

Larsen *et al.*<sup>[139]</sup> reported a perfect linear variation of the  $^2\text{H}$  nuclear quadrupolar coupling constant (NQCC) with the asymmetry of the hydrogen bond rendering NQCC a very useful parameter for determining the asymmetry of a given hydrogen bond. Generally the NQCC parameter for  $^2\text{H}$  increases with increasing asymmetry of the hydrogen bond, and for a long and asymmetric hydrogen bond it is about three times larger than of  $^2\text{H}$  in a short symmetric hydrogen bond.<sup>[140]</sup> Thus, for asymmetric hydrogen bonds, the NQCC for  $^2\text{H}$  should be quite large.

The static  $^2\text{H}$  spectrum (cf. Figure 4.8) of  $\alpha$ -truxillic acid dimer exhibits a Pake pattern with a quadrupolar splitting of  $\text{NQCC} = 155.9$  kHz, which indicates the presence of certain dynamics, most probably reflecting a two site jump of a proton along the hydrogen bond in the fast limit. The sharp center peak is attributed to mobile deuterons that undergo pseudo-isotropic reorientations. The extracted NQCC parameter of 155.9 kHz is quite large and suggests the presence of long and asymmetric hydrogen bonds. This leads to the assumption that at a given time each truxillic acid molecule possesses

two different carbonyl groups, one is an original carboxylic acid (COOH) and the other represents a carboxylate anion (COO<sup>-</sup>). In compounds that have asymmetric hydrogen bonds the two carboxy groups are different and give rise to different chemical shifts. The  $\delta$  (<sup>13</sup>C) is close to 180 ppm for carboxylate groups and close to 170 ppm for carboxylic acid group.<sup>[139]</sup> The isotropic <sup>13</sup>C chemical shift moved to higher frequencies as it passes from the carboxylic acid to the carboxylate form,<sup>[129]</sup> as noticed for truxillic acid as well, where the COOH signal appears at 178.9 ppm and COO<sup>-</sup> signal comes at a slightly higher frequency at 182.3 ppm. Hence, this results in a splitting of the cyclobutane ring signals. The intensities of the carbonyl signals are not equal and this is more prominent at lower conversion; the carboxylate signal is less intense than its neighboring carboxylic acid signal, it gradually increases as the conversion increases and becomes more or less equal to the carboxylic carbon signal after complete conversion. Dynamic hydrogen bonding also exists in *trans*-cinnamic acid monomer as suggested by the high NQCC value of about 149.1 kHz, but this does *not* affect the <sup>13</sup>C-CPMAS spectra (cf. Figure 4.3a), e.g. the carbonyl signals do not split. This can be explained by the fact that  $\alpha$ -truxillic acid possesses two carbonyl groups on the same molecule while *trans*-cinnamic acid has one carbonyl atom. Since NMR measures an averaged chemical shift *no* splitting is observed in the case of the monomer.

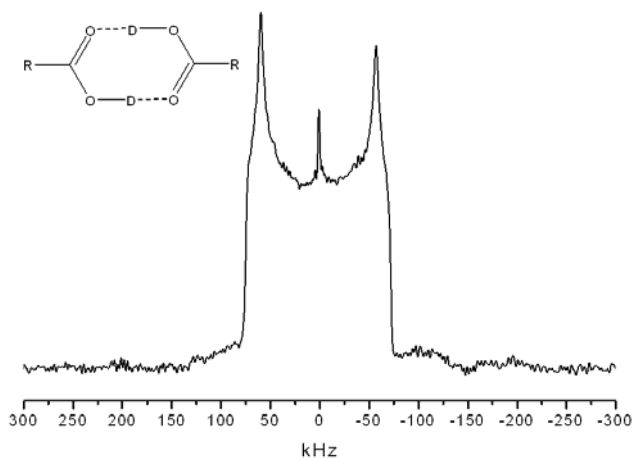


**Figure 4.8:** Solid-state <sup>2</sup>H spectrum of  $\alpha$ -truxillic acid dimer at room temperature ( R = (C<sub>6</sub>H<sub>5</sub>)<sub>2</sub> C<sub>4</sub>H<sub>4</sub>). The quadrupolar splitting of NQCC = 155.9 KHz suggests a two site jump in the fast limit.

#### 4.8. HIGH TEMPERATURE X-RAY ANALYSIS

The apparent discrepancy between NMR and X-ray analysis in case of truxillic acid may result from two reasons: the carboxylic acid protons experience motion (dynamics) on the NMR time scale, but appear rather rigid when observed by X-ray at very low temperature (30 K). Indeed, the presence of a carboxylate group in the compound is indicated by nearly equal C-O distances, with typical C-O values of 1.25-1.26 Å corresponding to a very small  $\Delta(\text{C-O})$  values.<sup>[129,132,139]</sup> The carboxylic acid group, COOH, with a C-O single bond ( $\approx 1.31$  Å) and a C=O double bond ( $\approx 1.21$  Å) has a  $\Delta(\text{C-O})$  value of around 0.1 Å. In the crystal structure of truxillic acid we observed that  $\Delta(\text{C-O})$  values are less than 0.1 Å, single C-O value is 1.312 Å, which is typical but the double bond is slightly larger than in the carboxylic acid group (about 1.231 Å) yielding  $\Delta(\text{C-O})$  less than 0.1 Å (0.081 Å). When we remeasured the crystal structure of the as-dimerized truxillic acid at different temperatures (120 K to 350 K), we observed a small gradual decrease of  $\Delta(\text{C-O})$  values at higher temperatures (cf. Figure 4.9). This trend is more prominent in case of  $\alpha$ -*trans*-cinnamic acid monomer where  $\Delta(\text{C-O})$  is far less than 0.1 Å ( $\sim 0.038$  Å) pointing towards the presence of asymmetric and dynamic hydrogen bond in the carboxyl moiety of monomer. We have also determined the crystal structure of truxillic acid methyl ester (the projection is given in Figure 4.10). The  $\Delta(\text{C-O})$  value amounts to 0.135 Å and clearly emphasizes an absence of carboxylates. This is quite expected since the ester cannot be involved in dynamic hydrogen bonding. Hence, the <sup>13</sup>C-CPMAS NMR spectrum truly reflects centrosymmetry showing no peak splitting.

#### 4.9. SYNPLANAR VS. ANTIPLANAR CONFORMATION

Leiserowitz has already discussed molecular packing modes of carboxylic acids.<sup>[132]</sup> He stated that in the crystal structures of  $\alpha$ ,  $\beta$ -saturated carboxylic acids R-CH<sub>2</sub>-CH<sub>2</sub>-COOH, the synplanar C <sup>$\beta$</sup> -C <sup>$\alpha$</sup> -C=O arrangement as shown in Figure 4.11a is adopted without *any* known exceptions, whereas the synplanar rule does not apply to the  $\alpha$ ,  $\beta$ -unsaturated acids R-CH=CH-COOH, with several compounds showing an antiplanar C <sup>$\beta$</sup> -C <sup>$\alpha$</sup> -C=O form (cf. Figure 4.11b). Concerning the photodimerization of  $\alpha$ -*trans* cinnamic

acid, the monomer (an  $\alpha$ ,  $\beta$ -unsaturated acid) adopts antiplanar conformation while the resulting photodimer adopts synplanar conformation.<sup>[29,127]</sup> Thus, upon increasing conversion ratios the molecule *slowly* changes from an antiplanar to synplanar conformation, possibly facilitated by proton exchange since reactions in solid state commonly occur with a minimum amount of atomic or molecular movement.<sup>[6]</sup> This strongly supports the presence of dynamic disorder in the carboxyl moiety of truxillic acid where the proton undergoes rapid oscillations across the O-H $\cdots$ O bond accompanied by interconversion between the carbonyl C=O and hydroxyl C-O(H) bond. The temperature dependence of  $\Delta(\text{C-O})$  in truxillic acid (cf. Figure 4.9) supports this assumption. Indeed, at highest temperature (350 K) the search for the H-atoms by difference fourier analysis revealed *two* carboxyl H atoms (cf. Figure 4.11c) each occupied by 50%. Crystal structure projection of the truxillic acid measured at elevated temperature (350 k) is shown in Figure 4.12 which clearly shows the presence of two carboxyl H atoms.

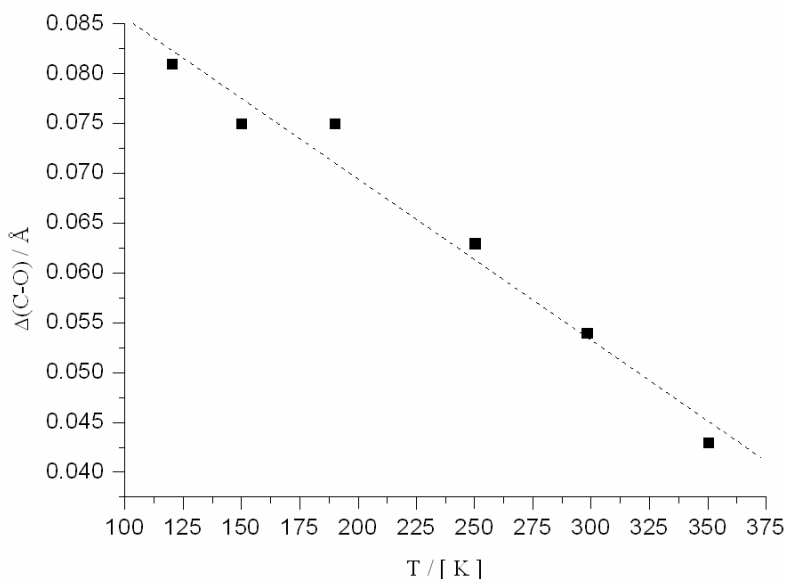


**Figure 4.9:** Plot of the  $\Delta(\text{C-O})$  values as a function of temperature showing that the truxillic acid C-O and C=O become less distinct with increase of temperature. The plot shows an approximate linear fit. C-O and C=O distance variations vs. temperature along with  $\Delta(\text{C-O})$  values are explicitly listed in Table 4.2.

COMPOUNDS	TEMPERATURES (K)	C-O (Å)	C=O (Å)	$\Delta(\text{C-O})$ (Å)
Trans-Cinnamic Acid	120	1.292(2)	1.254(2)	0.035(2)
$\alpha$ -Truxillic Acid	120	1.314(2)	1.231(2)	0.083(2)
	150	1.307(2)	1.232(2)	0.075(2)
	190	1.307(2)	1.232(2)	0.075(2)
	250	1.297(2)	1.234(2)	0.063(2)
	295	1.290(2)	1.236(2)	0.054(2)
	350	1.278(2)	1.234(2)	0.044(2)
Methyl Ester of $\alpha$ -Truxillic Acid	120	1.349(3)	1.206(3)	0.143(3)

**Table 4.2:** C-O distance variations vs. temperature along with their ESD's (estimated standard deviations) which is obtained by measuring the crystal structures of  $\alpha$ -truxillic acid at different temperature. One thing which is to be noted here is that only C-O distances changes substantially with temperature which causes the decrease in  $\Delta(\text{C-O})$  but C=O almost remain same.

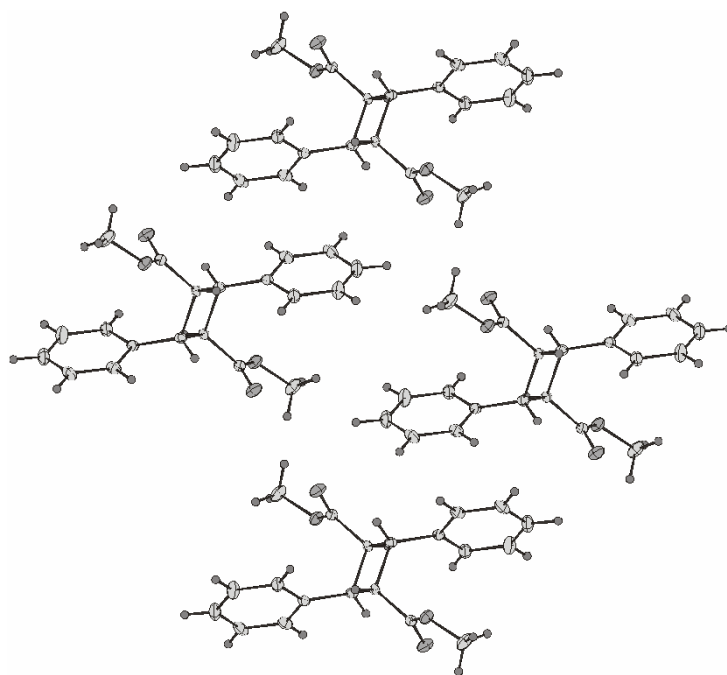


**Figure 4.10:** View of methyl ester of truxillic acid (dimethyl 2, 4-diphenylcyclobutane-1, 3-dicarboxylate) along b axis.



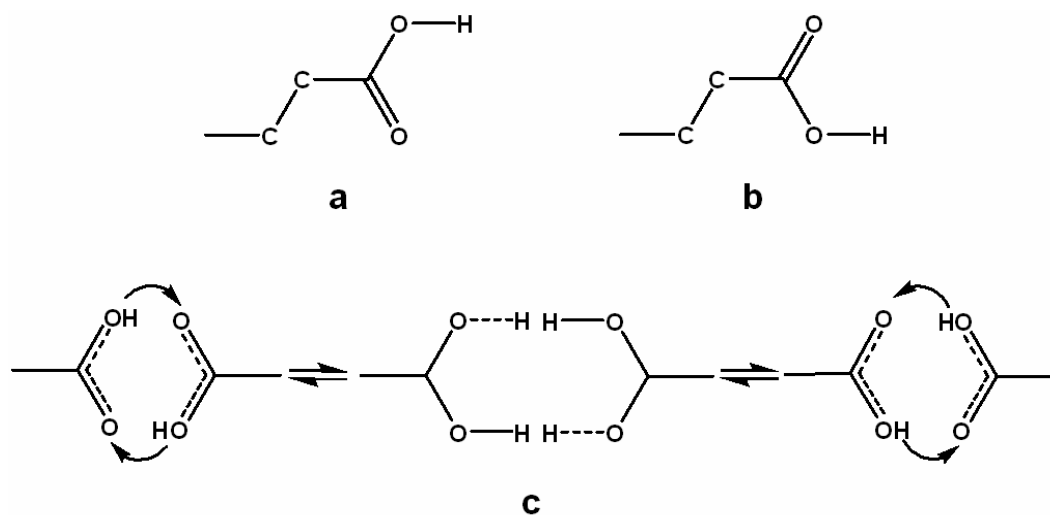


**Figure 4.11:** Conformations of a carboxyl moiety in a carboxylic acid: (a) synplanar conformation adopted by dimer; (b) antiplanar conformation adopted by monomer; (c) schematic representation of carboxyl moiety in the highest temperature (350K) crystal structure of truxillic acid. Here, the proton is located in a double-well potential so that two half occupied positions for H are observed.

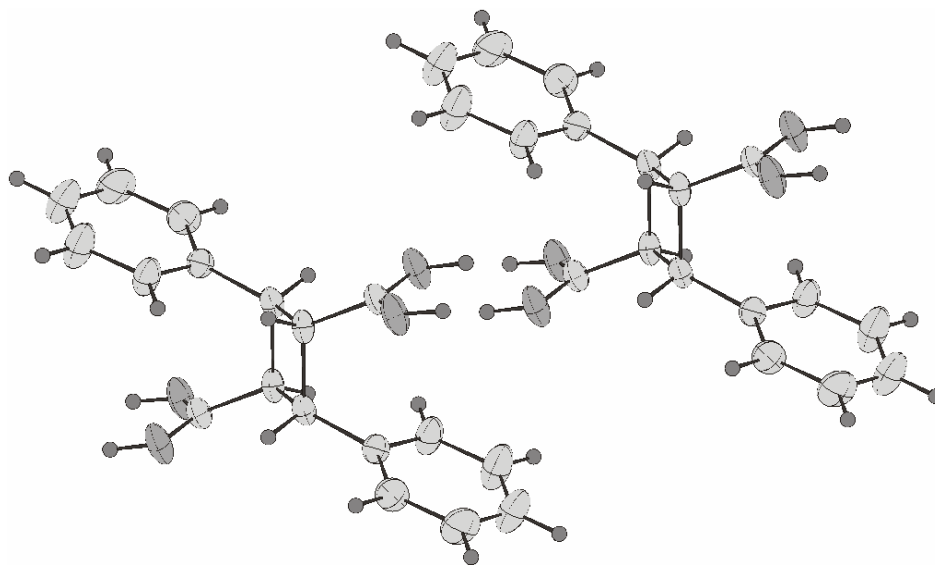


**Figure 4.12:** Crystal structure projection of  $\alpha$ -truxillic acid measured at higher temperatures (350 k). Note the presence of two protons on each carboxyl group of truxillic acid.

#### 4.10. AB INITIO COMPUTATIONS

Finally, the  $^{13}\text{C}$ -CPMAS data was compared with *ab initio*  $^{13}\text{C}$  chemical shift computations of both  $\alpha$ -truxillic acid and its anion (created by arbitrarily removing one proton from the carboxyl group). Notably, the truxillic acid structure did not reveal any splitting but the anionic structure yields similar signal splitting for the carbonyl and cyclobutane ring atoms as observed experimentally. Figure 4.13 shows the plot of computed  $^{13}\text{C}$  isotropic chemical shifts vs. the observed values; the agreement is good in the range of  $\pm 5$  ppm.

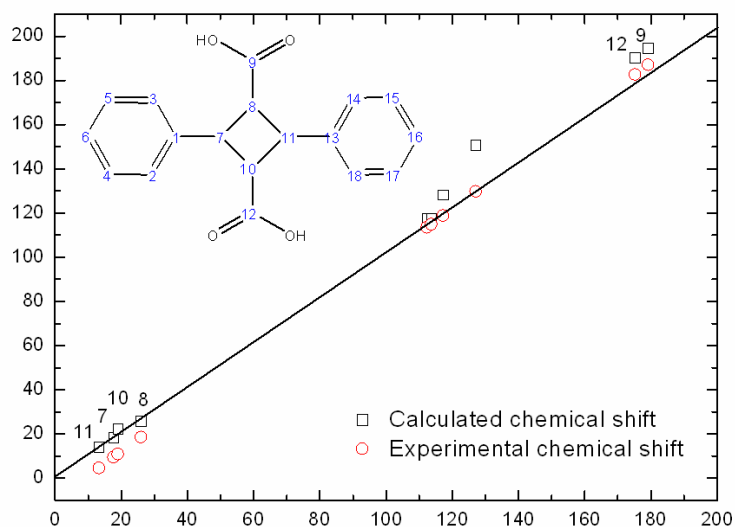


**Figure 4.13:** Computed  $^{13}\text{C}$  chemical shifts for carboxylate anion of truxillic acid vs. observed chemical shifts.

#### 4.11. CONCLUSIONS

Thus, it has been clearly demonstrated that dynamic hydrogen bonding results in the appearance of additional signals in the  $^{13}\text{C}$ -CPMAS spectra of photodimerized  $\alpha$ -*trans* cinnamic acid. The transient asymmetry of the hydrogen bonds in the crystal temporarily destroys the photodimer's center of symmetry so that the truxillic acid molecules may

exist in a non-centrosymmetric state in their crystal lattice. Indeed, this is a common phenomenon found for a majority of carboxylic acid-based dimeric compounds. Only the joint approach of both X-ray analysis and solid-state NMR successfully revealed the dynamic processes occurring in these topochemical reactions and thus, provided detailed insight into the reaction mechanism of organic solid-state transformations.

Crystal engineering is a rapidly developing interdisciplinary field of chemistry that focuses upon the rational design of solids. Basically, an understanding of factors (e.g. intermolecular forces, sizes and shapes of molecules) that influence how atoms and molecules assemble and pack in the solid-state will enable chemists to design solids with predictable and rather tailored properties (e.g. reactivity, optical, magnetic). Early efforts to control reactivity in the solid-state employed substituents to steer olefins, but in more recent studies more efforts have been put to steer the olefins using hydrogen-bonded molecular assemblies by applying crystal engineering principles. One prominent template is resorcinol that possesses two hydroxyl groups at a distance of  $\sim 4$  Å apart and is considered as reliable hydrogen bonding donor. Thus, in order to explore the robust nature of template resorcinols that are used as reliable spacers in organic solid-state reactions, a series of mono and di-pyridines were co-crystallized with different substituted resorcinols. The organizational consequences of hydrogen bonds in the O-H $\cdots$ N heterosynthon in the presence of other competitive hydrogen bonding functional groups will be discussed in next chapter.

## 4.12. EXPERIMENTAL

### 4.12.1. Synthesis of truxillic acid

*trans*-Cinnamic acid (Aldrich, 99%) was recrystallized from acetone (Aldrich) to obtain the  $\alpha$ -polymorph. The crystals were ground to small microcrystalline particles and about 400 mg of product was evenly distributed in a thin layer on a 100 mm Petri dish and placed in the focus of the lamp for irradiation. The powder sample was exposed to broad band irradiation (material exposed to both tail irradiation<sup>[29]</sup> as well as broad band

irradiation produced the same structure, except that samples obtained by tail irradiation resulted in intact crystals suitable for single crystal X-ray analysis) using 100 W high pressure Hg lamp (Müller electronic LXH100) for a period of 10 hrs to obtain 100% converted as-dimerized truxillic acid ( $P2_1/n$  phase),<sup>[127]</sup> which was confirmed by powder diffraction data provided in Figure 4.4c. (Powder diffraction data is also given (cf. Figure 4.4d) for the Donnay polymorph of truxillic acid ( $C2/c$  phase)<sup>[127]</sup> that was obtained by recrystallization of small amounts of 100% converted as-dimerized truxillic acid from acetone). About 100 mg of product was taken out at each interval of 2 hours for solid state NMR measurements. In order to obtain fast conversion, the powder was agitated after every 30 min and was simultaneously rotated using a home-built small rotating machine. Single crystals of  $\alpha$ -*trans*-cinnamic acid were obtained by slow evaporation of an acetone solution; crystals were then irradiated by tail irradiation technique using 345 nm edge filter to obtain intact crystals of  $P2_1/n$  phase truxillic acid. A suitable single crystal was picked up from the sample and crystal structures were determined on that crystal at different temperatures to investigate the temperature dependency of the bond length. The deuterated samples of *trans*-cinnamic acid and truxillic acid were obtained by using ethanol- $d_6$  (Carl Roth). About 100 mg of product was dissolved in 5 ml of solvent and left for slow evaporation.

#### 4.12.2. Synthesis of methyl ester of truxillic acid

Methyl ester of truxillic acid (dimethyl 2, 4-diphenylcyclobutane-1, 3-dicarboxylate) was synthesized by a simple esterification reaction. Truxillic acid (250 mg, 0.84 mmol) was dissolved in 30 ml of methanol in a 50 ml round bottomed flask, to this solution about 0.5 ml of thionyl chloride ( $\text{SOCl}_2$ ) was added, the mixture was allowed to reflux until TLC analysis indicated a complete reaction. The mixture was then concentrated in vacuo, and the residue was taken up in 50 ml of methylene chloride and washed with  $3 \times 50$  ml of water. The organic layer was dried over  $\text{Na}_2\text{SO}_4$ . Removal of the solvent in vacuo afforded white powder which was then purified over a short silica gel column using acetone and petrol ether as eluent in 1:9 ratio. Evaporation of the solvent afforded 248 mg of a white crystalline solid (methyl ester of truxillic acid) in

90% yield. Single crystals of methyl truxillic acid for X-ray analysis were obtained by the slow evaporation of an acetone solution.  $^1\text{H}$  NMR,  $\delta$ : 7.38-7.26 (M, 10H, Ar); 4.47 (T, 2H, Ar-CH-CH); 4.02 (T, 2H, OOC-CH-CH); 3.30 (S, 6H, O-CH<sub>3</sub>). EI MS:  $m/z$  324 ( $\text{M}^+$ ).  $\text{Mp} = 175^\circ\text{C}$ .

#### 4.12.3. Solid-State NMR measurement

All  $^{13}\text{C}$ -CPMAS spectra were collected at 125.77 MHz (Bruker Avance 500 spectrometer), with a CP-contact time of 5 ms coadding 4096 transients. The experiments were carried out using a standard Bruker 2.5 mm double resonance MAS probe spinning at 25 kHz, typical  $\pi/2$ -pulse length of 2.5  $\mu\text{s}$  and a recycle delay of 15 s. The spectra are referenced with respect to tetramethyl silane (TMS) using adamantane as secondary standard (29.46 ppm for  $^{13}\text{C}$ ).<sup>[141]</sup> If not stated otherwise, all spectra were acquired at room temperature. Static, variable-temperature  $^2\text{H}$  quadrupolar echo spectra<sup>[142]</sup> were recorded at 46.07 MHz using a home-built 7 mm probe and a Bruker Avance-II 300 spectrometer. The interpulse delay was set to 20  $\mu\text{s}$ , the  $\pi/2$ -pulse length to 2  $\mu\text{s}$ . The temperature was varied from 240 K to 400 K. Typically, 8096 scans were accumulated.

#### 4.12.4. Solution NMR and mass

The solution NMR spectra were recorded on a Bruker AC 250. The residual  $^1\text{H}$  peak of the deuterated solvent was used as an internal standard (Acetone,  $^1\text{H}$ ,  $\delta = 2.05$  ppm). The mass spectrum was obtained using a Varian Mat 7a (70e.v.).

#### 4.12.5. DFT-based chemical shift calculations

Geometry optimizations were performed based on the available crystal structures using the BLYP functional<sup>[143]</sup> and 6-311G<sup>[144]</sup> split valence basis set augmented with diffuse and polarization functions. Subsequently,  $^{13}\text{C}$  chemical shifts with respect to tetramethyl silane (TMS) were computed at B3LYP/6-311++G (2df, 2pd) level of theory with the GIAO approach as implemented in Gaussian98 program package.<sup>[30]</sup>

**4.12.6. Single Crystal X-ray Analysis**

All x-ray structures were recorded on a Kccd diffractometer with graphite monochromated Mo-K $\alpha$  radiation. Lattice parameters were obtained by least squares fits to the scattering angles of reflections observed in several pre-scans. The intensity data collection was performed by  $\phi$  and  $\omega$  scans. The raw data were corrected for Lorentz and polarization effects. The structures were solved by direct methods and refined by full matrix least squares analyses with anisotropic temperature factors for all atoms except H. Positions of the H atoms were calculated using the known molecular geometry and refined in the riding mode with fixed isotropic temperature factors. Empirical absorption corrections were applied to the data.

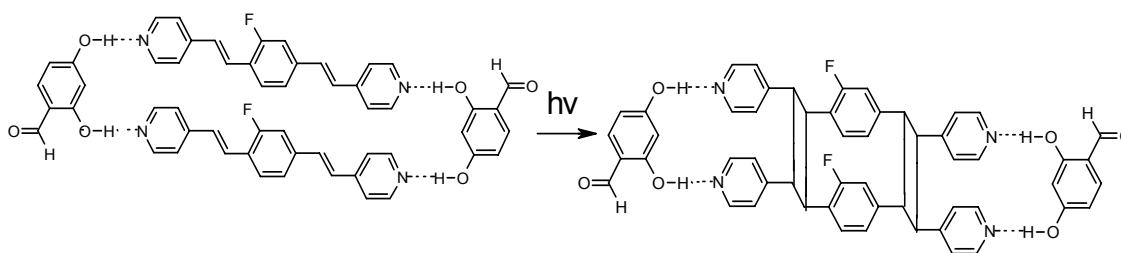
# CHAPTER 5

## O-H···N HETEROSYNTHON: A ROBUST SUPRAMOLECULAR UNIT FOR CRYSTAL ENGINEERING

### 5.1. INTRODUCTION

In recent years, great efforts have been put onto selective control or modification of reactant compounds yielding rationally designed crystal lattices.<sup>[146]</sup> A prominent example is given by [2+2] photodimerizations that has given access to a large variety of compounds.<sup>[5,108]</sup> In order to steer olefins to react, attractive intermolecular forces such as halogen-halogen<sup>[1]</sup> interaction as well as others were employed yielding molecules that may be difficult to achieve in solutions, such as donor-acceptor interactions<sup>[147]</sup> as well as hydrogen bonds.<sup>[148]</sup> Recently,<sup>[149,150]</sup> both the strength and directionality of hydrogen bonds of resorcinol have been exploited to enforce topochemical alignment of olefins in the solid state to allow selective [2+2] photoreaction. A thorough understanding of supramolecular synthons (resorcinol-pyridine, O-H···N) such as their preferred geometries, competitive hydrogen bonds, strength and recognition pattern is a prerequisite for rational design and supramolecular synthesis of novel co-crystals.<sup>[151]</sup> Two distinct categories of synthons are known: so-called supramolecular homosynthons, composed of self-complementary functional groups, e.g. carboxylic acid dimer,<sup>[152]</sup> and supramolecular heterosynthons,<sup>[153]</sup> that are composed of different but complementary functional groups. The latter category includes hydroxyl···pyridine,<sup>[151]</sup> hydroxyl···amine,<sup>[154]</sup> acid···pyridine<sup>[155]</sup> and acid···amide<sup>[156]</sup> supramolecular synthons.

Studies suggest that some supramolecular heterosynthons are strongly favoured over related supramolecular homosynthons.<sup>[154-156]</sup> It has been already established that<sup>[151]</sup> resorcinol, when co-crystallized with pyridine, largely forms hydroxyl...pyridine supramolecular heterosynthons. In some cases, however, the respective heterosynthons do not have the favourable orientation (ring formation, with parallel arrangement of double bonds separated at 4 Å as shown in Scheme 5.1) required for topochemical reactions.<sup>[157]</sup>



**Scheme 5.1:** Reaction scheme for the single-crystal-to-single-crystal [2+2] photodimerization of 2,4-dihydroxy benzaldehyde and 1,4-Bis[(E)-2-(4-pyridyl)ethenyl]2-fluorobenzene (BPEF)

In this chapter, the organizational consequences of hydrogen bonds within hydroxyl...pyridine (O-H...N) heterosynthons in the presence of competitive hydrogen bonding functional groups will be discussed. To explore the robust nature of template resorcinols that are used as reliable spacers in organic solid-state reactions, a series of mono and dipyridines were co-crystallized with different substituted resorcinols. The organizational consequences of hydrogen bonds in the hydroxyl...pyridine heterosynthon (O-H...N) in the presence of other competitive hydrogen bonding functional groups are discussed. The hydroxyl groups of the resorcinol are reliable hydrogen bonding donors that associate well with photoreactive hydrogen bonding acceptors molecules, therefore providing an approach for controlling distance and molecular orientation of constituent molecules in [2+2] photodimerization reactions. But such kinds of hydroxyl-pyridine supramolecular heterosynthon, the formation of six member ring intramolecular hydrogen bond due to the presence of hydrogen bonding active functional group in the close proximity of hydroxyl groups, C-O bond flexibility and steric hinderance, strongly affects



the ability of the spacer molecules. Finally, structural changes that occurred at molecular level during the photodimerization of one of the supramolecular adduct of 1,4-Bis[(E)-2-(4-pyridyl)ethenyl]2-fluorobenzene (bpef) with 2,4-dihydroxy benzaldehyde (cf. Scheme 5.1) were studied in detail by performing the rare single-crystal-to-single-crystal photoirradiation.

Type	Functional Group Involved
Reliable Donors	-OH, -NH <sub>2</sub> , -NHR, -CONH <sub>2</sub> , -CONHR, -COOH
Occasional Donors	-COH, -XH, -SH, -CH
Reliable Acceptors	-COOH, -CONHCO-, -NHCONH-, -CON, -OH.
Occasional Acceptors	-O, -NO <sub>2</sub> , -CN, -CO, -COOR, N<, -Cl

**Table 5.1:** List of reliable and occasional hydrogen-bonding donors and acceptors.

## 5.2. HYDROGEN BOND MEDIATED SELF ASSEMBLY

Hydrogen bonding has emerged as most powerful tool among the directional intermolecular interactions in noncovalent synthesis, mediating supramolecular assembly. From a detailed inspection of reported crystal structures, various rules to predict hydrogen-bonding arrangements<sup>[106,107,132]</sup> in single and two component crystals were derived. Nevertheless, there remains a strong need for hydrogen bonding motifs that can direct the formation of predictable and ordered solid-state structures tolerating changes in shape and size of the spacer. The discovery of such persistent hydrogen bonding motifs would not only allow more reliable prediction of solid structures but also rational construction of materials with a controlled positioning of key functional groups. Etter et al.<sup>[107]</sup> applied a graph theory approach for classifying and symbolically representing different types of hydrogen bonds that can be formed and proposed certain rules that govern hydrogen bonding in solids. Distinguishing “reliable” and “occasional” hydrogen-bond donors and acceptors (cf. Table 5.1)<sup>[107]</sup> three prominent rather general rules were devised, which indeed apply well to small organic molecules:

- i. All (or as many as possible) good proton donors and acceptors are used in hydrogen bonding.
- ii. If six-membered ring intramolecular hydrogen bonds can form, they will usually do so preferring intermolecular hydrogen bonds.
- iii. The best proton donors and acceptors remaining after intramolecular hydrogen bond formation will form intermolecular hydrogen bonds.

A major challenge<sup>[158]</sup> regarding molecular conformation of photoreactive conjugated molecules is control of required relative distances of less than 4 Å between the reactants. This can be achieved either by using a molecule that can be self assembled to provide desired functionality steering the molecules into favourable orientation or by a molecule which itself has a desired functionality to achieve the necessary preorganization of photoreactive molecules. Though single molecules that may incorporate suitable functionality can be effective for the preparation of tailored supramolecular structures, another potentially even more powerful strategy for the design of structures comprises a combination of molecules instead. According to Lauher *et al.*,<sup>[158]</sup> hydroxyl groups coupled to a pyridine hydrogen-bond acceptor constitute a useful heterosynthon for the design of molecular networks. Recently resorcinol has been used for selective preorientation of photodimerizable conjugated pyridines,<sup>[151]</sup> since it possesses two hydroxyl group at a distance of ~4 Å apart (cf. Figure 5.1). Indeed, as proposed by Etter,<sup>[107]</sup> resorcinol is among the so-called reliable hydrogen bonding donors. Hence, the association of hydrogen-bond donor resorcinol and photoactive hydrogen-bond acceptors molecules seems to provide an approach to controlling molecular orientation and spacing of constituent molecules in photodimerization reactions. But often the anticipated hydrogen-bonded pattern does not occur, due to several reasons like the presence of multiple hydrogen-bond sites, steric overcrowding, or competing dipolar and ionic forces etc. Here, in particular it is evaluated how hydrogen-bond pattern adjust to the presence of such perturbations.

Co-crystals are ideally suited to study competition among supramolecular heterosynthons,<sup>[106]</sup> that are obtained either from solutions containing more than one

molecular species or are derived by intimately mixing or grinding two solids. Co-crystal formation is rather important in topochemical reactions, where preorientation of the reactants is required. This can be achieved by using simple organic molecules with desired functionality. As stated earlier, the crystal structure is often a compromise among interactions of varying strengths, directionalities, and distance-dependent properties. In order to investigate the robustness or the ability of the hydroxyl-pyridyl supramolecular heterosynthon in a variety of situations, a number of co-crystals were prepared from different substituted resorcinols and simple mono- or dipyridines.

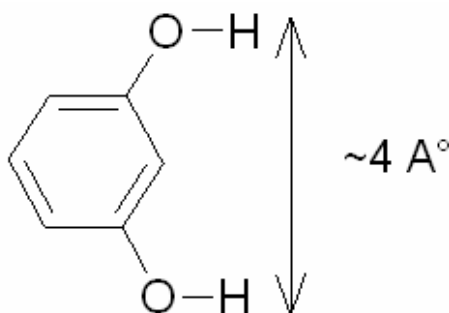


**Figure 5.1:** Shows the approximate 4 Å distance between two hydroxyl groups of resorcinol

### 5.3. CO-CRYSTALLIZATION OF RESORCINOLS AND MONOPYRIDINES LEADING TO THE DESIRED STRUCTURES

Figure 5.2 displays three examples where the desired structures with ~4 Å spacing were obtained by co-crystallization of resorcinols and monopyridines. A discrete two point molecular recognition, e.g. due to intermolecular hydrogen bonds between hydroxyl hydrogen and pyridyl nitrogen (OH...N) is common among all these crystal structures, orienting pyridine molecules parallel to each other. The pyridyl rings are further stabilized by  $\pi\cdots\pi$  interactions at a distance of around 4 Å relative to each other. This type of intermolecular hydrogen bonding facilitates the formation of centrosymmetric supramolecular adducts (if dipyridines are used), and is the most favourable kind of hydrogen bonding pattern for the design of photoreactive molecules. Other hydrogen

bonding active functional groups, like aldehyde and methoxy groups, that are also present in these crystal structures, potentially could interfere with the desired intermolecular hydrogen bonding but they are rather far away from the hydrogen bonding donor hydroxyl group. In addition, pyridyl nitrogen is a better (and hence favoured) hydrogen bonding acceptor than carbonyl and methoxy groups.<sup>[107]</sup>

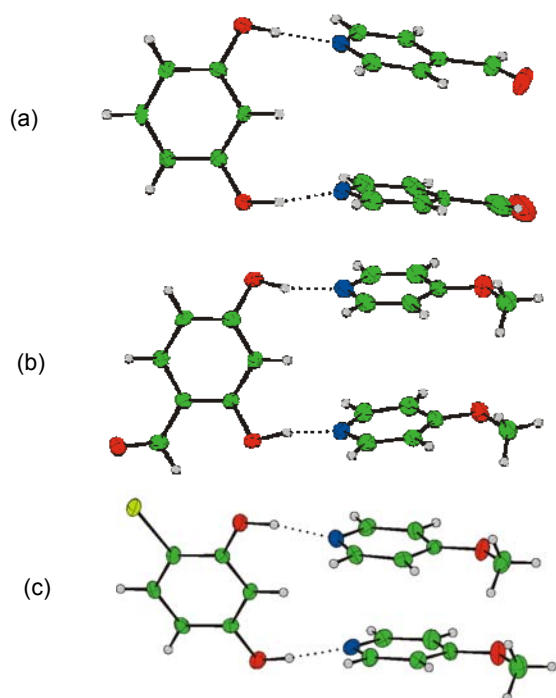


**Figure 5.2:** Two component adducts formed by different resorcinols and mono-pyridines (a) 1:1 supramolecular heterosynthon of resorcinol with 4-pyridinecarboxaldehyde (b) 2,4-dihydroxybenzaldehyde with 4-methoxy pyridine (c) 4-bromo-resorcinol with 4-methoxy pyridine

#### 5.4. CO-CRYSTALLIZATION OF RESORCINOLS AND DIPYRIDINES LEADING TO THE DESIRED STRUCTURES

Additionally, co-crystals of dipyridines and resorcinols were grown in order to explore the robustness of the design principle in more detail. In case of dipyridines the probability of parallel molecular recognition<sup>[107]</sup> is higher since they can be held from both

sides.<sup>[158]</sup> The supramolecular heterosynthon composed of 4,4-bipyridine and 4-bromoresorcinol (cf. Figure 5.3a) has 1:1 stoichiometry, where the asymmetric unit consists of two resorcinols and two pyridines. Both resorcinols act as double donor of hydrogen bonds and each pyridine act as double acceptor, thus forming a discrete ring-like structure. Even though that the hydroxyl groups of resorcinol steer two pyridines on top of each other, the pyridyl ring in each molecule cannot adopt a coplanar conformation due to the steric hindrance of the ortho H atoms of adjacent rings. A similar conformation is adopted in 1:1 molecular adducts of 3,5-dihydroxy benzonitrile with 4,4-bipyridine and 1,2 bis(4-pyridyl)ethane, respectively (cf. Figure 5.3b and 5.3c), where even the presence of hydrogen bonding acceptor cyano group did not hinder selective molecular recognition (nitrogen is a more reliable hydrogen bonding acceptor than the cyano group).

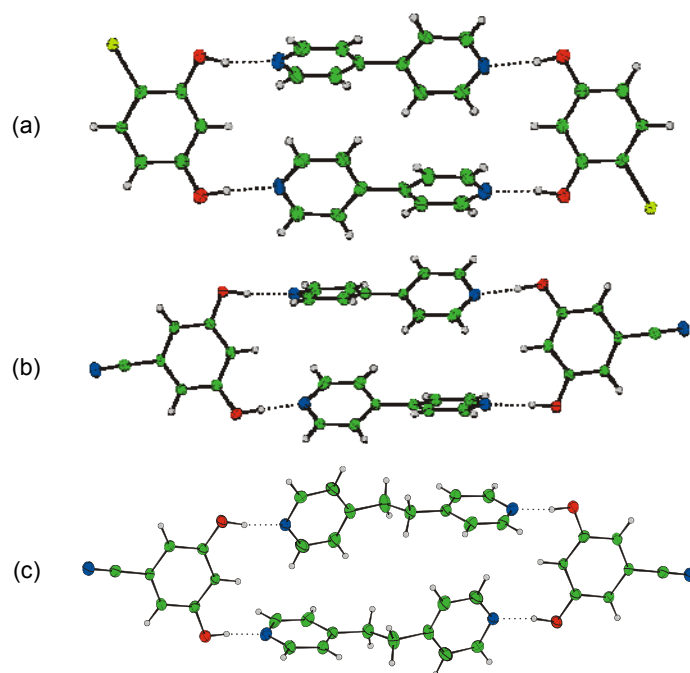


**Figure 5.3:** Four component molecular recognition of resorcinol and dipyridines a) 1:1 complex formation between 4-bromoresorcinol and 4,4-bipyridine b) 3,5-dihydroxy benzonitrile and 4,4-bipyridine c) 3,5-dihydroxy benzonitrile and 1,2 bis(4-pyridyl)ethane

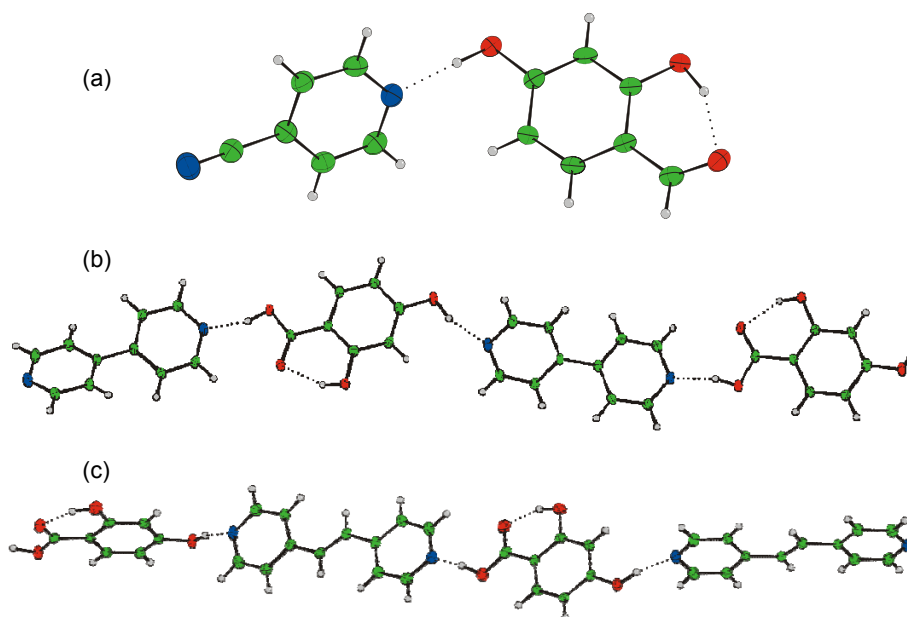


**Figure 5.4:** Co-crystallization of different substituted resorcinol with pyridines a) discrete single point molecular recognition between 2,4-dihydroxy benzaldehyde and 4-cyano pyridine b) infinite two point molecular recognition between 2,4-dihydroxy benzoic acid with 4,4-bipyridine c) 2,4-dihydroxy benzoic acid and 1,2-di-(4-pyridyl)ethylene

## 5.5. CO-CRYSTALLIZATION OF RESORCINOLS WITH MONO- OR DIPYRIDINES LEADING TO THE UNDESIRED STRUCTURES

Hydrogen-bonding patterns frequently involve many types of hydrogen bonds with multiple intertwined hydrogen-bonding networks, particularly in the presence of other competitive hydrogen bonding functional groups. To test the selectivity and preferences of O-H...N hydrogen-bond in the presence of other hydrogen bonding active moieties, substituted resorcinols containing additional hydrogen bonding donor functionality other than hydroxyl groups were co-crystallized with pyridines. The crystal structure of 1:1 co-crystals of 2,4-dihydroxy benzaldehyde and 4-cyano pyridine (cf. Figure 5.4a) reveals that the presence of carbonyl units next to hydroxyl groups has led to a preferred six membered ring of intramolecular hydrogen bonds.<sup>[107]</sup> Hence, only one hydroxyl group is involved in the desired intermolecular hydrogen bonding with pyridine. The corresponding crystal structures of 1:1 adducts of 2,4-dihydroxy benzoic acid with

4,4-bipyridine and 1,2-di-(4-pyridyl)ethelene, respectively, are given in Figures 5.4b and 5.4c. There are six hydrogen bonding donors and six hydrogen bonding acceptors present in each of these structures, but the selectivity of these hydrogen bondings are rather different. Altogether three types of H-bonds were observed: two intermolecular hydrogen bonds among pyridyl nitrogen and hydroxyl hydrogen, as well as pyridyl nitrogen and carboxyl hydrogen yielding an infinite one-dimensional chain rather than discrete zero dimensional four point molecular recognition assembly. The third motif is the most favoured six membered ring obtained via intramolecular hydrogen bonds between hydroxyl groups and carbonyl oxygens.

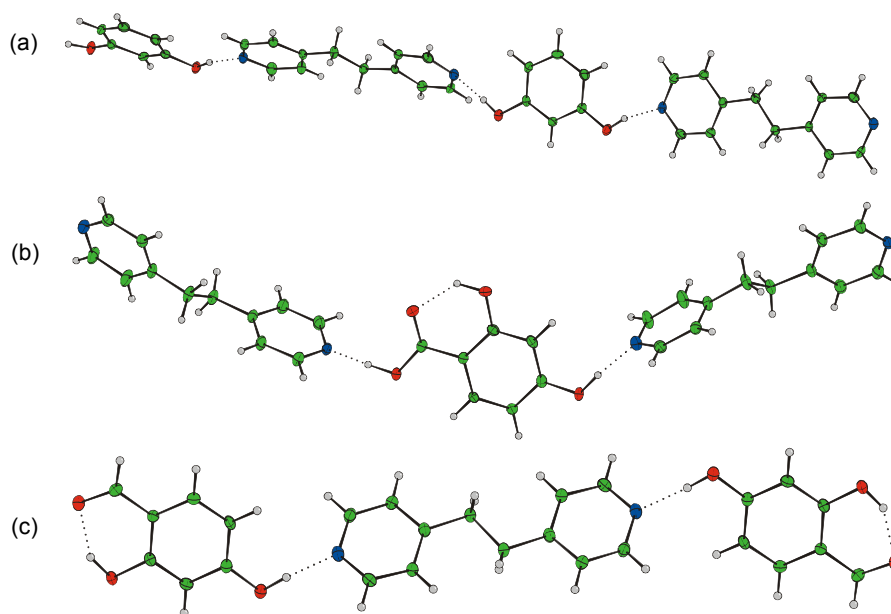


**Figure 5.5:** Complex formation of flexible 1,2-bis(4-pyridyl)ethane with different substituted resorcinols. a) resorcinol b) 2,4-dihydroxy benzoic acid c) 2,4-dihydroxy benzaldehyde.

Recently, MacGillivray et al<sup>[157]</sup> reported the ability of resorcinol to assemble with 1,2-bis(4-pyridyl)ethane yielding an infinite 1D array (cf. Figure 5.5a) where spacer adopt a divergent conformation preventing stacking of bipyridine. Therefore to achieve the desired 0D assembly, substituted resorcinols, such as 4-chlororesorcinol and 4,6-

dichlororesorcinol that possess the ability to block a possible formation of H-bonded chains were used. The main reason for chain formation in flexible 1,2-bis(4-pyridyl)ethane even in the absence of undesired intramolecular hydrogen bond, is the presence of bulky CH<sub>2</sub>---CH<sub>2</sub> linkages that preclude stacking of dipyridines. The formation of the chain like structure is facilitated by free rotation of the C-O bond in resorcinol, thus an O-H...N heterosynthon may be formed avoiding steric hinderance. However, due to this rotation, the two O-H bonds in resorcinol are not necessarily oriented parallel to each other. Similarly, adducts of 1,2-bis(4-pyridyl)ethane with 2,4-dihydroxy benzoic acid and 2,4-dihydroxy benzaldehyde, respectively, (cf. Figure 5.5b and 5.5c) do not show favourable molecular assembly but rather reveal unfavourable six membered ring intramolecular hydrogen bond formation.

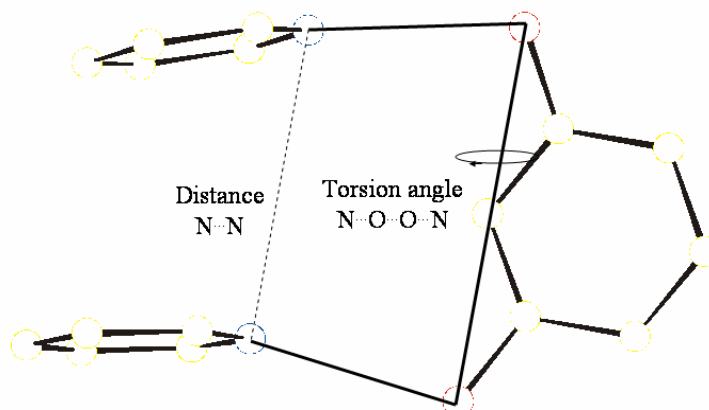


**Figure 5.6:** Hydrogen bonding geometry of resorcinol. Dependence of the N-N distance on the N··O··O··N torsion angle.

Owing to the possibility of free rotation along the C-O bond the hydrogen bonding geometry of resorcinol is quite flexible. Three different stable conformations of the OH groups with respect to the phenyl rings are possible (cf. Figure 6.8 next chapter). When two pyridines are hydrogen-bonded to a resorcinol molecule, the distance of the N atoms of the adjacent pyridyl rings can be described as a function of the torsion angle N··O··O··N (cf. Figure 5.6). It can be expected that this distance is smallest at a torsion



angle of  $0^\circ$ . In this geometry the pyridyl rings are eclipsed. In Figure 5.7 the distance between N atoms is plotted as a function of the torsion angle defined in Figure 5.6., the closed symbols shown in the figure are data taken from the literature (CCDC, 2008 edition) while the open circles represent the study presented in this work. As predicted N-N distances in the vicinity of  $4 \text{ \AA}$  are only observed in a small section of this map i.e. in an angular range of approximately  $-10$  to  $10^\circ$ . It can also be seen that the majority of the tested structures during the studies presented in this dissertation fall in this range. This demonstrates that indeed resorcinol can be successfully employed as a template for photoreactive molecules.

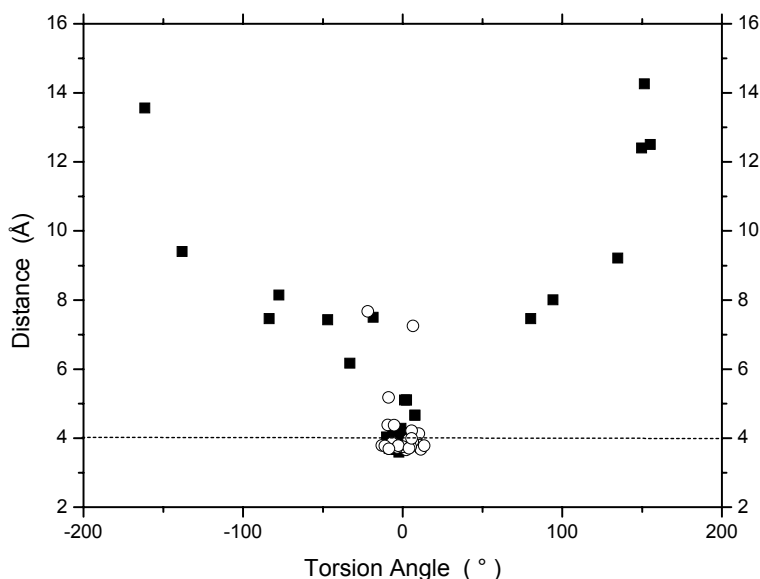


**Figure 5.7:** Plot of the observed N-N distances on the N··O··O··N torsion angle. Closed circles represent literature data and open circles are the results of the study presented in this work.

## 5.6. MOLECULAR RECOGNITION OF PHOTOREACTIVE CONJUGATED DIPYRIDINES

Clearly, by choosing appropriate resorcinols, rational design of photoreactive crystals can be achieved. In order to extend the approach of solid state molecular assembly in the presence of competitive hydrogen bonding active moieties different

conjugated dipyridines consisting of two hydrogen-bond acceptors and photoactive vinylic double bonds separated by aromatic moiety were synthesized e.g. 2,6-Bis[(E)-2-(4-pyridyl)ethenyl] naphthalene (bpen) was cocrystallised with 4-bromoresorcinol and 3,5-dihydroxy acetophenone (cf. Figure 5.8a and 5.8b). In each case, resorcinol spacers and polyenes form discrete four-component molecular assemblies that are stabilized by four O-H...N hydrogen bonds, in which the templates orient the polyenes in a parallel arrangement. The separation between the stacked C=C bonds ranges from 3.82 to 3.85 Å (cf. Figure 5.8a) and 4.23 to 4.31 Å (cf. Figure 5.8b). Nearest-neighbour assemblies of each solid pack in an antiparallel fashion so that olefins of hydrogen-bonded assemblies are sole C=C bonds organized to undergo reaction. Though the dipyridines are arranged parallel to each other, they may not be suited for the photoreaction since the distance between the reactive double bond in a pair exceeds the threshold value of 4.2 Å for the photoreaction to occur. This particular adduct possesses an additional hydrogen bonding acceptor C=O functional group, present on the spacer resorcinol, that is not involved in stabilizing four point molecular assemblies.

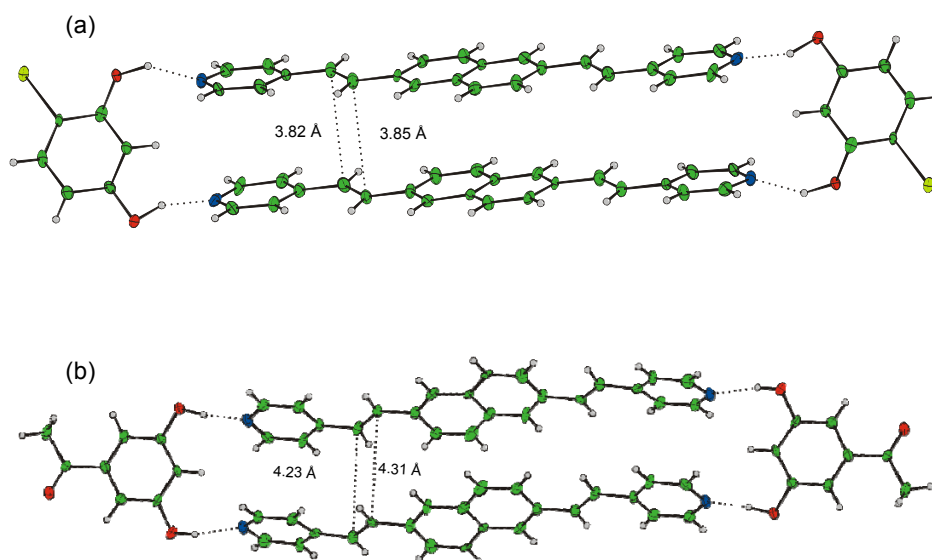


**Figure 5.8:** Complex formation of 2,6-Bis[(E)-2-(4-pyridyl)ethenyl]naphthalene (bpen) a) with 4-bromoresorcinol b) 3,5-dihydroxy acetophenone.

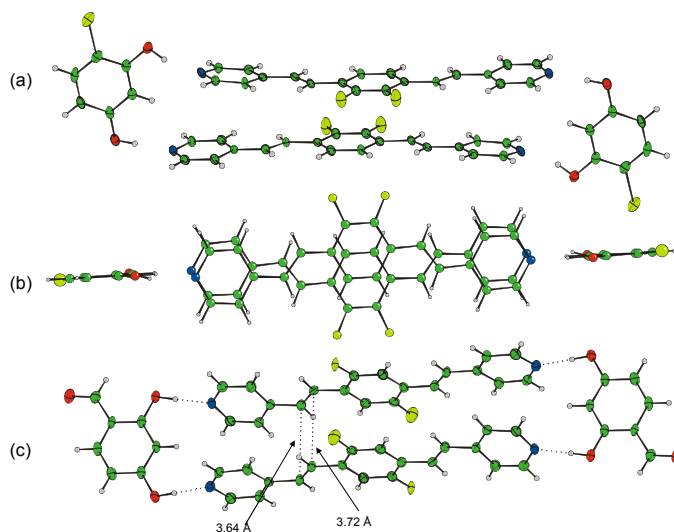


**Figure 5.9a:** Crystal projection of the co-crystals of 1,4-Bis[(E)-2-(4-pyridyl)ethenyl]2-fluorobenzene (bpef) with 4-bromoresorcinol b) identical complex shown in different projection. c) complex formation between bpef with 2,4-dihydroxy benzaldehyde.

Another photoreactive conjugate dipyridine synthesized is 1,4-Bis[(E)-2-(4-pyridyl)ethenyl]2-fluorobenzene (bpef) which is co-crystallized with 4-bromoresorcinol (cf. Figure 5.9a) and 2,4-dihydroxy benzaldehyde (cf. Figure 5.9c). The presence of two fluorine atoms in Figure 5.9 is explained by an orientational disorder, i. e. the asymmetric molecule is built into the complex in two orientations with 50% occupation leading to the disorder (cf. Figure 5.10). The supramolecular heterosynthon comprised of bpef and 4-bromoresorcinol (cf. Figure 5.9a) is one of the few examples of self assembled photoreactive molecules in cis arrangement. Even though the complex has adopted discrete 0D four point molecular recognition by O-H...N heterosynthon with a double bond separation of less than 4.2 Å, it is not photoreactive, since the cis arrangement of the molecules brought the reactive centers (double bond) perpendicular to each other contrary to the parallel orientation required for the photodimerization reaction to occur. From the projection of the crystal structure (cf. Figure 5.9c) it is evident that the monomer complex of bpef and 2,4-dihydroxy benzaldehyde has a perfect orientation with two dipyridines lying approximately parallel to each other and separated by less than 3.8 Å, thus fulfilling geometry criteria of Schmidt for [2+2] photodimerization.<sup>[6]</sup> This particular system is chosen for further analysis of reaction intermediates.

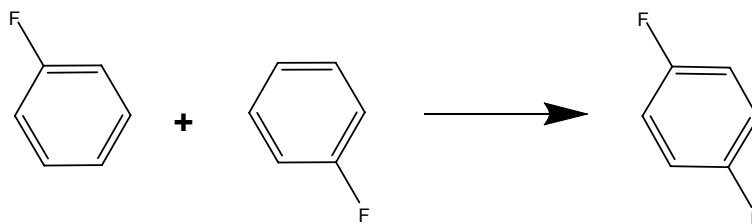


**Figure 5.10:** Schematic representation of orientational disorder seen in 1,4-Bis[(E)-2-(4-pyridyl)ethenyl]2-fluorobenzene (bpef)

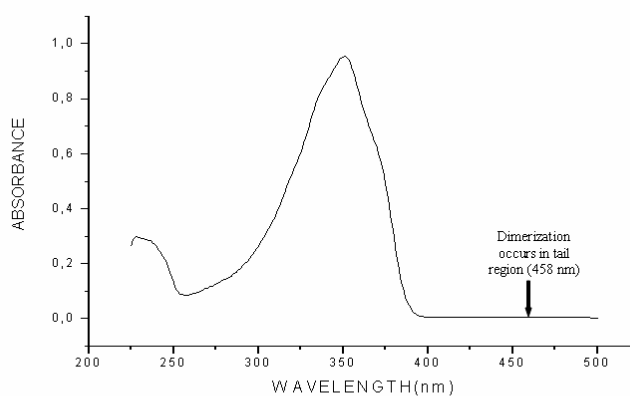


**Figure 5.11:** The UV-VIS absorption spectra of 1,4-Bis[(E)-2-(4-pyridyl)ethenyl]2-fluorobenzene (bpef)

## 5.7. MONITORING THE STRUCTURAL CHANGES BY X-RAY ANALYSIS

Single-crystal-to-single-crystal<sup>[13,29]</sup> transformation was performed on crystals of bpef and 2,4-dihydroxy benzaldehyde supramolecular heterosynthon, via tail irradiation with UV light using 458 nm filter (cf. Figure 5.11). Upon tail-irradiation crystals do not disintegrate (as described in section 2.4.3 and Figure 2.6) but rather remain intact facilitating single crystal X-ray analysis of the partially reacted crystals (mixed crystals). The projection of the crystal structure shown in figure 5.12 corresponds to the short (40% converted, Figure 5.12a) and long (60% converted, Figure 5.12b) irradiated crystals. Mixed crystals are like a solid solution in which monomer and dimer molecules statistically occupy identical lattice sites. In these structures separate atomic coordinates

are observed for olefinic carbon atoms, the cyclobutane ring, and for those carbon atoms of the pyridyl and phenyl rings that are directly connected to the cyclobutane ring. All other atoms occupy identical positions as in the monomer complex (cf. Figure 5.9c) within the error of analysis. The population parameter (i. e. the conversion) was obtained from least square refinement.

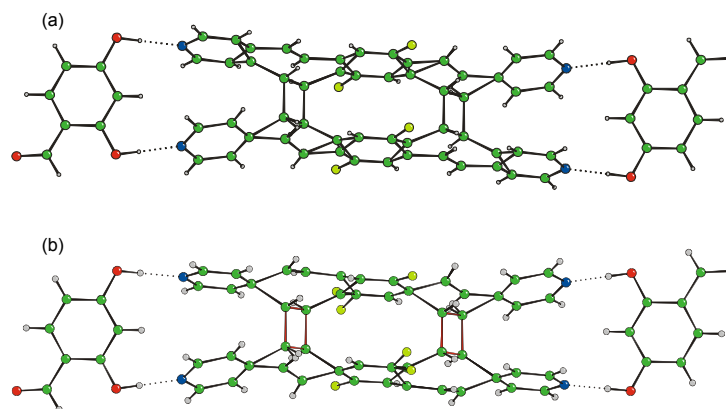


**Figure 5.12:** Projection of the crystal structure of mixed crystals obtained after short (3 hrs) and long irradiation (6 hrs) time. a) around 40% converted mixed crystals b) around 60% converted mixed crystals.

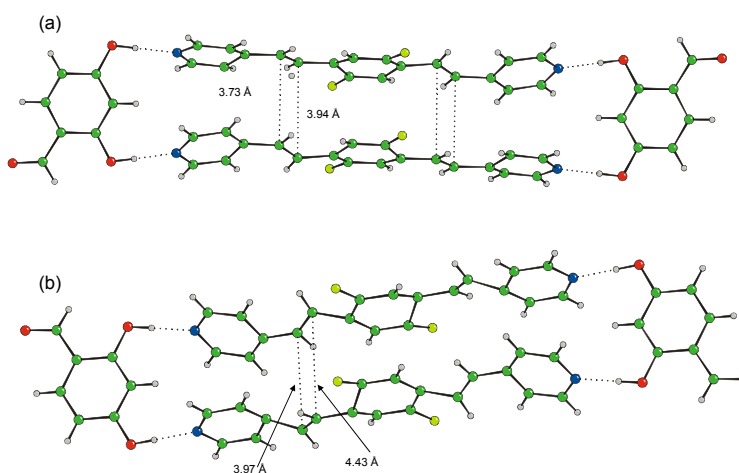


**Figure 5.13:** Projection of the crystal structure of the mixed crystals of complex bpef and 2,4-dihydroxy benzaldehyde. Atoms belonging to the dimer have been omitted here for clarity a) shorter period of irradiation less than 40% converted b) long irradiated about 60% converted.

Careful inspection of the corresponding structures revealed several interesting features. In contrast to changes observed during dimerization of cinnamic acid<sup>29</sup> where the side group atoms occupy the same lattice sites within the experimental error, some atoms belonging to the side groups split into monomer-associated and dimer associated sites. These are the carbon atoms of pyridyl or phenyl rings, which are directly attached to the cyclobutane ring (or) to the vinylic carbon atoms. This effect can be explained by the strain on the molecules present in the lattice of the mixed crystal of dimer and monomer. As shown in the Figure 5.9c a distance of around 4 Å separates the monomer pair double bonds. The bond length in the cyclobutane ring is around 1.5 Å. These two moieties share one site in the crystal lattice, and as a consequence, both are distorted from their most favourable conformation. A total conversion of 40% was achieved after 3 hrs of irradiation, whereas after 6 hrs the conversion had stopped (~ 60% conversion), and did not continue even after long irradiation, presumably due to changes of the distance between reacting centers. The distance between the reacting centers in the monomer before irradiation was 3.64 Å for the front carbon and 3.72 Å for the rear carbon as shown in Figure 5.9c. After 40% conversion this distance has changed to 3.73 Å and 3.94 Å and after 60% conversion had further increased to 3.97 Å and 4.43 Å for the front and rear carbon, (cf. Figure 5.13a and 5.13b ) respectively. In these structures the atoms belonging to the dimer have been omitted to obtain a clear picture of the monomer distortion.

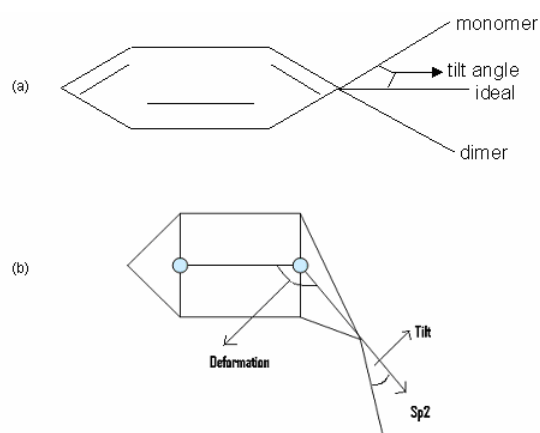


**Figure 5.14:** Schematic representation of a) tilt angle b) ring deformation.

Mixed Crystal Irradiated by	Tilt Angles				Structure	
	A	B	C	D		
458nm Xe lamp 40%	Monomer:	10.6°	7.5°	3.9°	1.3°	
	Dimer:	22.2°	24.2°	24.7°	15.4°	
458nm Xe lamp 60%	Monomer:	15.4°	26.2°	3.7°	26.4°	
	Dimer :	16.5°	23.0°	20.0°	29.9°	

**Table 5.2:** Tilt angles for the substitutional mixed crystals of the bpef molecular adduct at different conversions.

## 5.8. TILTING AND DEFORMATION OF PYRIDYL AND PHENYL RINGS

As reported,<sup>[29]</sup> the strain on the molecules in the mixed crystals of partially dimerized cinnamic acid leads to a deformation called “tilt”, e.g. the bond to the cyclobutane ring (or) residual double bond system is deformed out of its ideal  $sp^2$  orientation, which is characterized by the tilt angle as defined schematically in Figure 5.14a. Tilt angles as large as  $30^\circ$  have been observed in the case of mixed crystals of partially dimerized molecular adduct of bpef and 2,4-dihydroxy benzaldehyde (cf. Figure 5.9c). Table 5.2 gives the values of tilt angles obtained for both 40% and 60% converted mixed crystals of different moieties. It has been found that the tilt angle is mainly dependent on conversion i.e. the minority component is always more tilted than the majority component. For example, the dimer, which is in minority in the 40% converted mixed crystals (cf. Figure 5.12a) is more tilted ( $22.2^\circ$ ) than the monomer, whereas in 60% converted mixed crystals (cf. Figure 5.12b) it is found to be less tilted ( $16.5^\circ$ ). The tilt deformation in the mixed crystals of bpef is relieved by the distortion of pyridyl and phenyl rings, where the ring system bends so that it is no longer planar. The dimer which is formed in this kind of cycloaddition is a 2,2-cyclophane, i. e. a compound where two p-phenylene groups held face to face by  $—[CH_2]—_2$  bridges, such as in cyclophanes.<sup>159</sup>

Generally, these kinds of deformations are characterized by dihedral angle which is schematically defined in Figure 5.14b. The deformations particularly found in partially dimerized bpef adduct are more severe than in cyclophanes which is only in to order of  $15^\circ$ - $16^\circ$  on each side of the phenyl ring.<sup>[159]</sup> Dihedral angles obtained for different moieties in the bpef adduct are given in Table 5.3.

Mixed Crystal Irradiated by	Ring Deformation Angle				Structure
	A	B	C	D	
458nm Xe lamp 40%	----	23.8°	23.2°	23.5°	
458nm Xe lamp 60%	----	27.6°	----	----	

**Table 5.3:** Ring deformation angles for the substitutional mixed crystals of bpef molecular adduct.

Tilt and deformation both are dependent on each other. If the deformation of the ring is larger, then the tilt angle is smaller; this helps in reducing the total strain on the molecule. The larger the tilt angle, the more the arm of the pyridyl rings is driven away from the reacting partner. This is clearly visible in the crystal structure projection shown in Figure 5.15a and 5.15b (atoms belonging to the monomer have been removed for clarity). As mentioned above, mixed crystals are like solid solutions where the dimer mimics the monomer at low conversion and monomer mimic the dimer at high conversion. Therefore molecular deformations (tilt and ring deformation) of the monomer in the 60% converted crystal (cf. Figure 5.13b) is much larger as it is in minority compared to the 40% converted crystals (cf. Figure 5.13a) where monomer exist in majority and thus less deformed. Notably, with increasing conversion, the distance



between two reacting centers also increases due to the strain on the molecules, and therefore complete conversion can not be accomplished.

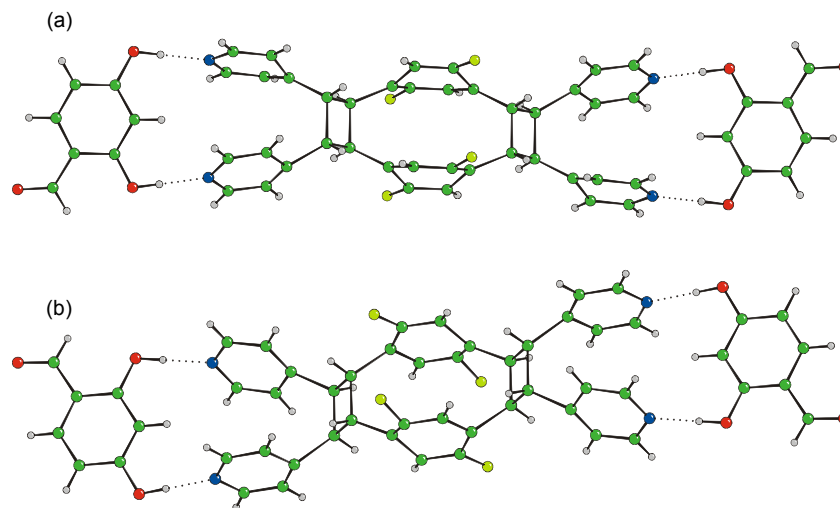


**Figure 5.15:** Projection of the crystal structure of the mixed crystals of complex bpef and 2,4-dihydroxy benzaldehyde. Atoms belonging to the monomer have been omitted here for clarity a) shorter period of irradiation less than 40% converted b) long irradiated about 60% converted.

Since the dimerization of bpef is a single-crystal-to-single-crystal transformation the intermediate states are substitutional mixed crystals in which both monomer and dimer share a common lattice. The consequences of this phenomenon are the molecular distortions (such as tilt and deformations) described above. Note that (cf. Figure 5.12a) the deformation observed for the pyridyl ring carbon attached to the cyclobutane ring is larger than that for the pyridyl ring carbon attached to the unreacted double bond. Thus, the crystal structure may be viewed as a compromise between the conformation of the monomer and dimer, with the expected result that the species of higher concentration in the lattice is less deformed. This deformation can be measured as the angle between the plane of the pyridyl ring and the axis corresponding to the bond linking the pyridyl ring to the cyclobutane carbon or the unreacted olefin carbon. In addition to these kinds of molecular deformation, small rotations of the pyridyl and phenyl rings were observed which accompany the dimerization (cf. Figure 5.13). All these molecular displacements

during the reaction can be viewed as the response of the molecules packed together in a common lattice to dimensional changes. Thus the side groups serve two functions in a topochemical reaction: one involves an anchoring effect, and the other involves the conformational mobility. The side groups can be seen as anchors in that they determine the intermolecular contacts existing in the crystal lattice. During the course of conversion, the atomic displacement in these side groups preserve the overall packing, stabilizing the evolving lattice changes and making the continuous shifts in the lattice parameters possible. On the other hand the side groups also provide the conformational flexibility required such that the reacting centers may approach each other.

## **5.9. CONCLUSIONS**

It is evident that most physical and chemical properties of organic solids are controlled by intermolecular orientation and packing. In order to engineer or design materials with optimal properties it is imperative to understand the laws governing the packing of organic crystals. In this report, an approach has been presented to achieve regiocontrol of [2+2] photoreactions supramolecularly in the solid state by using resorcinol as a spacer. The two hydroxyl groups of resorcinol are not only susceptible towards hydrogen bonding but are also separated at a distance which is required for the photoreaction to occur. The deliberate use of a variety of resorcinols containing different hydrogen bonding active functional groups allowed to determine the robust nature of this approach. Indeed, reliable design of photoreactive materials requires proper selection of a template. Major cause for the deviation of the design principle in case of hydroxyl-pyridine heterosynthons are, intramolecular hydrogen bond formation due to the presence of hydrogen bonding active functional groups in the close proximity, C-O bond flexibility of resorcinol and steric hindrance. Moreover the single-crystal-to-single-crystal transformation allowed to establish the topotactic nature of photoreaction, as well as to analyze the structural change that occurred at molecular level during the reaction.

Clearly, enforcement of topochemical alignment of olefins in the solid-state via hydrogen-bonds facilitates [2+2] photoreactions. The structural changes during the

photodimerization of 2(bpe):2(res) supramolecular heterosynthon have also been monitored and the corresponding findings will be discussed in next two chapters.

## 5.10. Experimental Section

### 5.10.1. General Details

All reagents and starting materials were obtained from commercial sources (Aldrich, Lancaster, Fluka) and used as received. Melting points were determined with a Büchi melting point B-545 capillary instrument, at heating rate of 5 K/minute. Solution NMR spectra were recorded on a Bruker AC 250, where the residual  $^1\text{H}$  peak of the solvent was used as an internal standard ( $\text{CHCl}_3$ :  $^1\text{H}$ ,  $\delta = 7.24$ ). UV-vis spectra were recorded using a Perkin-Elmer Lambda 2 spectrometer (dichloromethane as solvent) where mass spectra were obtained using a Varian Mat 7a (70 e.v). Preparative irradiations for single crystals of monomer complex of bpef were performed with a 450 Watt Xenon lamp from Photon Technology International Inc., Mod. A 5000. All x-ray structures were recorded on a Kccd diffractometer with graphite monochromated Mo-K $\alpha$  radiation. Lattice parameters were obtained by least squares fits to scattering angles of reflections observed in several pre-scans. The intensity data collection was performed by  $\phi$  and  $\omega$  scans, raw data were corrected for Lorentz and polarization effects. The structures were solved by direct methods and refined by full matrix least squares analyses with anisotropic temperature factors for all atoms except H. Positions of the H atoms were calculated using the known molecular geometry and refined in the riding mode with fixed isotropic temperature factors. Empirical absorption corrections were applied to the data.

### 5.10.2. Preparations of photoreactive conjugated dipyridines

All of photoreactive dipyridines were prepared in the same manner by reaction of dibromobenzene,<sup>[160]</sup> ca. 1.25 equiv of 4-vinylpyridine per aromatic bromine substituent and catalytic amounts (ca. 10 mol %) of triphenyl phosphine palladium dichloride in dry

Et<sub>3</sub>N at 100 °C under N<sub>2</sub>. A representative procedure is given here for the preparation of *1,4-Bis[(E)-2-(4-pyridyl)ethenyl]2-fluorobenzene (bpef)*. A mixture of 1,4-dibromo 2-fluorobenzene (0.507 g, 2 mmol), 4-vinyl pyridine (0.525 g, 5 mmol) and triphenyl phosphine palladium dichloride (0.140 g, 0.2 mmol) was placed in a nitrogen purged schlenk tube. About 1ml dry triethylamine was added, the tube sealed, and the mixture heated to 100 °C under stirring for three days. After cooling, the solid dark mass was dissolved in about 200 ml dichloromethane and extracted thoroughly with 150 ml water for three times. The residual organic phase was dried with MgSO<sub>4</sub>, concentrated in vacuo, and chromatographed over silica gel, using THF and low boiling petrol ether in 3:1 ratio. Traces of unreacted 4-vinylpyridine eluted first followed by bpef as a dark yellow band. Evaporation to dryness followed by recrystallization from ethanol and water affording pure 0.411 g (68 % yield) of bpef as yellow microcrystalline solid. <sup>1</sup>H NMR, δ: 8.60 (D, 4H, Py, N=CH, J = 6 Hz); 7.61 (D, 1H, Ar, Ipso-CH, J = 7.89 Hz); 7.46 (D, 1H, Py-CH=CH, J = 16.42 Hz); 7.36 (D, 4H, Py, Ipso-CH, J = 5.69 Hz); 7.30 (D, 1H, Ar, Ipso-CH, J = 7.59 Hz); 7.20 (S, 1H, Ar, Ipso-CH); 7.15 (D, 1H, Py-CH=CH, J = 16.42 Hz); 7.06 (D, 2H, Ar-CH=CH, J = 16.42 Hz). EI MS: m/z 302.6 (M<sup>+</sup>). m. p.: 225.8-226.7 °C.

### 5.10.3. 2,6-Bis[(E)-2-(4-pyridyl)ethenyl]naphthalene (bpen)

the yield was 48% , m.p. 253 °C, EI MS: m/z 334.4 (M<sup>+</sup>). <sup>1</sup>H NMR, δ: 8.60 (D, 4H, Py, N=CH, J = 6 Hz); 7.87 (S, 2H, Ar, Ipso-CH); 7.91 (D, 2H, Ar, Ipso-CH, J = 11.39 Hz); 7.76 (D, 2H, Ar, Ipso-CH-C=CH, J = 8.53 Hz); 7.48 (D, 2H, Ar-CH=CH, J = 16.43 Hz); 7.41 (D, 4H, Py, Ipso-CH, J = 6.32); 7.17 (D, 2H, Py-CH=CH, J = 16.42 Hz).

### 5.10.4. Crystal Preparation

All co-crystals presented in this work were synthesized by slow evaporation of solvent or mixture of solvents at room temperature in test tubes. As an example the co-crystallization of the supramolecular adduct of 1,4-Bis[(E)-2-(4-pyridyl)ethenyl]2-

flourobenzene (bpef) with 2,4-dihydroxy benzaldehyde is given here. To a mixture of 5 mg (0.0165 mm) of bpef and 2.27 mg (0.0165 mm) of 2,4-dihydroxy benzaldehyde (in equimolar ratio), a mixture of 5ml of acetone and 5ml of toluene were added. The resulting solution is heated slowly and left at room temperature for slow evaporation. After two days dark yellow needle-like crystals were formed. Co-crystallizations of other complexes were performed in similar fashion using suitable solvents (cf. Table 5.4)

Reactants	Solvents
(19.4mg)pyridine - 4- aldehyde + (10mg)resorcinol(1:2)	5ml acetone
(43.6mg)4-methoxy pyridine + (27.6mg) 2,4-dihydroxy benzaldehyde(1:2)	5ml acetone/5ml ethanol
(37.2mg)4-methoxy pyridine + (37.8mg) 4- bromoresorcinol(1:2)	5ml acetone
(31mg)4,4-bipyridine + (37.8mg) 4-bromoresorcinol(1:1)	5ml acetone
(31mg)4,4-bipyridine + (27mg) 3,5-dihydroxy benzonitrile	5ml acetone
(10mg)1,2-di-(4-pyridyl)ethane + (7.4mg) 3,5-dihydroxy benzonitrile.	5ml acetone/5ml ethanol
(53.2mg) 4-cyano pyridine + (27.6mg) 2,4-dihydroxy benzaldehyde(1:2)	5ml acetone
(31mg)4,4-bipyridine + (30.8mg) 3,5-dihydroxy benzoic acid.	5ml ethanol
(10mg)1,2-di-(4-pyridyl)ethylene + (8mg) 2,4-dihydroxy benzoic acid (1:1)	5ml acetone
(10mg) 1,2-di-(4-pyridyl)ethane + (5mg) resorcinol (1:1)	10ml acetone
(10mg)1,2-di-(4-pyridyl)ethane + (8.4mg) 2,4-dihydroxy benzoic acid.	5ml acetone/5ml ethanol
(10mg)1,2-di-(4-pyridyl)ethane + (7.5mg) 3,5-dihydroxy benzaldehyde.	5ml acetone/5ml ethanol
(5mg)2,6-Bis[(E)-2-(4-pyridyl)ethenyl]naphthalene +(2.8mg) 4-bromoresorcinol(1:1).	5ml acetone/5ml Toulene
(5mg)2,6-Bis[(E)-2-(4-pyridyl)ethenyl]naphthalene +(2.26mg) 3,5-dihydroxy acetophenone	5ml acetone/5ml toulene

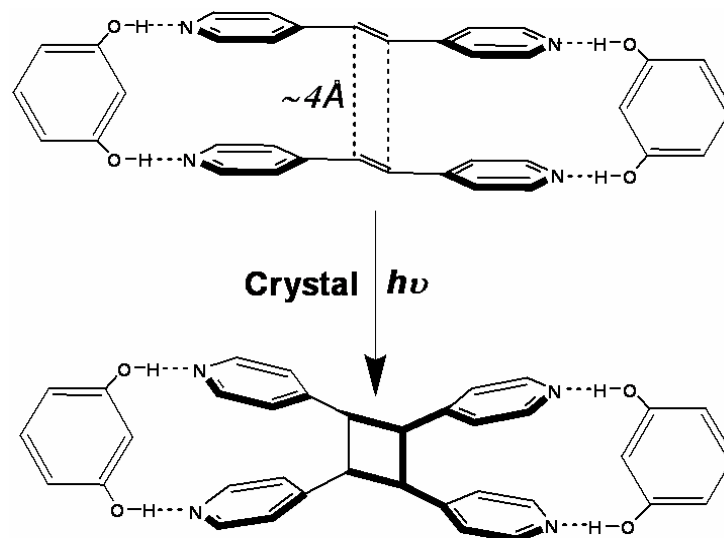
**Table 5.4:** Co-crystallization details of the complexes.

# CHAPTER 6

## PROBING STRUCTURAL TRANSFORMATIONS IN 2(BPE):2(RES) HETEROSYNTHON BY NMR METHODS IN THE SOLID- STATE

### 6.1. INTRODUCTION

An intriguing feature on the chemistry of organic crystals is that some are reactive and others are unreactive, even though the difference of their molecular structure is minor.<sup>[1]</sup> The reactivity and selectivity in the solid state is mostly controlled by the crystal structure, but unfortunately it is still difficult to construct a desired one. Therefore, an attempt for developing simple experimental methods to compel photoinert crystals to be reactive will be of great significance. In this connection, many researchers have been investigating the photochemical reactions of two component crystals.<sup>[149]</sup> Such an approach to synthesis can lead to the formation of covalent bond at will in solids to facilitate the high yield, solvent free synthesis of molecules which are either available in low yields, or as part of mixtures, or are not accessible in the liquid phase. [2+2] photodimerizations are among the most extensively studied organic solid state reactions, and as per Schmidt's topochemical postulates<sup>[6,7]</sup> the geometry criteria for such reactions in solids is that the two carbon-carbon double bonds should be aligned parallel to each other and separated less than 4Å apart.



**Scheme 6.1:** Reaction scheme for the [2+2] photodimerization of 1:1 cocrystal of resorcinol and trans-1,2-Bis(4-pyridyl)ethylene.

Pure trans-1,2-Bis(4-pyridyl)ethylene (bpe) crystallizes in a layered structure<sup>[161]</sup> in which olefins of neighbouring layers lie orthogonal and separated by 6.52 Å and therefore does not conform to topochemical principle and is photostable.<sup>[6]</sup> However, the 1:1 co-crystallization of resorcinol with trans-1,2-bis(4-pyridyl)ethylene (bpe) produced a so-called 0-D complex (forming discrete rings), 2(bpe):2(res), with the two C=C bonds oriented parallel and separated by 3.65 Å. This crystal arrangement complies with topochemical principles<sup>[5]</sup> and thus, upon broadband UV irradiation, yields the photodimer tetrakis(4-pyridyl) cyclobutane (cf. Scheme 6.1).

Moreover, the hydrogen-bond driven co-crystallization of trans-1,2-bis(4-pyridyl)ethylene (bpe) and resorcinol together with trans-1,2-bis(4-pyridyl)ethane (bpet) have produced 2(bpe):2(res) and 2(bpet):2(res) separately, both in chain form with almost identical lattice parameters, exploiting molecular specificity of resorcinol-pyridine OH⋯N recognition in the presence of multiple di-pyridines. However, the new polymorph of 2(bpe):2(res) in chain form (P2<sub>1</sub>/n, monoclinic) is not suitable for photodimerization, as it does not fulfil the topochemical requirements. Nevertheless, as stated earlier the ring form (P-1, triclinic) of 2(bpe):2(res) complex that complies well with topochemical principles undergoes [2+2]photodimerization that can be monitored by

applying  $^{13}\text{C}$ -CPMAS solid-state NMR and X-ray analysis techniques. Two different polymorphs of bpe dimer have also been revealed i.e centrosymmetric recrystallized dimer (monoclinic,  $P2_1/n$  phase) and as-dimerized dimer (triclinic, P-1 phase). Solid-state  $^{13}\text{C}$ -CPMAS spectra at different conversions ranging from monomer to dimer were recorded. In addition, removal of resorcinol template from the complex of 2(bpe):2(res) yields tetrakis(4-pyridyl)cyclobutane that consists of distorted cyclobutane ring revealing a different molecular geometry (orthorhombic, Pccn phase).

## 6.2. MOLECULAR CONFORMATION OF RESORCINOL

Recently resorcinol has been used for selective preorientation of photodimerizable conjugated pyridines,<sup>[151]</sup> since it possesses two hydroxyl group at a distance of  $\sim 4$  Å apart (cf. Figure 5.1). The co-crystal of resorcinol and trans-1,2-bis(4-pyridyl)ethylene 2(bpe):2(res) in ring form undergoes a homogeneous [2+2] photodimerization when crystals are irradiated at 385 nm. The intermediate crystals are substitutional mixed crystals<sup>[29]</sup> (substitutional mixed crystals are those where monomer and dimer molecules statistically occupy the same lattice sites). Such mixed crystals in principle provide detailed insights into atomic level changes that occurred during the respective topochemical reaction.

To begin with,  $^{13}\text{C}$ -CPMAS NMR spectra of both resorcinol and trans-1,2-Bis(4-pyridyl)ethylene (spectral assignment given in Table 6.1) were recorded. While the  $^{13}\text{C}$  solution NMR spectrum of resorcinol (cf. Figure 6.1a) exhibits four resonances reflecting its molecular structure, the solid-state  $^{13}\text{C}$ -CPMAS NMR spectrum (Figure 6.2a) of resorcinol displays not only six different carbon signals but also peak splittings. The latter is readily explained by the crystal structure of resorcinol<sup>[162,163]</sup> containing more than one molecule of resorcinol in the corresponding unit cell, which is frequently found for molecular crystals.<sup>[36,164]</sup> Such molecules are at crystallographically different sites, and hence, different environments giving rise to different chemical shifts. Though in some cases those differences will be rather small and not resolvable, peak multiplets are observed for most  $^{13}\text{C}$  resonances in such a situation.<sup>[36,40]</sup>



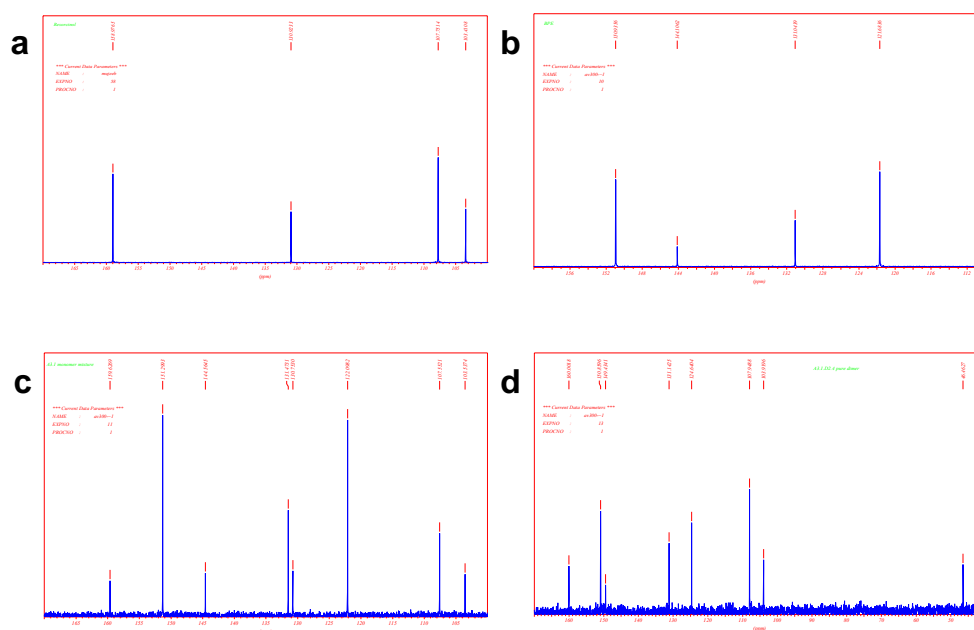


**Figure 6.1:**  $^{13}\text{C}$  solution NMR spectra of a) resorcinol b) trans-1,2-Bis(4-pyridyl)ethylene c) 2(bpe):2(res) monomer (P-1, triclinic) in chain form d) 2(bpe):2(res) dimer (monoclinic,  $P2_1/n$  phase)

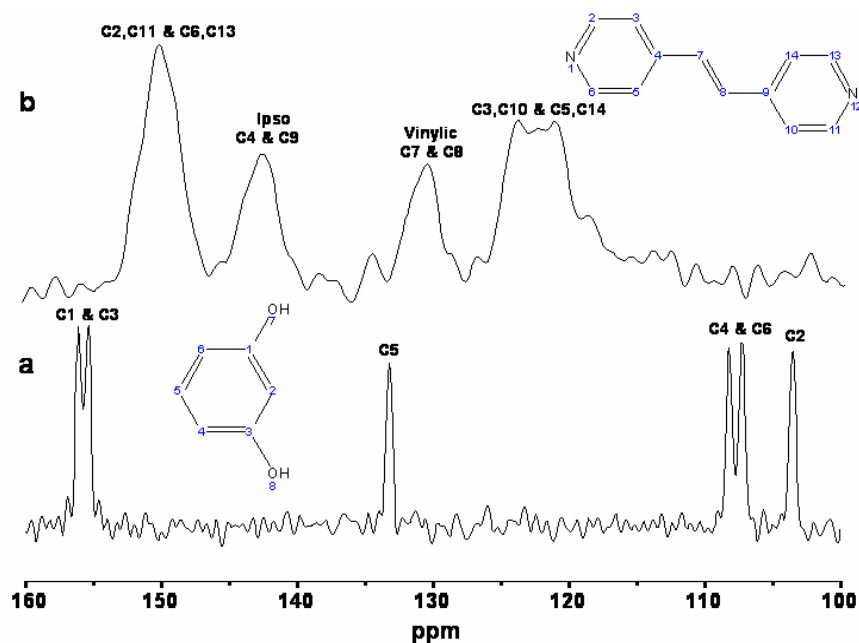


**Figure 6.2:** Solid-state  $^{13}\text{C}$ -CPMAS of a) 1,3-dihydroxybenzene (Resorcinol) b) Trans-1,2-Bis(4-pyridyl)ethylene. Chemical shift dispersion is mainly responsible for the broad lines in the spectrum of 1b).

Sample	$\delta$ (ppm)	Assignment
1,3-dihydroxy benzene (Resorcinol)	106.3	Center carbon (C2)
	107.2	Next to edge carbon (C4)
	108.2	Next to edge carbon (C6)
	133.2	Edge carbon (C5)
	155.3	Next to OH carbon (C1)
	156.1	Next to OH carbon (C3)
Trans-1,2-Bis(4-pyridyl)ethylene (BPE)	121.1	Next to ipso carbon (C5,C14)
	123.9	Next to ipso carbon (C3,C10)
	130.4	Vinyl carbons (C7,C8)
	142.4	Ipsos carbons (C4,C9)
	150.0	Next to N carbons (C2,C11 & C6,C13)
2(bpe):2(res) monomer (Prior to irradiation)	103.2	Res center carbons (C30,C38)
	106.7	Res carbons (C32,C34,40,42)
	120.4	Bpe carbons (C3,C10,C17,C24)
	125.0	Bpe carbons (C5,C14,C19,C28)
	128.8	Vinyl carbons (C7,C8,C21,C22)
	130.7	Res edge carbons (C33,C41)
	143.7	Ipsos carbons (C4,C9,C18,C23)
	148.6-150.5	Bpe carbons (C2,C6,C11,C13 & C16,C20,C25,C27)
162.7	Res carbons (C29,C31,C37,C39)	
2(bpe):2(res) Recrystallized Dimer Monoclinic P2 <sub>1</sub> /n phase	42.8	Cyclobutane carbons (C7,C8,C9,C10)
	100.9	Res carbons (C30,C38)
	106.8	Res carbons (C32,C34,C40,C42)
	125.1-126.5	Bpe carbons next to ipso (C3,C5,C24,C28,C12,C16,C22,C18)
	130.5	Res carbons (C33,C41)
	147.4	Bpe carbons next to N (C2,C6,C13,C15,C19,C21,C25,C27)
	151.4	Ipsos carbons (C4,C11,C17,C23)
	161.3	Res carbons (C29,C31,C37,C39)
tetrakis(4-pyridyl)cyclobutane (without resorcinol)	43.7	Cyclobutane carbons (C7,C8)
	50.3	Cyclobutane carbons (C9,C10)
	122.0	Next to ipso carbons (C5,C12)
	122.8	Next to ipso carbons (C18,C24)
	124.9	Next to ipso carbons (C3,C16,C22,C28)
	149.4	ipso carbons (C4,C11)
	150.3	Ipsos & next to N carbons (C17,C23 & C2,C15,C19,C25)
		carbons next to N (C6,C13,C21,C27)
	151.6	

**Table 6.1:** Resonance assignments for resorcinol, trans-1,2-Bis(4-pyridyl)ethylene, 2(bpe):2(res) monomer, 2(bpe):2(res) recrystallized dimer (monoclinic P2<sub>1</sub>/n phase) and tetrakis(4-pyridyl)cyclobutane based on *ab initio* chemical shift calculations.

The molecular packing of resorcinol within the orthorhombic crystals (space group No. 33  $Pna2_1$ ,  $Z=4$ , CSD code RESORA13 cf. Figure 6.3)<sup>[163]</sup> is comprised of four resorcinols that are linked via different hydrogen bonds. Signal splittings observed in the solid-state  $^{13}\text{C}$ -CPMAS NMR spectrum of the resorcinol (cf. Figure 6.2a), are attributed to the four conformationally different molecules packed in the unit cell. This was further confirmed with *ab initio*  $^{13}\text{C}$  chemical shift computations using the as-obtained structure from the cif file. Figure 6.4 reveal computed signal splittings of C1,C3 and C4,C6 respectively, of about 1.5 ppm as observed experimentally ( $\sim 1$  ppm). The agreement of computed  $^{13}\text{C}$  chemical shifts with experimental data is good in the range of  $\pm 5$  ppm except for the carbons attached to the hydroxyl group where the difference is  $\sim 9$  ppm.

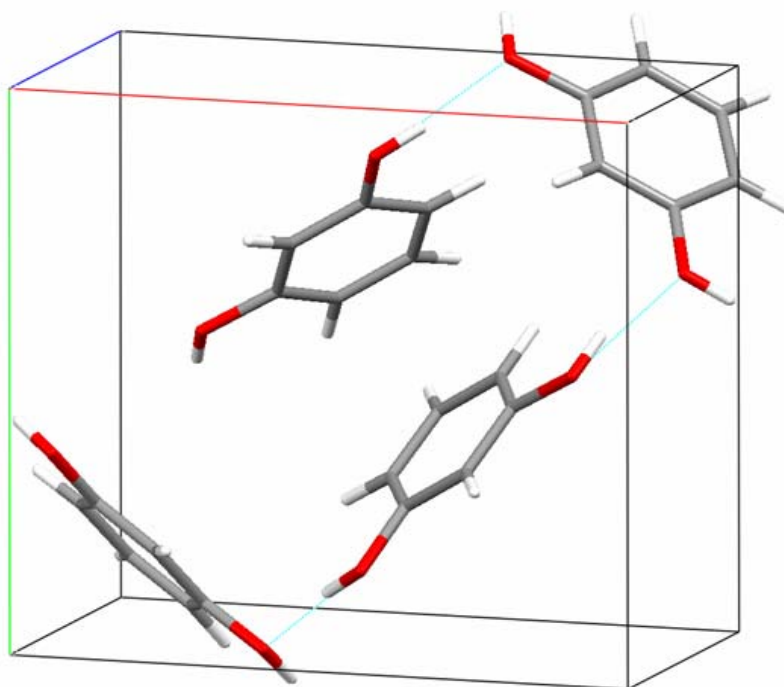


**Figure 6.3:** molecular packing of 1,3-dihydroxybenzene (Resorcinol). Single crystal data were from the Cambridge Structural Database (CSD) reference code RESORA13.<sup>[163]</sup> (green line in the figure represents H-bond between OH groups of resorcinol)

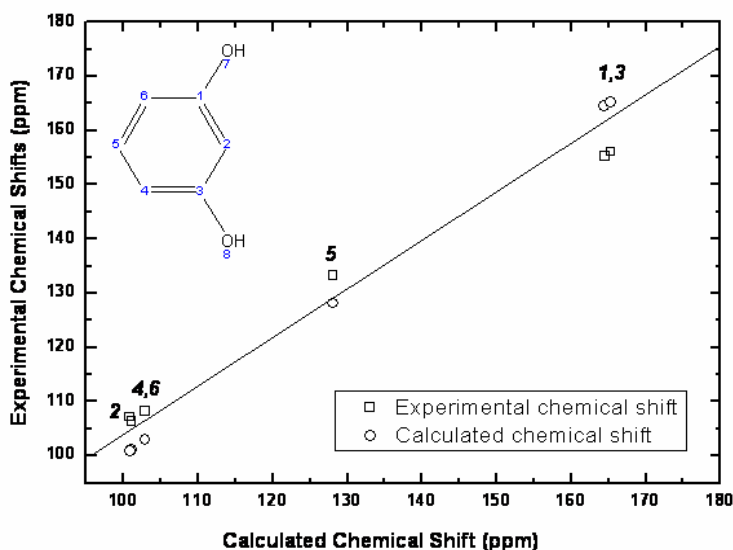


**Figure 6.4:** plot of computed  $^{13}\text{C}$  chemical shifts for the 1,3 dihydroxybenzene (Resorcinol) vs observed chemical shifts. (solid line in the middle of the graph is just a guide to eye)

### 6.3. MOLECULAR CONFORMATION OF BPE

The solid-state  $^{13}\text{C}$ -CPMAS spectrum of bpe (cf. Figure 6.2b) shows at least five rather broad resonances (there are *two* signals at 150 ppm that are unresolved) reflecting molecular packing effects as previously observed for resorcinol. However, unlike in the case of resorcinol where different hydrogen bonding environments have contributed to the peak splittings, peak splitting in case of bpe are most likely caused by different neighbours. As can be seen in Figure 6.5, carbons C3,C10 and C5,C14 (cf. Figure 6.2b) neighboring ipso carbon (non-protonated) have different interactions; one carbon (C3 or C10) is directly facing the nitrogen of neighboring bpe molecule in the same layer at a distance of  $\sim 3.5$  ppm, whereas another carbon (C5 or C14) in the same molecule does not have a similar contact. This effect also has an impact on (C2,C11 and C6,C13) carbons neighboring nitrogen, however, here the splitting is not that large as observed in the case of (C3,C10 and C5,C14) carbons neighboring ipso, and therefore are not resolved ( $\sim 150$  ppm).

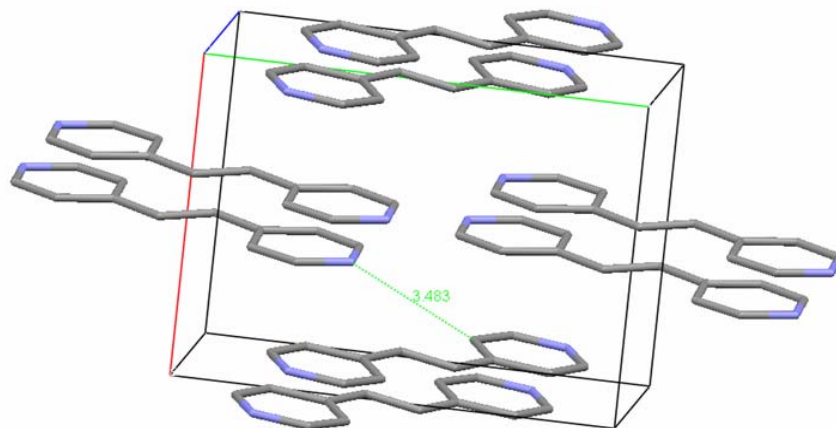


**Figure 6.5:** molecular packing of trans-1,2-Bis(4-pyridyl)ethylene (bpe). Single crystal data were from the Cambridge Structural Database (CSD) reference code AZSTBB.<sup>[161]</sup> (green dotted line in the figure represents next nearest neighbour of bpe molecule)

*Ab initio*  $^{13}\text{C}$  chemical shift computations based on the as-obtained crystal structure of bpe (cf. Figure 6.6, CSD code AZSTBB)<sup>[161]</sup> notably predict signal splittings of 7 ppm for carbons (C3,C10 and C5,C14) neighboring ipso carbon similar to experimentally observed splittings ( $\sim 4$  ppm). Moreover, the smaller computed peak splitting (1.4 ppm) of carbons (C2,C11 and C6,C13) next to nitrogen is in good agreement with the experimental  $^{13}\text{C}$  MAS NMR spectrum (cf. Figure 6.2b), where two signals have merged at 150 ppm yielding a rather broad signal. The unlikely broad signals in the  $^{13}\text{C}$ -CPMAS NMR spectrum of bpe have been reproduced several times, and were also found in respective fast MAS proton MAS NMR spectra (data not shown). This prompted for searching the origins of the broad linewidths. For perfectly well arranged (e.g. highly crystalline) solids, severe linebroadening in proton MAS spectra stems solely from homonuclear dipolar couplings among abundant protons. In that case, high-resolution proton MAS NMR spectra can, in principle, be obtained using so-called homonuclear dipolar decoupling sequences like windowed phase-modulated Lee-Goldburg (wPMLG)<sup>[165]</sup> or windowed DUMBO-1<sup>[166]</sup> that also constitute the key part of high-resolution proton double-quantum spectra (DQ-CRAMPS).<sup>[167]</sup> Since this approach did

not yield substantial line narrowing, the experimental linewidths were attributed to heterogeneous broadening e.g. due to a  $^{13}\text{C}$  chemical shift dispersion. This implies a rather ill-defined local ordering or poor crystallinity of the bulk NMR sample in contrast to the single-crystal used for X-ray analysis, as recently reported for enolizable chromophors.<sup>[168]</sup>

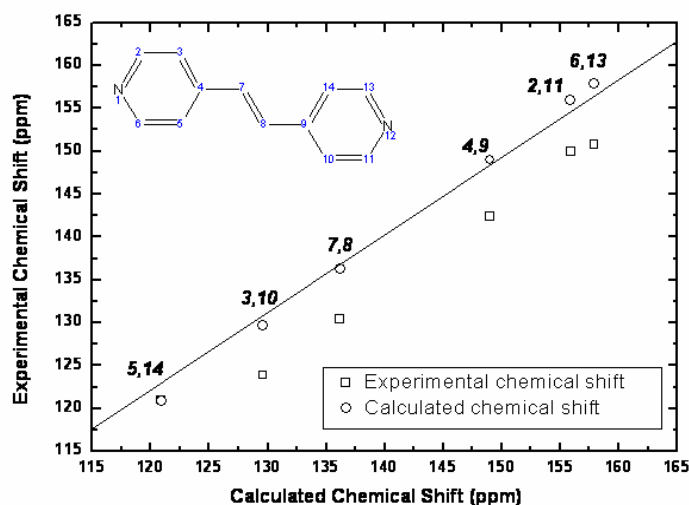


**Figure 6.6:** plot of computed  $^{13}\text{C}$  chemical shifts for the trans-1,2-Bis(4-pyridyl)ethylene (bpe) vs observed chemical shifts. (Solid line in the figure is just a guide to eye)

#### 6.4. MOLECULAR SPECIFICITY OF THE O-H...N HETEROSYNTHON

It has already been established that bpe does not exhibit the proper packing (or does not crystallize in a form that is) necessary for a solid-state dimerization. In the 2(bpe):2(res) OD complex (ring form) however, the double bonds are in parallel position suitable for [2+2]photoaddition. However, owing to the possibility of bond rotation about the C-O bond, resorcinols may consist of three different possible conformations of hydroxyl groups with respect to phenyl ring (cf. Figure 6.7): syn-syn, anti-anti, and syn-anti, respectively.<sup>[157]</sup> In order to achieve the required parallel arrangement of bpe for photodimerization, the OH group must adopt syn-syn conformation (cf. Scheme 6.1) as obtained in the case of 2(bpe)2(res), where resorcinol is co-crystallized with bpe alone

adopting ring form (triclinic, P-1). Notably, co-crystallization of bpe with resorcinol in the presence of saturated di-pyridine trans-1,2-Bis(4-pyridyl)ethane (bpet) in equimolar ratio (0.5:0.5:1) has produced a new monomer polymorph of (monoclinic,  $P2_1/n$ ) 2(bpe):2(res) along with 2(bpet):2(res) molecular adduct, where, both bpe and bpet have crystallized separately. Moreover, hydroxyl groups of resorcinol in both adducts (monoclinic  $P2_1/n$  2(bpe):2(res), and monoclinic  $P2_1/n$  2(bpet):2(res)) have adopted anti-anti conformation, facilitating chain formation with almost identical lattice parameters (cf. Figure 6.8). Thus, it is rather clear that the new polymorph is not suitable for photodimerization. Lattice parameters of both 2(bpe):2(res) monomer complexes (chain and ring forms), 2(bpet):2(res) molecular adduct as well as dimer polymorphs are provided in Table 6.2.

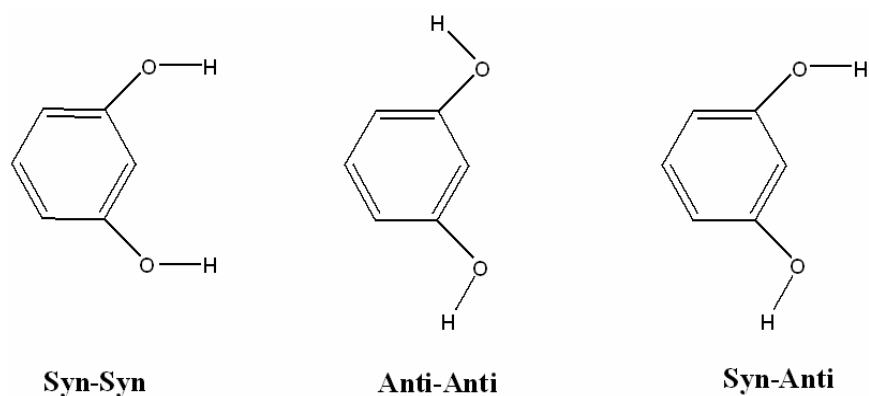


**Figure 6.7:** Three different possible hydroxyl conformation of resorcinol with respect to phenyl ring.

### 6.5. NEW POLYMORPH OF 2(BPE):2(RES) MONOMER

Apparently, the new polymorph of monomer 2(bpe):2(res) in chain form is relatively less stable than the reported ring form, as it has been kinetically driven in the presence of bpet. The latter presumably provides nucleation for the crystallization, as bpet indeed adopts a chain conformation upon crystallization with resorcinol.<sup>[157]</sup> Desiraju has previously suggested that<sup>[169]</sup> that, kinetically favoured crystals grow faster but the resulting crystals are less stable, since the activation energy barrier to that state is

lower. In contrast, the thermodynamically favoured crystal should take a longer time to form as the activation energy barrier is much higher, but is more stable. Indeed, this has been proven by DSC experiments (not shown here) where the melting temperatures of the stable (ring form) and metastable (chain form) differed by  $\sim 15$  °C (215 °C and 200 °C respectively).

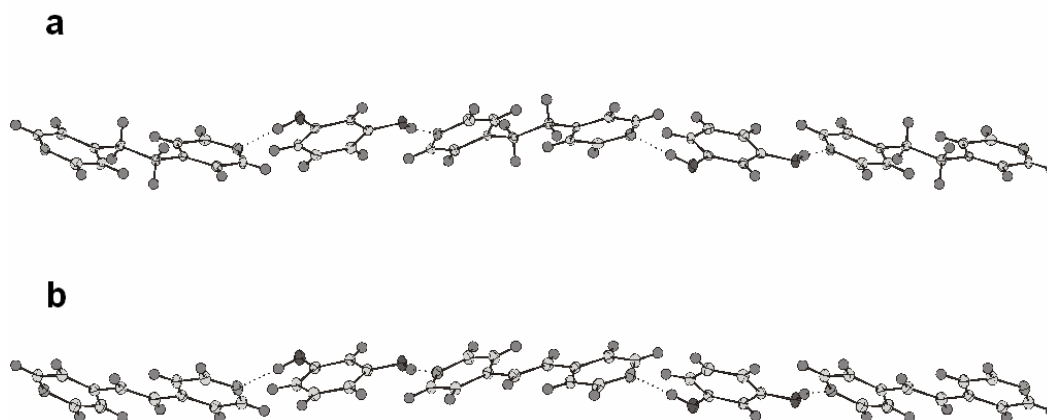


**Figure 6.8:** Chain conformation adopted by a) trans-1,2-Bis(4-pyridyl)ethane (bpet) b) trans-1,2-Bis(4-pyridyl)ethylene (bpe) with almost identical lattice parameters.

Lattice Parameters	2(bpe):2(res) chain form	2(bpet):2(res) chain form	2(bpe):2(res) ring form	2(bpe):2(res) As-dimerized dimer (42%)	2(bpe):2(res) Recrystallized dimer
<b>a</b>	10.1485 (4)	10.1927 (5)	8.070 (1)	7.7682 (1)	11.367 (1)
<b>b</b>	7.1265 (3)	7.1610 (9)	9.832 (1)	9.7938 (1)	9.749 (1)
<b>c</b>	20.0717 (6)	20.2559 (8)	10.876 (1)	11.0478 (1)	14.273 (1)
<b><math>\alpha</math></b>	90°	90°	73.119° (1)	94.4493° (1)	90°
<b><math>\beta</math></b>	94.6837° (21)	94.1624° (15)	72.563° (1)	104.8507° (1)	111.668° (15)
<b><math>\gamma</math></b>	90°	90°	66.184° (1)	111.4950° (1)	90°
<b>V</b>	1446.8	1474.6	738.868	742.068	1469.93
<b>Space group</b>	P2 <sub>1</sub> /n	P2 <sub>1</sub> /n	P-1	P-1	P2 <sub>1</sub> /n

**Table 6.2:** Lattice parameters of both the polymorphs of 2(bpe):2(res) monomer (chain form and ring form) as well as dimer (monoclinic P2<sub>1</sub>/n, and triclinic P-1) and 2(bpet):2(res) monomer (chain form)



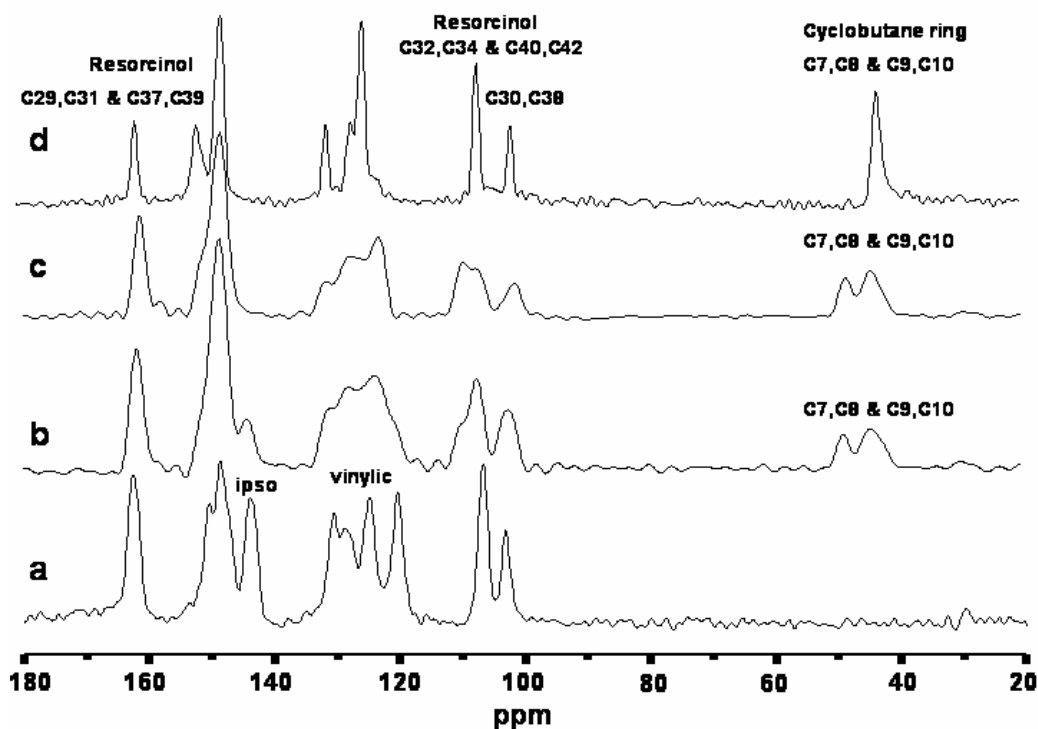
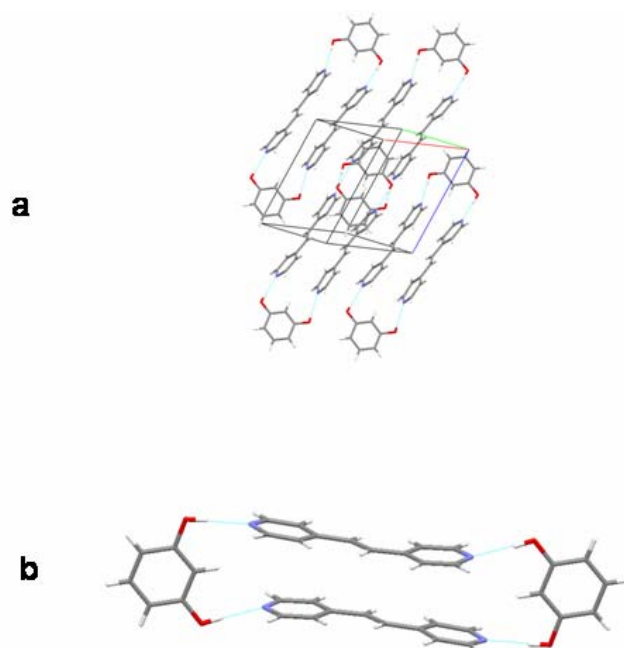


**Figure 6.9:** Solid-state  $^{13}\text{C}$ -CPMAS spectra ranging from monomer to dimer: a) 1:1 co-crystallized 2(bpe):2(res) monomer prior to irradiation b)  $\sim 50\%$  converted mixture c) 100% converted as-dimerized metastable dimer prior to recrystallization which consists of triclinic P-1 space group (absence of ipso carbon signal at  $\sim 140$  ppm in c is the clear indication of complete conversion) d) 100% converted recrystallized stable dimer consisting of monoclinic  $P2_1/n$  space group.

## 6.6. MOLECULAR CONFORMATION OF 2(BPE):2(RES) MONOMER

As stated earlier, co-crystallization of resorcinol and bpe in 1:1 ratio yields a 0-D complex of 2(bpe):2(res), where four hydroxyl groups of two resorcinol molecules hold two bpe molecules (ring form, triclinic, P-1) with relatively strong hydrogen bonds forcing them to stack parallel to each other. The corresponding  $^{13}\text{C}$ -CPMAS NMR spectrum of 2(bpe):2(res) displays well resolved peaks (Figure 6.9a) allowing to distinguish individual signals due to resorcinol and bpe. All signals of resorcinol in the complex 2(bpe):2(res) appear at quite similar chemical shifts compared to pristine resorcinol (2-3 ppm downfield shift), except for carbons (C1 and C3) next to hydroxyl group that are downfield-shifted from  $\sim 156$  ppm to 162 ppm due to the effect of

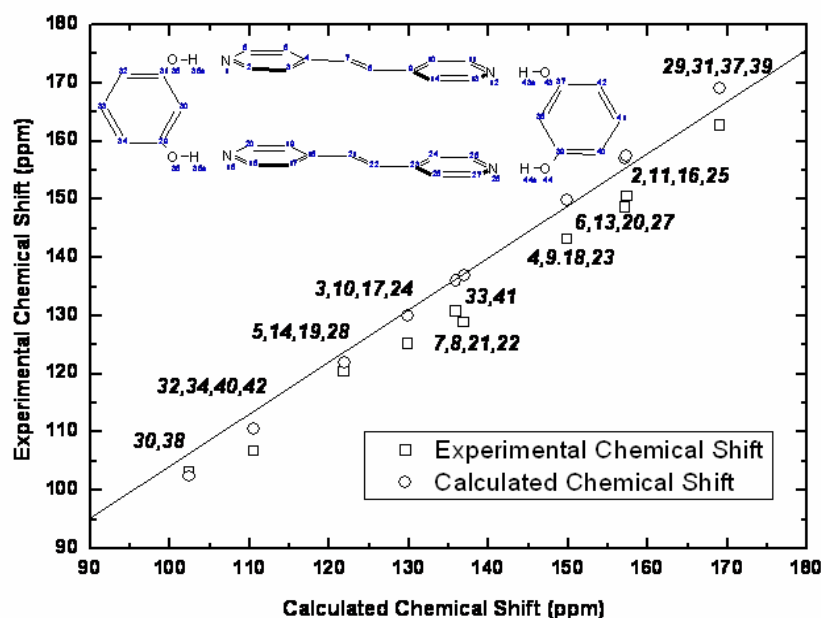
hydrogen bonding made with nitrogen of the pyridyl rings. Notably, signal splittings corresponding to the carbons neighbouring hydroxyl group (C1, C3) and carbons that are next to the peripheral carbon (C4, C6) in resorcinol (cf. Figure 6.2a) have vanished indicating changes of the hydrogen bonding pattern.



**Figure 6.10:** molecular packing of 1:1 cocrystallized 2(bpe):2(res) monomer prior to irradiation. a) shows the molecular packing of the monomer complex b) single block of 2(bpe):2(res) monomer complex where two bpe molecules do not lie parallel to each other but are slightly inclined. Single crystal data were from the Cambridge Structural Database (CSD) reference code ABEKLN.<sup>[161]</sup>

However, signal splittings corresponding to bpe are more pronounced in the monomer complex 2(bpe):2(res), particularly for signals assigned to the carbons (C3,C10 and C5,C14) next to ipso carbon of bpe which has further increased from 3 ppm in the pure form to about 5 ppm and appeared as two different signals at about 120 ppm and 125 ppm in the solid-state spectrum of 2(bpe):2(res) (cf. Figure 6.9a). Moreover, the signal at ~150 ppm corresponding to carbons (C2,C11 and C6,C13) next to nitrogen of the bpe molecule has split unlike in the original bpe <sup>13</sup>C-CPMAS NMR spectrum where it was unresolved (cf. Figure 6.2b). Remaining signals at ~143 ppm and 128 ppm,

respectively, can be assigned to ipso (C4,C9) and vinylic (C7,C8) carbons, respectively. Indeed, the observed signal splittings reflect the molecular packing of the 0-D monomer complex 2(bpe):2(res). Two adjacent bpe molecules in single block of 2(bpe):2(res) do not lie exactly parallel to each other but are slightly inclined due to which the arms of the hydrogen bonds between the hydroxyl group of resorcinol and the nitrogen of the pyridyl rings are not coplanar (cf. Figure 6.10). In order to account for solid-state packing effects, *ab initio*  $^{13}\text{C}$  chemical shift computations were performed on the monomer 2(bpe):2(res) cluster where the computed  $^{13}\text{C}$  chemical shifts fit well with experimental data (the agreement is good in the range of  $\pm 5$  ppm), including peak splittings (cf. Figure 6.11).



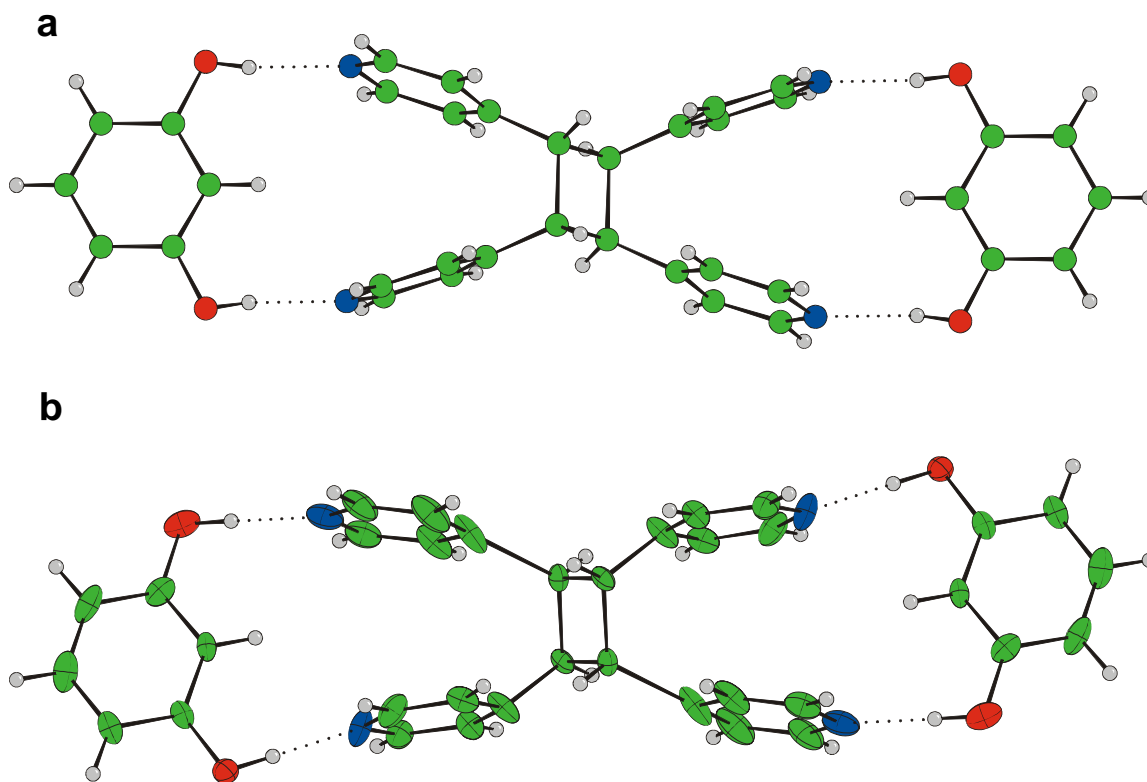
**Figure 6.11:** plot of computed  $^{13}\text{C}$  chemical shifts for the 1:1 cocrystallized trans-1,2-Bis(4-pyridyl)ethylene (bpe) and resorcinol vs observed chemical shifts. (Solid line in the middle of the graph is just a guide to eye)

Figure 6.9 shows a series of  $^{13}\text{C}$ -CPMAS NMR spectra ranging from 1:1 cocrystallized 2(bpe):2(res) monomer prior to irradiation (0% conversion) to as-dimerized tetrakis(4-pyridyl)cyclobutane (triclinic P-1, 100% converted metastable phase), including partial mixture containing both monomer and dimer at  $\sim 50\%$  conversion (cf. Figure. 6.9b), whereas the spectrum in Figure 6.9d corresponds to another stable

polymorph of tetrakis(4-pyridyl)cyclobutane with monoclinic  $P2_1/n$  space group. As the dimerization proceeds, corresponding intensities of both the olefinic carbon ( $\sim 130$  ppm) and ipso carbon signals ( $\sim 142$  ppm) assigned to the monomer decreased with a gradual rise of the new carbon signals attributed to the cyclobutane ring indicating successful formation of a photodimer. Additionally, the chemical shifts of the neighboring carbons, i.e., the ipso (non-protonated) carbon display a small downfield shift upon conversion of the monomer into a dimer, possibly due to differences in inductive effects of neighboring groups (vinyl vs. cyclobutane). Full assignments of the carbon sites in all samples are given in Table 6.1. Two signals in the cyclobutane ring region ( $\sim 40$  ppm) and two signals in the resorcinol carbons (C4,C6) neighboring resorcinol peripheral carbon ( $\sim 105$  ppm) are observed in the respective  $^{13}\text{C}$ -CPMAS NMR spectra of both partially and fully converted as-dimerized metastable dimer (cf. Figure 6.9b and 6.9c). In contrast, the  $^{13}\text{C}$  CPMAS NMR spectrum of 100% converted, stable recrystallized dimer complies with the  $^{13}\text{C}$  solution NMR spectrum (cf. Figure 6.1d) that exhibits a single peak in the respective regions reflecting the centrosymmetric molecular geometry.

## 6.7. OBSERVATION OF A NEW POLYMORPH OF 2(BPE):2(RES) DIMER

In homogeneous topochemical reactions the overall volume change may be small, while changes of lattice parameters can be larger, e.g. when Van der Waals contacts are transformed into chemical bonds.<sup>[29]</sup> Notably, it has been observed while monitoring [2+2]photodimerization of monomer 2(bpe):2(res) via single crystal X-ray analysis that the volume change during the transformation from monomer into dimer is less than 2%. However, even under tail irradiation conditions, crystals were observed to deteriorate, owing to an unusually large change of one angle in the unit cell (angle  $\alpha$ ), so that no single crystals of sufficient size were available for structure analysis at conversions exceeding approximately 50%. Nevertheless, powder diffractometry shows, that P-1 phase (100% converted as-dimerized dimer) persists until complete conversion which upon recrystallization adopted  $P2_1/n$  phase (100% converted recrystallized dimer) which is already been reported.<sup>[151]</sup>



**Figure 6.12:** Crystal structure projection of dimer molecules a) 100% converted recrystallized dimer with monoclinic P21/n space group<sup>[151]</sup> b) 6 hrs irradiated (42% converted) as-dimerized dimer with triclinic P-1 space group, from this structure atoms belonging to the monomer have been removed for clarity (further details related to complete crystal structure analysis will be discussed in next chapter).

Notably, the  $^{13}\text{C}$ -CPMAS NMR spectra in Figure 6.9c and 6.9d provide evidence that the 100%-converted as-dimerized and 100%-converted recrystallized dimers are indeed two different polymorphs. Two different signals in the cyclobutane ring region in Figure 6.9c indicate that, though crystallographically the dimer is located on a center of symmetry, this is not reflected in the NMR spectrum due to its local environment (distortion of pyridyl rings as well as other packing effects) that exist in as-dimerized dimer (triclinic, P-1 phase) resulting in signal splittings. In contrast, the single observed cyclobutane ring signal ( $\sim 40$  ppm) hints at an absence of such molecular distortions so that the local symmetry center in the recrystallized dimer (monoclinic, P21/n phase) is preserved. Even though  $^{13}\text{C}$  chemical shifts of the P-1 polymorph of tetrakis(4-pyridyl)

cyclobutane could not be computed due to lacking crystal structure coordinates, additional signals observed in the  $^{13}\text{C}$ -CPMAS spectrum of (cf. Figure 6.9c) 100%-converted as-dimerized dimer of 2(bpe):2(res) can be attributed to distortions in the structure caused by the tilt angle (i.e. the angle between the plane of the pyridyl ring and the bond connecting the pyridyl ring with cyclobutane ring) and strain developed during the SCSC transformation thereby enforcing pyridyl rings to adopt different conformations. Figure 6.12 clearly shows the different conformations of the pyridyl rings adopted in as-dimerized form and in recrystallized form.

### 6.8. THERMAL ANALYSIS OF 2(BPE):2(RES) DIMER

Apparently, the as-dimerized form is in a metastable state,<sup>[39,170]</sup> e.g. its as-dimerized conformation is not the equilibrium conformation. This results in lattice strain that facilitates adoption of a more stable conformation rather close to equilibrium conformation similar to the one adopted by the recrystallized dimer. Consequently, a polymorphic phase transformation from the metastable P-1 phase to the more stable  $P2_1/n$  phase of tetrakis(4-pyridyl)cyclobutane has been observed at  $\sim 109^\circ\text{C}$  (DSC data, cf. Figure 6.13). However, the reverse transformation upon subsequent cooling is *not* observed. As can be seen in Figure 6.13, the DSC experiment provide clear evidence that the metastable P-1 phase transforms to the stable  $P2_1/n$  phase, where small exotherm representing the phase transformation is observed at  $109.5^\circ\text{C}$  followed by melting at  $190.5^\circ\text{C}$  (endothermic peak). A comparable exotherm peak is not observed in the DSC trace of 100% converted recrystallized dimer ( $P2_1/n$  phase). Further evidence for the polymorphic transition stems from temperature-dependent solid-state  $^{13}\text{C}$  NMR studies. First, the  $^{13}\text{C}$ -CPMAS NMR spectrum of 100%-converted as-dimerized dimer was recorded at room temperature yielding a spectrum similar to the one shown in Figure 6.9c. Then, the same compound was subjected to higher temperature ( $\sim 110^\circ\text{C}$ ), where the obtained spectrum exhibited similar characteristics as shown in Figure 6.9d (explicitly the two signals in cyclobutane ring region have merged into a single signal) corresponding to the phase transition.

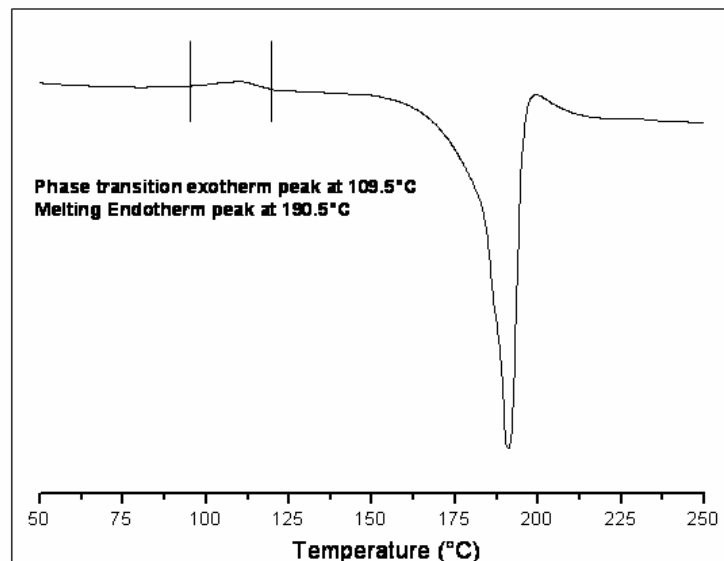


**Figure 6.13:** DSC plot for the 100% converted as-dimerized dimer of tetrakis(4-pyridyl)cyclobutane recorded for heating rate at 10°C per minute. The melting temperature is at ~190°C.

## 6.9. REMOVAL OF TEMPLATE FROM 2(BPE):2(RES) DIMER

Finally, the tetrakis(4-pyridyl)cyclobutane was separated by removal of resorcinol from the 2(bpe):2(res) dimer complex (P<sub>2</sub>/n phase) by column chromatography and recrystallized from acetone. Its purity was confirmed from both <sup>1</sup>H and <sup>13</sup>C solution NMR spectra (cf. Figure 6.14) which displayed four different resonances as expected for a centrosymmetric dimer. However, the solid-state <sup>13</sup>C-CPMAS NMR spectrum of the same compound exhibited more resonances than in solution; in particular, two different resonances were observed for the carbons (C7,C8,C9,C10) in the cyclobutane ring at ~44 ppm and ~50 ppm (cf. Figure 6.15), hinting at a non-centrosymmetric structure as a consequence of possible distortions present in the crystal. The molecular packing of the compound is shown in Figure 6.16, which clearly reveal the distortion of the cyclobutane ring and also the presence of a 2-fold axis passing through the center of cyclobutane ring of molecule.

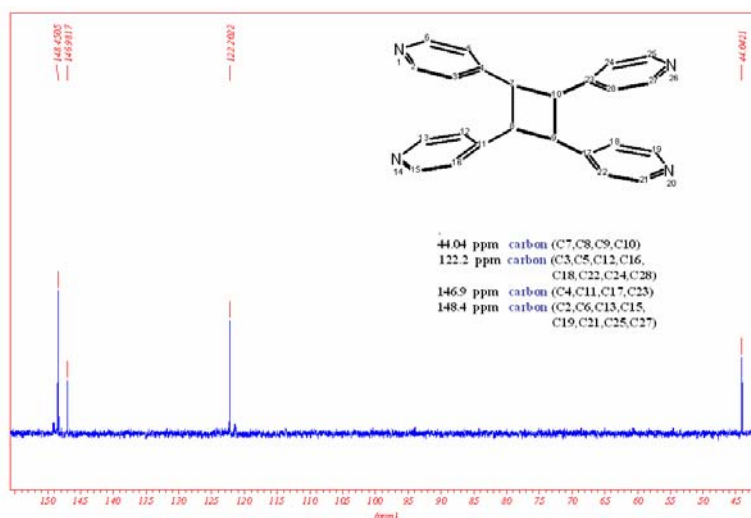


**Figure 6.14:**  $^{13}\text{C}$  solution NMR spectrum for pure tetrakis(4-pyridyl)cyclobutane (1,2,3,4-tetra(pyridine-4-yl)cyclobutane) with out resorcinol. Note, single resonance in cyclobutane ring region ( $\sim 44$  ppm).

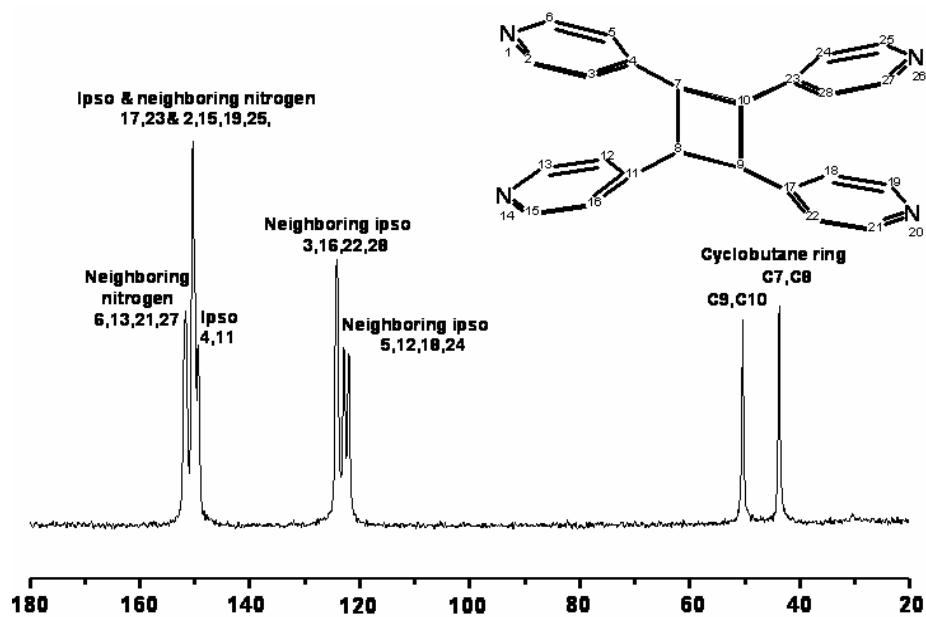


**Figure 6.15:**  $^{13}\text{C}$ -CPMAS spectrum of pure extracted tetrakis(4-pyridyl)cyclobutane (1,2,3,4-tetra(pyridine-4-yl)cyclobutane). Presence of two signals in the cyclobutane ring region points towards the distortion of center of symmetry in the pure dimer



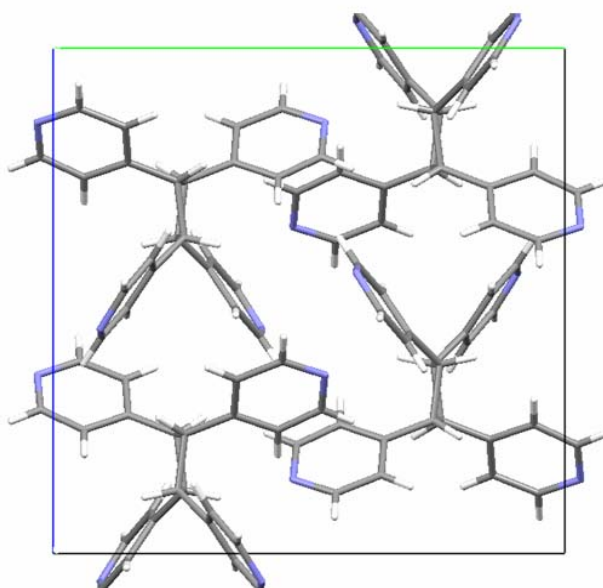


**Figure 6.16:** Molecular packing of pure extracted tetrakis(4-pyridyl)cyclobutane (1,2,3,4-tetra(pyridine-4-yl)cyclobutane). The compound has orthorhombic,  $Pccn$  space group, the cyclobutane ring is not planar but is puckered and all its hydrogen atoms are slightly staggered.

The compound adopted an entirely different molecular packing when compared to the metastable as-dimerized dimer (triclinic,  $P-1$  Phase) and relatively stable recrystallized dimer (monoclinic,  $P2_1/n$  phase), the system has an orthorhombic  $Pccn$  space group with cell lengths as 9.37, 13.94 and 14.05 Å for a, b, and c respectively with four molecules comprising a single unit cell. Indeed, the crystal structure of the compound has revealed substantial distortion in the cyclobutane ring as a consequence of removing resorcinol. In the absence of hydrogen bonding, all pyridyl rings moved away from each other along with significant rotations attaining different conformations. Therefore, the cyclobutane ring no longer remained planar but is puckered,<sup>[171]</sup> where all ring hydrogen atoms are slightly staggered as opposed to a totally eclipsed conformation adopted in the planar centrosymmetric ring of 2(bpe):2(res) dimer (Figure 6.12a).

The experimental  $^{13}\text{C}$ -CPMAS NMR data of tetrakis(4-pyridyl)cyclobutane were compared with *ab initio*  $^{13}\text{C}$  chemical shift computations. The computed shifts revealed that all five carbons present in each pyridyl ring have different chemical shifts; however,

the presence of 2-fold axis passing through the center of cyclobutane ring has reduced the number of resonances to twelve instead of twenty four as would be expected otherwise for all carbon atoms present in a single molecule. In contrast, the experimental  $^{13}\text{C}$ -CPMAS NMR spectrum (cf. Figure 6.15) exhibits only eight resonances as some of the chemical shift values are too similar to be resolved. Figure 6.17 shows the plot of computed  $^{13}\text{C}$  isotropic chemical shifts vs the observed values; the agreement is good in the range of  $\pm 5$  ppm.

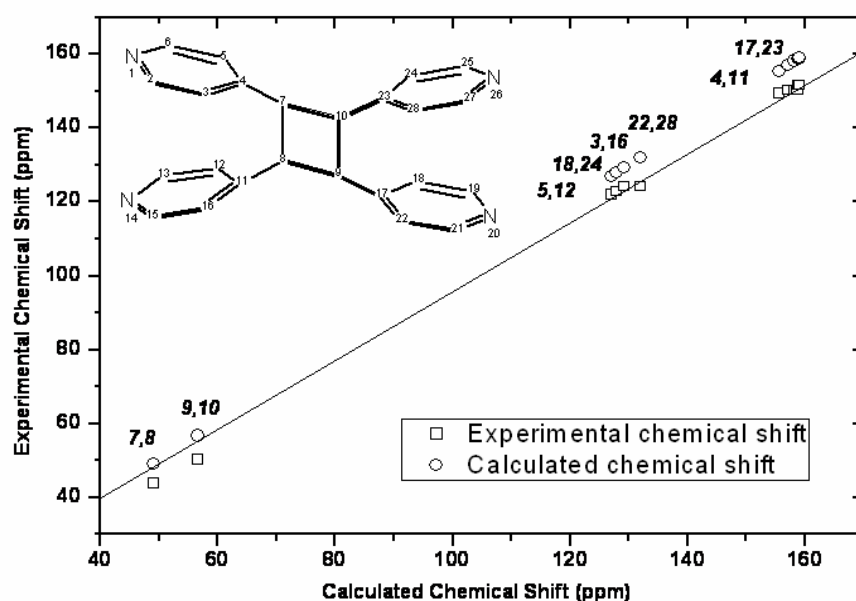


**Figure 6.17:** plot of computed  $^{13}\text{C}$  chemical shifts for the pure extracted tetrakis(4-pyridyl)cyclobutane (1,2,3,4-tetra(pyridine-4-yl)cyclobutane) vs observed chemical shifts. The molecule has a 2-fold axis passing through the center of the cyclobutane ring, thus computations have rendered twelve different chemical shifts which are symmetry related to other half of the molecule.

## 6.10. CONCLUSIONS

Two different polymorphs of the monomer complex 2(bpe):2(res) have been obtained, e.g. a ring form (P-1, triclinic) that is suitable for photodimerization and a chain

form ( $P2_1/n$ , monoclinic) while exploring molecular specificity during resorcinol-pyridine recognition. Moreover, it has been clearly demonstrated with the help of solid-state NMR analysis that the crystal-engineered monomer (ring form) complex of 2(bpe):2(res) also yielded *two* different dimer polymorphs upon photoirradiation, e.g. the centrosymmetric monoclinic,  $P2_1/n$  phase and triclinic, P-1 phase. In addition, removal of resorcinol template from the complex of 2(bpe):2(res) yields tetrakis(4-pyridyl)cyclobutane that consists of distorted cyclobutane rings along with a completely different molecular geometry (orthorhombic, Pccn phase). Ambiguous peak splittings and the presence of “unexpected” resonances in the respective  $^{13}\text{C}$ -CPMAS NMR spectra have been successfully explained by the joint approach of X-ray analysis and *ab initio* chemical shift computations. Since the computations are sensitive to intermolecular as well as solid-state packing effects, they yielded different chemical shifts for those atoms that are located in different environments (as extracted from the respective crystal structures).

## 6.11. EXPERIMENTAL

### 6.11.1. Preparation of 2(bpe):2(res) monomer complex

1,3-dihydroxybenzene (resorcinol), trans-1,2-bis(4-pyridyl)ethylene (bpe) and trans-1,2-bis(4-pyridyl)ethane (bpet) were purchased from Aldrich and used as obtained. Co-crystals of 2(bpe):2(res) were prepared by dissolving 2 mmol of resorcinol (220.4 mg) and 2 mmol of bpe (364.6 mg) in 50 ml of acetone and left for slow evaporation in an open container. After two days, yellow crystals were obtained and subsequently ground to small microcrystalline particles. 500 mg of co-crystals were evenly distributed in a thin layer on a 100 mm Petri dish and irradiated using a 100 W high-pressure Hg lamp (Muller electronic LXH100) for a period of 12 h yielding 100%-converted as-dimerized tetrakis(4-pyridyl)cyclobutane (triclinic, P-1 phase). Aliquots of 125 mg product were taken out at each interval of 2 h for solid-state NMR measurements. In order to reach fast conversion, the powder was agitated after every 30 min and

simultaneously rotated using a home built small rotating machine. 100%-converted, re-crystallized dimer of tetrakis(4-pyridyl)cyclobutane (monoclinic, P2<sub>1</sub>/n phase) was obtained by re-crystallization of as-dimerized bpe dimer from acetone.

### **6.11.2. Co-crystallization of resorcinol, bpe and bpet**

Co-crystallization of trans-1,2-bis(4-pyridyl)ethylene (bpe), trans-1,2-bis(4-pyridyl)ethane (bpet) with resorcinol in 0.5:0.5:1 ratio were performed by dissolving 0.5 mmol of bpe (91.15 mg), 0.5 mmol of bpet (92.15 mg) and 1 mmol of resorcinol (110.2 mg) in 25 ml of acetone and left for slow evaporation in an open container. After ~48 hrs, different kinds of crystals were obtained; yellow crystals were formed at the bottom of the container whereas colourless crystals were found on the walls. Yellow crystals were then first subjected to X-ray analysis and found to be co-crystals of new polymorph of 2(bpe):2(res) in chain conformation (monoclinic, P2<sub>1</sub>/n), whereas, colourless crystals were co-crystals of 2(bpet):2(res) also in chain form with almost identical lattice parameter with that of chain 2(bpe):2(res).

### **6.11.3. Extraction of tetrakis(4-pyridyl)cyclobutane**

Pristine 1,2,3,4-tetra(pyridine-4-yl)cyclobutane was extracted from 200 mg of dimerized co-crystals (monoclinic, P2<sub>1</sub>/n phase) of 2(bpe):2(res) via column chromatography using acetone. Resorcinol elutes first, followed by 1,2,3,4-tetra(pyridine-4-yl)cyclobutane. Subsequent evaporation of solvents yielded a yellow powder of 1,2,3,4-tetra(pyridine-4-yl)cyclobutane (orthorhombic, Pccn phase). Single crystals for X-ray analysis were obtained by the slow evaporation of an acetone solution. <sup>1</sup>H NMR, δ: 8.71-8.69 (D, 8H, N-CH); 7.26-7.24 (D, 8H, N-CH-CH); 4.73 (S, 4H, cyclobutane ring). <sup>13</sup>C NMR, δ: 150.43 (8C, N-C); 149.2 (4C, Ipso); 124.1 (8C, next to ipso); 46.2 (4C, cyclobutane ring). EI MS: m/z 363.6 (M<sup>+</sup>).

#### **6.11.4. Solid-State NMR analysis**

All  $^{13}\text{C}$ -CPMAS spectra were collected at 125.77 MHz (Bruker Avance 500 spectrometer), with a CP-contact time of 5 ms coadding 8k transients. The experiments were carried out using a standard Bruker 4 mm double resonance MAS probe spinning at 12 kHz, typical  $\pi/2$ -pulse length of 2.5  $\mu\text{s}$  and a recycle delay of 15 s. The spectra are referenced with respect to tetramethyl silane (TMS) using adamantane as secondary standard (29.46 ppm for  $^{13}\text{C}$ ).<sup>[141]</sup> If not stated otherwise, all spectra were acquired at room temperature.

#### **6.11.5. Solution NMR and mass**

Solution NMR spectra were recorded on a Bruker AC 250, where the residual  $^1\text{H}$  peak of deuterated solvent was used as an internal standard (Acetone,  $^1\text{H}$ ,  $\delta = 2.05$  ppm). Mass spectra were obtained using a Varian Mat 7a (70e.v.).

#### **6.11.6. DFT-based chemical shift calculations**

Geometries were used as obtained from crystal structures, where the protons were refined based on known geometries. Relaxing the structures during a geometry optimization may yield C-H bond lengths that differ up to 0.15 Å from the initial structure while keeping the heavy atoms almost unchanged. This, however, is not feasible for as-dimerized and intermediate states that are rather metastable states.<sup>[173]</sup>  $^{13}\text{C}$  chemical shifts with respect to tetramethyl silane (TMS) were computed at B3LYP/6-311++G(2df, 2pd) or B3LYP/6-311G(2df, 2pd) level of theory<sup>[143,144]</sup> with the GIAO approach as implemented in Gaussian03 program package.<sup>[145]</sup>

#### **6.11.7. Single Crystal X-Ray Analysis**

X-ray analysis has been performed using similar parameters that have been described in chapter 5.

# CHAPTER 7

## PROBING STRUCTURAL TRANSFORMATIONS IN 2(BPE):2(RES) HETEROSYNTHON VIA SINGLE CRYSTAL X-RAY ANALYSIS

### 7.1. INTRODUCTION

In this chapter the results obtained via single crystal X-ray analysis of the structural changes in a co-crystal of resorcinol (res) and trans-1,2-bis(4-pyridyl)ethylene (bpe) during the [2+2] photodimerization that are described in chapter 5 are discussed. It was observed that with increasing conversion the crystals lost their integrity. Thus, we deal here with an interesting case of a *non-ideal* single-crystal-to-single-crystal transformation. Clearly, 2(bpe):2(res) heterosynthon produces two different polymorphs upon photodimerization as established earlier by detailed NMR studies (chapter 6). The actual molecular displacements (atomic level molecular changes) as well as topotactic nature of the reaction can only be confirmed via X-ray analysis.

### 7.2. TAILORED [2+2] PHOTODIMERIZATION

The system shown in Scheme 6.1, undergoes the [2+2] photodimerization homogeneously, but through a rare *non-ideal* SCSC transformation. Here, like in the ideal case described previously (chapter 2), the transformation takes place

homogeneously i. e. with the formation of solid solutions of the product and reactant throughout the conversion, but the quality of mixed crystals obtained during the reaction deteriorated drastically into small fragments even under tail irradiation,<sup>[29-34]</sup> presumably, due to buildup of severe strain in the crystals. This makes it extremely difficult to monitor the complete conversion as the crystal size decreases continuously with conversion so that at certain level, the crystals were no longer suitable for single crystals X-ray analysis. Upon irradiation at the maximum absorption of the bpe chromophore (300 nm)<sup>[172]</sup> (cf. Figure 7.1), a heterogeneous reaction is observed.<sup>[45]</sup> The surface of the originally yellow crystals is slowly covered with a fine powder, while the crystals eventually shatter into microcrystalline particles.

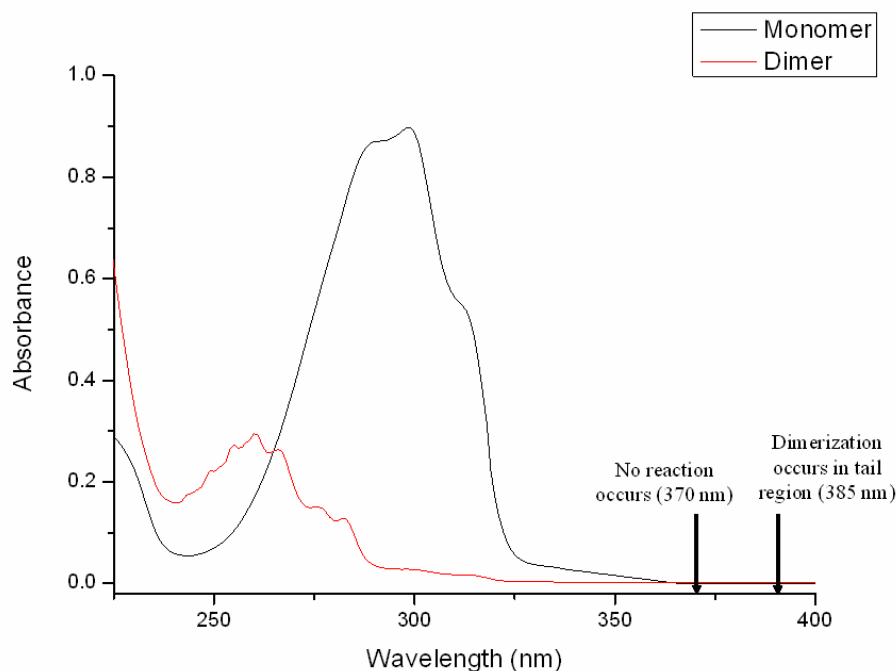


**Figure 7.1:** Electronic absorption spectrum for bpe monomer and dimer. The splitting of the absorption band is attributed to five different transitions in bpe monomer.<sup>172</sup> One  $n-\pi^*$  and others  $\pi-\pi^*$  transitions.

Even when crystals of 2(bpe):2(res) are irradiated at 370 nm (70 nm away from the absorption maximum), the crystals quickly start to disintegrate indicating product formation but not via SCSC transformation. When a filter with the flank of the absorption

more than 120 nm longer than the absorption maximum (420 nm) is used, even after hours of irradiation, no indication of product formation was found. Different edge filters were tried between 370 and 420 nm, with crystals either crumbling at an early stage or not reacting even after hours of irradiation (checked by X-ray analysis). In contrast, when a 385 nm edge filter was used, the crystal remained intact and did not lose its transparency after 2 hrs of irradiation. X-ray analysis revealed a ~14% converted mixed crystal, but with increasing conversion, the crystals split into small crystalline fragments which were used in the structure determination. A crystal of suitable size (~0.2 mm) could be isolated at 42% conversion but upon continued irradiation the crystal size decreased further so that in this range no suitable crystals were available for X-ray analysis. Even using an edge filter with a slightly larger value of filtration than 385 nm filter (389 nm) did not yield fruitful results. The projection of the crystal structure of 14 and 42% converted mixed crystals are given in Figure 7.2.

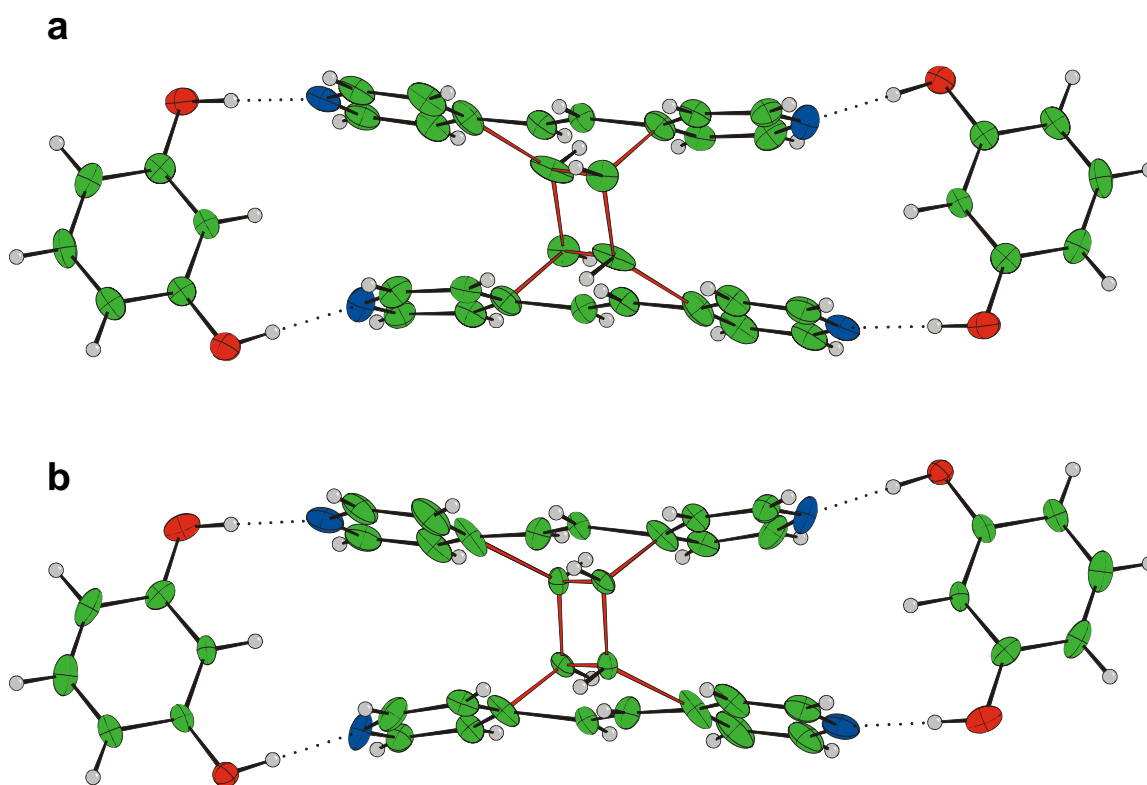


**Figure 7.2:** Crystal structure projection of a) 14% and b) 42% converted mixed crystal of 2(bpe):2(res) component.



Unit Cell Parameters	2(bpe):2(res) Monomer <sup>151</sup>	2(bpe):2(res) 14% Mixed Crystal	2(bpe):2(res) 42% Mixed Crystal	2(bpe):2(res) Dimer <sup>151</sup>
Space Group	Triclinic, P -1	Triclinic, P -1	Triclinic, P -1	Monoclinic, P2 <sub>1</sub> /n
a (Å)	8.070 (1)	7.9360 (4)	7.7682 (4)	11.367 (1)
b (Å)	9.832 (1)	9.8340 (5)	9.7938 (5)	9.749 (1)
c (Å)	10.876 (1)	10.9160 (5)	11.0478 (5)	14.273 (1)
$\alpha$ (°)	73.1190 (1)	86.9300 (12)	85.5507 (12)	90
$\beta$ (°)	72.563 (1)	73.8200 (13)	75.1493 (13)	111.668 (3)
$\gamma$ (°)	66.184 (1)	68.5050 (13)	68.5050 (13)	90
V (Å <sup>3</sup> )	733.868	733.657	742.068	734.965

**TABLE 7.1:** Unit cell parameters obtained during the photodimerization of 2(bpe):2(res). The monomer and the mixed crystal contains triclinic space group whereas the dimer has monoclinic space group.

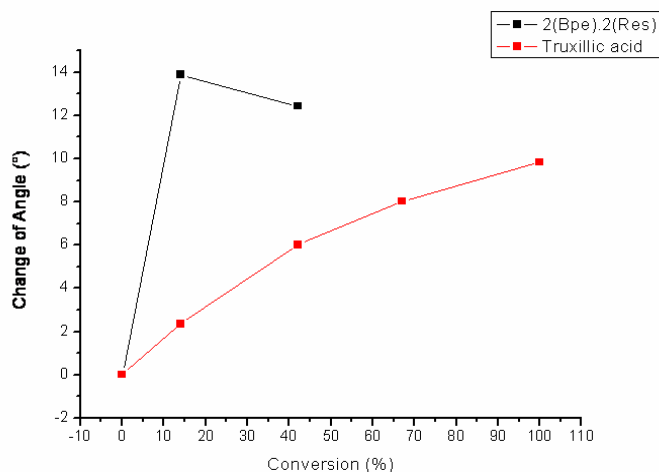


**Figure 7.3:** The drastic change of angle in the unit of 14% converted 2(bpe):2(res) mixed crystal is compared to that of the gradual changes that occur during the photodimerization of cinnamic acid.<sup>[29]</sup>

### 7.3. SOLID-STATE REACTIVITY

The key question in SCSC transformations is the lattice mismatch between reactants and products. At moderate mismatch (cinnamic acid, DSP, styrylpyrilium

triflate)<sup>[29,30,45]</sup> the uniform intensity distribution in the tail irradiation technique leads to high quality as-dimerized crystals. Indeed, in the case of benzylidenecyclopentanone (BBCP),<sup>[23]</sup> where there is very little lattice mismatch, a SCSC transformation is observed even with broad band irradiation (irradiation at the absorption maximum). Apparently, we deal here with a limiting case with substantial lattice changes during the reaction. The lattice parameters are summarized in Table 7.1. From the data it is evident that, in particular, one angle of the unit cell (angle  $\alpha$ ) changes abruptly by  $\sim 14^\circ$ . Similar large changes have also been observed with  $\alpha$ -trans-cinnamic acid<sup>[29]</sup> but here the change is gradual and not abrupt (cf. Figure 7.3).

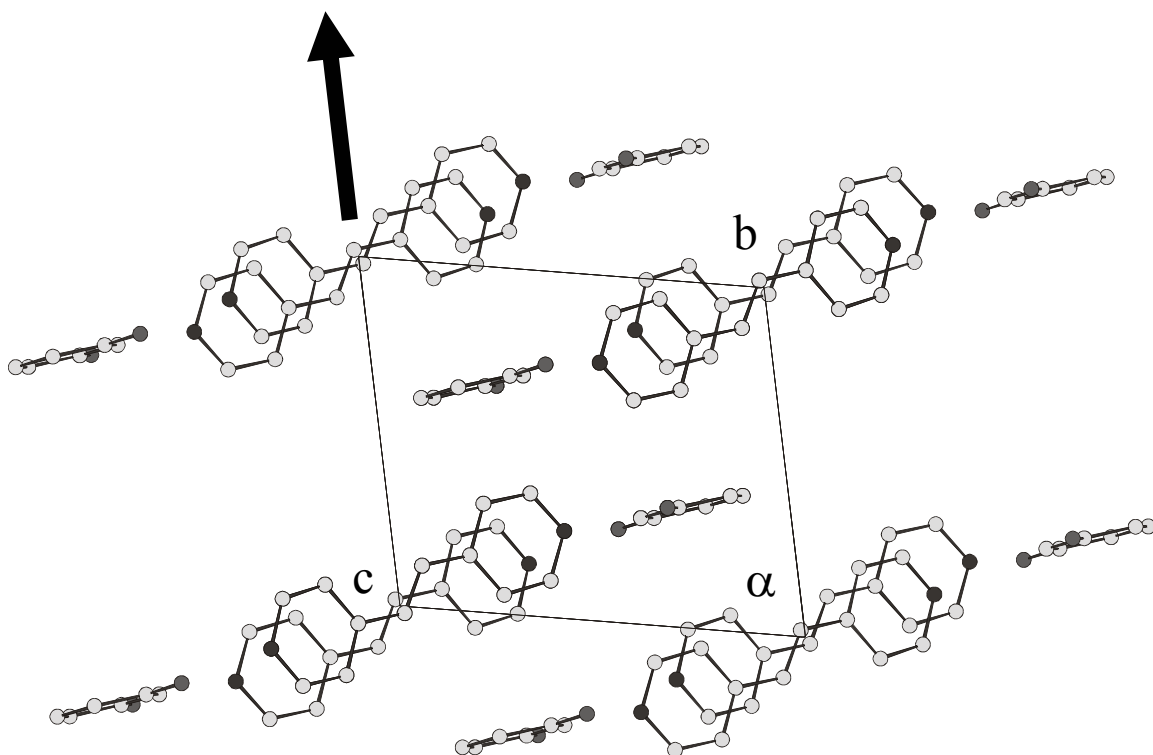


**Figure 7.4:** Schematic representation of cleavage plain in the crystals of 2(bpe):2(res) heterosynthon that occurs upon photodimerization

#### 7.4. CHANGES IN LATTICE PARAMETERS

Analysis of the lattice changes show that in this particular case the change of angle  $\alpha$  is accompanied with a shear movement in the  $a$ - $b$  plane (cf. Figure 7.4). This plane has been identified also as a prominent cleavage plane; i. e. crystals are easily cleaved by outer forces (e.g. cut with a razor blade) along this plane. The disintegration of the crystals is therefore a combination of two effects: abrupt change in angle  $\alpha$  and shear by large angular changes acting in the direction of the cleavage plane. Table 7.1 shows that the lattice changes of the other parameters are in the range of (<5%) usually observed in SCSC transformations.

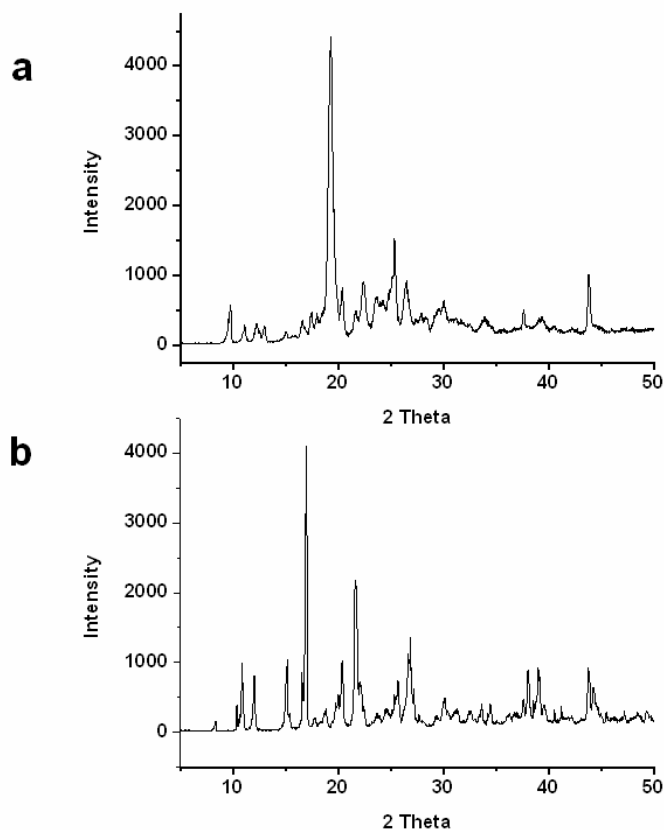


**Figure 7.5:** Powder diffractograms of a) 100% converted (P-1, triclinic) as-dimerized dimer of 2(bpe):2(res) b) 100% converted recrystallized dimer (monoclinic,  $P2_1/n$ )

---

## 7.5. POLYMORPHISM

By powder diffraction experiments (cf. Figure 7.5) it was checked that the small crystallites at higher conversions retained the triclinic structure. A simulated dimer structure (coordinates of the dimer of the 42% converted structure with an occupancy of 100%) matched the diffractogram of the 100% converted as-dimerized dimer (P-1 triclinic phase) quantitatively. However when this dimer is recrystallized, another polymorph is produced (monoclinic P2<sub>1</sub>/n phase). The lattice parameters of the stable monoclinic polymorph are included in the Table 7.1.

## 7.6. ANALYSIS OF SUBSTITUTIONAL MIXED CRYSTALS

In homogeneous topochemical reactions the overall volume change may be low, where-as the change in given lattice parameters can be larger since in certain directions Van der waals contacts are transformed into chemical bonds. This is the case here, where the volume change from monomer to dimer is less than 2%, but the percent change in cell parameters totals over 10%, particularly affecting the angle  $\alpha$  (larger than 18%) inducing a drastic effect on the quality of the crystal and causing it to shatter at latter stages of conversion. Therefore, we deal here with the interesting case of a truly homogeneous, but *non-ideal* SCSC reaction.

Prior to photodimerization the two substrate (bpe) molecules are related by a center of symmetry and held on top of each other by two resorcinol molecules. The center of symmetry is preserved even after the dimerization. As can be seen in Figure 7.6, (2(bpe):2(res) crystal structure projection prior to dimerization and after 42% conversion) the position and overall shape of the monomer in a mixed crystal are quite similar to the position and overall shape of the pair of monomer before irradiation. The major difference is observed in the reacting part of the species, i. e. the reacting atoms and their neighbours where the distance between the C=C of the two adjacent molecules has increased from 3.651 Å to 3.714 Å. Notably, the pyridyl ring occupies the same lattice

position whether it is attached to a double or a cyclobutane ring (cf. Figure 7.2) as defined in chapter 5. In crystals at intermediate conversion, non-planarity is observed for the bonds from the sp<sup>2</sup> carbon linking the pyridyl ring to the cyclobutane ring or double bond. This deformation is listed as pyridyl ring tilt; two tilts, each to the two different pyridyl rings which is listed in Table 7.2. As anticipated the deformation is less severe for unreacted species at lower conversion, which also increases along with the conversion.

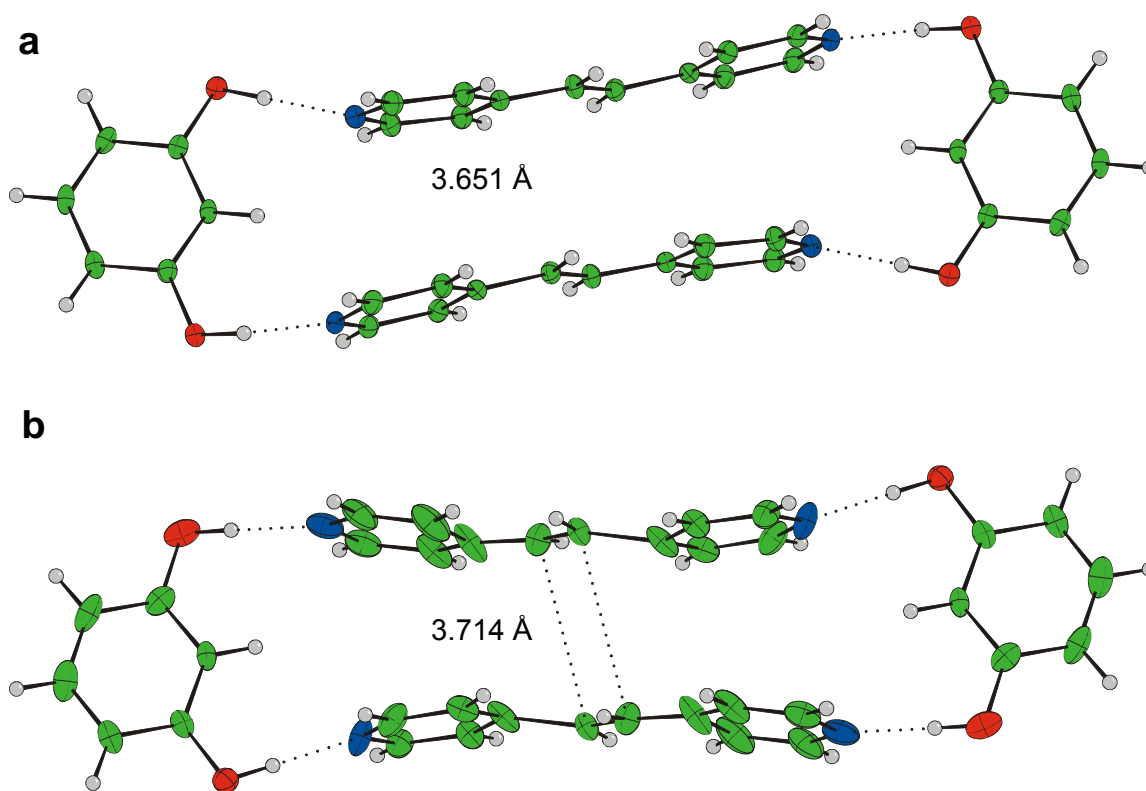


**Figure 7.6:** Crystal structure projection of monomer molecules a) prior to photodimerization, triclinic P-1 space group<sup>[151]</sup>b) 6 hrs irradiated (42% converted) crystal structure with triclinic P-1 space group, from the structure atoms belonging to the dimer have been removed for clarity

For clarity, the most stable recrystallized dimer is compared with the 42% converted as-dimerized dimer (cf. Figure 6.12, chapter 6). Two types of conformational changes are observed in the pyridyl rings with respect to the bonds connecting them to

the reacting centers: slight rotation along the axis of the bond and the tilt. Upon continuous evolution to the dimer lattice, the pyridyl groups reorient themselves to be increasingly planar with the  $sp^3$  bond off the cyclobutane ring as it increases in concentration. This can be visualized by the decrease in tilt angle with increasing conversion. This can be visualized by the decrease in tilt angle with increasing conversion (cf. Table 7.2). In the stable dimer however, the tilt angle is almost zero, as the pyridyl rings moved apart from each other and acquired stable conformation upon recrystallization. This illustrates that the crystal structures of the mixed crystals are a compromise between conformations of the monomer and dimer, respectively, with the anticipated results that the species of higher concentration in the lattice is rather less deformed.

Mixed Crystal Irradiated by	Tilt Angles		Structure
	A	B	
385 nm Xe lamp 14%	Monomer:	2.87°	7.57°
	Dimer:	24.76°	39.61°
385 nm Xe lamp 42%	Monomer:	9.53°	14.86°
	Dimer :	20.62°	30.12°

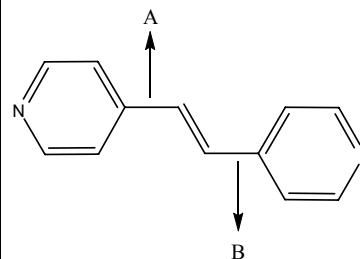


**Table 7.2:** Tilt angles for the substitutional mixed crystals of the 2(res):2(bpe) molecular adduct at different conversions.

## 7.7. CONCLUSIONS

Structural changes in the crystal of 2(bpe):2(res) (Scheme 6.1) obtained by tail irradiation, are in detail monitored by means of X-ray diffraction. Though the conversion was homogeneous, it occurred via a *non-ideal* SCSC transformation due to significant

---

changes in the lattice dimension at initial stages of the reaction. After the large variation in the cell constants in the beginning of the reaction, the structural changes observed in the latter stage were gradual as usual, where the monomer molecules moved from the position adopted in the crystal prior to the irradiation, whereas dimers moved towards the position occupied at the final stage. The dimer molecules moved gradually and fluently to the position occupied in the pure as-dimerized dimer crystal that is rather unstable and thus, turned into a stable conformation only after recrystallization. The cell parameters of monomer, and the mixed crystals, were compared to that of the stable polymorph of the dimer (Table 7.1).

# CHAPTER 8

## SUMMARY

Commonly, organic reactions are carried out in suitable solvents. Recently, however, it was discovered that organic reactions also proceed in the solid-state and in many cases even more efficiently and selectively than in solution. Though it has long been assumed that molecules in crystals do not move freely, the crystal lattice in fact tolerates slow motion of the molecules on their lattice sites. Reactions in the solid-state, however, occur with minimal atomic or molecular movement. Deeper understanding of packing effects will expand control and design of organic solid-state reactions. The combination of organic solid-state chemistry, single crystal X-ray analysis and high resolution solid-state NMR have revealed valuable insights into the reaction mechanism that govern the resulting structures. In particular, the topotactic nature of the reaction intermediates and products as well as structural changes on molecular level occurring in [2+2] photodimerizations under tail irradiation have been demonstrated.

Dynamic hydrogen bonding has been observed in both  $\alpha$ -*trans*-cinnamic and  $\alpha$ -truxillic acid obtained by [2+2] photodimerization. Unexpected peak splittings previously observed in the corresponding  $^{13}\text{C}$ -CPMAS spectra of  $\alpha$ -truxillic acid were so far attributed to packing effects. But, based on high-temperature X-ray analysis and solid-state NMR analysis it has been *clearly* shown that these splittings rather resulting from the *transient asymmetry* of the hydrogen bonds in the crystal that temporarily destroy the photodimer's center of symmetry. The presence of dynamic disorder in the carboxyl moiety of truxillic acid is mainly caused by the rapid oscillations of protons across O-H $\cdots$ O bonds accompanied by interconversion between the carbonyl C=O and hydroxyl C-



O(H) bond. Thus at a given time each truxillic acid molecule possesses two different carbonyl groups, e.g. original carboxylic acid (COOH) and carboxylate anion (COO<sup>-</sup>). Indeed, removing the hydrogen-bonds by esterification of  $\alpha$ -truxillic acid restores a centrosymmetric structure.

Also this work focuses onto selective control or modification of reactant compounds allowing for rationally designed crystal lattices. Topochemical alignment of olefins in the solid-state has been achieved using the molecular recognition of hydroxyl-pyridine (O-H $\cdots$ N) supramolecular heterosynthons. The deliberate use of a variety of resorcinols containing different hydrogen bonding active functional groups has allowed determining the robust nature of the given approach. In order to gain a better understanding of supramolecular synthons, their preferred geometries, possibly competitive hydrogen bond strengths as well as their recognition patterns, a series of mono- and dipyridines were co-crystallized with different substituted resorcinols. Hence, the organizational consequences of hydrogen bonds in the O-H $\cdots$ N heterosynthon in the presence of other competitive hydrogen bonding functional groups were explored. As major causes for the deviation of the design principle in case of O-H $\cdots$ N heterosynthons, intramolecular hydrogen bond formation due to the presence of hydrogen bonding active functional groups in close proximity, C-O bond flexibility of resorcinol and steric hindrance were identified.

Additionally, the crystal engineered [2+2] photodimerization of *trans*-1,2-bis(4-pyridyl)ethylene (bpe) yielding tetrakis(4-pyridyl) cyclobutane in the solid-state has been studied. Multi-component co-crystallization experiments were performed to probe the molecular specificity of resorcinol-pyridine recognition. Therefore, bpe and resorcinol were co-crystallized in the presence of *trans*-1,2-bis(4-pyridyl)ethane (bpet), where a new metastable polymorph (monoclinic P2<sub>1</sub>/n phase) of 2(bpe):2(res) in the chain form was obtained. This has been formed under kinetic control in the presence of the nuclei of 2(bpet):2(res) monomer complex (P2<sub>1</sub>/n phase, chain form). In contrast to the stable ring form, which is suitable for photodimerization, the new polymorph is comprised of hydrogen bonded chains. In addition, it has been clearly demonstrated that the crystal-

---

engineered monomer complex of 2(bpe):2(res) (ring form) yielded *two* different dimer polymorphs upon photoirradiation, that are the metastable as-dimerized dimer (triclinic, P-1 phase) and the stable recrystallized dimer (monoclinic, P2<sub>1</sub>/n phase). Moreover, upon removal of the template (e.g. resorcinol) from the latter compound, pure tetrakis(4-pyridyl) cyclobutane containing a distorted cyclobutane ring was found.

Also, while monitoring the structural changes in the crystals of 2(bpe):2(res) by means of X-ray diffraction it has been observed that the respective dimerization proceeds via *non-ideal* single-crystal-to-single-crystal transformation due to significant changes in the lattice dimension at the initial stages of the reaction. Thus, all examples presented here demonstrate the advantage of the joint approach of solid-state NMR and single crystal X-ray analysis at comparable temperatures, which has allowed determining the dynamic features of structural motifs in the organic solid-state.

# References

- [1] V. Ramamurthy, K. Venkatesan; *Chem. Rev.*, **1987**, 87, 433-481.
- [2] H. Stobbe, F. K. Steinberger; *Chem. Ber.*, **1922**, 55, 2225-2245.
- [3] R. B. Woodward, R. Hoffmann; The conservation of orbital symmetry, Verlag Chemie, Weinheim, **1970**.
- [4] A. Mustafa; *Chem. Rev.*, **1952**, 51, 1-23.
- [5] G. M. J. Schmidt; *Pure Appl. Chem.*, **1971**, 27, 647-678.
- [6] M. D. Cohen, G. M. J. Schmidt; *J. Chem. Soc.*, **1964**, 1996-2000.
- [7] G. M. J. Schmidt; *J. Chem. Soc.*, **1964**, 2000-2013.
- [8] G. M. J. Schmidt; *J. Chem. Soc.*, **1964**, 2014-2021.
- [9] J. Bregman, K. Osaki, G. M. J. Schmidt, F. I. Sonntag; *J. Chem. Soc.*, **1964**, 2021-2030.
- [10] K. Tanaka, F. Toda; *Chem. Rev.*, **2000**, 100, 1025-1074.
- [11] J. M. McBride, B. E. Segmuller, M. D. Hollingsworth, D. E. Mills, B. A. Weber; *Science*, **1986**, 234, 830-835.
- [12] M. D. Hollingsworth; *Science*, **2002**, 295, 2410-2413.
- [13] F. Tomislav, L. R. MacGillivray; *Z. Kristallogr.*, **2005**, 220, 351-363.
- [14] G. J. Desiraju; *Angew. Chem. Int. Ed.*, **1995**, 34, 2311-2327.
- [15] G. Kaupp; *Angew. Chem. Int. Ed.*, **1992**, 31, 592-595.
- [16] G. Kaupp; *Angew. Chem. Int. Ed.*, **1992**, 104, 606-609.
- [17] D. M. Samantha, J. A. Mathew, J. Brunel, G. Andrew, P. Hollins, J. Mascetti; *Spectrochim. Acta.*, **2000**, A56, 2423-2430.
- [18] P. N. Prasad, J. Swiatkewicz, G. Eisenhardt; *Appl. Spectrosc. Rev.*, **1982**, 18, 59-103.
- [19] T. N. Misra, P. N. Prasad; *Chem. Phys. Lett.*, **1982**, 85, 381-386.
- [20] P. N. Prasad; Studies in Organic Chemistry, Vol. 32, Organic Solid State Chemistry (Ed. DesiRaju) P. 117-150. Elsevier Science Publishing Company Inc. **1987**.
- [21] K. Honda, F. Nakanishi, N. Feeder; *J. Am. Chem. Soc.*, **1999**, 121, 8246-8250.
- [22] N. Feeder, K. Honda; *Mol. Cryst. Liq. Cryst.*, **1998**, 313, 327-334.
- [23] I. Turowska-Tyrk; *Acta. Cryst.*, **2003**, B59, 670-675.

## References

---

- [24] M. Khan, G. Brunklaus, V. Enkelmann, H. W. Spiess; *J. Am. Chem. Soc.*, **2008**, 130, 1741-1748.
- [25] S. G. Stitchell, K. D. M. Harris, A. E. Aliev; *Structural Chemistry*, **1994**, 5, 327-333.
- [26] K. D. M. Harris, J. M. Thomas; *J. Solid State Chem.*, **1991**, 94, 197-205.
- [27] A. Hilgeroth, G. Hempel, U. Baumeister, D. Reichert; *Solid Stat. Nucl. Magn. Reson.*, **1999**, 13, 231-243.
- [28] M. Bertmer, R. C. Nieuwendaal, A. B. Barnes, S. E. Hayes; *J. Phys. Chem. B*, **2006**, 110, 6270-6273.
- [29] V. Enkelmann, G. Wegner, K. Novak; *J. Am. Chem. Soc.*, **1993**, 115, 10390-10391.
- [30] K. Novak, V. Enkelmann, G. Wegner; *Angew. Chem., Int. Ed.*, **1993**, 32, 1614-1616.
- [31] W. Kohler, K. Novak, V. Enkelmann; *J. Chem. Phys.*, **1994**, 101, 10474-10480.
- [32] V. Enkelmann; *Mol. Cryst. Liq. Cryst.*, **1998**, 313, 15-23.
- [33] V. Buchholz, V. Enkelmann; *Mol. Cryst. Liq. Cryst.*, **1998**, 313, 309-314.
- [34] V. Buchholz, V. Enkelmann; *Mol. Cryst. Liq. Cryst.*, **2001**, 356, 315-325.
- [35] S. P. Brown, H. W. Spiess; *Chem. Rev.*, **2001**, 101, 4125-4155.
- [36] R. K. Harris; *Solid State Sci.*, **2004**, 6, 1025-1037.
- [37] K. D. M. Harris, E. Y. Cheung; *Chem. Soc. Rev.*, **2004**, 33, 526-538.
- [38] S. P. Brown; *Prog. Nucl. Magn. Reson. Spectrosc.*, **2007**, 50, 199-251.
- [39] T. L. Threlfall; *The Analyst*, **1995**, 120, 2435-2460.
- [40] R. K. Harris; *The Analyst*, **2006**, 131, 351-373.
- [41] C. N. Tam, J. A. Cowan, A. J. Schultz, V. G. Young, Jr, F. R. Trouw, A. G. Sykes; *J. Phys. Chem. B*, **2003**, 107, 7601-7606.
- [42] F. Toda; *Acc. Chem. Res.*, **1995**, 28, 480-486.
- [43] P. J. Thomas, S. E. Morsi; J. P. Desvergne; *Adv. Phys. Org. Chem.*, **1977**, 15, 63-151.
- [44] F. Toda; Organic Solid State Reactions, *Top. Curr. Chem.*, **2005**, 254,
- [45] V. Enkelmann; *Adv. Polym. Sci.*, **1984**, 63, 92-136.
- [46] G. Wegner; *Pure Appl. Chem.*, **1977**, 49, 443-454.
- [47] J. Bernstein, S. G. Bernard, M. Rejto; *J. Am. Chem. Soc.*, **1980**, 102, 323-328.

## References

---

- [48] M. Hasegawa; *Pure Appl. Chem.*, **1986**, 58, 1179-1188.
- [49] D. A. Dixon, A. Komornicki; *J. Phys. Chem.*, **1990**, 94, 5630-5636.
- [50] I. Fleming, A. Barbero, D. Walter; *Chem. Rev.*, **1997**, 97, 2063-2192.
- [51] D. Rabinovich, Z. Shakked; *Acta Cryst. B*, **1977**, B33, 809-815.
- [52] T. Obata, T. Shimo, M. Yasutake, T. shinmyozu, M. Kawaminam, R. Yoshida, K. Somekawa; *Tetrahedron*, **2001**, 57, 1531-1541.
- [53] R. H. Baughman; *J. Polym. Sci., Polym. Phys.*, **1974**, 12, 1511-1535.
- [54] R. H. Baughman, K. C. Yee; *J. Polym. Sci., Macromol. Rev.*, **1978**, 13, 219-239.
- [55] J. M. Thomas, J. O. Williams; *Progress in Solid-State Chemistry*; H. Reiss and J. O. McCaldin, Ed., Pergamon Press: New York, **1971**, p.119.
- [56] F. L. Hirshfeld, G. M. J. Schmidt; *J. Polym. Sci. A*, **1964**, 2, 2181-2190.
- [57] M. A. Fernandes, D. C. Levendis; *Acta Crystallogr. Sect. B*, **2004**, 60, 315-324.
- [58] V. Enkelmann, R. J. Leyrer, G. Wegner; *Makromol. Chem.*, **1979**, 180, 1787-1795.
- [59] M. Hasegawa; *Organic Solid State Chemistry*, G. R. Desiraju; Ed., Elsevier, New York, **1987**, p. 153.
- [60] M. D. Cohen; *Angew. Chem.*, **1975**, 87, 439-447.
- [61] M. D. Cohen; *Angew. Chem., Int. Ed. Engl.*, **1975**, 14, 386-393.
- [62] G. Wegner; *Makromol. Chem., Suppl.*, **1984**, 185, 347-357.
- [63] H. G. Braun, G. Wegner; *Mol. Cryst. Liq. Cryst.*, **1983**, 96, 121-139.
- [64] H. G. Braun, G. Wegner; *Makromol. Chem.*, **1983**, 184, 1103-1119.
- [65] M. Hasegawa; *Chem. Rev.*, **1983**, 83, 507-518.
- [66] R. R. Chance, G. N. Patel ; *J. Polym. Sci., Polym Phys. Ed.*, **1978**, 16, 859-881.
- [67] H. Nakanishi, W. Jones, J. M. Thomas, M. B. Hursthouse, M. Motevalli; *J. Phys. Chem.*, **1981**, 85, 3636-3642.
- [68] I. Turowska-tyrk; *Chem. Eur. J.*, **2001**, 7, 3401-3405.
- [69] Y. Ohashi, K. Yanagi, T. Kurihara, Y. Sasada, Y. Ohge; *J. Am. Chem. Soc.*, **1982**, 104, 6353-6359.
- [70] V. Enkelmann, G. Wegner; *J. Am. Chem. Soc.*, **1993**, 115, 10390-10391.
- [71] G. Wegner, E. W. Fischer, A. Munoz-Escalona; *Makromol. Chem. Suppl.*, **1975**, 1, 521-558.
- [72] K. Cheng, B. Foxman; *J. Am. Chem. Soc.*, **1977**, 99, 8102-8103.

## References

---

- [73] M. Hasegawa; *Adv. Polym. Sci.*, Springer-Verlag: Berlin, **1982**, p. 1.
- [74] S. K. Kearsley, G. R. Desiraju; *Proc. Roy. Soc. London A*, **1985**, 397, 157-181.
- [75] J. M. Thomas; *Phil. Trans. Roy. Soc. London A*, **1974**, 277, 251-286.
- [76] F. K. Lotgering; *J. Inorg. Nucl. Chem.*, **1959**, 9, 113-123.
- [77] K. Lonsdale, E. Nave, J. Stephens; *Phil. Trans. Roy. Soc. London A*, **1966**, 261, 1-31.
- [78] G. Kaupp; *Curr. Opin. Solid State Mat. Sci.*, **2002**, 6, 131-138.
- [79] H. C. Chang, R. Papovitz-Biro, M. Lahav, L. Leiserowitz; *J. Am. Chem. Soc.*, **1982**, 104, 614-616.
- [80] S. Ohba, H. Hosomi, Y. Ito; *J. Am. Chem. Soc.*, **2001**, 123, 6349-6352.
- [81] S. Kawata, Y. Kawata; *Chem. Rev.*, **2000**, 100, 1777-1788.
- [82] M. Irie; *Chem. Rev.*, **2000**, 100, 1685-1716.
- [83] R. H. Baughman, K. C. Yee; *J. Polym. Sci., Macromol. Rev.*, **1978**, 13, 219-239.
- [84] M Hasegawa, K. Kinbara, Y. Adegawa, K. Saigo; *J. Am. Chem. Soc.*, **1993**, 115, 3820-3821.
- [85] M. D. Choen; *Tetrahedron*, **1987**, 43, 1211-1224.
- [86] G. Kaupp, J. Schmeyers, M. Kato, K. Tanaka, N. Harada, F. Toda; *J. Phys. Org. Chem.*, **2001**, 14, 444-452.
- [87] N. Feeder, K. Honda; *Mol. Cryst. Liq. Cryst.*, **1998**, 313, 327-334.
- [88] S. D. M. Atkinson, M. J. Almond, G. A. Bowmaker, M. G. B. Drew, E. J. Feltham, P. Hollins, S. L. Jenkins, K. S. Wiltshire; *J. Chem. Soc., Perkin Trans. 2*, **2002**, 1533-1537.
- [89] R. H. Baughman; *J. Appl. Phys.*, **1971**, 42, 4579-4584.
- [90] D. Y. Curtin, I. C. Paul, E. N. Duesler, T. W. Lewis, B. J. Mann, W. I. Shiau ; *Mol. Cryst. Liq. Cryst.*, **1979**, 50, 25-42.
- [91] K. Novak, V. Enkelmann, G. Wegner; *Angew. Chem., Int. Ed.*, **1993**, **32**, 1614-1616.
- [92] V. Buchholz, V. Enkelmann; *Mol. Cryst. Liq. Cryst.*, **1998**, 313, 309-314.
- [93] W. Kohler, K. Novak, V. Enkelmann, *J. Chem. Phys.*, **1994**, 101, 10474-10480.
- [94] G. R. Desiraju; *Crystal Engineering, The Design of Organic Solids*, Elsevier, Amsterdam, **1989**.

## References

---

- [95] G. R. Desiraju; *Chem. Commun.*, **1997**, 1475-1482.
- [96] G. R. Desiraju; *The Crystal as a Supramolecular Entity*, ed. Perspectives in Supramolecular Chemistry 2, Wiley, Chichester, **1996**.
- [97] D. Braga; *Chem. Commun.*, **2003**, 2751-2754.
- [98] J. M. Lehn; *Angew. Chem., Int. Ed. Engl.*, **1988**, 27, 89-112.
- [99] J. D. Dunitz, *Pure Appl. Chem.*, **1991**, 63, 177-185.
- [100] D. Y. Curtin, I. C. Paul; *Chem Rev.*, **1981**, 81, 525-541.
- [101] G. R. Desiraju; in *Comprehensive Supramolecular Chemistry*, Vol. 6, (Ed. D. D. MacNicol, F. Toda, R. Bishop), Pergamon, Oxford, **1996**.
- [102] J. M. Lehn; *Supramolecular Chemistry: Concepts and Perspectives*; VCH, Weinheim, **1995**.
- [103] G. R. Desiraju; *Nature*, **2001**, 412, 397-400.
- [104] G. A. Jeffrey; *An Introduction to Hydrogen Bonding*, Oxford Univ. Press, New York, **1997**.
- [105] G. R. Desiraju; *Angew. Chem., Int. Ed.*, **2007**, 46, 8342-8356.
- [106] M. C. Etter; *Chem. Mater.*, **1994**, 6, 1090-1092.
- [107] M. C. Etter; *Acc. Chem. Res.*, **1990**, 23, 120-126.
- [108] J. MacDonald, G. M. Whitesides; *Chem. Rev.*, **1994**, 94, 2383-2420.
- [109] F. Lara-Ochoa, G. Espinosa-Perez; *Supramol. Chem.*, **2007**, 19, 553-557.
- [110] J. A. Bis, P. Vishweshwar, D. Weyna, M. J. Zaworotko; *Mol. Pharmaceutics*, **2007**, 4, 401-416.
- [111] J. F. Remenar, S. L. Morissette, M. L. Peterson, B. Moulton, J. M. Macphee, H. R. Guzman, O. Almarsson; *J. Am. Chem. Soc.*, **2003**, 125, 8456-8457.
- [112] E. M. Purcell, H.C. Torrey, R. V. Pound; *Phys. Rev.*, **1946**, 69, 37-38.
- [113] F. Bloch, W. W. Hansen, M. E. Packard; *Phys. Rev.*, **1946**, 70, 474-485.
- [114] E. R. Andrew, A. Bradbury, R. G. Eades; *Nature*, **1958**, 182, 1659.
- [115] H. W. Spiess; *Angew. Chem., Int. Ed.*, **2007**, 46, 2-7.
- [116] T. Gullion, J. Schaefer; *J. Magn. Reson.*, **1989**, 81, 196-200.
- [117] A. Abragam; *The Principles of Nuclear Magnetic Resonance*, Oxford Univ. Press, Oxford (**1961**)
- [118] Melinda Duer; *Introduction to Solid-State NMR Spectroscopy*; Wiley-VCH, **2004**.

## References

---

- [119] M. Levitt; *Spin Dynamics*, Wiley, Weinheim, **2001**.
- [120] C. P. Slichter; *Principles of Magnetic Resonance*, Springer-Verlag, Berlin, **1996**.
- [121] I. J. Lowe; *Phys. Rev. Lett.*, **1959**, 2, 285-287
- [122] A. Pines, W. K. Rhim, J. S. Waugh; *J. Magn. Reson.*, **1971**, 6, 457-465.
- [123] A. Pines, M. G. Gibby, J. S. Waugh; *J. Chem. Phys.*, **1973**, 59, 569-590.
- [124] G. Metz, X. Wu, S. O. Smith; *J. Magn. Reson.*, A, **1994**, 110, 219-227.
- [125] J. Davaasambuu, G. Busse, S. Techert; *J. Phys. Chem. A*, **2006**, 110, 3261-3265.
- [126] S. L. Jenkins, M. J. Almond, S. D. M. Atkinson, M. G. B. Drew, P. Hollins, J. L. Mortimore, M. J. Tobin; *J. Mol. Struct.*, **2006**, 786, 220-226.
- [127] I. Abdelmoty, V. Buchholz, L. Di, V. Enkelmann, G. Wegner, B. M. Foxman; *Cryst. Growth Design*, **2005**, 17, 2210-2217.
- [128] W. Schilf, B. Kamiński, A. Szady-Chełmieniecka, E. Grech; *J. Mol. Struct.*, **2004**, 700, 105-108.
- [129] R. Gobetto, C. Nervi, M. R. Chierotti, D. Braga, L. Maini, R. K. Harris, P. Hodgkinson; *Chem. Eur. J.*, **2005**, 11, 7461-7471.
- [130] S. Li, S. Zheng, Y. Su, H. Zhang, L. Chen, J. Yang, C. Ye, F. Deng; *J. Am. Chem. Soc.*, **2007**, 129, 11161-11171.
- [131] C. A. Fyfe, D. H. Brouwer, A. R. Lewis, L. A. Villaescusa, R. E. Morris; *J. Am. Chem. Soc.*, **2002**, 124, 7770-7778.
- [132] L. Leiserowitz; *Acta Cryst.*, **1976**, B32, 775-802.
- [133] T. Miyazawa, K. S. Pitzer; *J. Am. Chem. Soc.*, **1959**, 81, 74-79.
- [134] F. Graf, R. Meyer, R. R. Ernst; *J. Chem. Phys.*, **1981**, 75, 2914-2918.
- [135] B. H. Meier, F. Graf, R. R. Ernst; *J. Chem. Phys.*, **1982**, 76, 767-774.
- [136] A. Stoeckli, A. Furrer; *Physica, B*, **1986**, 136, 161-164.
- [137] J. L. Skinner, H. P. Trommsdorff; *J. Chem. Phys.*, **1988**, 89, 897-907.
- [138] A. J. Horsewill, A. J. Aibout; *J. Phys. Condens. Matter*, **1989**, 1, 9609-9622.
- [139] N. Kalsbeek, K. Schaumberg, S. Larsen; *J. Mol. Str.*, **1993**, 299, 155-170.
- [140] L. Mayas, M. Plato, J. Winscom, K. Mobius; *Mol. Phys.*, **1978**, 36, 753-764.
- [141] C. R. Morkombe, K. Zilm; *J. Magn. Reson.*, **2003**, 162, 479-486.
- [142] I. Furo, N. Hedin; *J. Magn. Reson.*, **2001**, 152, 214-216.
- [143] A. D. Becke; *Phys. Rev.* **1988**, A38, 3098-3100.



## References

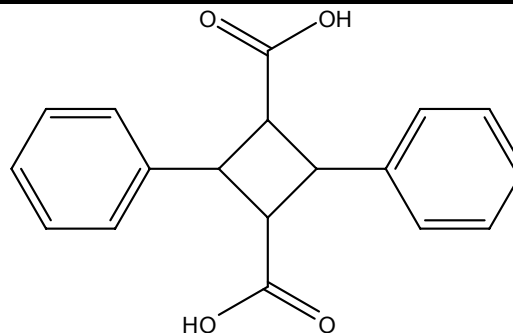
- [144] R. Krishnan, J. S. Binkley, R. Seger, J. A. Pople; *J. Chem. Phys.* **1980**, *72*, 650-654.
- [145] Gaussian 98, Revision A.7, Frisch, M. J. *et al*, *Gaussian, Inc.*, Pittsburgh PA, **1998**.
- [146] J. Xiao, M. Yang, J. W. Lauher, F. W. Flower; *Angew. Chem. Int. Ed.*, **2000**, *39*, 2132-2135.
- [147] C. V. K. Sharma, K. Panneerselvam, L. Shimoni, H. Katz, H. L. Karell, G. R. Desiraju; *Chem. Mater.*, **1994**, *6*, 1282-1292.
- [148] K. S. Feldman, R. F. Campbell; *J. Org. Chem.*, **1995**, *60*, 1924-1925.
- [149] L. R. MacGillivray; *J. Org. Chem.*, **2008**, *73*, 3311-3317.
- [150] L. R. MacGillivray, G. S. Papaefstathiou, T. Friscic, T. D. Hamilton, D. K. Bucar, Q. Chu, D. B. Varshney, I. G. Georgiev; *Acc. Chem. Res.*, **2008**, *41*, 280-291.
- [151] L. R. MacGillivray, J. L. Reid, J. Ripmeester; *J. Am. Chem. Soc.*, **2000**, *122*, 7817-7818.
- [152] D. K. Bucar, R. F. Henry, X. Lou, R. W. Durest, T. B. Borchardt, L. R. MacGillivray, G. Geoff, Z. Zhang; *Molecular Pharmaceutics*, **2007**, *4*, 339-346.
- [153] R. D. B. Walsh, M. W. Bradner, S. Fleishman, L. A. Morales, B. Moulton, N. Rodrigues-Hornedo, M. J. Zaworotko; *Chem. Commun.*, **2003**, *2*, 186-188.
- [154] V. R. Vangla, R. Mondal, C. K. Broder, J. A. K. Howard, G. R. Desiraju; *Cryst. Growth Des.*, **2005**, *5(1)*, 99-104.
- [155] C. B. Aakeroy, A. M. Beatty, B. A. Helfrich; *J. Am. Chem. Soc.*, **2002**, *124*, 14425-14432.
- [156] P. Vishweshwar, A. Nangia, V. M. Lynch; *Cryst. Growth Des.*, **2003**, *3*, 783-790.
- [157] G. S. Papaefstathiou, L. R. MacGillivray; *Org. Lett.*, **2001**, *3*, 3835-3838.
- [158] T. L. Nguyen, A. Scott, B. Dinkelmeyer, F. W. Fowler, J. W. Lauher; *N. J. Chem.*, **1998**, 129-135.
- [159] F. Bickelhaupt; *Pure & Applied Chem.*, **1990**, *62*, 373-382.
- [160] S. Z. Vatsadze, V. N. Nuriev, A. V. Chernikov, N. V. Zyk; *Russ. Chem. Bull.*, **2002**, *51*, 1957-1958.
- [161] J. Vansant, G. Smets, J. P. Declercq, G. Germain, M. Van Meerssche; *J. Org. Chem.*, **1980**, *45*, 1557-1565.

## References

---

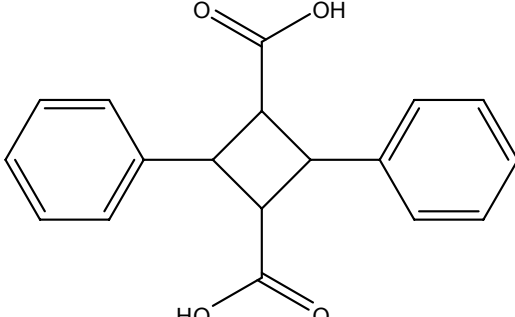
- [162] J. M. Robertson; *Proceedings of Royal Soc. London. Series A, Mathematical and Physical Sci.*, Vol. 1, **1936**, 157, 79-99.
- [163] G.E. Bacon, R. J. Jude; *Z. Kristallogr.*, **1973**, 19, 138.
- [164] K. Masuda, S. Tabata, H. Kono, Y. Sakata, T. Hayase, E. Yonemochi, K. Tarada; *Int. J. Pahrma.*, **2006**, 318, 146-153.
- [165] M. Leskes, P. K. Madhu, S. Vega; *J. Chem. Phys.*, **2008**, 128, 052309/1-052309/11.
- [166] A. Lesage, D. Sakellariou, S. Hediger, B. Elena, P. Charmont, S. Steuernagel, L. Emsley; *J. Magn. Reson.*, **2003**, 163, 105-113.
- [167] S. P. Brown, A. Lesage, B. Elena, L. Emsley; *J. Am. Chem. Soc.*, **2004**, 126, 13230-13231.
- [168] I. Bolz, C. Moon, V. Enkelmann, G. Brunklaus, S. Spange; *J. Org. Chem.*, **2008**, 73, 4783-4793.
- [169] G. R. Desiraju; *Nat. Mater.*, **2002**, 1, 77-79.
- [170] S. Ahn, K. D. M. Harris, B. M. Kariuki, D. M. S. Zin; *J. Sol. State. Chem.*, **2001**, 156, 10-15.
- [171] D.Henseler, G. Hohlneicher; *J. Phys. Chem. A.*, **1998**, 102, 10828-10833.
- [172] R. Abu-Eittah, M. M. Hamed, A. A. Mohamed; *Int. J. Quantum Chem.*, **1991**, 211-226.
- [173] J. Schmidt, A. Hoffmann, H. W. Spiess, D. Sebastiani; *J. Phys. Chem. B* **2006**, 110, 23204-23210.
- [174] P. G. Jones; *Chem. Soc. Rev.*, **1984**, 13, 157-172.
- [175] M. M. Woolfson; *An Introduction to X-ray Crystallography*, Cambridge University Press, Cambridge, **1970**.
- [176] W. H. Bragg; *Nature*, **1908**, 77, 270-271.
- [177] A. R. West; *Solid-State Chemistry and its Applications*, **1984**, Wiley, New York.

**Crystal structure details of  $\alpha$ -truxillic acid measured at 120 K**

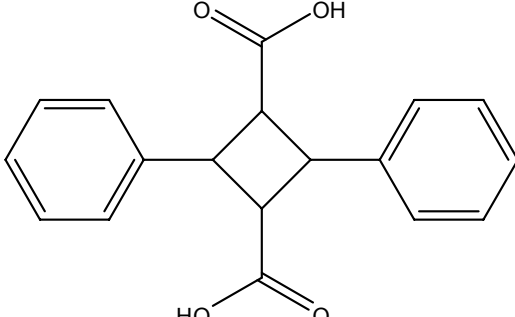


<b>a (Å)</b>	5.5993(4)	<b><math>\alpha</math> °</b>	90
<b>b (Å)</b>	18.2465(7)	<b><math>\beta</math> °</b>	106.3615(13)
<b>c (Å)</b>	7.6646(5)	<b><math>\gamma</math> °</b>	90
<b>V (Å<sup>3</sup>)</b>	751.362	<b>Z</b>	4
<b>D<sub>x</sub>g (cm<sup>3</sup>)</b>	-	<b>Space group</b>	P 2 <sub>1</sub> /n (14 iii)
<b>Atom</b>	<b>x/a</b>	<b>y/b</b>	<b>z/c</b>
<b>O1</b>	-0.5604	0.007	-0.2862
<b>O2</b>	-0.2283	0.0387	-0.379
<b>H1</b>	-0.6434	-0.0027	-0.4035
<b>H21</b>	-0.2953	0.04	0.0101
<b>H31</b>	0.1174	0.0763	-0.1106
<b>H51</b>	0.4218	0.1631	0.0457
<b>H61</b>	0.5517	0.2479	0.282
<b>H71</b>	0.351	0.2551	0.5115
<b>H81</b>	0.0232	0.1736	0.5082
<b>H91</b>	-0.108	0.0883	0.2736
<b>C1</b>	-0.3266	0.0261	-0.2574
<b>C2</b>	-0.1857	0.0244	-0.059
<b>C3</b>	0.0819	0.0557	-0.0054
<b>C4</b>	0.1457	0.1154	0.1365
<b>C5</b>	0.3401	0.1643	0.1403
<b>C6</b>	0.4166	0.2152	0.2801
<b>C7</b>	0.2983	0.2194	0.4164
<b>C8</b>	0.1049	0.1716	0.4137
<b>C9</b>	0.0279	0.1204	0.2739
<b>O1</b>	0.5604	-0.007	0.2862
<b>O2</b>	0.2283	-0.0387	0.379
<b>H1</b>	0.6434	0.0027	0.4035
<b>H21</b>	0.2953	-0.04	-0.0101
<b>H31</b>	-0.1174	-0.0763	0.1106
<b>H51</b>	-0.4218	-0.1631	-0.0457
<b>H61</b>	-0.5517	-0.2479	-0.282
<b>H71</b>	-0.351	-0.2551	-0.5115
<b>H81</b>	-0.0232	-0.1736	-0.5082
<b>H91</b>	0.108	-0.0883	-0.2736
<b>C1</b>	0.3266	-0.0261	0.2574
<b>C2</b>	0.1857	-0.0244	0.059
<b>C3</b>	-0.0819	-0.0557	0.0054
<b>C4</b>	-0.1457	-0.1154	-0.1365
<b>C5</b>	-0.3401	-0.1643	-0.1403
<b>C6</b>	-0.4166	-0.2152	-0.2801
<b>C7</b>	-0.2983	-0.2194	-0.4164
<b>C8</b>	-0.1049	-0.1716	-0.4137
<b>C9</b>	-0.0279	-0.1204	-0.2739

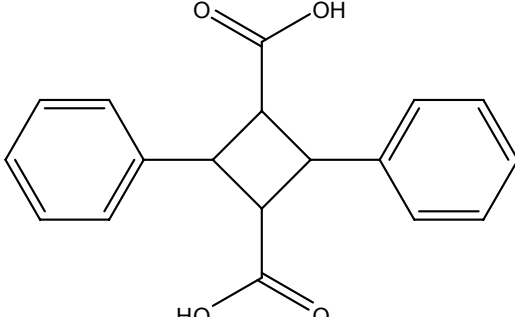
## Appendix

<b>Crystal structure details of <math>\alpha</math>-truxillic acid measured at 150 K</b>			
<b>a (Å)</b>	5.6073(5)	<b><math>\alpha</math> °</b>	90
<b>b (Å)</b>	18.2810(8)	<b><math>\beta</math> °</b>	106.2288(15)
<b>c (Å)</b>	7.6481(6)	<b><math>\gamma</math> °</b>	90
<b>V (Å<sup>3</sup>)</b>	752.745	<b>Z</b>	4
<b>D<sub>x</sub>g (cm<sup>3</sup>)</b>	-	<b>Space group</b>	P 2 <sub>1</sub> /n (14 iii)
Atoms	x/a	y/b	z/c
<b>O1</b>	0.2721	0.0386	0.6209
<b>O2</b>	-0.0587	0.0065	0.7139
<b>H1</b>	-0.1403	-0.0041	0.5915
<b>C4</b>	0.6439	0.1155	1.1351
<b>C1</b>	0.1735	0.0259	0.7429
<b>C3</b>	0.5818	0.0556	0.9937
<b>C9</b>	0.5274	0.1206	1.2729
<b>C2</b>	0.3148	0.0242	0.9412
<b>C5</b>	0.8376	0.1641	1.1386
<b>C6</b>	0.9136	0.2147	1.2777
<b>C7</b>	0.7964	0.219	1.414
<b>C8</b>	0.6035	0.1715	1.4117
<b>H31</b>	0.6266	0.0699	0.8877
<b>H91</b>	0.3941	0.0884	1.2718
<b>H21</b>	0.2196	0.0438	1.0152
<b>H51</b>	0.917	0.1625	1.044
<b>H61</b>	1.0471	0.247	1.2793
<b>H71</b>	0.8487	0.254	1.5088
<b>H81</b>	0.5227	0.1739	1.5055
<b>O1</b>	0.7279	-0.0386	1.3791
<b>O2</b>	1.0587	-0.0065	1.2861
<b>H1</b>	1.1403	0.0041	1.4085
<b>C4</b>	0.3561	-0.1155	0.8649
<b>C1</b>	0.8265	-0.0259	1.2571
<b>C3</b>	0.4182	-0.0556	1.0063
<b>C9</b>	0.4726	-0.1206	0.7271
<b>C2</b>	0.6852	-0.0242	1.0588
<b>C5</b>	0.1624	-0.1641	0.8614
<b>C6</b>	0.0864	-0.2147	0.7223
<b>C7</b>	0.2036	-0.219	0.586
<b>C8</b>	0.3965	-0.1715	0.5883
<b>H31</b>	0.3734	-0.0699	1.1123
<b>H91</b>	0.6059	-0.0884	0.7282
<b>H21</b>	0.7804	-0.0438	0.9848
<b>H51</b>	0.083	-0.1625	0.956
<b>H61</b>	-0.0471	-0.247	0.7207
<b>H71</b>	0.1513	-0.254	0.4912
<b>H81</b>	0.4773	-0.1739	0.4945

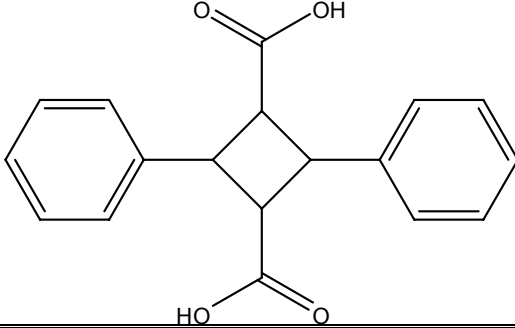
## Appendix

Crystal structure details of $\alpha$ -truxillic acid measured at 190 K			
<b>a (Å)</b>	5.2753(4)	<b><math>\alpha</math> °</b>	90
<b>b (Å)</b>	18.3713(6)	<b><math>\beta</math> °</b>	106.2270(15)
<b>c (Å)</b>	7.6644(5)	<b><math>\gamma</math> °</b>	90
<b>V (Å<sup>3</sup>)</b>	760.891	<b>Z</b>	4
<b>D<sub>x</sub>g (cm<sup>3</sup>)</b>	-	<b>Space group</b>	P 2 <sub>1</sub> /n (14 iii)
Atoms	x/a	y/b	z/c
O2	0.7281	0.0382	1.3786
O1	1.0571	0.0055	1.2864
H1	1.1312	-0.0021	1.4096
C4	0.3581	0.1154	0.8666
C1	0.8261	0.0252	1.2569
C3	0.42	0.0554	1.0067
C2	0.6849	0.0239	1.0591
C5	0.4747	0.1206	0.729
C9	0.166	0.1638	0.8634
C8	0.091	0.2147	0.7257
C6	0.3993	0.1717	0.5909
C7	0.208	0.2188	0.5898
H31	0.3756	0.0694	1.1127
H21	0.7799	0.0432	0.9852
H51	0.6062	0.0881	0.7292
H91	0.0869	0.1621	0.9578
H81	-0.042	0.2468	0.7242
H61	0.4798	0.1744	0.4973
H71	0.1573	0.254	0.496
O2	0.2719	-0.0382	0.6214
O1	-0.0571	-0.0055	0.7136
H1	-0.1312	0.0021	0.5904
C4	0.6419	-0.1154	1.1334
C1	0.1739	-0.0252	0.7431
C3	0.58	-0.0554	0.9933
C2	0.3151	-0.0239	0.9409
C5	0.5253	-0.1206	1.271
C9	0.834	-0.1638	1.1366
C8	0.909	-0.2147	1.2743
C6	0.6007	-0.1717	1.4091
C7	0.792	-0.2188	1.4102
H31	0.6244	-0.0694	0.8873
H21	0.2201	-0.0432	1.0148
H51	0.3938	-0.0881	1.2708
H91	0.9131	-0.1621	1.0422
H81	1.042	-0.2468	1.2758
H61	0.5202	-0.1744	1.5027
H71	0.8427	-0.254	1.504

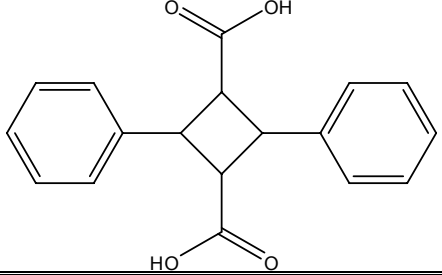
## Appendix

Crystal structure details of $\alpha$ -truxillic acid measured at 250 K			
<b>a (Å)</b>	5.6455(4)	<b><math>\alpha</math> °</b>	90
<b>b (Å)</b>	18.4798(6)	<b><math>\beta</math> °</b>	106.2997(14)
<b>c (Å)</b>	7.6562(5)	<b><math>\gamma</math> °</b>	90
<b>V (Å<sup>3</sup>)</b>	766.649	<b>Z</b>	4
<b>D<sub>x</sub>g (cm<sup>3</sup>)</b>	-	<b>Space group</b>	P 2 <sub>1</sub> /n (14 iii)
Atoms	x/a	y/b	z/c
O1	0.2719	0.0378	0.6221
O2	-0.0541	0.0043	0.7132
H1	-0.1465	-0.0036	0.5887
C3	0.5783	0.055	0.9923
C4	0.6383	0.1152	1.131
C1	0.1741	0.0244	0.7438
C2	0.3149	0.0234	0.9404
C9	0.5233	0.1207	1.2681
C5	0.8277	0.1635	1.1328
C6	0.901	0.2145	1.2692
C8	0.5969	0.1719	1.4043
C7	0.7855	0.2188	1.4047
H31	0.6216	0.0688	0.8857
H21	0.2204	0.0426	1.0145
H91	0.3924	0.0884	1.2682
H51	0.9052	0.1619	1.0376
H61	1.0337	0.2463	1.2703
H81	0.517	0.1746	1.498
H71	0.8357	0.2543	1.4974
O1	0.7281	-0.0378	1.3779
O2	1.0541	-0.0043	1.2868
H1	1.1465	0.0036	1.4113
C3	0.4217	-0.055	1.0077
C4	0.3617	-0.1152	0.869
C1	0.8259	-0.0244	1.2562
C2	0.6851	-0.0234	1.0596
C9	0.4767	-0.1207	0.7319
C5	0.1723	-0.1635	0.8672
C6	0.099	-0.2145	0.7308
C8	0.4031	-0.1719	0.5957
C7	0.2145	-0.2188	0.5953
H31	0.3784	-0.0688	1.1143
H21	0.7796	-0.0426	0.9855
H91	0.6076	-0.0884	0.7318
H51	0.0948	-0.1619	0.9624
H61	-0.0337	-0.2463	0.7297
H81	0.483	-0.1746	0.502
H71	0.1643	-0.2543	0.5026

Appendix

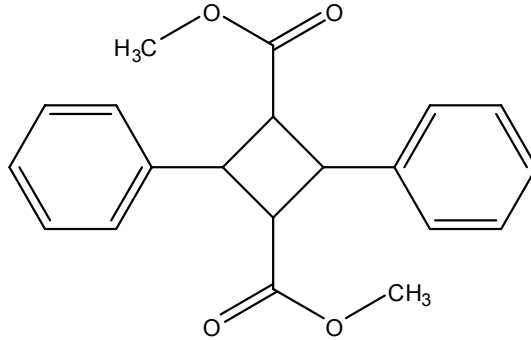
Crystal structure details of $\alpha$ -truxillic acid measured at 298 K			
<b>a (Å)</b>	5.6760(4)	<b><math>\alpha</math> °</b>	90
<b>b (Å)</b>	18.6088(6)	<b><math>\beta</math> °</b>	106.2673(12)
<b>c (Å)</b>	7.6826(5)	<b><math>\gamma</math> °</b>	90
<b>V (Å<sup>3</sup>)</b>	778.977	<b>Z</b>	4
<b>D<sub>x</sub>g (cm<sup>3</sup>)</b>	-	<b>Space group</b>	P 2 <sub>1</sub> /n (14 iii)
<b>Atoms</b>	<b>x/a</b>	<b>y/b</b>	<b>z/c</b>
<b>O1</b>	0.2712	0.0375	0.1222
<b>O2</b>	-0.0524	0.0035	0.213
<b>C3</b>	0.5759	0.0548	0.4923
<b>C4</b>	0.6356	0.1152	0.6291
<b>C1</b>	0.1734	0.0238	0.2435
<b>C2</b>	0.3156	0.0227	0.4404
<b>C9</b>	0.5221	0.1209	0.7663
<b>C5</b>	0.8216	0.1633	0.6296
<b>C6</b>	0.8938	0.2144	0.765
<b>C7</b>	0.7791	0.2186	0.8996
<b>C8</b>	0.5929	0.1719	0.9004
<b>H31</b>	0.6174	0.0685	0.3855
<b>H21</b>	0.222	0.0418	0.5144
<b>H91</b>	0.3932	0.0884	0.7668
<b>H51</b>	0.8987	0.1611	0.5348
<b>H61</b>	1.0244	0.2463	0.765
<b>H71</b>	0.8283	0.2544	0.9907
<b>H81</b>	0.5146	0.1747	0.9945
<b>H1</b>	-0.1237	-0.0123	0.082
<b>O1</b>	0.7288	-0.0375	0.8778
<b>O2</b>	1.0524	-0.0035	0.787
<b>C3</b>	0.4241	-0.0548	0.5077
<b>C4</b>	0.3644	-0.1152	0.3709
<b>C1</b>	0.8266	-0.0238	0.7565
<b>C2</b>	0.6844	-0.0227	0.5596
<b>C9</b>	0.4779	-0.1209	0.2337
<b>C5</b>	0.1784	-0.1633	0.3704
<b>C6</b>	0.1062	-0.2144	0.235
<b>C7</b>	0.2209	-0.2186	0.1004
<b>C8</b>	0.4071	-0.1719	0.0996
<b>H31</b>	0.3826	-0.0685	0.6145
<b>H21</b>	0.778	-0.0418	0.4856
<b>H91</b>	0.6068	-0.0884	0.2332
<b>H51</b>	0.1013	-0.1611	0.4652
<b>H61</b>	-0.0244	-0.2463	0.235
<b>H71</b>	0.1717	-0.2544	0.0093
<b>H81</b>	0.4854	-0.1747	0.0055
<b>H1</b>	1.1237	0.0123	0.918

Appendix

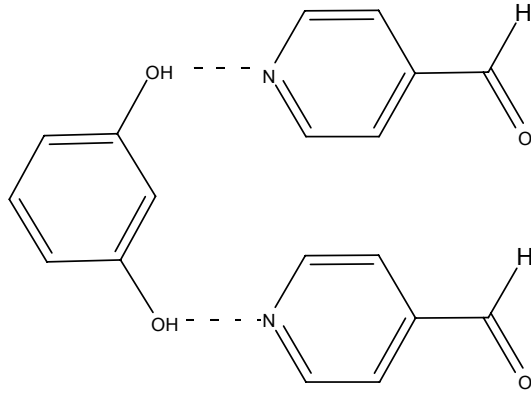
Crystal structure details of $\alpha$ -truxillic acid measured at 350 K			
<b>a (Å)</b>	5.7087(4)	<b><math>\alpha</math> °</b>	90
<b>b (Å)</b>	18.7650(7)	<b><math>\beta</math> °</b>	106.2886(13)
<b>c (Å)</b>	7.6914(5)	<b><math>\gamma</math> °</b>	90
<b>V (Å<sup>3</sup>)</b>	790.868	<b>Z</b>	4
<b>D<sub>x</sub>g (cm<sup>3</sup>)</b>	-	<b>Space group</b>	P 2 <sub>1</sub> /n (14 iii)
Atoms	x/a	y/b	z/c
O1	-0.2289	0.0371	0.1236
O2	-0.549	0.0027	0.2134
C1	-0.3271	0.0225	0.243
C2	-0.1836	0.022	0.4398
C3	0.0742	0.0545	0.4913
C4	0.132	0.1148	0.627
C5	0.315	0.1623	0.6263
C6	0.3852	0.2142	0.759
C7	0.2712	0.2178	0.8957
C8	0.0876	0.1722	0.8954
C9	0.0198	0.1206	0.7631
H21	-0.2761	0.041	0.5142
H31	0.1151	0.0678	0.3842
H51	0.3911	0.1603	0.5313
H61	0.5138	0.2462	0.7581
H71	0.3183	0.2541	0.9848
H81	0.011	0.175	0.99
H91	-0.1062	0.0878	0.7651
H2	-0.6177	-0.0104	0.0985
H1	-0.3146	0.0259	0.0036
O1	0.2289	-0.0371	0.8764
O2	0.549	-0.0027	0.7866
C1	0.3271	-0.0225	0.757
C2	0.1836	-0.022	0.5602
C3	-0.0742	-0.0545	0.5087
C4	-0.132	-0.1148	0.373
C5	-0.315	-0.1623	0.3737
C6	-0.3852	-0.2142	0.241
C7	-0.2712	-0.2178	0.1043
C8	-0.0876	-0.1722	0.1046
C9	-0.0198	-0.1206	0.2369
H21	0.2761	-0.041	0.4858
H31	-0.1151	-0.0678	0.6158
H51	-0.3911	-0.1603	0.4687
H61	-0.5138	-0.2462	0.2419
H71	-0.3183	-0.2541	0.0152
H81	-0.011	-0.175	0.01
H91	0.1062	-0.0878	0.2349
H2	0.6177	0.0104	0.9015
H1	0.3146	-0.0259	0.9964



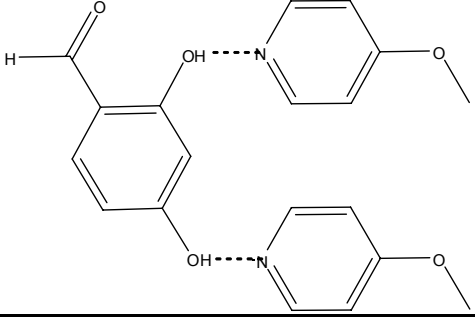
## Appendix

<b>Crystal structure details of methyl ester of <math>\alpha</math>-truxillic acid (dimethyl 2, 4-diphenylcyclobutane-1, 3-dicarboxylate) measured at 120 K</b>			
<b>a (Å)</b>	10.8535(5)	<b><math>\alpha</math> °</b>	90
<b>b (Å)</b>	5.5169(4)	<b><math>\beta</math> °</b>	100.4140(12)
<b>c (Å)</b>	13.9943(5)	<b><math>\gamma</math> °</b>	90
<b>V (Å<sup>3</sup>)</b>	824.123	<b>Z</b>	4
<b>D<sub>x</sub>g (cm<sup>3</sup>)</b>	-	<b>Space group</b>	P 2 <sub>1</sub> /n (14 iii)
Atoms	x/a	y/b	z/c
<b>O1</b>	0.3431	0.9531	0.1513
<b>O2</b>	0.3393	0.5778	0.0876
<b>C1</b>	0.3846	0.805	0.1022
<b>C2</b>	0.4893	0.8453	0.0468
<b>C3</b>	0.5567	1.092	0.0644
<b>C4</b>	0.6965	1.0914	0.1011
<b>C5</b>	0.7736	0.9102	0.0755
<b>C6</b>	0.903	0.92	0.1065
<b>C7</b>	0.9565	1.1123	0.1623
<b>C8</b>	0.8813	1.2934	0.1894
<b>C9</b>	0.7519	1.283	0.1588
<b>C10</b>	0.2281	0.5229	0.1277
<b>H21</b>	0.5474	0.7149	0.0553
<b>H31</b>	0.5157	1.1918	0.1043
<b>H51</b>	0.7376	0.7788	0.0363
<b>H61</b>	0.9545	0.7928	0.0903
<b>H71</b>	1.045	1.1218	0.1813
<b>H81</b>	0.9179	1.4237	0.229
<b>H91</b>	0.7005	1.4075	0.1774
<b>H101</b>	0.2037	0.3596	0.1133
<b>H102</b>	0.2456	0.5453	0.1961
<b>H103</b>	0.1622	0.6283	0.0998
<b>O1</b>	0.6569	1.0469	-0.1513
<b>O2</b>	0.6607	1.4222	-0.0876
<b>C1</b>	0.6154	1.195	-0.1022
<b>C2</b>	0.5107	1.1547	-0.0468
<b>C3</b>	0.4433	0.908	-0.0644
<b>C4</b>	0.3035	0.9086	-0.1011
<b>C5</b>	0.2264	1.0898	-0.0755
<b>C6</b>	0.097	1.08	-0.1065
<b>C7</b>	0.0435	0.8877	-0.1623
<b>C8</b>	0.1187	0.7066	-0.1894
<b>C9</b>	0.2481	0.717	-0.1588
<b>C10</b>	0.7719	1.4771	-0.1277
<b>H21</b>	0.4526	1.2851	-0.0553
<b>H31</b>	0.4843	0.8082	-0.1043
<b>H51</b>	0.2624	1.2212	-0.0363
<b>H61</b>	0.0455	1.2072	-0.0903
<b>H71</b>	-0.045	0.8782	-0.1813
<b>H81</b>	0.0821	0.5763	-0.229
<b>H91</b>	0.2995	0.5925	-0.1774
<b>H101</b>	0.7963	1.6404	-0.1133
<b>H102</b>	0.7544	1.4547	-0.1961
<b>H103</b>	0.8378	1.3717	-0.0998

## Appendix

<b>Crystal structure details of 1:1 co-crystals of resorcinol and 4-pyridinecarboxaldehyde measured at 120 K</b>			
<b>a (Å)</b>	9.2329(5)	<b>α °</b>	96.0275(13)
<b>b (Å)</b>	9.7253(5)	<b>β °</b>	92.7815(12)
<b>c (Å)</b>	10.0502(6)	<b>γ °</b>	116.3330(14)
<b>V (Å<sup>3</sup>)</b>	799.725	<b>Z</b>	2
<b>D<sub>x</sub>g (cm<sup>3</sup>)</b>	1.347	<b>Space group</b>	P-1 (2)
Atoms	x/a	y/b	z/c
O19	0.571	-0.1021	0.2184
O20	0.8874	0.2966	-0.0419
C5	0.8553	0.3643	0.1871
C3	0.7271	0.0955	0.0851
C4	0.8241	0.2515	0.0765
C2	0.663	0.0515	0.2054
C1	0.6919	0.1641	0.3158
C6	0.7879	0.3186	0.304
H1	0.6456	0.1339	0.3978
H3	0.7046	0.0192	0.008
H5	0.9235	0.4714	0.1808
H6	0.8071	0.3949	0.3803
H20	0.8671	0.2076	-0.1119
H19	0.5739	-0.1645	0.1468
C8	0.3741	0.2809	-0.0055
C11	0.3397	0.4659	0.2083
C7	0.4353	0.39	0.2285
C10	0.2623	0.4476	0.0799
O21	0.3836	0.5938	0.4323
C9	0.2831	0.3535	-0.0235
N23	0.4486	0.2986	0.1191
C12	0.3212	0.5672	0.321
H8	0.3864	0.2184	-0.0804
H9	0.2282	0.3418	-0.1106
H10	0.1965	0.4992	0.065
H7	0.4894	0.4022	0.3161
H12	0.252	0.6153	0.3055
N24	0.1543	-0.0532	0.2267
C17	0.2572	-0.0188	0.3358
C14	0.1696	0.1545	0.4459
C15	0.0615	0.1218	0.3319
C16	0.057	0.0186	0.2263
C18	0.2705	0.0838	0.4476
O22	0.1004	0.3081	0.5982
C13	0.1783	0.2587	0.5702
H13	0.2665	0.288	0.6391
H18	0.3482	0.1047	0.5234
H17	0.3276	-0.0674	0.3399
H16	-0.0206	-0.0032	0.1502
H15	-0.0085	0.1708	0.3282

## Appendix

<b>Crystal structure details of 1:1 co-crystals of 2,4-dihydroxy benzaldehyde and 4-methoxy pyridine measured at 120 K</b>			
<b>a (Å)</b>	7.8008(4)	<b><math>\alpha</math> °</b>	100.3489(12)
<b>b (Å)</b>	9.1219(5)	<b><math>\beta</math> °</b>	103.1973(13)
<b>c (Å)</b>	13.3305(6)	<b><math>\gamma</math> °</b>	102.8656(13)
<b>V (Å<sup>3</sup>)</b>	873.4(1)	<b>Z</b>	2
<b>D<sub>xg</sub> (cm<sup>3</sup>)</b>	1.355	<b>Space group</b>	P-1 (2)
Atoms	x/a	y/b	z/c
O14	0.4009	0.8059	0.0989
O15	-0.1867	0.7868	0.1553
O17	0.6535	0.9254	0.4106
C1	0.3726	0.8604	0.2741
C5	0.1032	0.7938	0.1231
C6	0.2932	0.8192	0.1636
C3	0.0763	0.8613	0.3021
C2	0.2608	0.8824	0.3412
C4	-0.0038	0.8131	0.1918
C18	0.5689	0.8835	0.3166
H18	0.6414	0.8648	0.2689
H5	0.0483	0.7634	0.0477
H3	0.0039	0.8783	0.3501
H2	0.3144	0.9144	0.4168
H15	-0.2099	0.7595	0.0796
H14	0.315	0.7896	0.0222
O13	1.0912	0.3968	0.4178
N7	0.7838	0.2568	0.1038
C9	0.8613	0.1999	0.274
C10	0.9875	0.3442	0.3165
C8	0.7641	0.1623	0.1683
C11	1.0104	0.4441	0.2495
C12	0.907	0.3967	0.1467
C26	1.0566	0.3026	0.4909
H26A	1.1398	0.3527	0.56
H26B	0.9329	0.2911	0.4945
H26C	1.0734	0.2023	0.4674
H9	0.8428	0.1292	0.3184
H11	1.0982	0.544	0.2762
H12	0.9249	0.4703	0.1042
H8	0.6794	0.0608	0.1419
O16	0.5545	0.4096	0.3808
N25	0.3101	0.3068	0.058
C19	0.4696	0.3681	0.2765
C20	0.3471	0.2256	0.221
C21	0.275	0.2015	0.1136
C24	0.5185	0.2981	0.4426
C23	0.4245	0.4454	0.1134
C22	0.5079	0.48	0.2198
H24A	0.5893	0.3431	0.5152
H24B	0.3905	0.2714	0.4387
H24C	0.5513	0.2064	0.4159
H22	0.5908	0.5802	0.256
H20	0.3157	0.1466	0.2576
H21	0.1943	0.1003	0.078
H23	0.4528	0.5264	0.0778

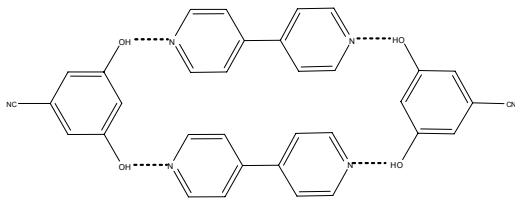
## Appendix

<b>Crystal structure details of 1:1 co-crystals of 4-bromoresorcinol and 4-methoxy pyridine measured at 120 K</b>			
<b>a (Å)</b>	7.5371(4)	<b><math>\alpha</math> °</b>	72.4005(13)
<b>b (Å)</b>	13.7054(6)	<b><math>\beta</math> °</b>	84.9185(12)
<b>c (Å)</b>	17.9557(7)	<b><math>\gamma</math> °</b>	87.5733(12)
<b>V (Å<sup>3</sup>)</b>	1763.7(1)	<b>Z</b>	4
<b>D<sub>x</sub>g (cm<sup>3</sup>)</b>	1.534	<b>Space group</b>	P-1 (2)
Atoms	x/a	y/b	z/c
Br1	-0.0232	0.4067	0.794
C1	0.4243	0.1545	0.8447
C3	0.1123	0.2008	0.831
C4	0.1585	0.3033	0.8121
O1	0.5553	0.082	0.863
O2	-0.061	0.1765	0.8344
C2	0.247	0.1266	0.8467
C5	0.3349	0.3308	0.8081
C6	0.4694	0.2563	0.8245
H1	0.5016	0.0175	0.8798
H2	-0.076	0.1052	0.8463
H21	0.2185	0.0564	0.8588
H51	0.3642	0.4012	0.7941
H61	0.5904	0.2749	0.8217
N11	0.4305	-0.1124	0.9048
O11	0.3268	-0.4218	0.9641
C13	0.3643	-0.3219	0.9414
C11	0.4727	-0.1646	0.854
C12	0.4464	-0.2684	0.869
C14	0.3176	-0.2684	0.9955
C15	0.3534	-0.1655	0.9747
H111	0.5246	-0.1278	0.8038
H121	0.4826	-0.3021	0.831
H141	0.2608	-0.3027	1.0453
H151	0.3228	-0.1303	1.0122
C16	0.3835	-0.4797	0.9114
H161	0.3494	-0.5491	0.9341
H162	0.5093	-0.4766	0.9014
H163	0.3291	-0.4515	0.8637
N21	-0.0764	-0.0324	0.8802
O21	-0.1354	-0.3471	0.9485
C23	-0.1119	-0.245	0.9227
C21	-0.0249	-0.0867	0.8311
C22	-0.0406	-0.1914	0.8483
C24	-0.1658	-0.1907	0.9752
C25	-0.1458	-0.087	0.9514
H211	0.0261	-0.0501	0.7806
H221	-0.0035	-0.2259	0.8109
H241	-0.2153	-0.2254	1.0264
H251	-0.1837	-0.0508	0.9876
C26	-0.0887	-0.404	0.8942
H261	-0.1107	-0.4745	0.9192
H262	0.034	-0.3951	0.8769
H263	-0.1583	-0.3799	0.8505

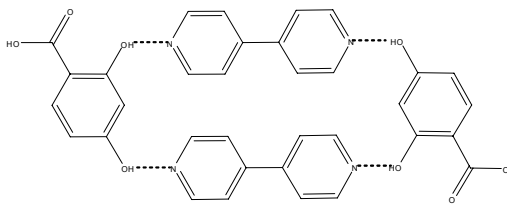
## Appendix

<b>Crystal structure details of 1:1 co-crystals of 4-bromoresorcinol and 4,4-bipyridine measured at 120 K</b>			
<b>a (Å)</b>	9.3362(4)	<b><math>\alpha</math> °</b>	77.3777(14)
<b>b (Å)</b>	9.3402(4)	<b><math>\beta</math> °</b>	78.7914(13)
<b>c (Å)</b>	9.5468(4)	<b><math>\gamma</math> °</b>	63.2167(14)
<b>V (Å<sup>3</sup>)</b>	720.8(5)	<b>Z</b>	2
<b>D<sub>x</sub>g (cm<sup>3</sup>)</b>	1.590	<b>Space group</b>	P-1 (2)
Atoms	x/a	y/b	z/c
N11	0.4562	0.6777	0.0676
N12	0.147	0.3517	0.7338
C13	0.335	0.5463	0.3291
C16	0.2684	0.4781	0.4721
C11	0.2983	0.7392	0.112
C12	0.2333	0.6757	0.2427
C14	0.5016	0.4809	0.2875
C15	0.5554	0.5513	0.1526
C17	0.1303	0.5761	0.5475
C18	0.0749	0.5091	0.6783
C19	0.284	0.2584	0.6583
C20	0.3463	0.3153	0.5283
H111	0.2263	0.8294	0.0536
H121	0.1203	0.7227	0.2709
H141	0.5754	0.3934	0.3466
H151	0.668	0.5064	0.1222
H171	0.0739	0.6877	0.511
H181	-0.0186	0.5784	0.7316
H191	0.3401	0.1474	0.6967
H201	0.4407	0.2453	0.4764
Br1	1.136	0.9169	-0.2484
C1	0.652	0.8661	-0.1992
C3	0.8891	0.8212	-0.0966
C4	0.9383	0.898	-0.2272
O1	0.5145	0.8485	-0.1914
O2	0.9844	0.7632	0.0115
C2	0.746	0.8083	-0.0851
C5	0.8442	0.9576	-0.34
C6	0.7027	0.9423	-0.3296
H1	0.5094	0.7774	-0.107
H2	0.9251	0.7343	0.0905
H21	0.7099	0.759	0.0038
H51	0.8782	1.0117	-0.4268
H61	0.6408	0.9819	-0.4091

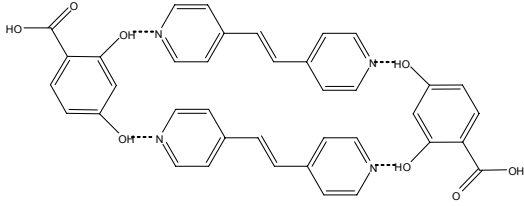
## Appendix

<p><b>Crystal structure details of 1:1 co-crystals of 3,5-dihydroxy benzonitrile and 4,4'-bipyridine measured at 120 K</b></p>			
<b>a (Å)</b>	7.5823(4)	<b><math>\alpha</math> °</b>	90
<b>b (Å)</b>	15.0926(6)	<b><math>\beta</math> °</b>	105.1219(13)
<b>c (Å)</b>	12.8462(5)	<b><math>\gamma</math> °</b>	90
<b>V (Å<sup>3</sup>)</b>	1419.2(1)	<b>Z</b>	4
<b>D<sub>x</sub>g (cm<sup>3</sup>)</b>	1.363	<b>Space group</b>	P2 <sub>1</sub> /n (14 iii)
Atoms	x/a	y/b	z/c
<b>O22</b>	0.3661	-0.1211	0.2956
<b>O21</b>	0.2184	0.1879	0.3123
<b>C19</b>	0.8208	0.0858	0.4841
<b>C1</b>	0.2852	0.0327	0.302
<b>C4</b>	0.637	0.0664	0.4209
<b>C6</b>	0.5145	0.1366	0.3967
<b>C5</b>	0.3363	0.1188	0.3359
<b>N20</b>	0.9663	0.103	0.5329
<b>C3</b>	0.5906	-0.0197	0.3872
<b>C2</b>	0.4112	-0.0362	0.3272
<b>H6</b>	0.5528	0.1953	0.4215
<b>H1</b>	0.1625	0.021	0.2606
<b>H3</b>	0.6809	-0.0657	0.4052
<b>N18</b>	-0.0008	0.1285	-0.1764
<b>N12</b>	0.8889	0.1519	0.1782
<b>C9</b>	0.5371	0.1438	0.0386
<b>C13</b>	0.351	0.1399	-0.0353
<b>C15</b>	0.2014	0.111	0.0002
<b>C14</b>	0.3177	0.1637	-0.1437
<b>C8</b>	0.596	0.0823	0.1212
<b>C11</b>	0.8324	0.2111	0.0986
<b>C10</b>	0.6607	0.209	0.0272
<b>C17</b>	0.0309	0.1062	-0.0723
<b>C7</b>	0.771	0.0885	0.1878
<b>C16</b>	0.142	0.1572	-0.2103
<b>H7</b>	0.8065	0.0445	0.2434
<b>H11</b>	0.9129	0.258	0.0898
<b>H10</b>	0.6258	0.252	-0.0295
<b>H8</b>	0.5151	0.0362	0.1316
<b>H14</b>	0.4164	0.1842	-0.1714
<b>H15</b>	0.2179	0.0949	0.0744
<b>H17</b>	-0.0676	0.0857	-0.0445
<b>H16</b>	0.1257	0.1747	-0.2841

## Appendix

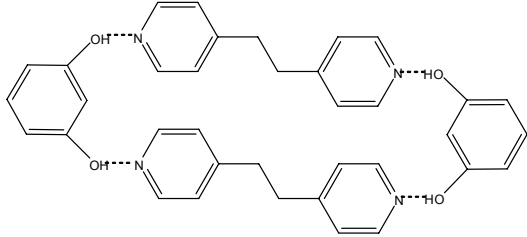
Crystal structure details of 1:1 co-crystals of 2,4-dihydroxy benzoic acid and 4,4'-bipyridine measured at 120 K			
<b>a</b> (Å)	6.5498(4)	<b>α</b> °	90
<b>b</b> (Å)	10.6928(6)	<b>β</b> °	96.9583(12)
<b>c</b> (Å)	20.6074(5)	<b>γ</b> °	90
<b>V</b> (Å <sup>3</sup> )	1432.6(1)	<b>Z</b>	4
<b>D<sub>xg</sub></b> (cm <sup>3</sup> )	1.439	<b>Space group</b>	P2 <sub>1</sub> /c (14 ii)
Atoms	x/a	y/b	z/c
O3	0.3651	0.261	0.2273
C1	0.7065	0.2314	0.1559
C3	0.9227	0.0889	0.1052
C6	0.5912	0.1306	0.1758
C7	0.4145	0.1545	0.2122
O1	0.6645	0.3513	0.17
O2	1.082	0.0628	0.0708
O4	0.3162	0.0536	0.2273
C2	0.8718	0.2098	0.1205
C4	0.8086	-0.0125	0.124
C5	0.6461	0.0093	0.1595
H1	0.5571	0.3464	0.1897
H2	1.1458	0.1398	0.0576
H4	0.2105	0.0869	0.2473
H21	0.9493	0.2782	0.1072
H41	0.8427	-0.0953	0.1124
H51	0.57	-0.0592	0.1734
N11	0.0065	0.1028	0.292
N12	-0.7088	0.2575	0.5108
C13	-0.2874	0.1618	0.3745
C16	-0.4345	0.1946	0.4216
C11	-0.0966	0.0125	0.3191
C12	-0.2438	0.0381	0.3609
C14	-0.1843	0.2558	0.3443
C15	-0.039	0.2217	0.304
C17	-0.6087	0.1215	0.4271
C18	-0.7409	0.1577	0.4718
C19	-0.5398	0.3254	0.5056
C20	-0.3997	0.2977	0.4619
H111	-0.0686	-0.0721	0.3092
H121	-0.3132	-0.028	0.38
H141	-0.2143	0.3413	0.3513
H151	0.0318	0.2858	0.2839
H171	-0.6353	0.0488	0.4009
H181	-0.8606	0.1088	0.4748
H191	-0.5139	0.3956	0.5336
H201	-0.2827	0.3491	0.4593

## Appendix

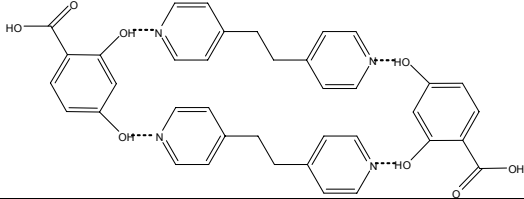
Crystal structure details of 1:1 co-crystals of 2,4-dihydroxy benzoic acid and 1,2-di-(4-pyridyl)ethylene measured at 120 K			
<b>a (Å)</b>	7.8326(5)	<b><math>\alpha</math> °</b>	90
<b>b (Å)</b>	10.3211(4)	<b><math>\beta</math> °</b>	90
<b>c (Å)</b>	39.4774(5)	<b><math>\gamma</math> °</b>	90
<b>V (Å<sup>3</sup>)</b>	3191.4(5)	<b>Z</b>	8
<b>D<sub>x</sub>g (cm<sup>3</sup>)</b>	1.400	<b>Space group</b>	pcab (61)
Atoms	x/a	y/b	z/c
O3	0.2303	0.4975	0.0662
C1	-0.0699	0.3671	0.1732
C3	0.1101	0.4787	0.1336
C4	0.0479	0.4015	0.1071
C7	0.1162	0.4175	0.0727
O1	-0.1295	0.3425	0.2046
O2	0.2303	0.5697	0.1279
O4	0.0502	0.3422	0.0497
C2	0.0513	0.4617	0.1667
C5	-0.0777	0.3096	0.1144
C6	-0.1374	0.2927	0.1469
H1	-0.0696	0.3794	0.2232
H2	0.2557	0.5632	0.1044
H4	0.0899	0.3697	0.0261
H21	0.0937	0.5146	0.1845
H51	-0.1222	0.2581	0.0965
H61	-0.2243	0.231	0.1515
N11	0.0364	0.4171	0.2601
N12	0.3358	0.3855	0.4898
C13	0.1456	0.3921	0.3273
C18	0.2199	0.4201	0.4236
C11	0.143	0.3224	0.2694
C12	0.2011	0.3072	0.3022
C14	0.0361	0.4912	0.3175
C15	-0.0144	0.5	0.2841
C16	0.2063	0.3739	0.362
C17	0.156	0.4409	0.3891
C19	0.3431	0.3276	0.4315
C20	0.3965	0.3135	0.4645
C21	0.2191	0.4756	0.4827
C22	0.1581	0.4955	0.4502
H111	0.1799	0.2629	0.2525
H121	0.2782	0.2393	0.3078
H141	-0.0035	0.5522	0.3338
H151	-0.0892	0.5683	0.2777
H161	0.2894	0.3084	0.3657
H171	0.0726	0.5064	0.3857
H191	0.3893	0.2743	0.4141
H201	0.4801	0.2497	0.4696
H211	0.1767	0.5279	0.5006
H221	0.0742	0.5599	0.4459



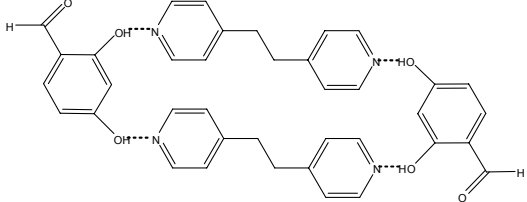
## Appendix

Crystal structure details of 1:1 co-crystals of Resorcinol and 1,2-di-(4-pyridyl)ethane 2(bpet): 2(res) measured at 120 K			
<b>a</b> (Å)	10.1927(5)	<b><math>\alpha</math></b> °	90
<b>b</b> (Å)	7.1610(4)	<b><math>\beta</math></b> °	94.1624(12)
<b>c</b> (Å)	20.2559(9)	<b><math>\gamma</math></b> °	90
<b>V</b> (Å <sup>3</sup> )	1474.6(3)	<b>Z</b>	4
<b>D<sub>xg</sub></b> (cm <sup>3</sup> )	1.330	<b>Space group</b>	P2 <sub>1</sub> /n (14 iii)
Atoms	x/a	y/b	z/c
N11	0.4048	0.2918	0.2731
N12	-0.3316	0.2875	0.5313
C13	0.215	0.2833	0.3683
C18	-0.1237	0.3289	0.4471
C11	0.4307	0.2127	0.3328
C12	0.3404	0.2055	0.381
C14	0.1889	0.3666	0.3063
C15	0.2847	0.3678	0.2616
C19	-0.1022	0.2583	0.5109
C20	-0.2072	0.2404	0.5505
C21	-0.3511	0.3603	0.4699
C22	-0.2524	0.3827	0.427
H111	0.5154	0.1598	0.3424
H121	0.3633	0.1477	0.4224
H141	0.1053	0.421	0.295
H151	0.265	0.4266	0.22
H191	-0.016	0.2229	0.5271
H201	-0.1903	0.1913	0.5939
H211	-0.4379	0.3974	0.4554
H221	-0.2715	0.434	0.3841
C16	0.1161	0.2725	0.4205
H161	0.1491	0.3429	0.4579
H162	0.107	0.1455	0.4329
C17	-0.02	0.3483	0.398
H171	-0.0107	0.4771	0.388
H172	-0.0497	0.2827	0.3589
C1	0.6702	0.3122	0.1648
C3	0.8706	0.324	0.1081
O1	0.5385	0.3533	0.1629
O2	0.9306	0.3778	0.0527
C2	0.7372	0.367	0.1102
C4	0.9381	0.2309	0.1608
C5	0.8701	0.179	0.215
C6	0.7365	0.2179	0.2174
H1	0.5059	0.3231	0.2042
H2	1.0145	0.3203	0.049
H21	0.6924	0.4325	0.0745
H41	1.029	0.2031	0.1595
H51	0.9155	0.117	0.2513
H61	0.6904	0.1792	0.2541

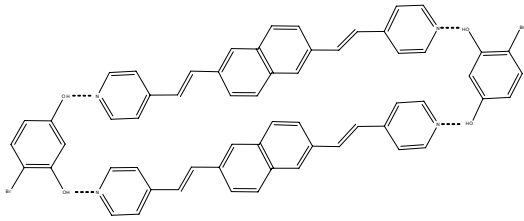
## Appendix

Crystal structure details of 1:1 co-crystals of 2,4-dihydroxy benzoic acid and 1,2-di-(4-pyridyl)ethane measured at 120 K			
<b>a (Å)</b>	9.5510(4)	<b>α °</b>	90
<b>b (Å)</b>	10.8258(5)	<b>β °</b>	102.4958(13)
<b>c (Å)</b>	16.3789(6)	<b>γ °</b>	90
<b>V (Å<sup>3</sup>)</b>	1653.4(1)	<b>Z</b>	4
<b>D<sub>x</sub>g (cm<sup>3</sup>)</b>	1.359	<b>Space group</b>	P2 <sub>1</sub> /c (14 ii)
Atoms	x/a	y/b	z/c
O24	0.5155	0.1746	0.2696
O23	0.2594	0.2453	0.1981
O25	0.5585	-0.025	0.3007
O22	-0.0996	-0.0667	0.1358
C3	0.3232	0.0329	0.2342
C4	0.2763	-0.0895	0.2349
C2	0.2231	0.1246	0.1998
C7	0.4737	0.0659	0.2696
C6	0.0368	-0.0304	0.1672
C1	0.0809	0.0921	0.1659
C5	0.135	-0.1215	0.2028
H1	0.0129	0.1549	0.1426
H5	0.1047	-0.2057	0.2053
H4	0.3428	-0.1536	0.2577
H22	-0.16	-0.006	0.1033
H23	0.3595	0.2687	0.2308
H25	0.6615	0.0018	0.3257
N21	-0.1901	0.048	0.3694
C14	0.2199	0.201	0.487
C15	0.0782	0.1442	0.4447
N20	0.7138	0.4031	0.5512
C10	0.5278	0.3563	0.4316
C9	0.6498	0.4202	0.4707
C19	-0.0471	0.1859	0.4663
C16	0.0636	0.0529	0.3835
C11	0.4679	0.269	0.4766
C8	0.6559	0.3208	0.5942
C13	0.3352	0.1972	0.4359
C17	-0.0714	0.0062	0.348
C12	0.5352	0.2508	0.5601
C18	-0.1775	0.1367	0.4275
H9	0.6882	0.4782	0.4369
H10	0.485	0.3734	0.3741
H12	0.4984	0.1905	0.593
H8	0.6976	0.3071	0.6523
H13A	0.2982	0.2322	0.3817
H13B	0.3628	0.113	0.4298
H14A	0.2578	0.1584	0.5384
H14B	0.2054	0.2864	0.4985
H16	0.1465	0.0216	0.3661
H17	-0.0771	-0.0578	0.3069
H19	-0.0418	0.2486	0.5084

## Appendix

Crystal structure details of 1:1 co-crystals of 2,4-dihydroxy benzaldehyde and 1,2-di-(4-pyridyl)ethane measured at 120 K			
<b>a (Å)</b>	6.2321(4)	<b><math>\alpha</math> °</b>	73.0489(14)
<b>b (Å)</b>	8.2972(5)	<b><math>\beta</math> °</b>	81.4402(13)
<b>c (Å)</b>	11.0296(5)	<b><math>\gamma</math> °</b>	80.6727(13)
<b>V (Å<sup>3</sup>)</b>	534.9(1)	<b>Z</b>	2
<b>D<sub>xg</sub> (cm<sup>3</sup>)</b>	1.430	<b>Space group</b>	P-1 (2)
Atoms	x/a	y/b	z/c
O3	0.714	-0.0289	0.5588
C1	0.5528	0.2251	0.9325
C3	0.5032	0.1421	0.7479
C4	0.7267	0.0769	0.735
O1	0.4611	0.2961	1.0263
O2	0.3664	0.1361	0.6649
C2	0.4178	0.2171	0.8452
C5	0.8602	0.0893	0.8231
C6	0.7764	0.1611	0.9208
C7	0.8199	-0.0039	0.6363
H1	0.5606	0.2925	1.0839
H2	0.4501	0.0795	0.607
H21	0.2678	0.2625	0.8523
H51	1.0113	0.0475	0.8144
H61	0.8679	0.167	0.9804
H71	0.9728	-0.0404	0.6303
N11	0.7351	0.3175	1.1896
C13	0.9466	0.4247	1.3558
C11	0.6398	0.3228	1.3061
C12	0.7377	0.374	1.3915
C14	1.0456	0.4187	1.2349
C15	0.9373	0.3647	1.1562
H111	0.4976	0.2889	1.3319
H121	0.6636	0.3749	1.4734
H141	1.1874	0.4528	1.2065
H151	1.0093	0.36	1.0746
C16	1.0692	0.4769	1.4431
H161	1.177	0.3854	1.4747
H162	1.1387	0.5729	1.3942
N11	1.2649	0.6825	1.8104
C13	1.0534	0.5753	1.6442
C11	1.3602	0.6772	1.6939
C12	1.2623	0.626	1.6085
C14	0.9544	0.5813	1.7651
C15	1.0627	0.6353	1.8438
H111	1.5024	0.7111	1.6681
H121	1.3364	0.6251	1.5266
H141	0.8126	0.5472	1.7935
H151	0.9907	0.64	1.9254
C16	0.9308	0.5231	1.5569
H161	0.823	0.6146	1.5253
H162	0.8613	0.4271	1.6058

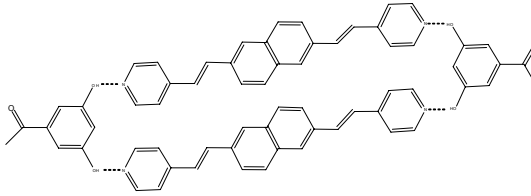
## Appendix

<b>Crystal structure details of 1:1 co-crystals of 4-bromoresorcinol and 2,6-Bis[(E)-2-(4-pyridyl)ethenyl]naphthalene measured at 120 K</b>			
<b>a (Å)</b>	7.5588(4)	<b><math>\alpha</math> °</b>	78.3305(14)
<b>b (Å)</b>	14.0628(5)	<b><math>\beta</math> °</b>	83.2372(13)
<b>c (Å)</b>	22.3358(6)	<b><math>\gamma</math> °</b>	84.6141(12)
<b>V (Å<sup>3</sup>)</b>	2303.0(2)	<b>Z</b>	4
<b>D<sub>xg</sub> (cm<sup>3</sup>)</b>	1.510	<b>Space group</b>	P-1 (2)
Atoms	x/a	y/b	z/c
Br1	0.7032	0.7921	-0.6937
C61	0.8704	0.75	-0.6341
C62	0.8061	0.7055	-0.575
C64	1.1119	0.6869	-0.5489
O1	0.6299	0.6944	-0.5601
O2	1.2337	0.6581	-0.5074
C63	0.9298	0.675	-0.5321
C65	1.1703	0.7326	-0.6082
C66	1.0483	0.763	-0.6506
H631	0.8929	0.6434	-0.4914
H651	1.2937	0.7405	-0.6196
H661	1.0879	0.7943	-0.6912
H1	0.5572	0.6813	-0.5136
H2	1.1433	0.6285	-0.4716
Br11	0.3808	0.7533	0.2048
C71	0.2163	0.7894	0.1443
C72	0.2773	0.8256	0.084
C74	-0.0284	0.8428	0.059
O11	0.4538	0.8335	0.0683
O12	-0.1503	0.8694	0.0178
C73	0.151	0.8542	0.0408
C75	-0.0887	0.8057	0.1195
C76	0.0354	0.7789	0.1624
H731	0.1902	0.8814	-0.0006
H751	-0.2124	0.799	0.131
H761	-0.0032	0.7541	0.2042
H3	0.4633	0.8664	0.0277
H4	-0.1231	0.8746	-0.0267
N1	0.4922	1.1181	-0.941
N2	0.0146	0.888	-0.1014
C3	0.4017	1.1123	-0.8154
C8	0.3173	1.0431	-0.6369
C11	0.2119	1.0429	-0.5118
C12	0.312	0.9619	-0.5299
C15	0.2095	0.9635	-0.4044
C20	0.1259	0.8944	-0.2265
C1	0.538	1.0379	-0.8991
C2	0.4935	1.0334	-0.8357
C4	0.3566	1.1937	-0.8585
C5	0.4042	1.1922	-0.9208
C6	0.3449	1.1135	-0.7497
C7	0.3736	1.0442	-0.7022
C9	0.2162	1.1234	-0.618
C10	0.1629	1.1253	-0.5568
C13	0.3624	0.9642	-0.5928
C14	0.1596	1.0422	-0.4482

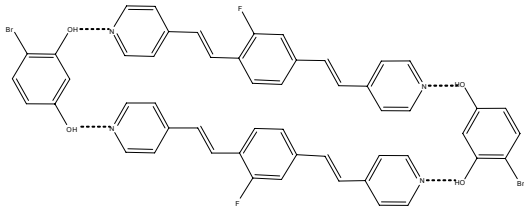
## Appendix

C16	0.3121	0.8829	-0.4234
C17	0.3604	0.8808	-0.4842
C18	0.1519	0.9626	-0.3389
C19	0.187	0.8924	-0.2913
C21	0.1632	0.813	-0.1815
C22	0.107	0.8132	-0.1203
C23	-0.0239	0.9678	-0.144
C24	0.0276	0.9728	-0.2064
H11	0.6012	0.9834	-0.913
H21	0.5279	0.9772	-0.8068
H41	0.2925	1.2491	-0.8461
H51	0.3745	1.2488	-0.9501
H61	0.2801	1.1708	-0.7402
H71	0.4381	0.987	-0.7119
H91	0.1874	1.1791	-0.6481
H101	0.0899	1.1788	-0.5454
H131	0.4293	0.9097	-0.6053
H141	0.0918	1.097	-0.4364
H161	0.3489	0.83	-0.3926
H171	0.4243	0.8246	-0.4956
H181	0.0803	1.018	-0.3297
H191	0.2605	0.8374	-0.3002
H211	0.2282	0.7568	-0.1925
H221	0.1346	0.7574	-0.0901
H231	-0.0907	1.0225	-0.1317
H241	0.0013	1.0308	-0.2351
N31	0.4207	0.4015	0.4387
N32	1.0678	0.5987	-0.3912
C33	0.5249	0.4631	0.314
C38	0.6412	0.4874	0.1372
C41	0.7685	0.5482	0.0134
C42	0.701	0.4548	0.0328
C45	0.8305	0.5156	-0.0911
C50	0.9455	0.5407	-0.2669
C31	0.4713	0.4911	0.4164
C32	0.5252	0.5234	0.3551
C34	0.4686	0.37	0.3363
C35	0.4183	0.3423	0.3984
C36	0.5874	0.4988	0.2487
C37	0.577	0.4543	0.2025
C39	0.7074	0.5804	0.1155
C40	0.7678	0.609	0.0555
C43	0.6355	0.4278	0.0956
C44	0.8367	0.5755	-0.0498
C46	0.7612	0.4234	-0.07
C47	0.6986	0.3941	-0.0093
C48	0.8958	0.55	-0.1553
C49	0.8821	0.5055	-0.2022
C51	1.0112	0.6314	-0.2888
C52	1.0678	0.6566	-0.3508
C53	1.0031	0.5122	-0.3702
C54	0.9409	0.4797	-0.3084
H311	0.4696	0.5334	0.4448
H321	0.5617	0.5876	0.3414
H341	0.4677	0.3257	0.3093
H351	0.3796	0.2787	0.4132
H361	0.642	0.5588	0.2387
H371	0.5223	0.3943	0.2126
H391	0.7067	0.6233	0.1435
H401	0.8129	0.6713	0.0421
H431	0.5878	0.3663	0.1098
H441	0.8876	0.6363	-0.0631
H461	0.7588	0.3815	-0.0984
H471	0.6542	0.3316	0.0041
H481	0.9558	0.6083	-0.1654
H491	0.8243	0.4464	-0.1923
H511	1.0133	0.6759	-0.2621
H521	1.1143	0.7184	-0.3653
H531	1.0003	0.4704	-0.3987
H541	0.8955	0.4174	-0.2955

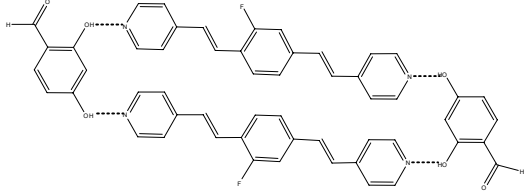
## Appendix

Crystal structure details of 1:1 co-crystals of 3,5-dihydroxy acetophenone and 2,6-Bis[(E)-2-(4-pyridyl)ethenyl]naphthalene measured at 120 K			
<b>a (Å)</b>	5.8860(4)	<b><math>\alpha</math> °</b>	90
<b>b (Å)</b>	25.8804(7)	<b><math>\beta</math> °</b>	98.6142(6)
<b>c (Å)</b>	16.1014(6)	<b><math>\gamma</math> °</b>	90
<b>V (Å<sup>3</sup>)</b>	2425.1(2)	<b>Z</b>	4
<b>D<sub>x</sub>g (cm<sup>3</sup>)</b>	1.333	<b>Space group</b>	P2 <sub>1</sub> /c (14 ii)
Atoms	x/a	y/b	z/c
O1	0.5176	-0.2462	1.0379
O3	-0.1874	-0.2349	0.8243
O4	0.5648	-0.0796	0.9074
C5	0.5485	-0.1625	0.9742
C6	0.4349	-0.2093	0.9817
C15	0.4581	-0.126	0.9147
C18	0.2572	-0.136	0.8612
C25	-0.0823	-0.1949	0.8141
C30	-0.182	-0.1569	0.7474
C31	0.1407	-0.1827	0.8684
C33	0.2281	-0.219	0.9284
H5	0.6898	-0.1558	1.0107
H33	0.1502	-0.2511	0.9343
H18	0.2008	-0.1104	0.8201
H30A	-0.0802	-0.128	0.7472
H30B	-0.3287	-0.1452	0.759
H30C	-0.2007	-0.1735	0.6935
H4	0.6944	-0.0772	0.9532
H1	0.6259	-0.2361	1.0834
N2	1.1023	0.0611	0.9584
N7	-1.1101	-0.2084	0.1472
C8	0.2689	-0.0774	0.6265
C9	0.7225	0.0368	0.8371
C10	0.0747	-0.0923	0.5686
C11	-0.1071	-0.0111	0.5996
C12	0.5203	0.0253	0.7745
C13	0.0625	-0.1399	0.5229
C14	0.2799	-0.031	0.6698
C16	-0.7242	-0.2212	0.2157
C17	-0.3206	-0.1187	0.453
C19	-0.5482	-0.1716	0.3394
C20	-0.1274	-0.1531	0.4682
C21	-0.1174	-0.0585	0.5551
C22	-0.3117	-0.0729	0.4967
C23	0.4827	-0.0178	0.729
C24	-0.7435	-0.1828	0.2743
C26	-0.955	-0.1565	0.2661
C27	1.104	0.0194	0.9095
C28	-1.1298	-0.1713	0.2032
C29	0.9199	0.0058	0.8487
C32	0.9136	0.091	0.9472
C34	-0.9072	-0.2325	0.1545
C35	-0.5226	-0.1304	0.3902
C36	0.7223	0.0799	0.8884
C37	0.0857	0.0025	0.6544
H34	-0.8858	-0.0495	0.4893
H26	-0.9757	-0.2596	0.1156
H28	-1.2712	-0.129	0.3042
		-0.1524	0.2007

## Appendix

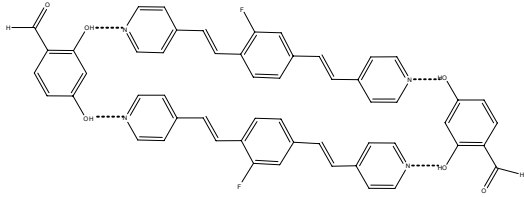
Crystal structure details of 1:1 co-crystals of 4-bromoresorcinol and 1,4-Bis[(E)-2-(4-pyridyl)ethenyl]2-fluorobenzene measured at 120 K			
<b>a (Å)</b>	8.3062(4)	<b><math>\alpha</math> °</b>	74.6320(14)
<b>b (Å)</b>	9.6762(7)	<b><math>\beta</math> °</b>	79.4944(13)
<b>c (Å)</b>	15.0568(6)	<b><math>\gamma</math> °</b>	65.8372(14)
<b>V (Å<sup>3</sup>)</b>	1060.9(1)	<b>Z</b>	2
<b>D<sub>x</sub>g (cm<sup>3</sup>)</b>	1.535	<b>Space group</b>	P-1 (2)
Atoms	x/a	y/b	z/c
Br1	0.1756	0.9285	0.1234
C31	-0.2489	0.8248	0.3524
C33	0.0453	0.832	0.3084
C34	0.0068	0.8821	0.2158
O1	-0.3765	0.8011	0.4168
O2	0.2049	0.8118	0.3304
C32	-0.0842	0.8047	0.3757
C35	-0.155	0.8997	0.1923
C36	-0.2823	0.8702	0.2592
H1	-0.3374	0.7697	0.4745
H2	0.1906	0.8137	0.3934
H321	-0.0599	0.7726	0.4389
H351	-0.1787	0.9315	0.1291
H361	-0.3923	0.8816	0.242
N1	0.2319	0.7248	0.5162
N2	1.2607	0.2618	1.414
F1	0.668	0.8091	1.053
F2	0.4979	0.8795	0.9138
C3	0.3921	0.6327	0.6825
C8	0.5965	0.6232	0.8956
C11	0.7856	0.5391	1.0533
C12	0.6829	0.6922	1.018
C13	0.5916	0.7336	0.9407
C16	1.0747	0.3308	1.2592
C1	0.3113	0.5758	0.555
C2	0.3923	0.5249	0.6368
C4	0.3032	0.7888	0.6428
C5	0.2281	0.8277	0.5621
C6	0.4884	0.5802	0.765
C7	0.4975	0.6722	0.8145
C9	0.7004	0.4674	0.9311
C10	0.7925	0.4261	1.0083
C14	0.8789	0.501	1.1349
C15	0.9796	0.3621	1.1787
C17	1.1873	0.1793	1.2951
C18	1.2776	0.1512	1.371
C19	1.1535	0.4068	1.379
C20	1.0595	0.4466	1.3041
H11	0.3123	0.5005	0.525
H21	0.4472	0.417	0.6617
H41	0.2958	0.8673	0.672
H51	0.1677	0.9345	0.5367
H61	0.5491	0.4717	0.7853
H71	0.4322	0.7801	0.7952
H91	0.706	0.3893	0.9022
H101	0.8633	0.3203	1.0304
H141	0.8681	0.5859	1.1591
H151	0.9901	0.2758	1.1561
H171	1.2025	0.0969	1.2673
H181	1.3548	0.048	1.3941
H191	1.1438	0.4875	1.4068
H201	0.9836	0.5511	1.2828

## Appendix

Crystal structure details of 1:1 co-crystals of 2,4-dihydroxy benzaldehyde and 1,4-Bis[(E)-2-(4-pyridyl)ethenyl]2-fluorobenzene measured at 120 K			
<b>a</b> (Å)	9.2422(4)	<b>α</b> °	112.7274(13)
<b>b</b> (Å)	10.4559(5)	<b>β</b> °	91.7353(12)
<b>c</b> (Å)	11.7721(5)	<b>γ</b> °	94.9818(13)
<b>V</b> (Å <sup>3</sup> )	1042.8(1)	<b>Z</b>	2
<b>D<sub>x</sub></b> (cm <sup>3</sup> )	1.400	<b>Space group</b>	P-1 (2)
Atoms	x/a	y/b	z/c
N1	-0.1964	0.9985	-0.3822
N2	0.3514	0.3954	0.6026
F1	-0.0737	0.7401	0.2941
F11	0.2206	0.6038	-0.0997
C3	-0.1263	0.8989	-0.1987
C8	0.04	0.7236	0.0026
C10	-0.0021	0.7119	0.2
C11	0.1133	0.6321	0.1928
C13	0.1542	0.6422	-0.005
C16	0.2766	0.4663	0.4028
C1	-0.2729	1.0262	-0.2819
C2	-0.2414	0.9786	-0.1905
C4	-0.047	0.8696	-0.3038
C5	-0.0862	0.92	-0.3912
C6	-0.0954	0.8501	-0.1001
C7	0.0081	0.7711	-0.0963
C9	-0.0392	0.7563	0.1081
C12	0.1914	0.5979	0.0875
C14	0.1482	0.5904	0.2953
C15	0.2447	0.504	0.2973
C17	0.2167	0.5257	0.5162
C18	0.2561	0.4878	0.6118
C19	0.408	0.3361	0.4928
C20	0.3744	0.3681	0.3922
H11	-0.3516	1.0812	-0.2736
H21	-0.2994	0.9991	-0.1216
H41	0.0327	0.8154	-0.3148
H51	-0.0326	0.8984	-0.4627
H61	-0.1559	0.8762	-0.0328
H71	0.0676	0.7433	-0.1643
H91	-0.1198	0.8091	0.1168
H121	0.2719	0.5451	0.0793
H141	0.0976	0.6288	0.368
H151	0.2961	0.4646	0.2253
H171	0.1478	0.5912	0.5271
H181	0.2144	0.5299	0.6886
H191	0.4741	0.2687	0.4839
H201	0.4172	0.324	0.3162
O3	0.4846	0.2426	1.0986
C31	0.322	-0.0225	0.6512
C33	0.3983	0.2171	0.7874
C34	0.4203	0.1737	0.8857
O1	0.2704	-0.1188	0.5401
O2	0.425	0.3526	0.8082
C32	0.3481	0.1178	0.6702
C35	0.3943	0.0308	0.8615
C36	0.3461	-0.0667	0.7474
C37	0.4666	0.272	1.0086
H1	0.2446	-0.0765	0.4851
H2	0.3991	0.3673	0.7358
H321	0.3323	0.1462	0.6037
H351	0.4109	0.001	0.9271
H371	0.4852	0.3673	1.0204



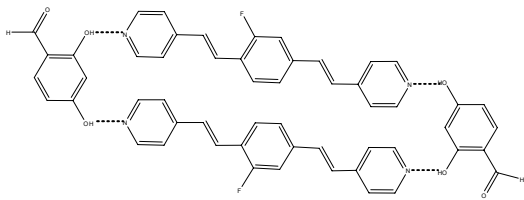
## Appendix

Crystal structure details of 40% converted mixed 1:1 co-crystals of 2,4-dihydroxy benzaldehyde and 1,4-Bis[(E)-2-(4-pyridyl)ethenyl]2-fluorobenzene measured at 120 K			
<b>a (Å)</b>	9.4058(4)	<b>α °</b>	113.2456(13)
<b>b (Å)</b>	10.3076(5)	<b>β °</b>	91.7465(13)
<b>c (Å)</b>	11.7323(5)	<b>γ °</b>	93.5649(12)
<b>V (Å<sup>3</sup>)</b>	1041.3(1)	<b>Z</b>	2
<b>D<sub>x</sub>g (cm<sup>3</sup>)</b>	1.402	<b>Space group</b>	P-1 (2)
Atoms	x/a	y/b	z/c
N1	-0.3592	0.5958	-0.1042
N2	0.1928	-0.0013	0.8784
F1	-0.2286	0.3989	0.5989
F11	0.0799	0.2717	0.2119
C3	-0.2765	0.5472	0.1051
C8	-0.1179	0.3642	0.3089
C10	-0.1567	0.3612	0.504
C11	-0.0439	0.2636	0.4874
C13	0.0019	0.2967	0.3055
C16	0.1252	0.0939	0.6935
C81	-0.0899	0.4126	0.324
C111	-0.0393	0.3144	0.5169
C161	0.1458	0.1492	0.722
C1	-0.4164	0.6604	0.0049
C2	-0.3782	0.6382	0.1095
C4	-0.215	0.4803	-0.0085
C5	-0.2617	0.5081	-0.1076
C6	-0.2405	0.4937	0.201
C7	-0.1514	0.4006	0.2011
C9	-0.1902	0.4107	0.4157
C12	0.0373	0.2468	0.3942
C14	-0.0137	0.2147	0.5859
C15	0.0914	0.1419	0.5935
C17	0.0504	0.1401	0.8071
C18	0.0847	0.0819	0.8896
C19	0.2696	-0.0261	0.7781
C20	0.2429	0.0297	0.6925
C61	-0.2222	0.5852	0.2488
C71	-0.0894	0.5209	0.2656
C141	0.0222	0.3265	0.6499
C151	0.15	0.2573	0.6644
H11	-0.4869	0.7243	0.0099
H21	-0.4211	0.6868	0.1854
H41	-0.1437	0.4165	-0.0161
H51	-0.2206	0.4612	-0.1848
H61	-0.2886	0.5338	0.2756
H71	-0.1061	0.3529	0.1263
H91	-0.2797	0.4486	0.4157
H121	0.1222	0.1996	0.3874
H141	-0.0774	0.2386	0.651
H151	0.1528	0.1167	0.5266
H171	-0.0404	0.176	0.8081
H181	0.029	0.1013	0.9599
H191	0.3462	-0.085	0.7671
H201	0.2993	0.0068	0.6225
H611	-0.2963	0.5581	0.2902
H711	-0.0434	0.4871	0.1895

## Appendix

H1411	-0.0524	0.3016	0.6921
H1511	0.1973	0.225	0.589
N1	0.3592	0.4042	1.1042
N2	-0.1928	1.0013	0.1216
F1	0.2286	0.6011	0.4011
F11	-0.0799	0.7283	0.7881
C3	0.2765	0.4528	0.8949
C8	0.1179	0.6358	0.6911
C10	0.1567	0.6388	0.496
C11	0.0439	0.7364	0.5126
C13	-0.0019	0.7033	0.6945
C16	-0.1252	0.9061	0.3065
C81	0.0899	0.5874	0.676
C111	0.0393	0.6856	0.4831
C161	-0.1458	0.8508	0.278
C1	0.4164	0.3396	0.9951
C2	0.3782	0.3618	0.8905
C4	0.215	0.5197	1.0085
C5	0.2617	0.4919	1.1076
C6	0.2405	0.5063	0.799
C7	0.1514	0.5994	0.7989
C9	0.1902	0.5893	0.5843
C12	-0.0373	0.7532	0.6058
C14	0.0137	0.7853	0.4141
C15	-0.0914	0.8581	0.4065
C17	-0.0504	0.8599	0.1929
C18	-0.0847	0.9181	0.1104
C19	-0.2696	1.0261	0.2219
C20	-0.2429	0.9703	0.3075
C61	0.2222	0.4148	0.7512
C71	0.0894	0.4791	0.7344
C141	-0.0222	0.6735	0.3501
C151	-0.15	0.7427	0.3356
H11	0.4869	0.2757	0.9901
H21	0.4211	0.3132	0.8146
H41	0.1437	0.5835	1.0161
H51	0.2206	0.5388	1.1848
H61	0.2886	0.4662	0.7244
H71	0.1061	0.6471	0.8737
H91	0.2797	0.5514	0.5843
H121	-0.1222	0.8004	0.6126
H141	0.0774	0.7614	0.349
H151	-0.1528	0.8833	0.4734
H171	0.0404	0.824	0.1919
H181	-0.029	0.8987	0.0401
H191	-0.3462	1.085	0.2329
H201	-0.2993	0.9932	0.3775
H611	0.2963	0.4419	0.7098
H711	0.0434	0.5129	0.8105
H1411	0.0524	0.6984	0.3079
H1511	-0.1973	0.775	0.411
O3	-0.4905	0.7573	-0.5975
C31	-0.3179	1.0212	-0.1502
C33	-0.3992	0.7799	-0.2871
C34	-0.4228	0.8256	-0.3855
O1	-0.266	1.1193	-0.0395
O2	-0.4303	0.6442	-0.3078
C32	-0.3483	0.8805	-0.1699
C35	-0.3925	0.9686	-0.3607
C36	-0.3428	1.066	-0.2475
C37	-0.4717	0.7269	-0.5062
H1	-0.241	1.0776	0.0176
H2	-0.4052	0.6263	-0.2366
H321	-0.3337	0.8515	-0.1033
H351	-0.4078	0.9987	-0.4266
H361	-0.3238	1.1628	-0.2339
H371	-0.4906	0.6308	-0.5178

## Appendix

<p><b>Crystal structure details of 60% converted mixed 1:1 co-crystals of 2,4-dihydroxy benzaldehyde and 1,4-Bis[(E)-2-(4-pyridyl)ethenyl]2-fluorobenzene measured at 120 K</b></p>			
<b>a (Å)</b>	9.5710(4)	<b>α °</b>	112.5270(13)
<b>b (Å)</b>	10.0360(5)	<b>β °</b>	91.0090(13)
<b>c (Å)</b>	11.7106(5)	<b>γ °</b>	92.7797(12)
<b>V (Å<sup>3</sup>)</b>	1037.0(1)	<b>Z</b>	2
<b>D<sub>x</sub>g (cm<sup>3</sup>)</b>	1.399	<b>Space group</b>	P-1 (2)
Atoms	x/a	y/b	z/c
O3	0.9886	0.2431	1.5938
C31	0.8159	-0.0207	1.1531
C33	0.8993	0.2209	1.2846
C34	0.9212	0.1745	1.3836
O1	0.7639	-0.1186	1.0462
O2	0.9321	0.3607	1.3048
C32	0.8482	0.1227	1.1715
C35	0.8902	0.0287	1.3618
C36	0.84	-0.0684	1.251
C37	0.9735	0.2751	1.5029
H1	0.7387	-0.0763	0.9893
H2	0.9073	0.378	1.2332
H321	0.8343	0.1542	1.1055
H351	0.9048	-0.0044	1.4267
H361	0.8203	-0.1666	1.2393
H371	0.996	0.3718	1.5111
N1	0.1392	0.5893	-0.1025
N2	0.6923	0.0017	0.8833
F1	0.2681	0.3955	0.5992
F11	0.5858	0.2789	0.2162
C3	0.2273	0.5533	0.1124
C8	0.3978	0.3887	0.3217
C10	0.3422	0.3562	0.505
C11	0.4466	0.2319	0.4739
C111	0.4651	0.3116	0.5173
C13	0.5079	0.2996	0.3097
C16	0.6383	0.1163	0.7062
C1	0.0804	0.6575	0.0058
C2	0.1204	0.6417	0.1129
C4	0.2873	0.4819	0.0011
C5	0.2405	0.5027	-0.1034
C9	0.3127	0.4112	0.4205
C12	0.539	0.2464	0.3961
C17	0.5542	0.1429	0.8074
C18	0.5852	0.0854	0.8919
C19	0.7713	-0.0242	0.7843
C20	0.7487	0.0308	0.6972
H11	0.007	0.7183	0.0075
H21	0.0756	0.6922	0.1876
H41	0.358	0.4171	-0.0041

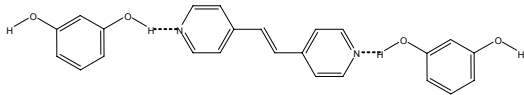
## Appendix

H51	0.2827	0.453	-0.1797
H91	0.2318	0.4644	0.4282
H121	0.6006	0.1706	0.3809
H171	0.4744	0.1977	0.8156
H181	0.5288	0.1066	0.9619
H191	0.8474	-0.0838	0.7763
H201	0.8071	0.0083	0.6284
C6	0.2613	0.5004	0.201
C7	0.3478	0.3988	0.1992
C61	0.2818	0.5855	0.2569
C71	0.4167	0.5189	0.2723
C14	0.4643	0.1467	0.5502
C15	0.5908	0.0959	0.574
C141	0.5178	0.3281	0.646
C151	0.6521	0.2579	0.6615
H61	0.2153	0.5427	0.2766
H71	0.3794	0.3353	0.1221
H141	0.3844	0.1231	0.5871
H151	0.6479	0.0486	0.5065
H611	0.21	0.5591	0.3005
H711	0.4612	0.4854	0.1953
H1411	0.4445	0.3011	0.6879
H1511	0.6958	0.2265	0.5842
N1	0.8608	0.4107	1.1025
N2	0.3077	0.9983	0.1167
F1	0.7319	0.6045	0.4008
F11	0.4142	0.7211	0.7838
C3	0.7727	0.4467	0.8876
C8	0.6022	0.6113	0.6783
C10	0.6578	0.6438	0.495
C11	0.5534	0.7681	0.5261
C111	0.5349	0.6884	0.4827
C13	0.4921	0.7004	0.6903
C16	0.3617	0.8837	0.2938
C1	0.9196	0.3425	0.9942
C2	0.8796	0.3583	0.8871
C4	0.7127	0.5181	0.9989
C5	0.7595	0.4973	1.1034
C9	0.6873	0.5888	0.5795
C12	0.461	0.7536	0.6039
C17	0.4458	0.8571	0.1926
C18	0.4148	0.9146	0.1081
C19	0.2287	1.0242	0.2157
C20	0.2513	0.9692	0.3028
H11	0.993	0.2817	0.9925
H21	0.9244	0.3078	0.8124
H41	0.642	0.5829	1.0041
H51	0.7173	0.547	1.1797
H91	0.7682	0.5356	0.5718
H121	0.3994	0.8294	0.6191
H171	0.5256	0.8023	0.1844
H181	0.4712	0.8934	0.0381
H191	0.1526	1.0838	0.2237
H201	0.1929	0.9917	0.3716
C6	0.7387	0.4996	0.799
C7	0.6522	0.6012	0.8008
C61	0.7182	0.4145	0.7431
C71	0.5833	0.4811	0.7277
C14	0.5357	0.8533	0.4498
C15	0.4092	0.9041	0.426
C141	0.4822	0.6719	0.354
C151	0.3479	0.7421	0.3385
H61	0.7847	0.4573	0.7234
H71	0.6206	0.6647	0.8779
H141	0.6156	0.8769	0.4129
H151	0.3521	0.9514	0.4935
H611	0.79	0.4409	0.6995
H711	0.5388	0.5146	0.8047
H1411	0.5555	0.6989	0.3121
H1511	0.3042	0.7735	0.4158

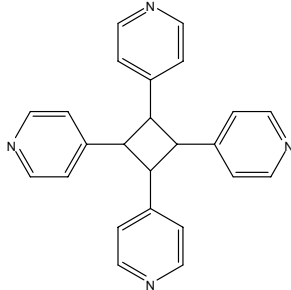
## Appendix

<b>Crystal structure details of 1:1 co-crystals of resorcinol and 1,2-di-(4-pyridyl)ethylene, 2(bpe):2(res) momomer ring form measured at 120 K</b>			
<b>a (Å)</b>	8.070(1)	<b><math>\alpha</math> °</b>	73.119(1)
<b>b (Å)</b>	9.832(1)	<b><math>\beta</math> °</b>	72.563(1)
<b>c (Å)</b>	10.876(1)	<b><math>\gamma</math> °</b>	66.184(1)
<b>V (Å<sup>3</sup>)</b>	738-862(1)	<b>Z</b>	2
<b>D<sub>xg</sub> (cm<sup>3</sup>)</b>	-	<b>Space group</b>	P-1 (2)
Atoms	x/a	y/b	z/c
O1	-0.0086	0.3429	0.3051
O2	-0.5958	0.2701	0.4324
C1	-0.1631	0.3464	0.2769
C2	-0.3029	0.3073	0.3734
C3	-0.4583	0.3102	0.3409
C4	-0.4757	0.3545	0.2098
C5	-0.3363	0.3938	0.1145
C6	-0.1802	0.3909	0.1456
H1	-0.0151	0.3164	0.3866
H2	-0.5647	0.2356	0.5056
H3	-0.2921	0.2782	0.4628
H4	-0.5818	0.3576	0.1865
H5	-0.3477	0.4235	0.0253
H6	-0.0861	0.4187	0.0786
N1	-0.0152	0.2534	0.5687
N2	0.4775	-0.1512	1.3337
C7	-0.0497	0.3538	0.6422
C8	0.0026	0.3135	0.7613
C9	0.0945	0.1622	0.8107
C10	0.1252	0.0565	0.7366
C11	0.0699	0.1073	0.6178
C12	0.1602	0.1213	0.9332
C13	0.2507	-0.0171	0.9899
C14	0.3251	-0.059	1.1089
C15	0.3062	0.0452	1.1807
C16	0.3835	-0.0049	1.2905
C17	0.4946	-0.2506	1.2648
C18	0.4223	-0.2103	1.1541
H7	-0.1149	0.4596	0.6071
H8	-0.022	0.3908	0.8105
H9	0.1831	-0.0531	0.7677
H10	0.0924	0.0351	0.5629
H11	0.1354	0.2016	0.9755
H12	0.2696	-0.0976	0.9498
H13	0.2428	0.1518	1.1548
H14	0.3752	0.064	1.339
H15	0.5588	-0.3526	1.2977
H16	0.4425	-0.2861	1.1048

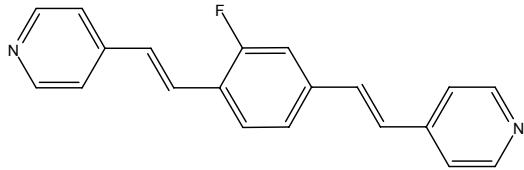
## Appendix

<b>Crystal structure details of 1:1 co-crystals of resorcinol and 1,2-di-(4-pyridyl)ethylene, 2(bpe):2(res) momomer chain form measured at 120 K</b>			
<b>a (Å)</b>	10.1485(4)	<b>α °</b>	90
<b>b (Å)</b>	7.1265(3)	<b>β °</b>	94.648(1)
<b>c (Å)</b>	20.0717(6)	<b>γ °</b>	90
<b>V (Å<sup>3</sup>)</b>	1446.8(1)	<b>Z</b>	2
<b>D<sub>xg</sub> (cm<sup>3</sup>)</b>	-	<b>Space group</b>	P2 <sub>1</sub> /n (14 iii)
Atoms	x/a	y/b	z/c
N1	1.094	-0.2019	0.2248
C8	1.1627	-0.2858	0.1167
N2	1.8308	-0.2159	-0.0315
C9	1.2868	-0.2052	0.1314
C18	1.7472	-0.1146	0.0712
C12	1.3872	-0.2159	0.0823
C14	1.6198	-0.1743	0.0503
C13	1.5151	-0.157	0.0968
C11	1.2123	-0.1214	0.2381
C10	1.3108	-0.1188	0.1941
C15	1.6004	-0.2512	-0.0138
C16	1.7071	-0.2693	-0.0522
C7	1.0704	-0.2813	0.1643
C17	1.8479	-0.1371	0.0292
H81	1.1415	-0.3435	0.0745
H181	1.7645	-0.0587	0.114
H121	1.3627	-0.2653	0.0391
H131	1.5371	-0.1021	0.1394
H111	1.23	-0.062	0.2802
H101	1.3934	-0.0602	0.2061
H151	1.5146	-0.2903	-0.0309
H161	1.6924	-0.323	-0.0955
H71	0.9863	-0.3371	0.1536
H171	1.934	-0.0947	0.0442
O1	0.9591	-0.1515	0.3353
O2	0.5689	-0.1204	0.4463
C1	0.7609	-0.133	0.3883
C6	0.6276	-0.1744	0.3905
C3	0.7589	-0.2801	0.2796
C4	0.625	-0.3158	0.2819
C2	0.8272	-0.1886	0.3333
C5	0.5574	-0.265	0.337
H11	0.8068	-0.0667	0.4241
H31	0.8037	-0.3171	0.242
H41	0.578	-0.3767	0.2452
H51	0.4658	-0.2908	0.3382
H1	0.9927	-0.184	0.296
H2	0.488	-0.1797	0.4478

Appendix

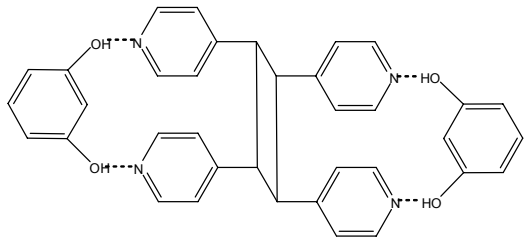
Crystal structure details of tetrakis(4-pyridyl)cyclobutane (1,2,3,4-tetra(pyridine-4-yl)cyclobutane) measured at 120 K			
<b>a (Å)</b>	9.3732(5)	<b>α °</b>	90
<b>b (Å)</b>	13.9484(6)	<b>β °</b>	90
<b>c (Å)</b>	14.0455(6)	<b>γ °</b>	90
<b>V (Å<sup>3</sup>)</b>	1836.32(1)	<b>Z</b>	4
<b>D<sub>s</sub>g (cm<sup>3</sup>)</b>	-	<b>Space group</b>	Pccn (56)
Atoms	x/a	y/b	z/c
N1	0.034	-0.031	0.1466
N2	-0.1137	0.0926	0.5554
C8	0.0748	0.1954	0.4359
C3	0.1191	0.1469	0.2257
C9	0.1234	0.1442	0.5138
C7	0.1683	0.256	0.3746
C4	0.1776	0.0605	0.2552
C10	0.0265	0.095	0.571
C2	0.0147	0.1412	0.1555
C6	0.1664	0.2424	0.2632
C1	-0.0236	0.052	0.1195
C11	-0.1601	0.1406	0.4786
C5	0.1343	-0.0244	0.2151
C12	-0.0717	0.1915	0.4177
H91	0.2223	0.1432	0.5286
H71	0.1474	0.3212	0.3883
H41	0.2481	0.0608	0.3038
H101	0.0627	0.06	0.6238
H21	-0.0302	0.1977	0.1326
H61	0.1185	0.2935	0.2319
H11	-0.0961	0.0496	0.0723
H111	-0.2592	0.1382	0.4648
H51	0.1762	-0.082	0.2379
H121	-0.1102	0.2246	0.3645
N1	0.466	0.531	0.1466
N2	0.6137	0.4074	0.5554
C8	0.4252	0.3046	0.4359
C3	0.3809	0.3531	0.2257
C9	0.3766	0.3558	0.5138
C7	0.3317	0.244	0.3746
C4	0.3224	0.4395	0.2552
C10	0.4735	0.4051	0.571
C2	0.4853	0.3588	0.1555
C6	0.3336	0.2576	0.2632
C1	0.5236	0.448	0.1195
C11	0.6601	0.3594	0.4786
C5	0.3657	0.5244	0.2151
C12	0.5717	0.3085	0.4177
H91	0.2777	0.3568	0.5286
H71	0.3526	0.1788	0.3883
H41	0.2519	0.4392	0.3038
H101	0.4373	0.44	0.6238
H21	0.5302	0.3023	0.1326
H61	0.3815	0.2065	0.2319
H11	0.5961	0.4504	0.0723
H111	0.7592	0.3618	0.4648
H51	0.3238	0.582	0.2379
H121	0.6102	0.2754	0.3645

## Appendix

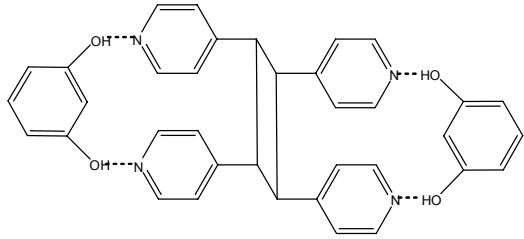
<b>Crystal structure details of 1,4-Bis[(E)-2-(4-pyridyl)ethenyl]2-fluorobenzene (bpef) measured at 120 K</b>			
<b>a (Å)</b>	9.3732(5)	<b>α °</b>	90
<b>b (Å)</b>	13.9484(6)	<b>β °</b>	90
<b>c (Å)</b>	14.0455(6)	<b>γ °</b>	90
<b>V (Å<sup>3</sup>)</b>	1836.32(1)	<b>Z</b>	4
<b>D<sub>x</sub>g (cm<sup>3</sup>)</b>	-	<b>Space group</b>	Pccn (56)
Atoms	x/a	y/b	z/c
F1	0.6183	-0.0937	0.4952
C2	-0.0475	0.0301	0.6734
C3	0.5526	-0.2206	0.5246
N4	-0.5296	0.1683	0.7802
C5	-0.2135	0.0761	0.7138
N6	0.9796	-0.419	0.396
C7	-0.053	-0.0315	0.6917
C8	0.1078	-0.0789	0.6516
C9	-0.1749	0.1391	0.6968
C10	0.3036	-0.0632	0.5918
C11	0.0664	-0.1417	0.669
C12	-0.4138	0.0598	0.7659
C13	-0.3337	0.1829	0.7322
C14	0.5279	-0.282	0.5284
C15	-0.5617	0.1068	0.7964
C16	0.7814	-0.4343	0.4425
C17	0.4012	-0.1734	0.5709
C18	0.4403	-0.1096	0.5548
C19	0.8891	-0.3119	0.4334
C20	0.6806	-0.3277	0.4817
C21	0.2044	-0.1887	0.6306
C22	0.6312	-0.3914	0.4841
C23	1.0262	-0.3577	0.3906
F24	-0.1034	-0.1575	0.7188
H3	0.6843	-0.2039	0.4889
H14	0.3976	-0.2987	0.565
H22	0.4888	-0.4051	0.5144
H16	0.7404	-0.4776	0.4489
H23	1.1627	-0.3438	0.3554
H19	0.9359	-0.2688	0.4297
H21	0.1646	-0.2314	0.6458
H10	0.3399	-0.02	0.5784
H7	-0.1723	-0.0483	0.7355
H2	0.0783	0.044	0.6307
H9	-0.0383	0.1527	0.6614
H12	-0.4461	0.0166	0.7808
H15	-0.6979	0.0934	0.8324
H13	-0.2974	0.2261	0.72



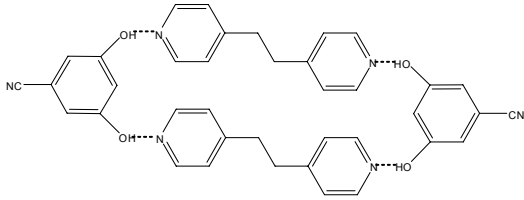
## Appendix

<b>Crystal structure details of 14% converted mixed 1:1 co-crystals of resorcinol and 1,2-di-(4-pyridyl)ethylene measured at 120 K</b>			
<b>a (Å)</b>	7.9360(4)	<b><math>\alpha</math> °</b>	93.0700(12)
<b>b (Å)</b>	9.8340(5)	<b><math>\beta</math> °</b>	106.7800(13)
<b>c (Å)</b>	10.9160(5)	<b><math>\gamma</math> °</b>	113.5611(13)
<b>V (Å<sup>3</sup>)</b>	733-647(1)	<b>Z</b>	2
<b>D<sub>x</sub>g (cm<sup>3</sup>)</b>	-	<b>Space group</b>	P-1 (2)
Atoms	x/a	y/b	z/c
O1	-0.3265	0.7684	0.5687
O2	0.342	0.8428	0.6947
C1	-0.1475	0.8087	0.6599
C2	0.008	0.8061	0.6269
C3	0.1871	0.8458	0.723
C4	0.2112	0.8893	0.8523
C5	0.0567	0.893	0.8839
C6	-0.1237	0.8529	0.7893
H21	-0.0089	0.7767	0.5382
H41	0.3334	0.9165	0.9186
H51	0.0742	0.9239	0.9724
H61	-0.2291	0.8557	0.8123
H1	-0.3264	0.7281	0.4877
H2	0.3086	0.8124	0.6035
N11	0.2461	0.7556	0.4326
N12	0.326	0.3477	-0.3351
C11	0.1827	0.6089	0.3827
C12	0.1812	0.5572	0.2638
C13	0.25	0.6608	0.1875
C14	0.3144	0.8128	0.238
C15	0.3089	0.8553	0.3577
C18	0.2622	0.438	-0.1104
C19	0.2095	0.2876	-0.1563
C20	0.2425	0.2472	-0.2662
C21	0.3783	0.4927	-0.2908
C22	0.3497	0.5419	-0.1822
C16	0.2811	0.6192	0.0637
C17	0.2353	0.4803	0.0072
C26	0.12	0.602	0.0516
C27	0.108	0.4483	-0.009
N11	-0.2461	0.2444	-0.4326
N12	-0.326	0.6523	0.3351
C11	-0.1827	0.3911	-0.3827
C12	-0.1812	0.4428	-0.2638
C13	-0.25	0.3392	-0.1875
C14	-0.3144	0.1872	-0.238
C15	-0.3089	0.1447	-0.3577
C18	-0.2622	0.562	0.1104
C19	-0.2095	0.7124	0.1563
C20	-0.2425	0.7528	0.2662
C21	-0.3783	0.5073	0.2908
C22	-0.3497	0.4581	0.1822
C16	-0.2811	0.3808	-0.0637
C17	-0.2353	0.5197	-0.0072
C26	-0.12	0.398	-0.0516
C27	-0.108	0.5517	0.009

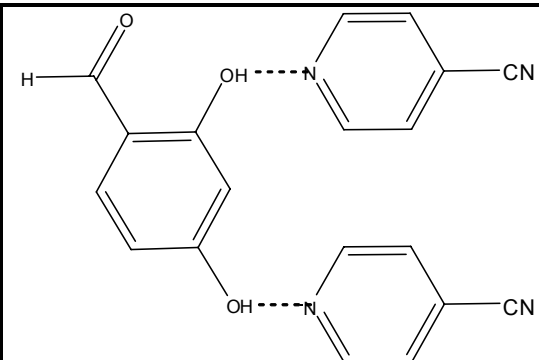
## Appendix

<p><b>Crystal structure details of 42% converted mixed 1:1 co-crystals of resorcinol and 1,2-di-(4-pyridyl)ethylene measured at 120 K</b></p>			
<b>a (Å)</b>	7.7682(4)	<b><math>\alpha</math> °</b>	94.4493(12)
<b>b (Å)</b>	9.7930(5)	<b><math>\beta</math> °</b>	104.8507(13)
<b>c (Å)</b>	11.0478(5)	<b><math>\gamma</math> °</b>	111.4950(13)
<b>V (Å<sup>3</sup>)</b>	742.068(1)	<b>Z</b>	2
<b>D<sub>xg</sub> (cm<sup>3</sup>)</b>	-	<b>Space group</b>	P-1 (2)
Atoms	x/a	y/b	z/c
C1	0.354	0.8051	0.6615
C2	0.373	0.8507	0.7893
C3	0.5508	0.8891	0.8796
C4	0.7115	0.8871	0.8493
C5	0.692	0.8437	0.7204
C6	0.5132	0.8024	0.6277
H21	0.2659	0.855	0.8134
H31	0.5622	0.9198	0.966
H41	0.8323	0.9134	0.9134
H61	0.4999	0.7732	0.5406
O1	0.1753	0.764	0.5736
O2	0.8534	0.8415	0.6928
H1	0.1755	0.726	0.4918
H2	0.8245	0.8133	0.6033
C11	0.8711	0.4897	-0.2886
C12	0.837	0.5361	-0.1799
C13	0.7474	0.4318	-0.112
C14	0.7028	0.2821	-0.1594
C15	0.7389	0.2448	-0.2699
C16	0.7434	0.4759	0.0013
C17	0.7825	0.6152	0.0571
C18	0.7389	0.6593	0.1866
C19	0.8085	0.8102	0.2362
C20	0.8202	0.8563	0.359
C21	0.6998	0.6133	0.3874
C22	0.6816	0.5591	0.2655
C26	0.6062	0.4473	0.0008
C27	0.6257	0.605	0.0538
N11	0.821	0.3454	-0.3364
N12	0.7675	0.7609	0.4359
C11	0.1289	0.5103	-0.3336
C12	0.163	0.4639	0.2886
C13	0.2526	0.5682	0.1799
C14	0.2972	0.7179	0.112
C15	0.2611	0.7552	0.1594
C16	0.2566	0.5241	0.2699
C17	0.2175	0.3848	-0.0571
C18	0.2611	0.3407	-0.1866
C19	0.1915	0.1898	-0.2362
C20	0.1798	0.1437	-0.359
C21	0.3002	0.3867	-0.3874
C22	0.3184	0.4409	-0.2655
C26	0.3938	0.5527	-0.0008
C27	0.3743	0.395	-0.0538
N11	0.179	0.6545	0.3364
N12	0.2325	0.2391	-0.4359

## Appendix

Crystal structure details of 1:1 co-crystals of 3,5-dihydroxy benzonitrile and 1,2-di-(4-pyridyl)ethane measured at 120 K			
<b>a (Å)</b>	8.8590(4)	<b>α °</b>	109.9067(13)
<b>b (Å)</b>	9.2056(5)	<b>β °</b>	98.4738(12)
<b>c (Å)</b>	11.0052(6)	<b>γ °</b>	94.2813(12)
<b>V (Å<sup>3</sup>)</b>	827.1(2)	<b>Z</b>	2
<b>D<sub>x</sub>g (cm<sup>3</sup>)</b>	1.282	<b>Space group</b>	P-1 (2)
Atoms	x/a	y/b	z/c
<b>O24</b>	0.2489	0.5896	0.0846
<b>O23</b>	0.5294	0.6702	-0.2349
<b>C15</b>	0.1342	0.499	-0.1394
<b>C13</b>	0.3958	0.6287	-0.0717
<b>C17</b>	0.2773	0.5378	-0.301
<b>N20</b>	-0.0923	0.3393	-0.4508
<b>C16</b>	0.1447	0.4816	-0.2682
<b>C18</b>	0.4028	0.6136	-0.2014
<b>C14</b>	0.2622	0.5742	-0.04
<b>C19</b>	0.0128	0.4027	-0.3706
<b>H13</b>	0.4841	0.6773	-0.0035
<b>H17</b>	0.2815	0.522	-0.3912
<b>H15</b>	0.0405	0.4599	-0.1203
<b>H23</b>	0.5991	0.7334	-0.1588
<b>H24</b>	0.3398	0.6337	0.1471
<b>N21</b>	0.4864	0.7379	0.2806
<b>N22</b>	1.2574	1.1425	1.0285
<b>C8</b>	1.0218	0.9837	0.8117
<b>C9</b>	1.0143	1.1335	0.897
<b>C2</b>	0.5521	0.7972	0.5128
<b>C3</b>	0.6791	0.901	0.5234
<b>C7</b>	0.8992	0.896	0.6928
<b>C1</b>	0.4593	0.7194	0.3909
<b>C10</b>	1.1508	0.9161	0.8399
<b>C11</b>	1.1339	1.2074	1.0024
<b>C5</b>	0.6116	0.8358	0.2914
<b>C4</b>	0.7089	0.9183	0.4083
<b>C12</b>	1.2634	0.9972	0.947
<b>C6</b>	0.7818	0.9902	0.6548
<b>H1</b>	0.3729	0.6481	0.3879
<b>H2</b>	0.5276	0.7801	0.5893
<b>H5</b>	0.6384	0.8497	0.2142
<b>H4</b>	0.7961	0.9888	0.4113
<b>H9</b>	0.9273	1.1858	0.8827
<b>H10</b>	1.163	0.8132	0.7844
<b>H11</b>	1.1233	1.3106	1.0584
<b>H12</b>	1.3492	0.9445	0.9634
<b>H7A</b>	0.9465	0.8534	0.6174
<b>H7B</b>	0.8429	0.8129	0.7084
<b>H6A</b>	0.8354	1.083	0.6515
<b>H6B</b>	0.7194	1.0181	0.7214

## Appendix

<b>Crystal structure details of 1:1 co-crystals of 2,4-dihydroxy benzaldehyde and 4-cyano pyridine measured at 120 K</b>			
<b>a (Å)</b>	6.3774(5)	<b><math>\alpha</math> °</b>	89.8480(12)
<b>b (Å)</b>	7.1407(5)	<b><math>\beta</math> °</b>	81.2542(13)
<b>c (Å)</b>	13.2920(7)	<b><math>\gamma</math> °</b>	74.2996(13)
<b>V (Å<sup>3</sup>)</b>	575.2(1)	<b>Z</b>	2
<b>D<sub>x</sub>g (cm<sup>3</sup>)</b>	1.399	<b>Space group</b>	P-1 (2)
Atoms	x/a	y/b	z/c
N1	0.8768	0.177	0.7681
N2	1.3329	0.216	1.0718
C13	1.115	0.1885	0.9258
C16	1.2365	0.2023	1.0075
C11	1.0977	0.1042	0.7548
C12	1.2217	0.1052	0.8304
C14	0.8846	0.2659	0.9409
C15	0.7764	0.2549	0.8601
H111	1.171	0.0474	0.69
H121	1.3773	0.0514	0.8186
H141	0.8069	0.3238	1.0049
H151	0.6204	0.3053	0.8701
O3	0.7144	0.4389	0.174
C1	0.6579	0.2261	0.5373
C3	0.5651	0.3076	0.371
C4	0.7687	0.3557	0.3432
O2	0.4223	0.3221	0.3042
O1	0.5971	0.1656	0.6309
C2	0.5132	0.2431	0.4675
C5	0.9119	0.3336	0.4146
C6	0.8615	0.2716	0.5105
C7	0.8278	0.4195	0.2428
H1	0.6924	0.1661	0.6782
H21	0.3785	0.2095	0.4858
H51	1.0479	0.3652	0.3964
H61	0.9616	0.2568	0.558
H71	0.9656	0.4489	0.2278
H2	0.4998	0.3436	0.2433